



micromachines

Micro/Nano Devices for Blood Analysis, Volume II

Edited by

Rui A. Lima, Susana Catarino and Graça Minas

Printed Edition of the Special Issue Published in *Micromachines*

Micro/Nano Devices for Blood Analysis, Volume II

Micro/Nano Devices for Blood Analysis, Volume II

Editors

Rui A. Lima

Susana Catarino

Graça Minas

MDPI • Basel • Beijing • Wuhan • Barcelona • Belgrade • Manchester • Tokyo • Cluj • Tianjin



Editors

Rui A. Lima

MEtRICs

Universidade do Minho

Guimarães

Portugal

Susana Catarino

Center for

MicroElectromechanical Systems

(CMEMS-UMinho) and

LABBELS

Universidade do Minho

Guimarães

Portugal

Graça Minas

Center for

MicroElectromechanical Systems

(CMEMS-UMinho) and

LABBELS

Universidade do Minho

Guimarães

Portugal

Editorial Office

MDPI

St. Alban-Anlage 66

4052 Basel, Switzerland

This is a reprint of articles from the Special Issue published online in the open access journal *Micromachines* (ISSN 2072-666X) (available at: www.mdpi.com/journal/micromachines/special-issues/micro_nano_devices_for_blood_analysis_v2).

For citation purposes, cite each article independently as indicated on the article page online and as indicated below:

LastName, A.A.; LastName, B.B.; LastName, C.C. Article Title. <i>Journal Name</i> Year , <i>Volume Number</i> , Page Range.
--

ISBN 978-3-0365-3229-5 (Hbk)

ISBN 978-3-0365-3228-8 (PDF)

© 2022 by the authors. Articles in this book are Open Access and distributed under the Creative Commons Attribution (CC BY) license, which allows users to download, copy and build upon published articles, as long as the author and publisher are properly credited, which ensures maximum dissemination and a wider impact of our publications.

The book as a whole is distributed by MDPI under the terms and conditions of the Creative Commons license CC BY-NC-ND.

Contents

About the Editors	vii
Preface to "Micro/Nano Devices for Blood Analysis, Volume II"	ix
Ahmed Fadlelmoula, Diana Pinho, Vitor Hugo Carvalho, Susana O. Catarino and Graça Minas Fourier Transform Infrared (FTIR) Spectroscopy to Analyse Human Blood over the Last 20 Years: A Review towards Lab-on-a-Chip Devices Reprinted from: <i>Micromachines</i> 2022 , <i>13</i> , 187, doi:10.3390/mi13020187	1
Violeta Carvalho, Inês M. Gonçalves, Andrews Souza, Maria S. Souza, David Bento and João E. Ribeiro et al. Manual and Automatic Image Analysis Segmentation Methods for Blood Flow Studies in Microchannels Reprinted from: <i>Micromachines</i> 2021 , <i>12</i> , 317, doi:10.3390/mi12030317	21
Junchao Hu, Zhian Jian, Chunxiang Lu, Na Liu, Tao Yue and Weixia Lan et al. New Method for Preparing Small-Caliber Artificial Blood Vessel with Controllable Microstructure on the Inner Wall Based on Additive Material Composite Molding Reprinted from: <i>Micromachines</i> 2021 , <i>12</i> , 1312, doi:10.3390/mi12111312	41
Zaidon T. Al-aqbi, Salim Albukhaty, Ameerah M. Zaroor, Ghassan M. Sulaiman, Khalil A. A. Khalil and Tareg Belali et al. A Novel Microfluidic Device for Blood Plasma Filtration Reprinted from: <i>Micromachines</i> 2021 , <i>12</i> , 336, doi:10.3390/mi12030336	55
Yang Jun Kang Microfluidic-Based Biosensor for Blood Viscosity and Erythrocyte Sedimentation Rate Using Disposable Fluid Delivery System Reprinted from: <i>Micromachines</i> 2020 , <i>11</i> , 215, doi:10.3390/mi11020215	65
Yang Jun Kang Blood Viscoelasticity Measurement Using Interface Variations in Coflowing Streams under Pulsatile Blood Flows Reprinted from: <i>Micromachines</i> 2020 , <i>11</i> , 245, doi:10.3390/mi11030245	91
Yang Jun Kang Experimental Investigation of Air Compliance Effect on Measurement of Mechanical Properties of Blood Sample Flowing in Microfluidic Channels Reprinted from: <i>Micromachines</i> 2020 , <i>11</i> , 460, doi:10.3390/mi11050460	111
Ezekiel O. Adekanmbi, Anthony T. Giduthuri and Soumya K. Srivastava Dielectric Characterization and Separation Optimization of Infiltrating Ductal Adenocarcinoma via Insulator-Dielectrophoresis Reprinted from: <i>Micromachines</i> 2020 , <i>11</i> , 340, doi:10.3390/mi11040340	131
Diana Pinho, Denis Santos, Ana Vila and Sandra Carvalho Establishment of Colorectal Cancer Organoids in Microfluidic-Based System Reprinted from: <i>Micromachines</i> 2021 , <i>12</i> , 497, doi:10.3390/mi12050497	151

Mariana S. Costa, Vitória Baptista, Gabriel M. Ferreira, Duarte Lima, Graça Minas and Maria Isabel Veiga et al.

Multilayer Thin-Film Optical Filters for Reflectance-Based Malaria Diagnostics

Reprinted from: *Micromachines* **2021**, *12*, 890, doi:10.3390/mi12080890 **163**

About the Editors

Rui A. Lima

Rui A. Lima is an associate professor at the Department of Mechanical Engineering, University of Minho (UMinho), and a researcher at the Mechanical Engineering and Resource Sustainability Center (MEtRICs, UMinho) and Transport Phenomena Research Center (CEFT), FEUP, University of Porto. His main research mostly focuses on microfluidics, nanofluidics and blood flow in biomedical microdevices. Currently, he lectures for several master's degree courses in mechanical, biomedical and industrial engineering. In the past, he has lectured for several master's degree courses in biomedical technology such as cardiovascular biomechanics and micro/nanotechnologies, and biomedical applications at the Bragança Polytechnic Institute (IPB). Currently, he also supervises several PhD and master's students in the field of mechanical and biomedical engineering.

Susana Catarino

Susana Oliveira Catarino received her PhD degree in biomedical engineering, from the University of Minho, Portugal, in 2014. She is currently an assistant researcher at the Center for Microelectromechanical Systems (CMEMS-UMinho) and in the LABBELS (Associate Laboratory on Biotechnology, Bioengineering and MicroElectromechanical Systems) at the same University. Starting in October 2016, she has also been a visiting assistant professor at the same institution, lecturing for the Department of Industrial Electronics, in the areas of modeling and simulation for microtechnologies, electronics, microsensors and microactuators. She has published 50 articles and book chapters, and 2 patents and has co-edited 1 book that was internationally distributed. She supervises several PhD and master theses, and several research fellows. She has also participated in 10 research projects, being the principal investigator for 2 of them. Her research interests include diagnosis and lab-on-a-chip devices, optical and acoustic sensors and actuators, and numerical studies of acoustic streaming and microfluidic devices.

Graça Minas

Graça Maria Henriques Minas is an associate professor at and the director of the Department of Industrial Electronics as well as a researcher in the CMEMS-UMinho (Center for Microelectromechanical Systems) and in the LABBELS (Associate Laboratory on Biotechnology, Bioengineering and MicroElectromechanical Systems) at University of Minho, Portugal. Her main research mostly focuses on biomedical microdevices, specifically on the lab-on-a-chip integration of electronic circuits; optical filters; and solid-state integrated sensors, biosensors and actuators in those LOC devices. She also develops organ-on-a-chip systems that aim to mimic human response to various chemicals in vitro. She lectures for master's degree courses in biomedical and physics engineering and in micro/nanotechnology as well as for the doctoral program of biomedical engineering in the field of biosensors, microelectronics and microsystems fabrication. She also supervises several PhD and master's students in those fields.

Preface to “Micro/Nano Devices for Blood Analysis, Volume II”

The development of micro- and nanodevices for blood analysis continues to be a growing interdisciplinary subject that demands the careful integration of different research fields. Particularly, such devices target the precise integration of mechanics, microfluidics, micro/nanotechnologies, chemistry, optics, electronics, materials engineering, informatics, biotechnology and medicine, among many other fields.

Microelectromechanical systems (MEMS) combine electrical, optical and mechanical components at the microscale level and are a result of continuous efforts in the miniaturization of mechanical microdevices. The integration of these devices with microflows, in the form of micropumps, microvalves or even sensors, has gained the interest of scientific communities dealing with fluid flow and transport phenomena happening at the microscale. Microfluidic systems have considerable advantages over macroscale devices, as they offer the ability to work with low power consumption, small samples and reagent volumes; provide good manipulation and control of samples; decrease the reaction times; and allow multiplexer and parallel operations to be carried out in a single step. Thus, microdevices have great potential in developing portable and point-of-care diagnostic devices, particularly for cellular and blood analyses. Moreover, the recent progress in nanotechnology is gaining popularity and has expanded its areas of application for microfluidic devices, which include the manipulation and analysis of flows on the scale of DNA, proteins and nanoparticles, which has led to the creation to a new field—nanoflows. In spite of the enormous scientific achievements that micro- and nanofluidics have had in recent decades, they are still considered in the early stages, with some drawbacks and challenges to overcome, such as the difficulty in achieving cost-effective, large-scale production and a complete understanding of the physics of fluids at the micro- and nanoscale levels. As a consequence, many research groups worldwide are devoting significant efforts to research on microfabrication and microfluidics to enhance the potential of such microdevices as portable and point-of-care diagnostic devices, particularly for blood analysis, as we target in this book.

Following the success of the Special Issue “Micro/Nano Devices for Blood Analysis”, which led to the publication of a book with the same title [1], once again, we invited the scientific community to participate in and submit their research to the Special Issue “Micro/Nano Devices for Blood Analysis, Volume II”. Researchers from different areas and backgrounds cooperated actively and submitted high-quality research, focusing on the latest advances and challenges in micro- and nanodevices for diagnostics and blood analysis, micro- and nanofluidics, technologies for flow visualization and diagnosis, biochips, organ-on-a-chip and lab-on-a-chip devices, and their applications to research and industry. Thus, this book assembles ten scientific documents, including comprehensive reviews and experimental research papers, in the areas of microsystems design, simulation, experimental characterization and diagnosis.

In this Special Issue, Fadlelmoula et al. [2] presented a review of current Fourier Transform Infrared (FTIR) spectroscopy techniques and their potential for human blood analysis. The authors discussed advancements of the technology and its variations in recent decades and reported the latest research focusing on FTIR spectroscopy applications in the biological field, which distinguish between healthy and pathological samples and help in the diagnosis of different diseases. Finally, the authors explored the current challenges of integrating FTIR into microfluidic and lab-on-a-chip

devices [2].

In another review on blood flows and RBC characterization and visualization, Carvalho et al. [3] carefully reviewed and compared different manual and automatic image analysis segmentation methods for blood flow studies in microfluidic domains. The authors discussed the role and importance of image analysis in the processing of blood flow data when acquired from high-speed video microscopy. The authors showed that, while manual methods are reliable, they are highly time-consuming, user-intensive and repetitive, and the results can be subject to user-induced errors. For that purpose, the authors presented, discussed and compared manual and automatic methods that are able to achieve similar accuracy in the data analysis, both to individually track RBCs and to measure cell-free layer thicknesses in different kinds of microchannels [3].

In addition to these reviews, this Special Issue contains several research papers that cover different subjects related to microfluidic structures, cell characterization, data analysis and diagnosis. Hu et al. [4] presented a novel method of creating small-diameter artificial vascular grafts (with diameters below 6 mm), which can form a controllable, multi-material composite microstructure on the inner wall of a blood vessel. The authors combined different additive composite molding in the inner walls and outer walls of artificial vessels to promote endothelialization and to ensure the stability, good structure and mechanical performance of the structure [4].

Al-aqbi et al. [5] also developed novel microfluidic devices for blood applications. The authors proposed a new geometry for blood plasma filtration based on a nano-junction formed by dielectric breakdown. The authors achieved the on-chip filtration and out-chip collection of blood plasma from a whole blood sample, with a high extraction yield of 62%, within less than 5 min. The authors characterized the filtered plasma, showing that it presented a low concentration of analytes from whole blood, confirming the success of the proposed microdevice [5].

Adekanmbi et al. [6] focused on the design, numerical modeling and simulation of a microfluidic device for the dielectrophoretic separation of infiltrating ductal adenocarcinoma cells (ADCs) from isolated peripheral blood mononuclear cells (PBMCs). The proposed device successfully combined a 1.4 mm long, Y-shaped microfluidic channel with semi-circular insulating constrictions and dielectrophoresis promoted by a DC electric actuation with varying voltage conditions [6].

Kang [7] presented a microfluidic-based biosensor for the measurement of blood viscosity and red blood cells' (RBCs') sedimentation rates. The author used two air-compressed syringes to deliver blood samples and a reference fluid into a T-shaped microfluidic channel and measured the average velocity of the fluids using micro-particle image velocimetry and digital image processing. The sedimentation rate was quantified based on the analysis of the image intensity of the blood sample over time. Then, blood viscosity was determined using a parallel co-flowing method with a correction factor. The author was able to measure blood viscosity and the RBCs' sedimentation rates consistently for samples with hematocrit 30%, 40% and 50% [7].

The same author [8] also designed a T-shaped microfluidic device with two inlets, one outlet, two guiding channels (one for the blood sample and the other for the reference fluid) and one co-flowing channel for the measurement of blood viscoelasticity through an analysis of the interface variations in co-flowing streams of the sample and the reference fluid. For that purpose, the author proposed a sinusoidal flow-rate pattern to pump the blood samples, while the reference fluid was pumped at a constant flow rate. Based on that setup, the author measured the compliance (influenced by the period of the flow rate) and the viscosity of the fluid (dependent on the hematocrit and solvent). Finally, from those variables, the author analytically calculated and monitored the viscoelasticity of

the blood samples [8].

Related to his other published works, Kang [9] also studied, under periodic on–off blood flows, the contributions of air compliance to dynamic blood flows in microfluidic channels for successful evaluation of the mechanical properties of blood samples. The author analyzed the image intensity and interface in a co-flowing channel and concluded that air cavities in the blood sample syringe contributed to delays in the transient behaviors of blood flows, hindering the quantification of RBC aggregation and blood viscoelasticity [9].

In addition to the above work, which focused on the mechanical characterization of blood samples and RBCs in microfluidic devices, one paper, presented by Pinho et al. [10], explored the potential integration of microfluidic structures in organ-on-a-chip technologies, targeting personalized cancer medicine. The authors developed preclinical models of colorectal cancer by combining microfluidic technologies with 3D, patient-derived tumor organoid models. The authors used a low-cost microfluidic device to culture and expand the colorectal cancer organoids and evaluated their viability and proliferative activity, having concluded that the developed chip had the potential to generate organotypic structures for disease modeling and drug screening applications [10].

Finally, the last paper, while not being related to microfluidics, presents a novel microdevice for malaria diagnosis based on blood analysis. Costa et al. [11] designed, simulated and experimentally characterized bandpass optical filters based on multiple layers of thin films for implementation in a device for reflectance-based malaria diagnosis. The authors proposed the detection of malaria parasites in RBCs through the optical quantification of hemozoin. For that purpose, a set of eight thin-film optical filters, based on multilayer stacks of MgO/TiO₂ and SiO₂/TiO₂ thin films, with high transmittance and low full width at half maximum at specific wavelengths in the 400 nm–800 nm range of the optical spectrum, was designed and characterized. The results showed that optical measurements with the developed filters allowed one to distinguish between healthy and malaria-infected samples, up to a detection limit of 12 parasites/L of RBCs.

As Guest Editors, we hope this book can, once again, provide an opportunity for the biomedical, biotechnology and engineering communities to access novel information and knowledge, particularly in the application of micro- and nanofluidics in the biomedical field. We believe that this book can contribute significantly to the scientific community as a demonstration of the latest results, achievements, breakthroughs, challenges and trends in micro- and nanodevices for diagnostics and blood analysis, cell characterization, micro- and nanofluidics, flows visualization, MEMS, biochips, organ-on-a-chip and lab-on-a-chip devices, and their application to research and industry.

As a final remark, we acknowledge, congratulate and thank all of the researchers and authors for submitting and contributing their original manuscripts to this Special Issue as well as the reviewers for their time, efforts and careful participation in the peer-review processes, which were essential to improving the quality of these documents.

References

1. Lima, R.A.; Minas, G.; Catarino, S.O., Eds. *Micro/Nano Devices for Blood Analysis*, 1st Edition. MDPI: Basel, Switzerland, 2019.
2. Fadlelmoula, A.; Pinho, D.; Carvalho, V.H.; Catarino, S.O.; Minas, G. Fourier Transform Infrared (FTIR) Spectroscopy to Analyse Human Blood over the Last 20 Years: A Review towards Lab-on-a-Chip Devices. *Micromachines* 2022, 13, 187.

3. Carvalho, V.; Gonçalves, I.M.; Souza, A.; Souza, M.S.; Bento, D.; Ribeiro, J.E.; Lima, R.; Pinho, D. Manual and Automatic Image Analysis Segmentation Methods for Blood Flow Studies in Microchannels. *Micromachines* 2021, 12, 317.
4. Hu, J.; Jian, Z.; Lu, C.; Liu, N.; Yue, T.; Lan, W.; Liu, Y. New Method for Preparing Small-Caliber Artificial Blood Vessel with Controllable Microstructure on the Inner Wall Based on Additive Material Composite Molding. *Micromachines* 2021, 12, 1312.
5. Al-aqbi, Z.T.; Albukhaty, S.; Zarzoor, A.M.; Sulaiman, G.M.; Khalil, K.A.A.; Belali, T.; Soliman, M.T.A. A Novel Microfluidic Device for Blood Plasma Filtration. *Micromachines* 2021, 12, 336.
6. Adekanmbi, E.O.; Giduthuri, A.T.; Srivastava, S.K. Dielectric Characterization and Separation Optimization of Infiltrating Ductal Adenocarcinoma via Insulator-Dielectrophoresis. *Micromachines* 2020, 11, 340.
7. Kang, Y.J. Microfluidic-Based Biosensor for Blood Viscosity and Erythrocyte Sedimentation Rate Using Disposable Fluid Delivery System. *Micromachines* 2020, 11, 215.
8. Kang, Y.J. Blood Viscoelasticity Measurement Using Interface Variations in Coflowing Streams under Pulsatile Blood Flows. *Micromachines* 2020, 11, 245.
9. Kang, Y.J. Experimental Investigation of Air Compliance Effect on Measurement of Mechanical Properties of Blood Sample Flowing in Microfluidic Channels. *Micromachines* 2020, 11, 460.
10. Pinho, D.; Santos, D.; Vila, A.; Carvalho, S. Establishment of Colorectal Cancer Organoids in Microfluidic-Based System. *Micromachines* 2021, 12, 497.
11. Costa, M.S.; Baptista, V.; Ferreira, G.M.; Lima, D.; Minas, G.; Veiga, M.I.; Catarino, S.O. Multilayer Thin-Film Optical Filters for Reflectance-Based Malaria Diagnostics. *Micromachines* 2021, 12, 890.

Rui A. Lima, Susana Catarino, Graça Minas

Editors

Review

Fourier Transform Infrared (FTIR) Spectroscopy to Analyse Human Blood over the Last 20 Years: A Review towards Lab-on-a-Chip Devices

Ahmed Fadlelmoula ^{1,2}, Diana Pinho ³, Vitor Hugo Carvalho ^{4,5}, Susana O. Catarino ^{1,2} and Graça Minas ^{1,2,*}

- ¹ Center for MicroElectromechanical Systems (CMEMS-UMinho), University of Minho, 4800-058 Guimaraes, Portugal; id9247@alunos.uminho.pt (A.F.); scatarino@dei.uminho.pt (S.O.C.)
² LBBELS–Associate Laboratory, Braga/Guimaraes, Portugal
³ International Iberian Nanotechnology Laboratory (INL), 4715-330 Braga, Portugal; diana.pinho@inl.int
⁴ Algoritmi Research Center, University of Minho, 4800-058 Guimaraes, Portugal; vcarvalho@ipca.pt
⁵ 2Ai, School of Technology, IPCA, 4750-810 Barcelos, Portugal
* Correspondence: gminas@dei.uminho.pt

Abstract: Since microorganisms are evolving rapidly, there is a growing need for a new, fast, and precise technique to analyse blood samples and distinguish healthy from pathological samples. Fourier Transform Infrared (FTIR) spectroscopy can provide information related to the biochemical composition and how it changes when a pathological state arises. FTIR spectroscopy has undergone rapid development over the last decades with a promise of easier, faster, and more impartial diagnoses within the biomedical field. However, thus far only a limited number of studies have addressed the use of FTIR spectroscopy in this field. This paper describes the main concepts related to FTIR and presents the latest research focusing on FTIR spectroscopy technology and its integration in lab-on-a-chip devices and their applications in the biological field. This review presents the potential use of FTIR to distinguish between healthy and pathological samples, with examples of early cancer detection, human immunodeficiency virus (HIV) detection, and routine blood analysis, among others. Finally, the study also reflects on the features of FTIR technology that can be applied in a lab-on-a-chip format and further developed for small healthcare devices that can be used for point-of-care monitoring purposes. To the best of the authors' knowledge, no other published study has reviewed these topics. Therefore, this analysis and its results will fill this research gap.

Keywords: blood cells; fourier transform infrared (FTIR) spectroscopy; functional group; lab-on-a-chip



Citation: Fadlelmoula, A.; Pinho, D.; Carvalho, V.H.; Catarino, S.O.; Minas, G. Fourier Transform Infrared (FTIR) Spectroscopy to Analyse Human Blood over the Last 20 Years: A Review towards Lab-on-a-Chip Devices. *Micromachines* **2022**, *13*, 187. <https://doi.org/10.3390/mi13020187>

Academic Editor: Nam-Trung Nguyen

Received: 31 December 2021

Accepted: 24 January 2022

Published: 26 January 2022

Publisher's Note: MDPI stays neutral with regard to jurisdictional claims in published maps and institutional affiliations.



Copyright: © 2022 by the authors. Licensee MDPI, Basel, Switzerland. This article is an open access article distributed under the terms and conditions of the Creative Commons Attribution (CC BY) license (<https://creativecommons.org/licenses/by/4.0/>).

1. Introduction

Millions of blood test analyses are performed every day worldwide in order to provide blood diagnostic services for the patients [1]. Usually, these tests are performed in clinical laboratories, simultaneously using different devices and relying on different specialties [2]. These devices are needed to run routine blood tests [2] and examine multiple parameters to assist the physicians in haematology-, chemistry-, and immunology-related diagnosis, among others. They require human resources, dedicated facilities, and time, which, in an ideal device, should be less than one hour from taking a sample to printing out the results [3,4]. Moreover, the reagents needed to run all these tests are expensive, and most of them are toxic, having a significant direct and indirect effect on the environment [5].

Diagnostic devices currently available on the market rely on the same measuring techniques developed in the last century (mainly spectrophotometry or electrochemical assays) [6]. Meanwhile, viruses, bacteria, and fungi are rapidly evolving [7], pushing further the need to develop new, quick, and reliable diagnostic tools. The primary, commercially available measuring techniques for such devices are spectrophotometry, enzyme-linked

immunosorbent assay (ELISA), electrophoresis, and blood cell counting or complete blood count (CBC). However, all of these methods have limitations. In ultraviolet–visible (UV–VIS) spectrophotometry, the main limitation is the requirement for sample and setup preparation time to avoid light interferences [8]. ELISA limitations are related to the cost of the assays due to the use of antibodies, the risk of cross-reactivity, the high background noise, and extended analysis time [9]. Electrophoresis requires a large sample for the assays, as well as high analysis precision [10]. Finally, CBC limitations are related to the manual examination of blood smears, difficulty recognising abnormal red cell shapes (such as fragmented cells), and high running costs [11]. Hence, the pressing need for new, fast, and precise analysing techniques.

Fourier transform infrared (FTIR) spectroscopy is a field that has undergone significant development over the past decade, promising easier, more rapid, and more objective diagnoses [12,13]. FTIR spectroscopy studies the interactions between matter and electromagnetic radiation that appear in the form of a spectrum. Each molecule has a spectrum fingerprint that makes it unique and allows it to be distinguished from other molecules [14]. FTIR spectroscopy is also an effective and nondestructive method for monitoring cellular alterations [15,16]. FTIR spectral analysis has allowed the characterisation of several organs' diseases, as well as the quantification of different biomolecules such as proteins [16], nucleic acids [17,18], and lipids [19]. Several research documents highlighting the importance of spectroscopic techniques in cancer detection have been published in the literature [15,20,21]. FTIR focuses on the differentiation and characterisation of cells and tissues by looking at individual bands or groups to precisely identify the molecular conformations, bonding types, functional groups, and intermolecular interactions that compose the specimen [13,20]. Thus, this paper describes the main concepts and terminologies related to FTIR and presents the latest published research focusing on FTIR spectroscopy technology and its integration in lab-on-a-chip devices for application in the biological field. To the best of the authors' knowledge, no other studies have reviewed these topics, making this review the first to fill this research gap.

The paper is organised into five sections. Section 1 presents an introductory overview and the primary motivation guiding the study. Section 2 presents FTIR spectroscopy's theoretical, conceptual elements and clarifies the salient terminology, including the concepts of infrared (IR) regions, radiation, molecular vibration, FTIR, and Michelson Interferometer. Section 3 describes the methods used in the presented study, while Section 4 offers the results of the analysis of twenty-year-long research on the application of FTIR spectroscopy in the biological field, focusing on the possibility of applying this technology in lab-on-a-chip devices. Finally, Section 5 presents the conclusion and future trends.

2. Theoretical Considerations

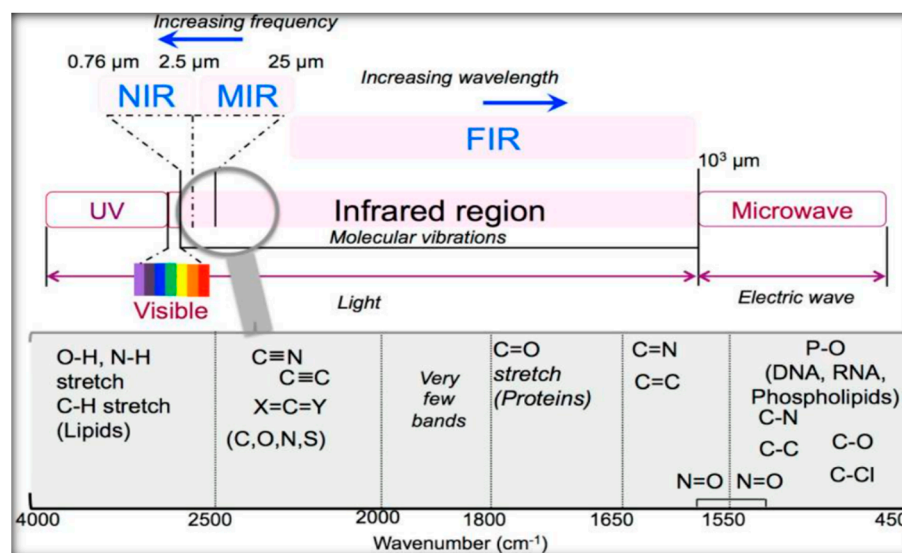
Here the terminologies and concepts associated with FTIR spectroscopy, namely the IR region, IR radiation and molecular vibrations in biological matters, FTIR techniques and Michelson interferometer, are presented.

2.1. Infrared Region

IR radiation is a group of electromagnetic waves (EMR) with wavelengths longer than visible radiation, invisible to the human eye. The IR region of the electromagnetic spectrum ranges in wavelengths from 0.8–100 μm , illustrated in Table 1 [22,23]. Typically, the IR is broken into three ranges, near-IR, mid-IR, and far-IR. Most of the IR used in medical applications are in the mid-IR range, considering radiation from the electromagnetic spectrum, in the wavenumber interval from 4000 cm^{-1} to 400 cm^{-1} . The frequency of the absorbed radiation is responsible for each subatomic vibrational interaction, as schematised in Figure 1.

Table 1. InfraRed Regions [22,23].

Region	Wavelength (μm)	Wavenumbers (cm^{-1})	Frequency ($\times 10^{14}$ Hz)
Near-IR	0.8–2.5	12,500–4000	3.75–1.2
Mid-IR	2.5–25	4000–400	1.2–0.12
Far-IR	25–100	400–100	0.12–0.03
Frequently Used	2.5–15	4000–670	1.2–0.20

**Figure 1.** Scheme of the optical spectrum, focusing on the infrared region. Reprinted from [23], MDPI, under a Creative Commons Attribution (CC BY) license.

2.2. IR Radiation and Molecular Vibrations in Biological Matter

As a type of electromagnetic wave, IR propagates energy and momentum, with properties similar to both a wave and a particle—the photon. IR is emitted or absorbed by molecules as they change their rotational, vibrational motions. It excites wave modes in a molecule by changing them instantaneously, making it a helpful frequency variation for studying the molecular energy states with correct symmetry. Therefore, IR chemical analysis studies the absorption and transmission of photons in the IR region [24]. The IR spectrum of biological samples consists of a combination of the characteristic absorption bands of proteins, lipids, nucleic acids, and carbohydrates within that sample [25,26].

The protein absorption bands are often assigned to amino acid side groups or peptide backbone in the 1700 cm^{-1} – 1500 cm^{-1} range. The vibrational modes of the peptide backbone produce the amide I and II bands. The amide I band (1700 cm^{-1} – 1600 cm^{-1}) is mainly associated with the bending vibration of the N–H bond. The bands of amides I and II are usually used to analyse the secondary protein structure [27]. The presence of absorption bands at 1450 cm^{-1} and 1400 cm^{-1} is due to asymmetric and symmetric methyl bending modes, respectively [28].

In the spectra of lipids, absorption bands are found in numerous spectral regions: the range of 3050 cm^{-1} – 2800 cm^{-1} for asymmetric and symmetric stretching vibrations of $-\text{CH}_2$ and $-\text{CH}_3$, the range of 1500 cm^{-1} – 1350 cm^{-1} for deformation vibrations of $-\text{CH}_2$ and $-\text{CH}_3$ from the acyl chains of lipids, the range of 1745 cm^{-1} – 1725 cm^{-1} for symmetric stretching vibrations of ester–carbonyl bond ($\text{C}=\text{O}$), and the range of 1270 cm^{-1} – 1000 cm^{-1} for odd (1240 cm^{-1}) and symmetric (1080 cm^{-1}) vibrations of $-\text{PO}_2^-$ in phospholipids [29]. The IR spectra of nucleic acids are characterised in four spectral regions: the region of 1780 cm^{-1} – 1550 cm^{-1} for in-plane vibrations of double bonds of bases, the region of 1550 cm^{-1} – 1270 cm^{-1} for the deformation vibrations of bases that include the sugar vibrations, the region of 1270 cm^{-1} – 1000 cm^{-1} for vibrations of $-\text{PO}_2^-$ and, finally, the region of 1000 cm^{-1} – 780 cm^{-1} for the vibrations of the sugar-phosphate backbone [30]. The carbohy-

drate spectra contain bands in the following ranges: the region of 3600 cm^{-1} – 3050 cm^{-1} is assigned to the stretching vibration of O-H, the range of 3050 cm^{-1} – 2800 cm^{-1} to the stretching vibrations of $-\text{CH}_3$ and $-\text{CH}_2$, the region of 1200 cm^{-1} – 800 cm^{-1} to the stretching vibrations of the C-O/C-C species, and, finally, the 1500 cm^{-1} – 1200 cm^{-1} relates to the deformational modes of the CH_3/CH_2 species [31]. In the blood analysis applications, the spectral bands of 3000 cm^{-1} – 2800 cm^{-1} are the most relevant ones for analysing red blood cells and platelets, while for the white blood cells, the most relevant band ranges are 513 cm^{-1} – 1445 cm^{-1} . Thus, those targeted cells and corresponding spectral bands are the most used for blood analysis, particularly lab-on-a-chip applications.

2.3. Fourier Transform Infrared Spectroscopy (FTIR) Techniques

FTIR spectroscopy is a technique used to obtain the absorption or emission infrared spectrum of a solid, liquid, or gas [14,32]. The FTIR spectrometer simultaneously collects high-resolution information over a wide spectral range (between 4000 and 400 cm^{-1}), a distinct advantage over a dispersive spectrometer, which estimates power over a narrow range of frequencies at once. The aim of spectroscopy techniques (FTIR or bright perceptible (UV–Vis) spectroscopy) is to quantify how much light a sample absorbs at each frequency [14]. The most direct approach, the “dispersive spectroscopy” method, consists of focusing a monochromatic light beam at a sample, measuring the amount of absorbed light, and recalculating it for each frequency [14]. Fourier transform spectroscopy is a less instinctive approach for obtaining similar data. Rather than focusing a monochromatic (single frequency) light emission at the sample, this strategy might focus a bar, or array, which contains numerous frequencies of light at once and measures how much of that beam is absorbed by the sample. Then, the wave is changed to contain a different mixture of frequencies giving a second data point. This cycle is repeated many times within a short period of time, and the information is acquired by a computer. For instance, the wave plotted in Figure 2, called an interferogram, is created by applying a broadband light source—one that contains the entire range of frequencies to be estimated. The light sparks into a Michelson interferometer (detailed in the next section), consisting of a special array of mirrors, one of which is moved by a motor. As this mirror moves, each light frequency in the column is occasionally obstructed, mediated, impeded, and transmitted by the interferometer. The different frequencies are tweaked at different rates so that the column exiting the interferometer has a different range at each second or mirror position [14,32].

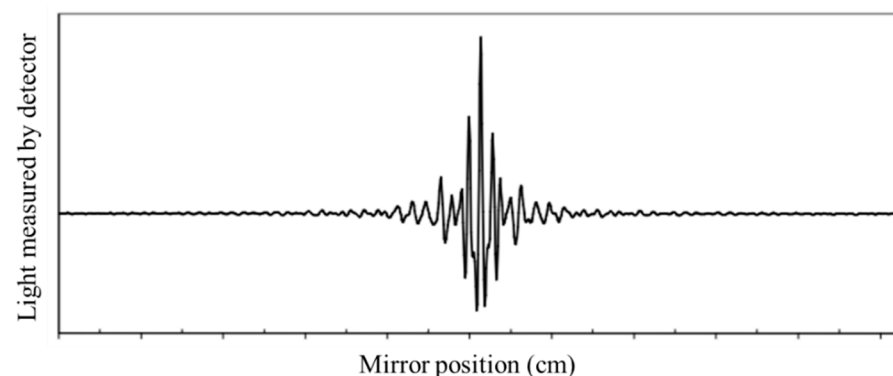


Figure 2. Example of a general FTIR interferogram. The central peak is positioned at the ZPD position (zero path difference or zero retardation), where the maximal amount of light passes through the interferometer to the detector.

Computational postprocessing based on Fourier frequencies is required to calculate the results (light pickup for each frequency) from the coarse raw information (light pickup for each mirror position), as presented in the example of Figure 2 [14,32]. Then, the Fourier transform converts a space (for this situation, the mirror’s distance in cm) into its opposite space (wavenumbers in cm^{-1}).

The main limitations of FTIR spectroscopy relate to the tissue depth penetration of the infrared light, which only allows biochemical analysis of the tissues up to a few dozens of micrometres [20]. Additionally, in the conventional FTIR spectroscopy, which works in transmission mode and consequently with no incidence angle between emitter and sample, there is difficulty in assuring the reproducibility of the spacer thickness when using liquid samples [33].

The attenuated total reflectance Fourier transform (ATR-FTIR) technique as a complementary technique has helped FTIR spectroscopy overcome this limitation. ATR-FTIR is a particular FTIR spectroscopy method, which measures the reflected signal from a sample. In this reflectance setup, the IR radiation passes through a crystal with a high refractive index (typically with an angle of 45°) and undergoes total internal reflection before exiting the crystal and being directed to an IR detector [33,34]. ATR-FTIR has a lower penetration depth than conventional FTIR (around 200 nm) but, since it measures the reflected light, it is an adequate method for measuring high absorbing and high thickness samples that typically do not allow the transmission of IR radiation [33]. Additionally, this technique can direct measurements of gas, fluidic and thin-film solid-state samples without complex sample preparation and with enhanced surface sensitivity [33,34].

Finally, microscopic FTIR (micro-FTIR) [35] relates to another particular FTIR technique that couples an IR spectrometer to a visible light microscope in order to achieve better sensitivity when detecting condensed-phase compounds [36] and is adequate for measuring solid or liquid thin films samples. In this technique, the microscope focuses the IR laser beam on the sample, and the measurement mainly comes from the target focal point, meaning that even a short displacement in the laser beam or the sample could provide a significant difference in the results. Therefore, micro-FTIR distinguishes by allowing local measuring of a particular point in the sample, while the conventional FTIR gives the average information from a complete homogenised sample [35,36].

Besides helping to identify organic compounds based on their specific IR spectral fingerprint, FTIR also has a relevant role in detecting alterations or pathological states of the molecules and samples, leading to different spectra between patients and healthy controls, as presented in several examples in Section 4. In the presence of pathology, the IR spectrum of a sample will change, either by changing its intensity or shifting its peak frequencies [37]. These shifts can be due to multiple chemical alterations in the molecules' composition, including weakening of the bonds, decreasing mass of the molecules, or even shifting the stretching vibrations due to temperature variations, which will change the vibrational frequencies of the bands. More details on this can be found elsewhere [37].

2.4. Michelson Interferometer

The Michelson Interferometer technique was adapted for FTIR so that the light from the polychromatic IR source, effectively a blackbody radiator, is collimated and directed onto a beam splitter, with 50% of the photons by the fixed mirror and 50% transmitted by the movable mirror [32]. In this configuration, light is reflected from the two mirrors back to the beam splitter, and some fraction of the original light passes into the sample compartment Figure 3.

There, the light is focused on the sample. When leaving the sample compartment, the light is refocused on the detector. The difference in the optical path length between the two mirrors to the interferometer is known as the retardation or optical path difference (OPD) [32]. An interferogram (as in Figure 2) is obtained by varying the retardation and recording the signal from the detector for different retardation values. When no sample is present, the interferogram profile depends on the variation of the source intensity and splitter efficiency with wavelength. This results in a maximum at zero retardation when there is constructive interference at all wavelengths, followed by a series of wiggles [32]. This problem is critical in the case of zero default when there is constructive interference within the smallest wavelengths followed by a series of wiggles. The location of the null default is determined by locating the purpose of the excessive intensity within the

interferogram. When a pattern is given away, the course interferogram is modulated with the aid of the absorption bands within the pattern (as exemplified in Figure 3) [32].

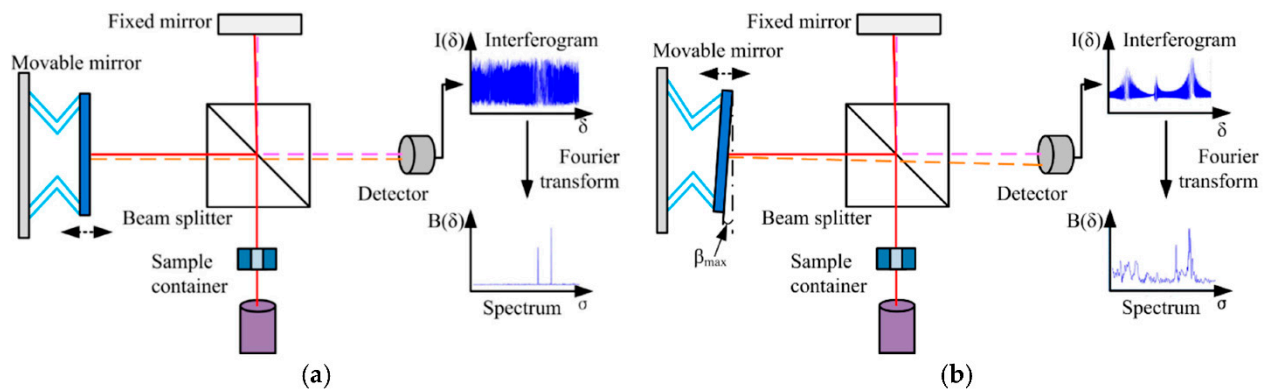


Figure 3. Schematic diagram of a Michelson interferometer configured for FTIR. (a) An ideal Michelson interferometer; (b) a Michelson interferometer with the movable mirror tilting. The continuous and dashed lines represent the different directions of light. Reprinted from [32], MDPI, under a Creative Commons Attribution (CC BY) license.

3. Methods

The research and data collecting strategy was based on evaluating a wide scale of papers (matching the topic keywords) published in the FTIR spectroscopy field, in the last decades, with all adequate reference and copyright permissions. For that, a comprehensive electronic search on ScienceDirect, Scopus and PubMed databases was performed (up to October 2021, Q3), as well as a direct search on different publishers' specific databases, such as MDPI, Wiley, or Nature, among others. Search keywords included: FTIR, spectroscopy, optics, infrared, blood, blood cells, Functional Group, Michelson Interferometer, lab-on-a-chip, microfluidics, microdevice and diagnostics. The search strategy was established by combining several keywords and using AND/OR Boolean operators. The relevant studies resulting from the database search were manually analysed to identify other potential studies to be included. The exclusion criteria were: reviews, comments, overviews, case reports, viewpoints and perspectives, as well as documents reporting tests with data ambiguity. Studies not written in the English language were also excluded, as well as duplicate results. From there, titles and abstracts were screened. All abstracts were read, and those that did not fit the purpose of this review were excluded. The information regarding the application, quantitative outcomes, reported study limitations, and other relevant comments were selected and extracted from the remaining articles. Specifically, the authors selected papers that reported FTIR spectroscopy for analysing between normal blood samples and pathological blood samples for cancer detection, HIV early recognition in pregnant women, and blood grouping identification, among others. These applications were chosen to illustrate the wide range of FTIR applications. Finally, the most important conclusions and limitations on the analysed papers were summarised.

4. Results

This section presents the data collection results examining the most relevant studies over the last twenty years addressing FTIR in the biological field, organised by their application field.

4.1. Collection of Data Seeking Applications of FTIR Spectroscopy

FTIR is widely used as a diagnostic method to analyse different materials and samples. According to the PubMed search results, FTIR spectroscopy was first studied as a new potential method in 1972, and until now (2021, Q3), more than 76,900 papers have been published on FTIR spectroscopy. A few years later, in 1982, researchers in the biological

field recognised the potential of the FTIR techniques and their suitability for diagnostics, including diagnoses of a long list of diseases that included cancer, microbes, bacteria, and viruses detection. The number of papers relating to FTIR published in the biological field in 2021 (up to Q3) is around 4810. Figure 4a,b illustrate the evolution of FTIR studies over the last two decades.

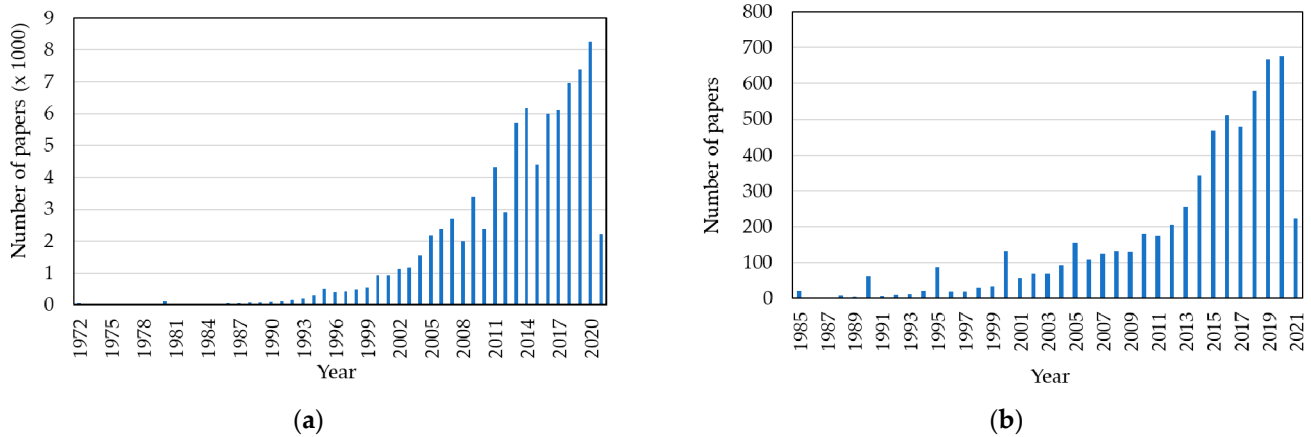


Figure 4. Published papers focusing FTIR: (a) Overall papers, since 1972; (b) papers in the biological field, since 1985 (until 2021, Q3).

In particular, by analysing the PubMed search results, a short number of papers addressed the use of FTIR spectroscopy to analyse and distinguish between normal blood sample cells and pathological blood samples. From the research undertaken until 2021, this number is less than 100 (Figure 5).

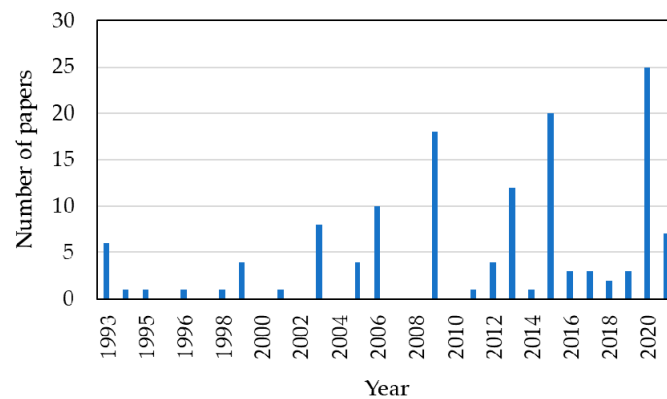


Figure 5. Published papers focusing FTIR for addressing differentiation between normal/pathological blood samples, from 1999 until 2021 (Q3).

Figure 6 summarises the number of published papers considering the FTIR subject (total of 76,900 papers) and its specificity in the application of the biology domain (4810) and subdomain for distinguishing between normal and pathological blood samples (around 100).

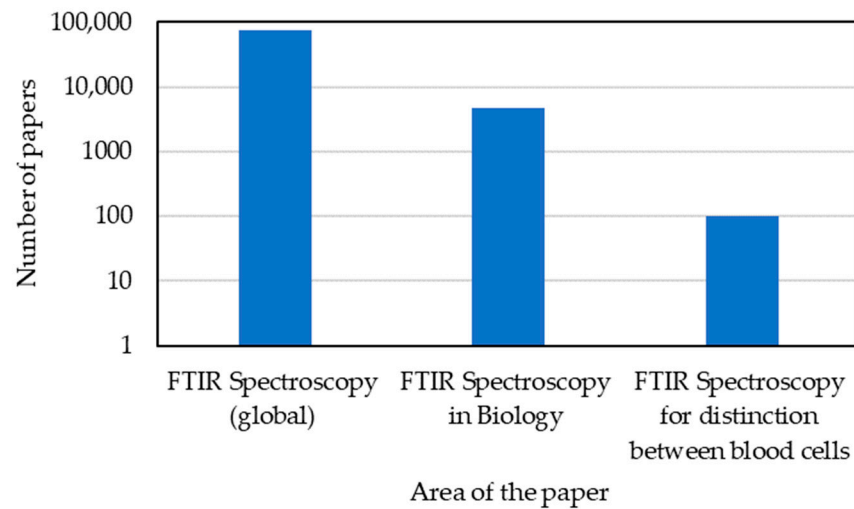


Figure 6. Summary of the total published papers focusing FTIR from 1999 until 2021 (Q3).

4.2. Applications of FTIR Spectroscopy in Cancer Diagnosis

Among the different spectroscopic techniques developed to distinguish between normal and cancerous blood tissues, Fourier transformed spectroscopy has shown tremendous potential. Additionally, biomedicine’s IR-based techniques have become a reality with a large amount of information accumulated from clinical studies, trials, and developments [38–40].

In 2013, FTIR spectroscopy was applied to study healthy and cancerous blood samples, using a diffuse reflectance technique from SHIMADZU 8000 series FTIR spectrophotometer. The spectra of cancerous and healthy blood were registered at a resolution of 4 cm^{-1} in the region of 900 cm^{-1} to 2000 cm^{-1} , as observed in Figure 7a. The obtained results show that the bands of proteins, lipids, carbohydrates, and nucleic acids from cancerous samples are clearly different from the normal ones dominated by two absorption bands at 1643 cm^{-1} – 1550 cm^{-1} , known as amide I and amide II. Amide I appears from the C=O stretching vibrations and amide II from the C–N stretching and CNH bending vibrations. This wavelength band looks strong and sharp in a healthy blood sample [38], as seen in Figure 7b.

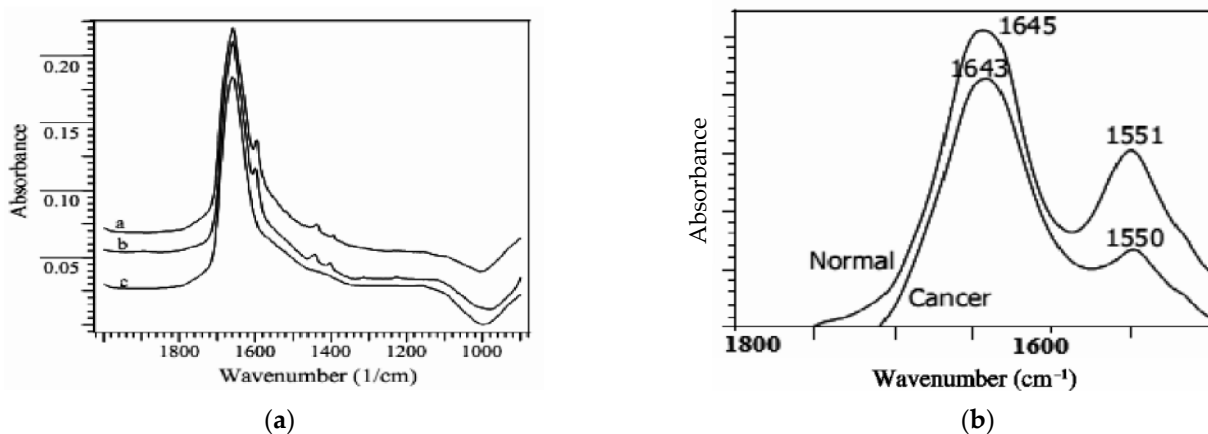


Figure 7. (a) FTIR absorption spectra of ‘a’ cancerous blood, ‘b’ normal blood and ‘c’ water samples using air as a reference; (b) detail of the FTIR absorption spectra of the normal and cancerous blood. Reprinted from [38], Copyright 2010 Convener, MMSETLSA-2009, with permission from the authors.

In 2016, label-free FTIR was used for early cancer detection in blood samples. This technique allowed detecting and verifying spectral biomarker candidate patterns to detect non-small cell lung carcinoma (NSCLC). The study was conducted on 161 patients where

blood serum and plasma samples were analysed using an automatic FTIR spectroscopic system, together with pattern recognition algorithms, such as Monte Carlo cross-validation, linear discriminant analysis and random forest classification. Marker patterns for cancer discrimination (both from squamous-cell carcinoma and adenocarcinoma patients) from clinically relevant disease control patients were identified in FTIR spectra of blood samples. The analysis was constrained to the respective C–H-stretching in the 2800 cm^{-1} – 3200 cm^{-1} region and the fingerprint regions 1750 cm^{-1} – 875 cm^{-1} [39]. Accuracy of up to 79% was recorded [39]. According to the authors, the study demonstrates the applicability of FTIR spectroscopy using blood for lung cancer detection. Evidence for cancer subtype discrimination was given. With improved performance, the method could be developed as a routine diagnostic tool for blood testing of NSCLC [39].

Another study from 2018 demonstrated that ATR-FTIR spectroscopy is a potential technique that can be used for cutaneous melanoma (i.e., skin cancer) diagnosis and for differentiating the metastatic potential of cancer cells. By using IR spectroscopy, one can identify various types of cancer such as basal cell carcinoma, malignant melanoma, nevus, as well as metastatic potential by evaluating the alterations in hydration level and molecular changes [40]. The spectra obtained by the authors show different intensities and frequencies of normal and cancerous samples in the spectral range between 4000 cm^{-1} and 400 cm^{-1} . The region between 4000 cm^{-1} and 3000 cm^{-1} shows stretching vibrations of O–H and N–H corresponding to the spectral bands of collagens and proteins of the skin. As cancer changes, the permeability of the cells' membrane and the metastatic potential also change with the hydration grade of the cell membrane; the ATR-FTIR spectroscopy is an approach that allows successful differentiation of the metastatic potential of cancer cells [40]. In particular, the comparison between fewer and more metastatic cells shows that the hydration level of the plasma membrane leads to a significant difference between both states of cancer [40].

A study from 2020 presented an easy to use, a reagent-free method based on (ATR-FTIR) spectroscopy to quantify the protein content of extracellular vesicles (EV) samples with no sample preparation [41]. After calibration with bovine serum albumin, the protein concentration of red blood cell-derived EVs (REVs) was investigated by ATR-FTIR spectroscopy. The integrated region of the amide I band was calculated from the IR spectra of REVs, which was proportional to the protein quantity in the sample. Discriminatory protein bands of amide A, amide I and amide II were set at 3298 , 1657 , and 1546 cm^{-1} , respectively. In the reported study, vibrations corresponding to the lipid components were also witnessed as antisymmetric and symmetric methylene stretching of acyl chains in the range 2924 cm^{-1} to 2850 cm^{-1} , and the C=O stretching at 1738 cm^{-1} of the glycerol esters, respectively [41], as shown in Figure 8.

This new method presents a reagent-free alternative to traditional colourimetric protein determination assays and requires no special sample preparation to investigate EVs [41]. Therefore, this IR spectroscopy-based protein quantification method can be successfully adapted to the routine analysis of extracellular vesicles.

FTIR was also used to detect biomarkers for early screening of pediatric leukaemia [42]. In the reported study, the spectra were acquired from blood serum samples of ten child patients with B-cell precursor lymphoblastic leukaemia (BCP-ALL) and were contrasted with ten control samples. No clear peak shift was spotted between the averaged spectra of leukaemia patients and healthy individuals at the first trial. Thus, the authors applied the ratios of particular corrected peaks heights and the second derivatives analytical approaches to better distinguish between BCP-ALL and the control sample. A significant shift was observed for the peak corresponding to the amide I band (1700 cm^{-1} to 1600 cm^{-1}) due to the C=O stretch vibrations of the peptide linkages. The frequencies of the amide I band are originally fixed to the secondary structure of the proteins. The position of the amide I band was at 1645 cm^{-1} in the FTIR spectrum of the control group, whereas for the BCP-ALL patients, the peak was shifted to 1641 cm^{-1} [42], as seen in Figure 9.

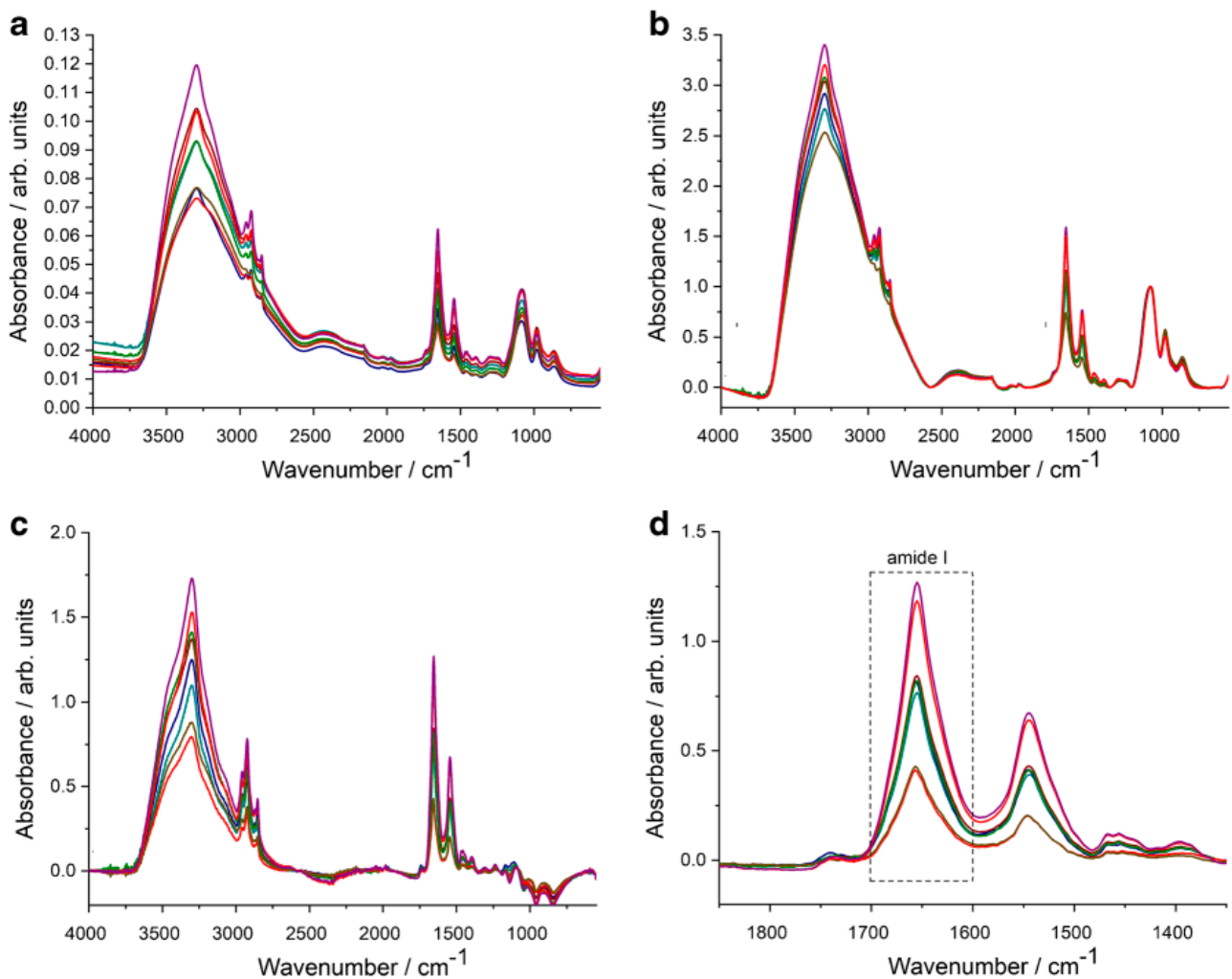


Figure 8. ATR-FTIR spectroscopy quantifies the protein content of extracellular vesicles (EV) samples. (a) Raw absorbance spectra after ATR correction. (b) Absorbance spectra after baseline correction and normalisation. (c) Absorbance spectra after buffer subtraction. (d) Zoomed absorbance spectra for calculating area under the curve (AUC) values of the amide I band by integration in 1700 cm^{-1} – 1600 cm^{-1} wavenumber region. Reprinted from [41], SpringerLink, under a Creative Commons Attribution 4.0 International License.

Thus, the differences between the FTIR spectral profile of leukemic and normal serum may offer a potential route to the early identification of children with BCP-ALL, limiting the number of invasive procedures and accelerating the diagnosis of individuals. The possibility of the early detection of leukaemia in children based only on the FTIR analysis of their serum seems an attractive tool for routine medical practice [42].

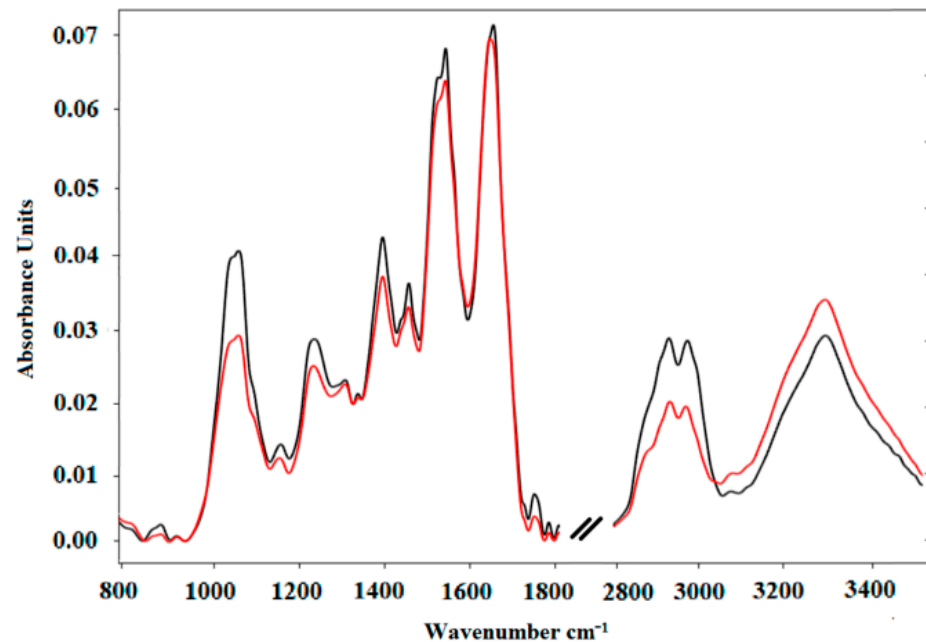


Figure 9. FTIR as a tool for detecting BCP-ALL biomarkers for early screening of pediatric leukaemia. Normalised average FTIR spectra of serum samples: control (black) and Acute Lymphoblastic Leukemia Precursor B (red). The presented spectra cover the range of 800 cm^{-1} – 3500 cm^{-1} . Reprinted from [42], MDPI, under a Creative Commons Attribution (CC BY) license.

4.3. Applications of FTIR Spectroscopy in HIV Early Detection

In 2020, ATR-FTIR spectroscopy was considered for distinguishing HIV-infected patients from healthy uninfected controls [43]. This study comprised one hundred and twenty blood plasma samples of pregnant women and allowed to obtain good sensitivity (83%) and specificity (95%) using a genetic set of rules with linear discriminant assessment (GA-LDA). In the range of 1800 cm^{-1} to 900 cm^{-1} , the spectra displayed some particular feature absorptions, including the amide I band at 1635 cm^{-1} , an amide II band at 1560 cm^{-1} (due to C=O, Amide II) and three small depth absorptions at 1480 cm^{-1} (corresponding to the C-H asymmetric deformation of methyl agencies), at 1404 cm^{-1} (due to the COO—symmetric stretching of proteins and lipids) and 1060 cm^{-1} (due to the C-O nucleic acids). Due to the similarity between the spectral features in the groups (uninfected control and HIV infected), chemometric patterns were used to identify spectral features responsible for class differentiation Figure 10. ATR-FTIR spectroscopy with multivariate analysis was able to accurately identify HIV-infected pregnant women based on blood plasma, showing the potential of this method for early detection of HIV in a fast and reagent-free approach. Successful development of this method in a clinical environment could aid early diagnosis of gestational HIV and help treatment [43].

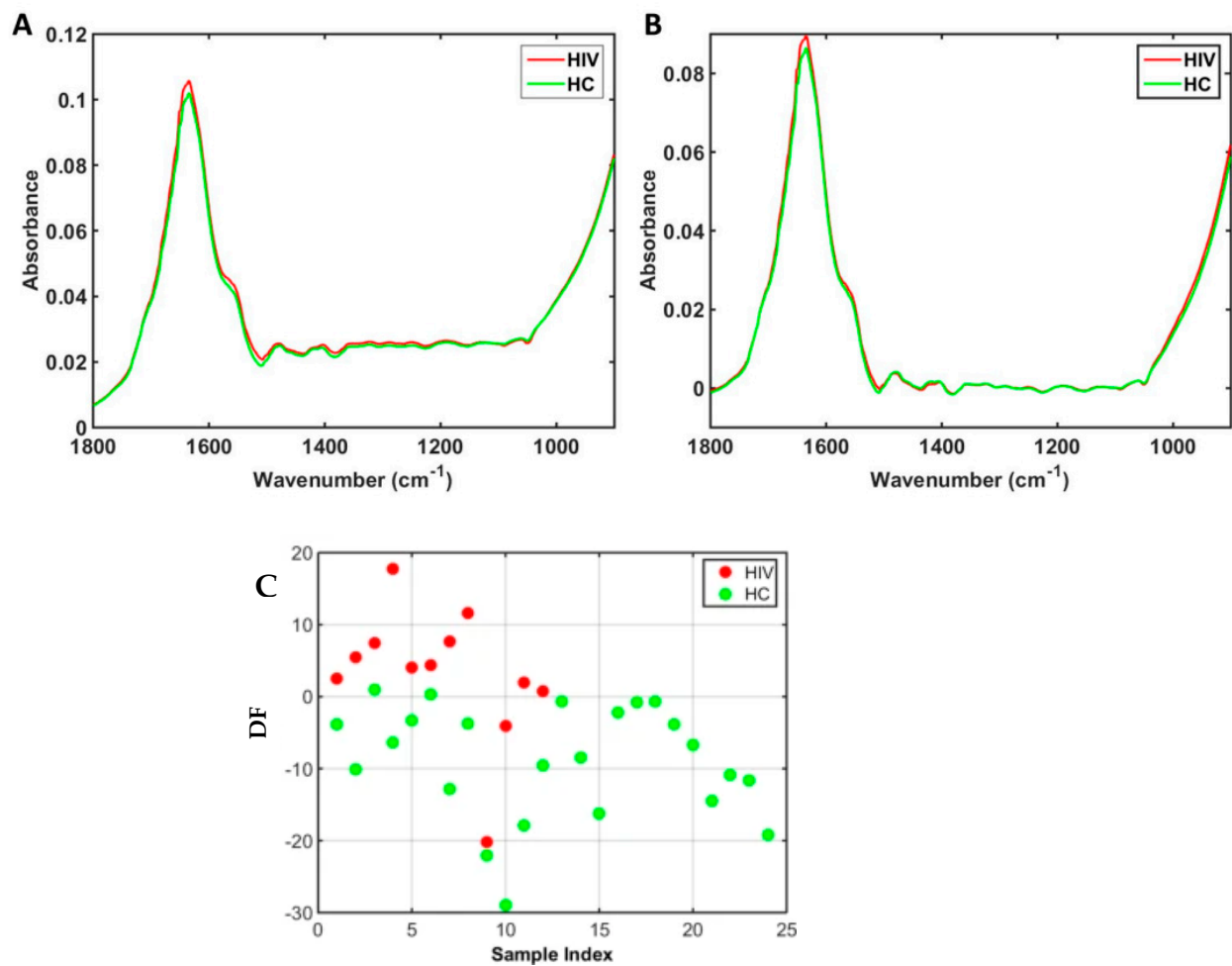


Figure 10. ATR-FTIR spectra for distinguishing between HIV infected and healthy blood samples. (A) Mean raw IR spectra in the biofingerprint region (1800 cm^{-1} – 900 cm^{-1}) for HIV-infected (HIV) and healthy uninfected controls (HC) samples. (B) Mean preprocessed IR spectra (AWLS baseline correction) in the biofingerprint region (1800 cm^{-1} – 900 cm^{-1}) for HIV-infected (HIV) and healthy uninfected controls (HC) samples. (C) Discriminant function (DF) for the samples in the test set, where HIV stands for HIV-infected samples and HC for healthy uninfected controls, allowing their distinction. Reprinted from [43], Nature, under a Creative Commons Attribution 4.0 International License.

4.4. Applications of FTIR Spectroscopy in Blood Grouping Analysis

In 2017, a study explored the potential for the spectroscopic identification of blood antigens using an FTIR spectrophotometer (Shimadzu FTIR-8400S) within the range of 4000 cm^{-1} to 400 cm^{-1} [44]. The ABO blood type system is reflected in the FTIR spectra of human blood. Specific bands at 1166 cm^{-1} and 1020 cm^{-1} represent the fucose molecules linked glycosidically with galactose and -GlcNAc-, respectively, related to the O antigen.

When -GalNAc- is linked to -O antigen- through glycoside linkage, it exhibits a band at 1022 cm^{-1} , due to the -A antigen-. A band at 1166 cm^{-1} reveals additional galactose glycosidically bonded to -O antigen-, as seen in Table 2. Summarily, the IR spectroscopic data on human blood of groups A, B, AB, and O explores the possibility of the nonlabelled and reagent free identification of blood antigens using FTIR [44].

Table 2. Characteristic FTIR spectral data of human blood antigens (a-antigen) for blood grouping applications [44]. Reprinted with permission from the authors and the International Journal of Science, Environment and Technology.

a				Functional Groups
A	B	AB	O	
1166	1166	1166	1163	Fucose linked to galactose via glycosidic linkage
1022	1020	1022	1020	Fucose residues linked to GlcNAc via glycosidic linkage
1022	-	1022	-	GalNAc glycosidically bonded to O antigen
-	1166	1166	-	Additional Galactose glycosidically bonded to O antigen

4.5. Applications of FTIR Spectroscopy in Blood Analysis

FTIR spectroscopy has also been considered in human blood analysis [13]. In 2004, a study presented a novel methodology for predicting the health status using FTIR-MC (micro-spectroscopy) data on blood components. In this study, FTIR-MC was complemented by cluster analysis algorithms (i.e., the task of grouping a set of objects in such a way that objects in the same group are more similar to each other than to those in other groups) [45]. The FTIR microscopic spectra of the major blood components, which include white blood cells (WBCs), red blood cells (RBCs), and plasma, were isolated from ten controls (average population). All the spectra were normalised to the amide I peak at 1643 cm^{-1} .

The results reported by the authors showed that there are spectral variations between the three blood components to evaluate the validity of the method. Cluster analysis of the WBCs spectra in the 945 cm^{-1} to 1282 cm^{-1} range (comprises both symmetric and asymmetric regions of phosphate) and, more particularly, in the more specific range, from 1146 cm^{-1} to 1282 cm^{-1} , provided similar results, as shown in Figure 11a,b. The predictions (FTIR has also been used to analyse the body fluids for diagnostic and characterisation) matched the physician's diagnosis with 100% accuracy, proving the FTIR-MC as a potential tool to predict the health status of blood samples [45].

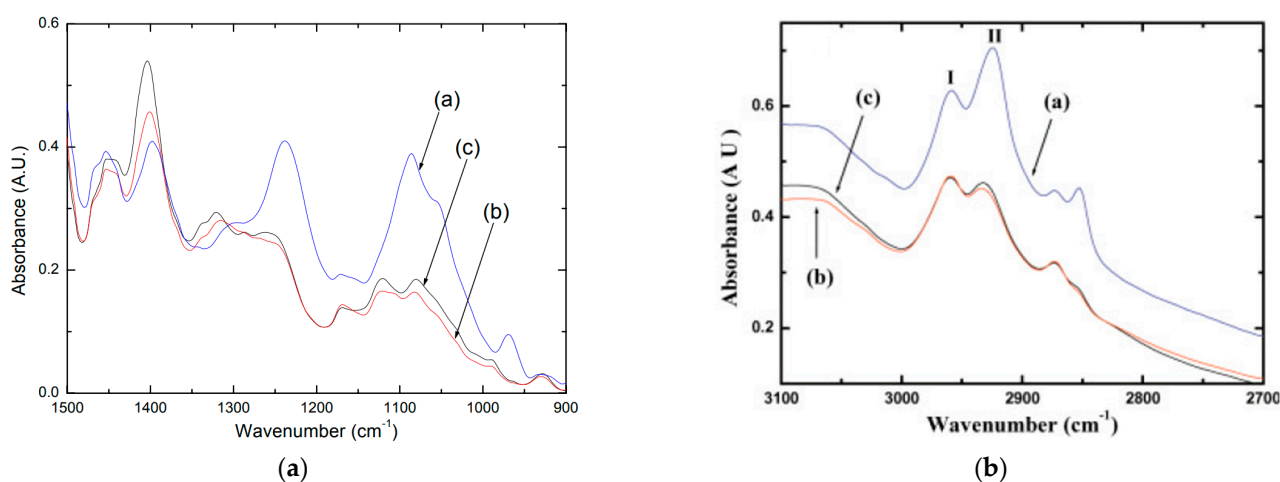


Figure 11. FTIR spectra of the major blood components: WBCs, RBCs and plasma, aiming for blood analysis. (a) Expanded region of FTIR-MC spectra ($900\text{--}1500\text{ cm}^{-1}$) displaying the spectral differences in the symmetric and asymmetric stretching regions of the phosphate group, obtained by the average of ten representative controls; (b) FTIR-MSP spectra of the blood components of the averages of 10 representative controls in the $2700\text{--}3100\text{ cm}^{-1}$ region. (a) WBCs (blue); (b) RBCs (red); (c) Plasma (black) [45]. Adapted from [45] with permission from Wiley.

Summarily, FTIR-MC can distinguish between the three main components of blood using spectral variations and cluster analysis. Specific spectral changes were observed between infected patients and age-matched healthy controls, providing good classification [45].

4.6. Other Applications of FTIR Spectroscopy in the Biological Field

Table 3 presents applications for the FTIR in the biological field tackled rather than blood cell distinction. As observed, FTIR is widely used in biology applications due to its potential to distinguish between different types of molecules.

Table 3. Examples of applications of FTIR in the biological field.

Authors	FTIR Technique	Sample	Analytes	Application	Ref.
L. M. Rodrigues et al.	micro-FTIR	lesions and normal oral mucosa	collagen, lipids, fat acids, proteins, and amino acids	Evaluation of inflammatory	[46]
M. Pachetti et al.	ATR-FTIR	sperm	Proteins (α -helix, β -structures) and lipids	Reveal Lipid and Protein Changes Induced on Sperm by Capacitation	[47]
S. HamanBayarı et al.	ATR-FTIR	archaeological bone	carbonation of a phosphate	discrimination of human bone remains	[48]
A. Rutter et al.	FTIR	peripheral blood mononuclear cells, a leukaemia cell line, and a lung cancer cell line	lipids	Identification of a Glass Substrate to Study Cells	[49]
R. Minnes et al.	ATR-FTIR	mouse and human melanoma cells	amide II	distinguish between melanoma cells with a different metastatic potential	[50]
M. Polakovs et al.	EPR and FTIR	blood	g-factor In Methemoglobin	Study of Human Blood after Irradiation	[51]
P. Zarnowiec et al.	FTIR	human bacteria	Protein	Identification and Differentiation of Pathogenic Bacteria	[52]
M. J. Baker et al.	FTIR	blood	lipids, proteins, carbohydrate, and nucleic acids	Analyse biological materials	[53]
S. Mordechai et al.	FTIR	white blood cells (WBCs) and plasma	Protein and amino acids	Early diagnosis of Alzheimer's disease	[54]
M. Martin et al.	ATR-FTIR	plasma and whole blood	proteins, nucleic acids, lipids, and carbohydrates	The effect of common anticoagulants in detection and quantification of malaria parasitemia in human red blood cells	[55]
I. C. C. Ferreira et al.	ATR-FTIR	saliva	proteins, nucleic acids, lipids, and carbohydrates	Analysis of Saliva for Breast Cancer Diagnosis	[56]
C. Aksoy et al.	FTIR spectroscopy and imaging	stem cells	lipids, proteins, glycogen, and nucleic acids	Effect of the donor age on human bone marrow mesenchymal stem cells	[57]
V. Shapaval et al.	FTIR	food-related fungal strains cultures	fungi detection through protein quantification	Characterisation of food spoilage fungi	[58]
G. Güler et al.	ATR-FTIR	prostate cancer stem cells	Protein, nucleic acid, lipid, and carbohydrate	CD133+ / CD44+ human prostate cancer stem cells	[59]

4.7. Applications of FTIR Spectroscopy Integrated with Lab-on-a-Chip Devices

Besides the macroscale FTIR applications, it has also been introduced into many modern technologies. In particular, lab-on-a-chip is a technology that has revolutionised and continues to revolutionise the medical field [60]. It intends to convert health care equipment into small devices that can be applied as point-of-care (PoC) methods for monitoring proposes. There are several examples in the literature of the combination of IR radiation and lab-on-a-chip technology [61]. Figure 12 presents an example of a pseudo-continuous flow FTIR system integrated on a microfluidic device for sugar identification [61]. Furthermore, the literature has already reported other miniaturised systems based on μ FTIR for biological applications.

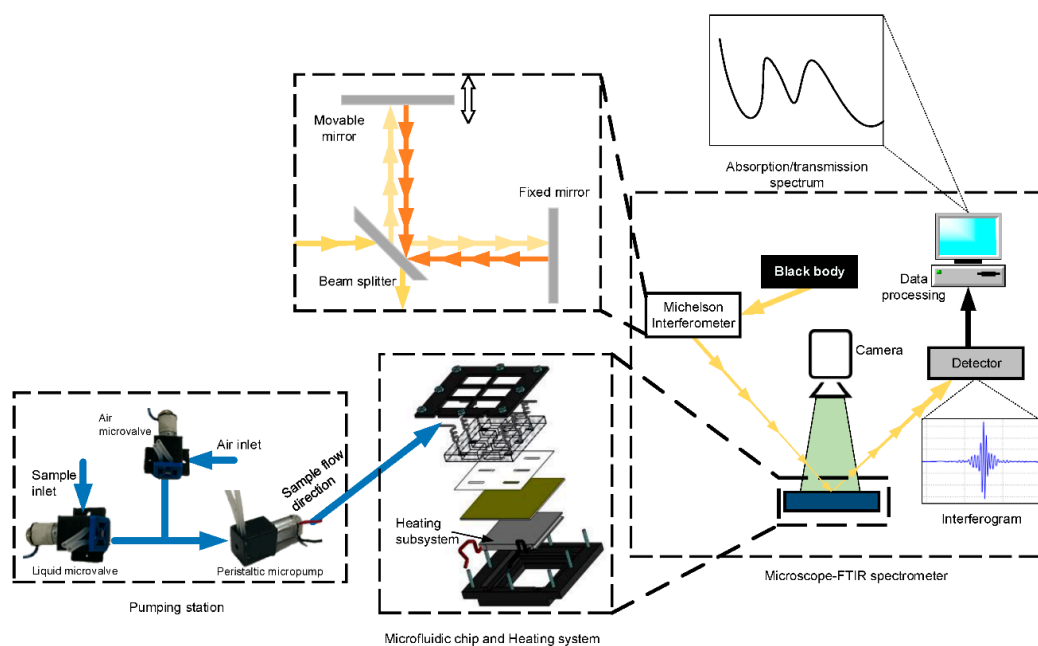


Figure 12. Schematic of the working principle of a pseudo-continuous flow FTIR system, integrated on a microfluidic device for sugar identification. The system includes a pumping station, a microfluidic device, a heating system (for temperature control), and a microscope-FTIR spectrometer. Reprinted from [61], MDPI, under a Creative Commons Attribution (CC BY) license.

A study reported by G. Birarda et al. [62] demonstrated a protocol to build a low-cost IR-Live microfluidic chip for real-time 2D infrared imaging of living cells or tissues with a resolution in the range of micrometres. In this study, FTIR compatible microfluidic chips were produced by direct photolithography of a resist layer coated onto one large IR window (40 mm diameter), with an inlet connected to a tubing system and an outlet attached to a circular reservoir [62]. In the centre of the device, there is an IR-transparent experimental chamber sandwiched between two CaF₂ crystal discs. The results of IR imaging on migrating cells with the subcellular spatial resolution can distinguish different cellular organelles and identify their peculiar chemical composition at a functional group level. The authors, through the performed assays (n = 14), were able to show the characteristic shapes of the proteins (amide II bands) and lipids (CH₂-CH₃ stretching) in the cells. The spectrum has a sharp protein signal centred at 1654 cm⁻¹, mainly attributed to an α -helix protein structure [62].

Another method was developed for rapid ATR-FTIR monitoring solute concentrations in solutions flowing through microchannels [63]. The method involves the interface of commercially available ATR-FTIR instrumentation with a customised microfluidic device, which is sufficiently robust to withstand flow rates of the liquids of at least 20 mL h⁻¹. The authors reported that the paper opened the way for on-chip identification of chemical compounds, measurements of their concentrations in solutions, and studies of reaction kinetics. Furthermore, the method can be used to characterise the adsorption of chemical and biological species adsorbed on the ATR surface under flow. From the spectrum in the region of 1400 cm⁻¹–900 cm⁻¹, the authors reported peaks at 1100 cm⁻¹ and 1250 cm⁻¹, which correspond to the antisymmetric and symmetric vibrational modes of the COC groups, respectively, and a peak at 950 cm⁻¹, which is from the C=C bonds in its phenyl ring. The authors also focused on the dominant band at 1100 cm⁻¹ and plotted the variation of its absorbance vs. concentration of TX-100 (CTX-100) in the solution. For CTX-100 \geq 5 mM, the absorbance of the band linearly increased with the increasing solute concentration. According to the authors, the method allows the rapid acquisition of spectra and enables chemical characterisation and concentration measurements independent of the flow rate of liquids. The method enables the independent measurement of concentrations

of solutes with distinct spectral features in mixed solutions. For the polymer solutes, the authors report that the method has a sensitivity of at least 10 μM (0.01 wt%). The authors also proposed the method's applicability for the differentiation between dissolved and adsorbed amphiphilic species [63].

5. Conclusions

In this review paper, among the various spectroscopic techniques developed, FTIR is presented as a technique with the potential for distinguishing healthy from pathological samples. Numerous works have used FTIR with other techniques, such as ATR or micro-FTIR, to improve and simplify the spectral result of FTIR spectroscopy. The ATR-FTIR method promises the potential for the study of cells and tissues in general and, in particular, as a tool for estimating the metastatic potential of cancer cells. ATR-FTIR spectroscopy was also able to accurately identify HIV-infected pregnant women based on blood plasma, demonstrating the potential of this method for early detection of HIV in a rapid and reagent-free approach.

Label-free FTIR spectroscopy allows greater accuracy and reproducibility in cancer diagnosis while eliminating the need for complex and time-consuming clinical processing of tissue samples, currently required by existing computerised histopathological diagnosis. In addition, FTIR spectroscopy has also shown the potential to rapidly and objectively evaluate surgical resection margins to aid in surgical decision making, which may improve long-term survival and postoperative patient recovery compared with standard intraoperative pathological examination.

FTIR has also been used to monitor the response to cancer treatments and follow-up patients for treatment planning, early detection of recurrence, and assistance with psychological or psychosocial distress, with results that are faster, more sensitive, and more specific than conventional methods. Therefore, FTIR spectroscopy would be crucial to accelerate point-of-care decisions and potentially revolutionise cancer diagnostics in personalised medicine.

FTIR is the future measurement technique that shows tremendous potential and effective solutions to a large number of diagnostic complexities now faced by medical professionals. For instance, due to the limitations of the current gold standard techniques, FTIR may be advantageous to distinguish between normal samples and cancerous samples at an early stage, which offers the chance to diagnose and treat samples before any symptoms appear in patients. All these advantages force the researchers to dive deep into FTIR technology to move from a recognised to a viable technique used in the biological field, as in the other fields (environmental and chemical engineering, for instance) that are already recruiting FTIR for several applications.

6. Future Trends

Although FTIR is in continuous development in the biology field, the number of studies focusing on topics within the FTIR framework is steadily growing. In the future, FTIR may have a significant impact on various aspects of the medical field (i.e., hospital design, lab technician practices), including the financial. FTIR might bypass much equipment currently in use, as well as a large number of reagents used to perform the blood tests, thus proving to be a fast, convenient, economical, practical, and accurate method with high-quality results and minor environmental impact. However, to the best of the authors' knowledge, despite the great interest of the scientific community in FTIR, there are only a few microdevice platforms reported in the literature. Lab-on-a-chip devices, with integrated ATR-FTIR measurements for medical applications in real-time label-free living biological systems analysis, deal with the problem of water presence, either using cell culture medium, plasma, or serum samples, once the absorption values could overlap the bands of other components [64]. In this perspective, ATR-FTIR is the best option to be integrated to study both hydrated and dried biological samples, such as cells and fluid flow [64]. Specifically, in the field of biomechanics and living mechanobiology, ATR-FTIR spectroscopy visualisation

and quantification have also been demonstrated to be an excellent method for nondestructive biological analysis. Apart from all the cancer diagnostics biomarkers discussed in this work, cells' alterations related to diseases occur in most blood pathologies associated with mechanical and rheological changes. The detection and quantification of mechanical alterations have hundreds of applications in diverse fields, ranging from the analysis of cell biomechanics to the classification of tissue biopsies [64–66]. For example, mechanical differences in exosomes and microvesicles reflect changes in cell biomechanics and the cell type, state, treatment, and phenotype [66]. Thus, their quantification and analysis are important for diseases stratification and personalised medicine, showing ATR-FTIR as an advantageous strategy.

Another example is the RBC deformability analysis that is affected by several factors, such as ageing, high blood sugar levels, total cholesterol, or functional oxidative stress. Thus, their membrane and internal cytoplasm suffer changes which biochemical analysis (particularly ATR-FTIR) with morphological and rheological techniques can define and then provide a profile indicative of deformability alteration [67]. As ATR-FTIR technology for blood or body fluids analysis requires proper sample preparation, integration of microfluidics can play, once more, an important role in the development of strategies for sample preparation, such as cells or plasma separation devices, single-cell sorting, cell deformability devices, droplet generators, and cell traps, among others. It is known that spectral analysis demonstrated that deeply deformed cells have different cellular biochemistry compared to nondeformed ones. So, it is expected that significant improvements can be obtained by integrating sample preparation microfluidic systems, enabling the RBCs, white blood cells, or circulating tumour cells analysis, in terms of their membrane biochemical quantification and consequently their biomechanical behaviour [68]. Looking forward to applications in tumour-on-a-chip devices, transparent 3D microfluidic devices will allow ATR-FTIR microspectroscopy applications to monitor the biochemical response to both mechanical and chemical stimulations (i.e., drug resistance).

The development of such devices will be a step ahead in state of the art and will overcome the limitations of current technologies. Thus, to achieve such a goal, future works need to consider the design, fabrication, characterisation, and optimisation of lab-on-a-chip platforms, with IR radiation and Fourier Transform postprocessing, to examine blood cells, distinguishing between normal and pathological ones, and to better understand several mechanisms of treatment resistance and progression.

Author Contributions: Conceptualization, A.F., V.H.C. and G.M.; methodology, A.F., V.H.C., S.O.C. and G.M.; investigation, A.F., D.P., V.H.C., S.O.C. and G.M.; writing—original draft preparation, A.F.; writing—review and editing, D.P., V.H.C., S.O.C. and G.M.; supervision, V.H.C., S.O.C. and G.M.; funding acquisition, S.O.C. and G.M. All authors have read and agreed to the published version of the manuscript.

Funding: This work results of the projects NORTE-01-0145-FEDER-029394, RTChip4Theranostics, and NORTE-01-0145-FEDER-028178, MalariaChip, supported by Programa Operacional Regional do Norte-Norte Portugal Regional Operational Programme (NORTE 2020), under the PORTUGAL 2020 Partnership Agreement, through the European Regional Development Fund (FEDER) and by Fundação para a Ciência e Tecnologia (FCT), IP, projects reference PTDC/EMD-EMD/29394/2017 and PTDC/EEI-EEE/28178/2017. The authors also acknowledge the partial financial support by FCT national funds, under the national support to R&D units grant, through the reference project UIDB/04436/2020, UIDP/04436/2020 and UID/CEC/00319/2020. Susana Catarino thanks FCT for her contract funding provided through 2020.00215.CEECIND.

Data Availability Statement: Not applicable.

Conflicts of Interest: The authors declare no conflict of interest. The funders had no role in the design of the study; in the collection, analyses, or interpretation of data; in the writing of the manuscript, or in the decision to publish the results.

References

- O'Sullivan, J.W.; Stevens, S.; Hobbs, F.D.R.; Salisbury, C.; Little, P.; Goldacre, B.; Bankhead, C.; Aronson, J.K.; Perera, R.; Heneghan, C. Temporal trends in use of tests in UK primary care, 2000–2015: Retrospective analysis of 250 million tests. *BMJ* **2018**, *363*, k4666. [CrossRef] [PubMed]
- National Academies of Sciences, Engineering, and Medicine. *Improving Diagnosis in Health Care*; National Academies Press: Washington, DC, USA, 2015. [CrossRef]
- Rohde, T.; Martinez, R. Equipment and Energy Usage in a Large Teaching Hospital in Norway. *J. Healthc. Eng.* **2015**, *6*, 419–434. [CrossRef] [PubMed]
- Pati, H.P.; Singh, G. Turnaround Time (TAT): Difference in Concept for Laboratory and Clinician. *Indian J. Hematol. Blood Transfus.* **2012**, *30*, 81–84. [CrossRef] [PubMed]
- National Research Council (US) Committee on Prudent Practices in the Laboratory. *Prudent Practices in the Laboratory: Handling and Management of Chemical Hazards: Updated Version*; National Academies Press (US): Washington, DC, USA, 2011. Available online: <https://www.ncbi.nlm.nih.gov/books/NBK55878/> (accessed on 1 June 2021). [CrossRef]
- Luppa, P.B.; Müller, C.; Schlichtiger, A.; Schlebusch, H. Point-of-care testing (POCT): Current techniques and future perspectives. *Trends Anal. Chem.* **2011**, *30*, 887–898. [CrossRef] [PubMed]
- Cole, L.; Kramer, P.R. Bacteria, Virus, Fungi, and Infectious Diseases. In *Human Physiology, Biochemistry and Basic Medicine*; Academic Press: Cambridge, MA, USA, 2016; pp. 193–196. [CrossRef]
- Morris, R. Spectrophotometry. *Curr. Protoc. Essent. Lab. Tech.* **2015**, *11*, 2.1.1–2.1.30. [CrossRef]
- Olaniyan, M.F. *Lecture Notes on Laboratory Instrumentation and Techniques*, 1st ed.; Achievers University: Owo-Nigeria, Nigeria, 2017; pp. 1–244.
- Orange County Biotechnology Education Collaborative, “Introduction to Biotechnology”, LibreTexts. 2013, pp. 1–148. Available online: <https://batch.libretexts.org/print/Letter/Finished/bio-36736/Full.pdf> (accessed on 1 July 2021).
- How an Automated Blood Cell Counter Works? *Medsource Ozone Biomedicals*. 2020. Available online: <https://www.ozonebio.com/india/product-detail/alphacount-60#insights> (accessed on 1 July 2021).
- Diem, M.; Chiriboga, L.; Lasch, P.; Pacifico, A. IR spectra and IR spectral maps of individual normal and cancerous cells. *Biopolymers* **2002**, *67*, 349–353. [CrossRef]
- Byrne, H.J.; Bonnier, F.; McIntyre, J.; Parachalil, D.R. Quantitative analysis of human blood serum using vibrational spectroscopy. *Clin. Spectrosc.* **2020**, *2*, 100004. [CrossRef]
- Griffiths, P.R.; de Haseth, J.A. *Fourier Transform Infrared Spectrometry*; John Wiley & Sons: New York, NY, USA, 1986.
- Mantsch, H.H.; Chapman, D. *Infrared Spectroscopy of Biomolecules*; John Wiley & Sons Inc.: New York, NY, USA, 1996.
- Cooper, E.A.; Knutson, K. Fourier transform infrared spectroscopy investigations of protein structure. *Vaccine Des.* **1995**, *7*, 101–143.
- Liquier, J.; Taillandier, E. Infrared spectroscopy of nucleic acids. In *Infrared Spectroscopy of Biomolecules*; Mantsch, H.H., Chapman, D., Eds.; Wiley-Liss: New York, NY, USA, 1996; pp. 131–158.
- Banyay, M.; Sarkar, M.; Graslund, A. A library of IR bands of nucleic acids in solution. *Biophys. Chem.* **2003**, *104*, 477–488. [CrossRef]
- Brandenburg, K.; Seydel, U. Infrared spectroscopy of glycolipids. *Chem. Phys. Lipids* **1998**, *96*, 23–40. [CrossRef]
- Mostaço-Guidolin, L.B.; Murakami, L.S.; Nomizo, A.; Bachmann, L. Fourier transform infrared spectroscopy of skin cancer cells and tissues. *Appl. Spectrosc. Rev.* **2009**, *44*, 438–455. [CrossRef]
- Gremlich, H.U. *Infrared and Raman Spectroscopy of Biological Materials*; Marcel Dekker: New York, NY, USA, 2001.
- Near, Mid and Far-Infrared (dur.ac.uk), Infrared Processing and Analysis Center, NASA Official: Brian Dunbar. 10 April 2009. Available online: <http://www.icc.dur.ac.uk/~tt/Lectures/Galaxies/Images/Infrared/Regions/irregions.html> (accessed on 1 June 2021).
- Balan, V.; Mihai, C.T.; Cojocaru, F.D.; Uritu, C.M.; Dodi, G.; Botezat, D.; Gardikiotis, I. Vibrational Spectroscopy Fingerprinting in Medicine: From Molecular to Clinical Practice. *Materials* **2019**, *12*, 2884. [CrossRef] [PubMed]
- Bramson, M.A. *Infrared Radiation: A Handbook for Applications*; Springer: New York, NY, USA, 1968.
- Talari, A.C.S.; Martinez, M.A.G.; Movasaghi, Z.; Rehman, S.; Rehman, I.U. Advances in Fourier transform infrared (FTIR) spectroscopy of biological tissues. *Appl. Spectrosc. Rev.* **2017**, *52*, 456–506. [CrossRef]
- Movasaghi, Z.; Rehman, S.; Rehman, I.U. Fourier Transform Infrared (FTIR) Spectroscopy of Biological Tissues. *Appl. Spectrosc. Rev.* **2008**, *43*, 134–179. [CrossRef]
- Barth, A. Infrared spectroscopy of proteins. *Biochim. Biophys. Acta Bioenerg.* **2007**, *1767*, 1073–1101. [CrossRef] [PubMed]
- Fringeli, V.P. *Membrane Spectroscopy*; Springer: New York, NY, USA, 1981.
- Casal, H.L.; Mantsch, H.H. Polymorphic phase behaviour of phospholipid membranes studied by infrared spectroscopy. *Biochim. Biophys. Acta Rev. Biomembr.* **1984**, *779*, 381–401. [CrossRef]
- Siebert, P.H.F. *Vibrational Spectroscopy in Life Science*; John Wiley & Sons: Berlin/Heidelberg, Germany, 2008.
- Wiercigroch, E.; Szafraniec, E.; Czamara, K.; Pacia, M.Z.; Majzner, K.; Kochan, K.; Kaczor, A.; Baranska, M.; Malek, K. Raman and infrared spectroscopy of carbohydrates: A review. *Spectrochim. Acta Part A Mol. Biomol. Spectrosc.* **2017**, *185*, 317–335. [CrossRef] [PubMed]

32. Chai, J.; Zhang, K.; Xue, Y.; Liu, W.; Chen, T.; Lu, Y.; Zhao, G. Review of MEMS Based Fourier Transform Spectrometers. *Micromachines* **2020**, *11*, 214. [CrossRef]
33. Grdadolnik, J. ATR-FTIR Spectroscopy: Its Advantages and Limitations. *Acta Chim. Slov.* **2002**, *49*, 631–642.
34. Jelle, B.P.; Nilsen, T.N.; Hovde, P.J.; Gustavsen, A. Accelerated Climate Aging of Building Materials and their Characterization by Fourier Transform Infrared Radiation Analysis. *J. Build. Phys.* **2012**, *36*, 99–112. [CrossRef]
35. La Russa, M.F.; Ruffolo, S.A.; Barone, G.; Crisci, G.M.; Mazzoleni, P.; Pezzino, A. The Use of FTIR and Micro-FTIR Spectroscopy: An Example of Application to Cultural Heritage. *Int. J. Spectrosc.* **2009**, *2009*, 893528. [CrossRef]
36. Liu, Y.; Yang, Z.; Desyaterik, Y.; Gassman, P.L.; Wang, H.; Laskin, A. Hygroscopic Behavior of Substrate-Deposited Particles Studied by micro-FT-IR Spectroscopy and Complementary Methods of Particle Analysis. *Anal. Chem.* **2008**, *80*, 633–642. [CrossRef] [PubMed]
37. Coates, J. Interpretation of Infrared Spectra, A Practical Approach. In *Encyclopedia of Analytical Chemistry*; Meyers, R.A., McKelvy, M.L., Eds.; John Wiley & Sons Ltd.: Chichester, UK, 2000. [CrossRef]
38. Prabhakar, S.; Jain, N.; Singh, R.A. FT-IR Spectroscopy as a Bio-Diagnostic Tool for Detection of Leukemia. In *Emerging Trends in Laser & Spectroscopy and Applications*, 2010th ed.; Allied Publishers: New Delhi, India, 2010; Chapter 40; pp. 337–341.
39. Ollesch, J.; Theegarten, D.; Altmayer, M.; Darwiche, K.; Hager, T.; Stamatis, G.; Gerwert, K. An infrared spectroscopic blood test for non-small cell lung carcinoma and subtyping into pulmonary squamous cell carcinoma or adenocarcinoma. *Biomed. Spectrosc. Imaging* **2016**, *5*, 129–144. [CrossRef]
40. Andleeb, F.; Atiq, A.; Atiq, M.; Malik, S. Attenuated total reflectance spectroscopy to diagnose skin cancer and to distinguish different metastatic potential of melanoma cell. *Cancer Biomark.* **2018**, *23*, 373–380. [CrossRef]
41. Szentirmai, V.; Wacha, A.; Németh, C.; Kitka, D.; Rácz, A.; Héberger, K.; Mihály, J.; Varga, Z. Reagent-free total protein quantification of intact extracellular vesicles by attenuated total reflection Fourier transform infrared (ATR-FTIR) spectroscopy. *Anal. Bioanal. Chem.* **2020**, *412*, 4619–4628. [CrossRef]
42. Chaber, R.; Kowal, A.; Jakubczyk, P.; Arthur, C.; Łach, K.; Wojnarowska-Nowak, R.; Kusz, K.; Zawlik, I.; Paszek, S.; Cebulski, J. A Preliminary Study of FTIR Spectroscopy as a Potential Non-Invasive Screening Tool for Pediatric Precursor B Lymphoblastic Leukemia. *Molecules* **2021**, *26*, 1174. [CrossRef]
43. Silva, L.G.; Péres, A.F.S.; Freitas, D.L.D.; Morais, C.L.M.; Martin, F.L.; Crispim, J.C.O.; Lima, K.M.G. ATR-FTIR spectroscopy in blood plasma combined with multivariate analysis to detect HIV infection in pregnant women. *Sci. Rep.* **2020**, *10*, 20156. [CrossRef]
44. Vijaya, U. Ushasree and Adeel Ahmad Ftir Spectroscopic Analysis on Human Blood Groups. *Int. J. Sci. Environ. Technol.* **2017**, *6*, 1685–1689. Available online: <https://www.ijset.net/journal/1736.pdf> (accessed on 1 September 2021).
45. Mordehai, J.; Ramesh, J.; Cohen, Z.; Kleiner, O.; Talyshinsky, M.; Erukhimovitch, V.; Cahana, A.; Salman, A.; Sahu, R.K.; Guterman, H.; et al. Studies on acute human infections using FTIR microspectroscopy and cluster analysis. *Biopolymers* **2004**, *73*, 494–502. [CrossRef]
46. Rodrigues, L.M.; Carvalho, L.F.D.C.E.S.; Bonnier, F.; Anbinder, A.L.; Martinho, H.D.S.; Almeida, J.D. Evaluation of inflammatory processes by FTIR spectroscopy. *J. Med. Eng. Technol.* **2018**, *42*, 228–235. [CrossRef]
47. Pachetti, M.; Zupin, L.; Venturin, I.; Mitri, E.; Boscolo, R.; D’Amico, F.; Vaccari, L.; Crovella, S.; Ricci, G.; Pascolo, L. FTIR Spectroscopy to Reveal Lipid and Protein Changes Induced on Sperm by Capacitation: Bases for an Improvement of Sample Selection in ART. *Int. J. Mol. Sci.* **2020**, *21*, 8659. [CrossRef] [PubMed]
48. Bayarı, S.H.; Özdemir, K.; Sen, E.H.; Araujo-Andrade, C.; Erdal, Y.S. Application of ATR-FTIR spectroscopy and chemo-metrics for the discrimination of human bone remains from different archaeological sites in Turkey. *Spectrochim. Acta Part A Mol. Biomol. Spectrosc.* **2020**, *237*, 118311. [CrossRef] [PubMed]
49. Rutter, A.V.; Crees, J.; Wright, H.; Raseta, M.; Van Pittius, D.G.; Roach, P.; Sulé-Suso, J. Identification of a Glass Substrate to Study Cells Using Fourier Transform Infrared Spectroscopy: Are We Closer to Spectral Pathology? *Appl. Spectrosc.* **2020**, *74*, 178–186. [CrossRef] [PubMed]
50. Minnes, R.; Nissinmann, M.; Maizels, Y.; Gerlitz, G.; Katzir, A.; Raichlin, Y. Using Attenuated Total Reflection–Fourier Transform Infra-Red (ATR-FTIR) spectroscopy to distinguish between melanoma cells with a different metastatic potential. *Sci. Rep.* **2017**, *7*, 4381. [CrossRef]
51. Polakovs, M.; Mironova-Ulmane, N.; Pavlenko, A.; Reinholds, E.; Gavare, M.; Grube, M. EPR and FTIR Spectroscopies Study of Human Blood after Irradiation. *Spectroscopy* **2012**, *27*, 367–371. [CrossRef]
52. Zarnowiec, P.; Lechowicz, Ł.; Czerwonka, G.; Kaca, W. Fourier Transform Infrared Spectroscopy (FTIR) as a Tool for the Identification and Differentiation of Pathogenic Bacteria. *Curr. Med. Chem.* **2015**, *22*, 1710–1718. [CrossRef]
53. Baker, M.J.; Trevisan, J.; Bassan, P.; Bhargava, R.; Butler, H.J.; Dorling, K.M.; Fielden, P.R.; Fogarty, S.W.; Fullwood, N.J.; Heys, K.A.; et al. Using Fourier transform IR spectroscopy to analyze biological materials. *Nat. Protoc.* **2014**, *9*, 1771–1791. [CrossRef]
54. Mordechai, S.; Shufan, E.; Katz, B.S.P.; Salman, A. Early diagnosis of Alzheimer’s disease using infrared spectroscopy of isolated blood samples followed by multivariate analyses. *Analyst* **2017**, *142*, 1276–1284. [CrossRef]
55. Martin, M.; Perez-Guaita, D.; Andrew, D.W.; Richards, J.S.; Wood, B.R.; Heraud, P. The effect of common anticoagulants in detection and quantification of malaria parasitemia in human red blood cells by ATR-FTIR spectroscopy. *Analyst* **2017**, *142*, 1192–1199. [CrossRef]

56. Ferreira, I.C.C.; Aguiar, E.M.G.; Silva, A.T.F.; Santos, L.L.D.; Cardoso-Sousa, L.; Araújo, T.G.; Santos, D.W.; Goulart, L.R.; Sabino-Silva, R.; Maia, Y.C.P. Attenuated Total Reflection-Fourier Transform Infrared (ATR-FTIR) Spectroscopy Analysis of Saliva for Breast Cancer Diagnosis. *J. Oncol.* **2020**, *2020*, 4343590. [CrossRef]
57. Aksoy, C.; Çetinkaya, D.U.; Kuşkonmaz, B.B.; Uçkan, D.; Severcan, F. Structural investigation of donor age effect on human bone marrow mesenchymal stem cells: FTIR spectroscopy and imaging. *Age* **2014**, *36*, 1–17. [CrossRef] [PubMed]
58. Shapaval, V.; Schmitt, J.; Møretrø, T.; Suso, H.; Skaar, I.; Åsli, A.; Lillehaug, D.; Kohler, A. Characterization of food spoilage fungi by FTIR spectroscopy. *J. Appl. Microbiol.* **2013**, *114*, 788–796. [CrossRef] [PubMed]
59. Güler, G.; Guven, U.; Oktem, G. Characterization of CD133+/CD44+ human prostate cancer stem cells with ATR-FTIR spectroscopy. *Analyst* **2019**, *144*, 2138–2149. [CrossRef] [PubMed]
60. Stoytcheva, M.; Zlatev, R. *Lab on a Chip Fabrication and Application*, 1st ed.; InTechOpen: Rijeka, Croatia, 2016; ISBN 978-953-51-2457-3.
61. Landari, H.; Roudjane, M.; Messaddeq, Y.; Miled, A. Pseudo-Continuous Flow FTIR System for Glucose, Fructose and Sucrose Identification in Mid-IR Range. *Micromachines* **2018**, *9*, 517. [CrossRef] [PubMed]
62. Birarda, G.; Ravasio, A.; Suryana, M.; Maniam, S.; Holman, H.-Y.N.; Greci, G. IR-Live: Fabrication of a low-cost plastic microfluidic device for infrared spectromicroscopy of living cells. *Lab Chip* **2016**, *16*, 1644–1651. [CrossRef] [PubMed]
63. Greener, J.; Abbasi, B.; Kumacheva, E. Attenuated total reflection Fourier transform infrared spectroscopy for on-chip monitoring of solute concentrations. *Lab Chip* **2010**, *10*, 1561–1566. [CrossRef]
64. Sabbatini, S.; Conti, C.; Orilisi, G.; Giorgini, E. Infrared spectroscopy as a new tool for studying single living cells: Is there a niche? *Biomed. Spectrosc. Imaging* **2017**, *6*, 85–99. [CrossRef]
65. Edmond, V.; Dufour, F.; Poiroux, G.; Shoji, K.; Malleter, M.; Fouqué, A.; Tauzin, S.; Rimokh, R.; Sergent, O.; Penna, A.; et al. Downregulation of ceramide synthase-6 during epithelial-to-mesenchymal transition reduces plasma membrane fluidity and cancer cell motility. *Oncogene* **2015**, *34*, 996–1005. [CrossRef]
66. Di Santo, R.; Romanò, S.; Mazzini, A.; Jovanović, S.; Nocca, G.; Campi, G.; Papi, M.; De Spirito, M.; Di Giacinto, F.; Ciasca, G. Recent Advances in the Label-Free Characterization of Exosomes for Cancer Liquid Biopsy: From Scattering and Spectroscopy to Nanoindentation and Nanodevices. *Nanomaterials* **2021**, *11*, 1476. [CrossRef]
67. Blat, A.; Stepanenko, T.; Bulat, K.; Wajda, A.; Dybas, J.; Mohaissen, T.; Alcicek, F.; Szczesny-Malysiak, E.; Malek, K.; Fedorowicz, A.; et al. Spectroscopic Signature of Red Blood Cells in a D-Galactose-Induced Accelerated Aging Model. *Int. J. Mol. Sci.* **2021**, *22*, 2660. [CrossRef]
68. Mitri, E.; Birarda, G.; Vaccari, L.; Kenig, S.; Tormen, M.; Greci, G. SU-8 bonding protocol for the fabrication of microfluidic devices dedicated to FTIR microspectroscopy of live cells. *Lab Chip* **2014**, *14*, 210–218. [CrossRef] [PubMed]

Review

Manual and Automatic Image Analysis Segmentation Methods for Blood Flow Studies in Microchannels

Violeta Carvalho ¹, Inês M. Gonçalves ², Andrews Souza ³, Maria S. Souza ⁴, David Bento ^{5,6}, João E. Ribeiro ^{6,7}, Rui Lima ^{1,5,*} and Diana Pinho ^{1,4,6}

- ¹ Mechanical Engineering and Resource Sustainability Center (MEtRICs), Mechanical Engineering Department, University of Minho, 4800-058 Guimarães, Portugal; violeta.carvalho@dem.uminho.pt (V.C.); diana.pinho@inl.int (D.P.)
- ² Instituto Superior Técnico, Universidade de Lisboa, Av. Rovisco Pais, 1049-001 Lisboa, Portugal; inesmaia@gmail.com
- ³ Centro para a Valorização de Resíduos (CVR), University of Minho, 4800-028 Guimarães, Portugal; andrewsv81@gmail.com
- ⁴ Center for MicroElectromechanical Systems (CMEMS), University of Minho, 4800-058 Guimarães, Portugal; sabrinasouza680@gmail.com
- ⁵ Transport Phenomena Research Center (CEFT), Faculdade de Engenharia da Universidade do Porto (FEUP), Rua Dr. Roberto Frias, 4200-465 Porto, Portugal; davidbento@ipb.pt
- ⁶ Polytechnic Institute of Bragança, ESTiG/IPB, C. Sta. Apolónia, 5300-857 Bragança, Portugal; jribeiro@ipb.pt
- ⁷ Centro de Investigação de Montanha (CIMO), Polytechnic Institute of Bragança, 5300-252, Bragança, Portugal
- * Correspondence: rl@dem.uminho.pt



Citation: Carvalho, V.; Gonçalves, I.M.; Souza, A.; Souza, M.S.; Bento, D.; Ribeiro, J.E.; Lima, R.; Pinho, D. Manual and Automatic Image Analysis Segmentation Methods for Blood Flow Studies in Microchannels. *Micromachines* **2021**, *12*, 317. <https://doi.org/10.3390/mi12030317>

Academic Editor: Stefano Guido

Received: 20 February 2021

Accepted: 14 March 2021

Published: 18 March 2021

Publisher's Note: MDPI stays neutral with regard to jurisdictional claims in published maps and institutional affiliations.



Copyright: © 2021 by the authors. Licensee MDPI, Basel, Switzerland. This article is an open access article distributed under the terms and conditions of the Creative Commons Attribution (CC BY) license (<https://creativecommons.org/licenses/by/4.0/>).

Abstract: In blood flow studies, image analysis plays an extremely important role to examine raw data obtained by high-speed video microscopy systems. This work shows different ways to process the images which contain various blood phenomena happening in microfluidic devices and in microcirculation. For this purpose, the current methods used for tracking red blood cells (RBCs) flowing through a glass capillary and techniques to measure the cell-free layer thickness in different kinds of microchannels will be presented. Most of the past blood flow experimental data have been collected and analyzed by means of manual methods, that can be extremely reliable, but they are highly time-consuming, user-intensive, repetitive, and the results can be subjective to user-induced errors. For this reason, it is crucial to develop image analysis methods able to obtain the data automatically. Concerning automatic image analysis methods for individual RBCs tracking and to measure the well known microfluidic phenomena cell-free layer, two developed methods are presented and discussed in order to demonstrate their feasibility to obtain accurate data acquisition in such studies. Additionally, a comparison analysis between manual and automatic methods was performed.

Keywords: blood flow; particle tracking; red blood cells; manual methods; automatic methods; image analysis; biomicrofluidics

1. Introduction

Blood flow in microcirculation is crucial for the normal function of tissues and organs. Therefore, a detailed study of blood flow patterns and blood cells flowing in microvessels, microchannels and organs-on-chip is essential to provide a better understanding of the blood rheological properties and disorders in microcirculation [1–7]. One of the first techniques used for the study of flow patterns was the phase-contrast magnetic resonance imaging (PC-MRI). However, the technique requires long acquisition times and has low resolution [8,9]. Other techniques have been developed and combined to improve the acquisition and image processing. One of the most reliable ways to measure velocity fields in microcirculation is using Eulerian methods, such as the conventional micro-particle image velocimetry (PIV) [1,6,10–12] or the confocal micro-PIV [1,2,6,13]. The micro-PIV

technique is one of the best suitable methodologies to study blood flow phenomena in microcirculation. Some studies have also combined PIV with ultrasounds (Echo-PIV) [14,15]. However, most in vivo measurements contain physiological fluids with high concentrations of blood cells and as a result, the amount of tracer particles captured within the fluid is often very low [5]. Other approaches for blood flow studies are particle illumination photography, laser doppler velocimetry, fluorescent cytometry [16,17] and computer fluid dynamics [17,18].

In microcirculation, the study of red blood cells (RBCs) flowing in microvessels and microchannels and the study of the cell-free layer (CFL) thickness in different microchannels geometries are very important to get a better understanding of the blood rheological properties and disorders in microvessels in a fast and accurate way. The presence and physiological characteristics of other cell types are also of great clinical relevance [19]. In this kind of study, the image analysis has an important role to obtain crucial information about blood rheology. For blood flow in microvessels, where there is a large number of interacting cells, manual tracking methods have been used to accurately track individual deformable cells flowing through glass capillaries [1,11,20], straight polydimethylsiloxane microchannels [21], stenotic arteries [22,23], hyperbolic contractions [24], and bifurcations [25]. However, the manual data collection is extremely time-consuming to have a statistically representative number of samples and may introduce operators' errors that eventually limit the application of these methods many times at different conditions [26]. Hence, it is crucial to develop versatile and automatic methods able to automatically track and compute multiple cell trajectories and able to measure the cell-free layer thickness in a network of microchannels.

The purpose of this work is to review the state of the art of techniques used in in vitro blood flow studies and two developed methods (i) an automatic method to track RBCs flowing through microchannels and (ii) an automatic method to measure the CFL thickness in microchannels with bifurcations and confluences will be present and discuss.

This work is organized as follows, firstly an overview of methods used over the last years in the study of blood cells' morphology and tracking in in vitro blood flows is described. Secondly, a brief introduction to ImageJ, the image analysis software used to obtain manual data, will be made. Then, in Section 4, the results of manual and automatic methods applied were demonstrated and are discussed by the comparison with the manual data. Finally, a conclusion and future directions for the present work were discussed in Section 5.

2. An Overview of Image Analysis Methods for Microfluidic Blood Phenomena Quantification

2.1. Image Segmentation and Thresholding

Image analysis processing is a vast area that provides a large number of viable applications that can involve some steps such as image acquisition, image preprocessing, image segmentation, image post-processing and image analysis. Image segmentation is one of the most important and critical elements in automated image analysis, which consists in dividing a digital image into multiple regions, based on a set of pixels or objects, to simplify and/or change the representation of an image [27–29]. A variety of techniques can be applied: simple methods such as thresholding, or complex methods such as edge/boundary detection or region growing.

The literature contains hundreds of segmentation techniques [30,31], but there is no single method that can be considered good enough for all kinds of images. The main purpose of segmentation is to divide an image into regions of interest with similar gray-levels and textures in each region [32]. Segmentation methods change according to the imaging modality, application domain, method type—automatic or semi-automatic, depending on the image quality and the image artifacts, such as noise. Some segmentation methods may require image preprocessing prior to the segmentation algorithm [33,34]. Databases with algorithms to compensate for the uncertainties present in real-life datasets were developed [35]. On the other hand, some other methods apply post-processing to overcome the

problems arising from over-segmentation. Overall, segmentation methods can be grouped into thresholding, boundary detection, and region growing [27,29,31,36,37]. Those methods vary in the way that the image features are treated and the way the appearance and shape of the target are modeled [38].

Thresholding methods assign pixels with intensities below a certain threshold value into one class and the remaining pixels into another class and form regions by connecting adjacent pixels of the same class, that is, in the thresholding process, each pixel in a grayscale is recognized as either an object or background. The more advanced method creates histograms, oriented to the intensity of grayscale or color, showing the frequency of occurrence of certain intensities in an image so that the regions and objects are recognized from these data [28–30]. Thresholding methods work well on simple images where the objects and background have distinctively different intensity distributions. Boundary extraction methods use information about intensity differences between adjacent regions to separate the regions from each other. If the intensities within a region vary gradually but the difference of intensities between adjacent regions remains large, boundary detection methods can successfully delineate the regions [28–30,39]. Region growing methods form regions by combining pixels of similar properties [39,40].

2.2. Blood Cell Image Segmentation and Tracking

Over the last years, many studies have been conducted in the area of general segmentation methods that can analyze different types of medical images. Most used images are acquired during a diagnostic procedure and useful information is extracted for the medical professional. The development of image analysis in biomedical instrumentation engineering has the purpose of facilitating the acquisition of information useful for diagnosing, monitoring, treating or even investigating certain pathological conditions. It is important to always have in mind that the main purpose of biomedical imaging and image analysis is to provide a certain benefit to the subject or patient [41,42].

In normal human blood microscopic images, a high accumulation of RBCs could be observed, which results in the existence of touch and overlap between these cells [42]. These are two difficult issues in image segmentation where common segmentation algorithms cannot solve this problem [43]. Besides that, staining and illumination inconsistencies also act as uncertainty to the image [44]. This uncertainty makes the blood cell image segmentation a difficult and challenging task [43]. Numerous segmentation methods from peripheral blood or bone marrow smears have been proposed and most of them are region-based or edge-based schemes [42,45].

Jianhua et al. [46] developed an iterative Otsu's approach based on a circular histogram for the leukocyte segmentation. R. Suresh Kumar et al. [47] developed two methods of color image segmentation using the RGB space as the standard processing space. These techniques might be used in blood cell image segmentation. Color images are a very rich source of information, because they provide a better description of a scene as compared to grayscale images. Hence, color segmentation becomes a very important and valuable issue [42,47]. For instance, Huang et al. [48] investigated a method based on the Otsu's method to segment and then recognize the type of leukocyte based on the characteristics of the nucleus. Willenbrock et al. [49] developed a program for image segmentation to detect both moving and stagnated cells in phase-contrast images. The program contributed to the study of the integrin LFA-1 mediation of lymphocyte arrest.

Khoo Boon et al. [50] performed comparisons between nine image segmentation methods which are gray-level thresholding, pattern matching, morphological operators, filtering operators, gradient-in method, edge detection operators, RGB color thresholding, color matching, HSL (hue, saturation, lightness) and color thresholding techniques on RBC. They concluded that there is no single method that can be considered good for RBC segmentation [42,50]. Meng Wang et al. [51] presented segmentation and online learning algorithms in acquiring, tracking and analyzing cell-cycle behaviors of a population of cells generated by time-lapse microscopy. Kan Jiang et al. [45] combined two techniques for

white blood cells (WBCs) segmentation. Two components of WBCs, nucleus and cytoplasm, are extracted respectively using different methods. First, a sub-image containing WBCs is separated from the cell image. Then, scale-space filtering is used to extract the nucleus region from the sub-image. Later, watershed clustering in a 3-D HSV (hue, saturation, value) histogram is processed to extract the cytoplasm region. Finally, morphological operations are performed to obtain the entire connective scheme successfully. Li et al. [52] developed a new method for WBCs identification. The method consists of the combination of an acousto-optic tunable filter (AOTF) adapter and a microscope for the image acquisition and an algorithm for data treatment. The results showed the high accuracy of the system. Pan et al. [53] trained a support vector machine model to simulate the human visual neuronal system and identify leukocytes from blood and bone marrow smear images.

Farnoosh et al. [54] developed a framework that consists of an integration of several digital image processing techniques, such as active contours, the snake algorithm and Zack thresholding for white blood cells, aiming to separate the nucleus and cytoplasm. Ritter et al. [55] presented an automatic method for segmentation and border identification of all objects that do not overlap the boundary [54]. Ongun et al. [56] did segmentation by morphological preprocessing followed by the snake-balloon algorithm [54]. Jiang et al. [45] proposed a WBC segmentation scheme on color space images using feature space clustering techniques for nucleus extraction [54]. Al-Dulaimi et al. [57] developed a WBC segmentation method using edge-based geometric active contours and the forces curvature, normal direction, and vector field. Maitra et al. [58] presented an approach to automatic segmentation and counting of RBCs in microscopic blood cell images using the Hough transform [54]. Another interesting investigation was carried out by Banik and colleagues [59]. They proposed an automatic WBC nucleus segmentation method, based on the HSI (hue, saturation, intensity), the $L \times a \times b$ color space, and the k-means algorithm. This increases the generalization capability and evaluation result with a higher score on quality metrics. Then, to classify the localized WBC, they proposed a new convolutional neural network (CNN) model, which is the key factor to reduce the performance dependency between the proposed nucleus segmentation and classification method. In the end, they proved that segmentation performance does not affect the accuracy of the proposed classification method. Kawaguchi et al. [60] presented an image-based analytical method for time-lapse images of RBC and plasma dynamics with automatic segmentation. This method enabled the quantification of the perturbation-induced changes of the RBC and plasma passages in individual vessels and parenchymal microcirculation.

The literature has many more methods, however, most of the techniques presented previously were based in morphological analysis or in the form and constitution of the various blood constituents. Techniques developed for blood flows are still under development because there are many ways and methods for tracking movement. A good summary of object tracking methods can be found in [61] and cell tracking can be found in Miura et al. [62].

Recently other works appeared, for example, Dobbe et al. [63] presented a method applied to the sublingual microcirculation in a healthy volunteer and in a patient during cardiac surgery. Iqbal et al. [64] developed a novel method for the detection of abnormal behavior in cells through real-time images. The method was based in pixel classification using k-means and Bayesian classification. Chang et al. [32] segmented medical images through a charged fluid model. The model is divided in two steps defined by Poisson's equation. Measurements of functional microcirculatory geometry and velocity distributions using image techniques have been made, such as capillaroscopy, orthogonal polarized spectral and a side-stream dark field image [63]. Ashraf et al. [65] said that "cell mobility analysis is an essential process in many biology studies", so they have focused in developing a novel algorithm to image segmentation and tracking system conjugating the advantages of topological alignments and snakes, transforming the output of the topological alignments into the input of the active contour model to begin the analysis in the cells' boundaries and to determine cell mobility [65]. Pan et al. [66] proposed a bacterial foraging-based edge

detection (BFED) algorithm for cell image segmentation. The method was compared with the other four edge detector algorithms and showed more accurate and effective results.

In the case of Möller et al. [67], a semi-automatic tracking method with minimal user interaction was proposed. The framework was based on a topology-preserving variational segmentation approach applied to normal velocity components obtained from optical flow computations. Using the advantages of the optical flow, Kirisits et al. [68] introduced variational motion estimation for images that are defined on an evolving surface. Niazi et al. [69] studied an open-source computational method of particle tracking using MATLAB (2014 b, MathWorks, Natick, MA, US). The size and velocity of the particles are acquired from the video sequences from video-microscopic systems. The images are processed by a set of filters, selected by the user, to improve the accuracy. Park et al. [70] developed a deep learning-based super-resolution ultrasound (DL-SRU) for particle tracking. The method is based on a convolutional neural network and deep ultrasound localization microscopy. The DL-SRU was able to identify the positions of the RBCs reconstruct vessel geometry. Carboni et al. [71] used fluorescence to track blood particles flowing through a microfluidic channel. The recordings of the flow were analyzed with an algorithm developed using MATLAB to evaluate the margination parameter at relevant flows. The image processing consisted of three parts: background correction, calculation of the position and size of the particles through a gradient-based method and calculation of the displacements and velocities. Varga et al. [72] trained conventional-, deep- and convolutional neural networks to segment optical coherence tomography images to identify the number of hyperreflective foci. The networks coincide in the majority of the cases with the evaluation performed by different physicians. Chen et al. [73] studied a new approach for the segmentation of erythrocyte (red blood cell) shape. The technique was called complex local phase based subjective surfaces (CLAPSS) and presented a new variation scheme of stretching factor and was embedded with complex local phase information. The processed images were acquired by differential interference contrast (DIC) microscopy.

Some methods can also be used to track particles for diagnostic or treatments. For instance, Siegmund et al. [74] tested the use of nanoparticle labeling and magnetic resonance imaging (MRI) for in vivo tracking of adipose tissue-derived stromal cells (ASC). The labeling was stable for four months. This method has the disadvantage of not being able to identify the cell since it is an indirect method. Optimization is still required to reduce the amount of nanoparticles. Müller et al. [75] investigated the transport of magnetic particles in vessels of hen's egg models. The flow was subjected to the influence of a magnetic field in dark field reflected light and fluorescence mode. The particles were tracked by single-particle tracking (SPT). Irreversible agglomerates were visualized after stopping the magnetic field. Consequently, further studies of the interaction between cells and particles and of the particle coating are required. Also to support the diagnosis, Kucukal et al. [76] quantified the viscosity of preprocessing-free whole blood samples from the sickle cell disease patient population by using the micro-PIV technique for in vitro assessment of whole blood viscosity and RBC adhesion. More recently, Kucukal et al. [77] have been able to measure the velocity of whole blood flow in a microchannel during coagulation using a simple optical setup and processing the images using PIV and wavelet-based optical flow velocimetry. Both studies demonstrated the viability of image processing methods to obtain data with clinical relevance. Table 1 below shows the chronological progress of the studies and that, recently, the studies have been based on automatic methods with specific algorithms and particle tracking techniques.

For studies based on in vitro approaches, there are different automatic algorithms, however, most of them still under development because the results tend to overlap at high hematocrits (Hcts), and most of them are based on images that the researchers have, taking into account their aim. Therefore, to have a good method and take advantage of all its capabilities, it is ideal to develop our own algorithm for the objective that we want to achieve. In the following sections, we will discuss the application of two automatic methods.

Table 1. Summary of image analysis methods used for cell tracking and segmentation.

Reference, Year	Goal	Technical	Conclusion
[45], 2003	White blood cell (WBC) segmentation	Scale-space filtering and watershed clustering	Extracts the WBC region; The HSV space is better than the RGB space due to its low correlation.
[47], 2007	Color image segmentation	Using RGB space as the standard processing space: (1) Non-exclusive RGB segmentation. (2) Exclusive RGB segmentation.	Color images provide a better description of a scene as compared to grayscale images
[54], 2009	WBC segmentation: to separate the nucleus and cytoplasm	It is based on the morphological analysis and the pixel intensity threshold, respectively.	The method is able to yield 92% accuracy for nucleus segmentation and 78% for cytoplasm segmentation.
[60], 2012	To quantify the perturbation-induced changes of the RBC and plasma passages in the individual vessels.	The image-based analytical method for time-lapse images of RBC and plasma dynamics with automatic segmentation	Arterial tones and parenchymal blood flow can be individually coordinated.
[52], 2013	To segment the nuclei and cytoplasm of WBCs	It is based on the pixel-wise ISAM segmentation algorithm	the accuracy of the proposed algorithm is 91.06% (nuclei) and 85.59% (cytoplasm)
[67], 2014	Cell tracking	Topology preservation techniques	The method has good accuracy
[71], 2016	Direct particle tracking	Algorithm developed in MATLAB	Results obtained confirm experimental results
[66], 2017	Optimize traditional edge detection	Edge detection algorithm based on bacterial liner	Identifies boundaries more effectively and provides more accurate image segmentation
[69], 2019	Determine particle velocity and size distributions of large groups of particles by video-microscopic systems.	Open-source computational implementation with MATLAB	It allows the automatic tracking of any fluid with particles, classifies the particles according to their size and calculates the speed.
[70], 2020	Particle tracking	The method is based on a convolutional neural network and deep ultrasound localization microscopy	Its robust, fast and accurate RBC localization, compared with other ULM techniques
[76], 2020	In vitro assessment of whole blood viscosity (WBV) and RBC adhesion	Micro-PIV	WBV and RBC adhesion may serve as clinically relevant biomarkers and endpoints in assessing emerging targeted and curative therapies in SCD.
[77], 2021	Measurements of the velocity of whole blood flow in a microchannel during coagulation	PIV and wavelet-based optical flow velocimetry (wOFV)	The high-resolution wOFV results yield highly detailed information regarding thrombus formation and corresponding flow evolution

3. ImageJ Manual Plugins

ImageJ is a public domain Java image processing program. It can display, edit, analyze, process, save and print 8-bit, 16-bit, and 32-bit images. It can read many image formats including TIFF, GIF, JPEG, BMP, DICOM, FITS and “raw” data and supports “stacks”, a series of images that share a single window. It is multithreaded, so time-consuming operations such as image file reading can be performed in parallel with other operations [78].

With ImageJ [78], it is possible to calculate the area and pixel value statistics of user-defined selections. It can measure distances and angles and create density histograms and line profile plots. Moreover, it supports standard image processing functions such as contrast manipulation, sharpening, smoothing, edge detection, and median filtering [78].

There are also different plugins to track RBCs, to count, or to measure the CFL thickness such as MtrackJ or ZProject. For example, in the study of the RBCs or other blood cell tracking, the plugin MtrackJ [49] is often used, facilitating the manual tracking of moving objects in image sequences and the measurement of basic track statistics. Through the MtrackJ plugin, the centroid of individual RBCs can be tracked, allowing obtaining the trajectory of each RBC. Additionally, it can be used to estimate RBC velocity, taking into consideration the x and y positions at each point (Figure 1a). To study the phenomena of CFL, manual tracking by MtrackJ can also be used or, as an alternative, the automatic function ZProject in ImageJ can be applied to process several images at once, creating a stack, and allowing observing the path of RBCs in the channel (Figure 1b). In Figure 1 is possible to see the application of the MtrackJ plugin to determine the CFL thickness in blood flow study [79].

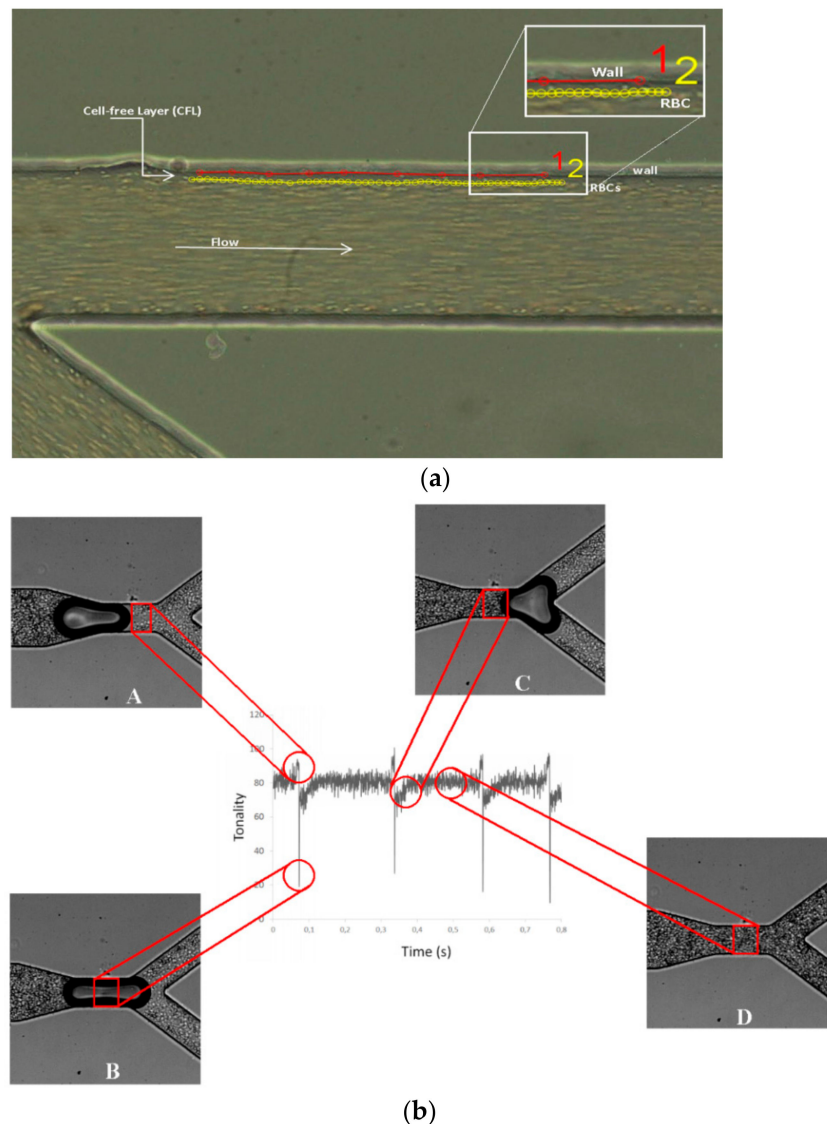


Figure 1. ImageJ plugins: (a) MtrackJ used to obtain the RBC trajectory [79] and (b) application of the *plot Z-axis profile* function at the selected ROI [80].

Another tool from ImageJ used in studies of blood flow is the *Plot Z-axis profile*. This function allows determining the tonality of the pixels in a region of the interest (ROI) through time. After selecting a particular area of the video the *Plot Z-axis profile* tool measures the average of tonality of the pixels in the ROI and this tonality was used as a proxy of the local hematocrit. High tonality corresponds to low hematocrit and low tonality corresponds to high hematocrit [80]. Figure 2 represents the variation in the tonality in the ROI, and consequently the variation of the hematocrit in that region, over time.

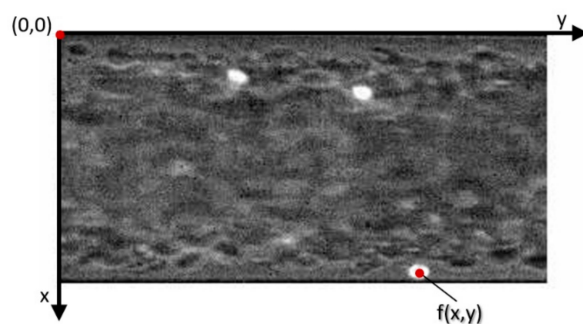


Figure 2. Image of blood flow in the microchannel with labeled bright RBCs, $f(x,y)$ and the centroid of the tracking cell.

Note that in MATLAB [27,39] there are some algorithms that researchers provide and also an application to work with ImageJ. A promising particle tracking velocimetry (PTV) plug-in for Image J is the “Particle tracker 2D and 3D” [81,82].

4. Automatic Image Analysis Methods

4.1. Red blood Cells Trajectory in a Glass Capillary

4.1.1. Set-Up and Working Fluids

The confocal system used in this study consists of an inverted microscope (IX71; Olympus, Tokyo, Japan) combined with a confocal scanning unit (CSU22; Yokogawa Tokyo, Japan), a diode-pumped solid-state (DPSS) laser (Laser Quantum, Stockport, UK) with an excitation wavelength of 532 nm and a high-speed camera (Phantom v7.1; Vision Research, Wayne, NJ, USA). The laser beam was illuminated from below the microscope stage through a dry 40x objective lens with a numerical aperture (NA) equal to 0.9.

The light emitted from the fluorescent flowing RBCs, passes through a color filter into the scanning unit CSU22, where, by means of a dichromatic mirror, the light is reflected onto a high-speed camera to record the confocal images. The physiological fluid used was a solution of Dextran 40 (Dx40) with a Hct of 12%. Such was selected to obtain images with the best possible quality and consequently to reduce errors during cell tracking.

The RBCs were fluorescently labeled with a lipophilic carbocyanine derivative dye, chloromethylbenzamido (CM-Dil, C-7000, Molecular Probes, Eugene, OR, USA) using a procedure previously described [1,83]. This dye was well retained by the RBCs and had a strong light intensity, which allowed good visualization and tracking of labeled RBCs flowing in concentrated suspensions.

The microchannel used in this study was a 100 μm circular borosilicate glass capillary fabricated by Vitrocom (Mountain Lakes, NJ, USA). The capillary was mounted on a sliding glass with a thickness of $170 \pm 20 \mu\text{m}$ and was immersed in glycerin to minimize the refraction from the walls.

4.1.2. Manual Method

All confocal images were captured around the middle of the capillary with a resolution of 640×480 pixels, at a rate of 100 frames/second and then transferred to a computer for evaluation using Phantom camera control software (PH607). The manual method to track individual RBCs relies on the manual tracking plugin MTrackJ [84]. The bright centroid of the selected RBC was manually computed through successive images. After obtaining

x and y positions, the data were exported for the determination of each individual RBC trajectory.

The output of this process is:

- x [μm]: The calibrated x coordinate of the point. The pixel width and unit of length used here can be set as described above.
- y [μm]: The calibrated y coordinate of the point. The pixel height and unit of length used here can be set as described above.

Figure 2 is an example of the blood flow image acquired with labeled bright RBCs and x-y coordinates.

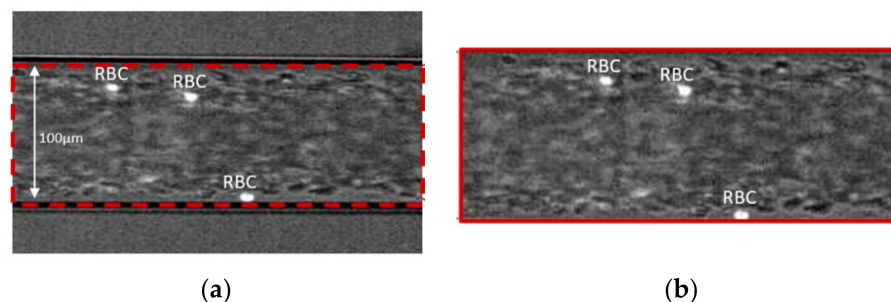
4.1.3. Automatic Method

A graphical user interface (GUI) in MATLAB was developed, for a better work environment for all users. This application must detect and track all objects that are present in a video sequence.

The algorithm is based on the steps as follows:

- Preprocessing is executed in order to remove noise and correct the brightness, and to enhance specific features of the image for increasing the robustness of the tracking procedure;
- A level of threshold is applied, in which it is possible to divide the image into different parts. The result is a binary image with a clear division between the background and objects of interest;
- The extraction procedure is done to obtain the objects' characteristics necessary for the study.

Firstly, the sequences of images were loaded to the GUI. Then, the region of interest (defined by the user) was cropped from the original images with the function *imcrop*; also a standard region is defined, but the user can change it for a better purpose. With this operation, we can work only with the region which needs to be analyzed (the region between the microchannel walls), making it easier to handle the images for the next steps, as presented in Figure 3.



```

I1{c} = (imread([name, int2str(c), '.jpg']));
I{c} = imcrop(I1{c}, rect);
J{c} = medfilt2(I{c}, [5 5]);

```

Figure 3. Image sequences imported (a) and respective region of interest cropped (b).

The next operation is the image noise elimination by applying the median filter, *medfilt2*, with one 5×5 pixel mask. With that, the background of the images was smooth, and the objects are enhanced preserving the edges. Figure 4 presents the result of these processes.

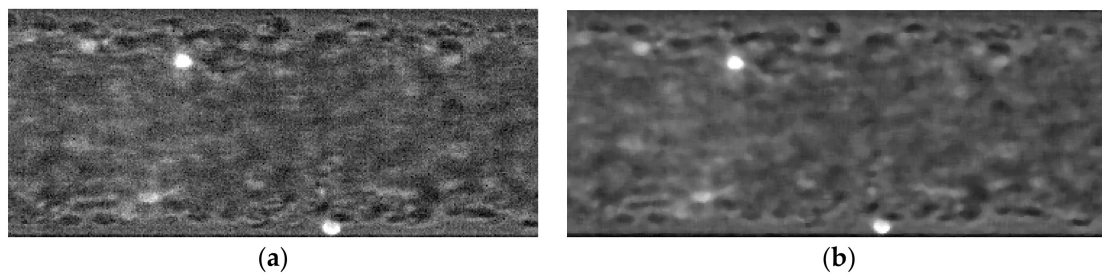


Figure 4. The region of interest (a) and the image filtered by using the median function *medfilt2* (b).

In the next stage, the images were subject to a segmentation step using a threshold method. The definition of one or more values of separation is enough to divide the image into one or more regions, that is, differentiate the area of interest (the RBCs) from the not-interest area (background image). The level of threshold is calculated by default, by an iterative method, which means that for each image an adequate level of threshold is calculated. However, users can apply the value that they think to be more appropriate. After thresholding, the objects were defined with the Sobel filter (see Figure 5), which shows only the edge of the objects. The *Sobel* computes an approximation of the gradient of the image intensity. At each pixel point in the image, the result of the Sobel operator is either the corresponding gradient vector or the norm of this vector [31].

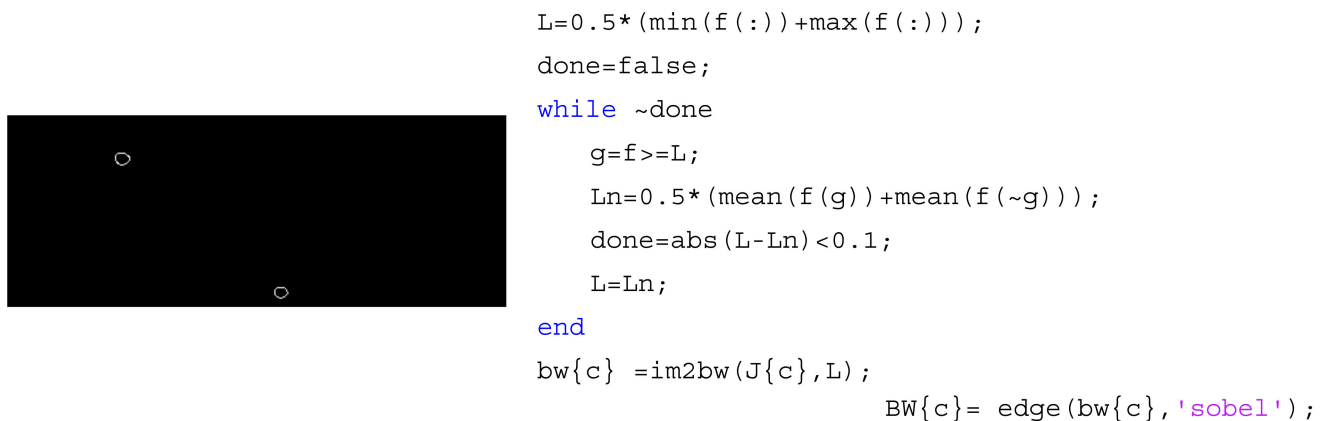
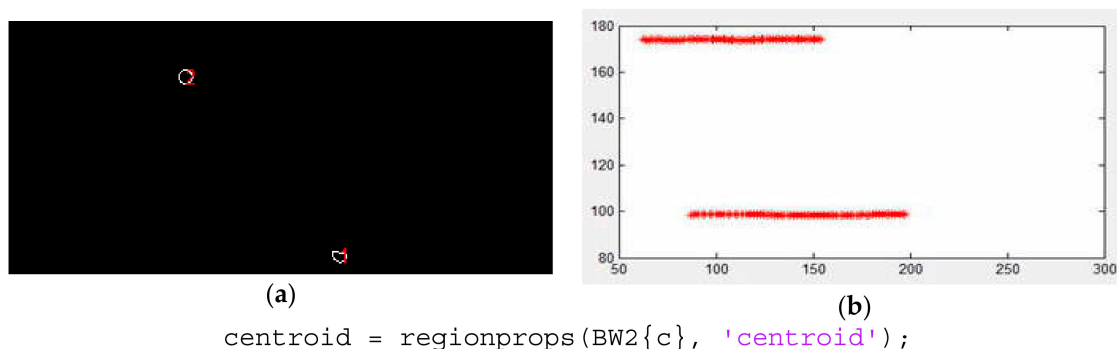


Figure 5. The obtained image of the iterative threshold method and the application of the Sobel filter.

After the segmentation processing, the RBCs were tracked and sets of data (and positions) were obtained with the MATLAB function from the image processing toolbox, *regionprops* [27] (cf. Figure 6). This function measures a set of properties (area, centroid, etc.) for each connected component (RBC) in the binary image.



centroid = regionprops(BW2{c}, 'centroid');

Figure 6. (a) Data extraction and (b) RBCs trajectories.

The data obtained were filtered because some of the objects are not RBC (that is, white blood cells or platelets that have higher or lower, respectively, area than the RBCs). Therefore, it is possible to filter the data by area, by imposing a minimum and maximum value. Another filter applied was the number of images where the objects are visible, because if the object has only a tracking with 10 positions, this data is not enough to be analyzed. The data with an extremely low number of tracking positions per object was eliminated.

Another approach for this type of application is underway, which is based on optical flow. Optical flow is a technique used in computer vision algorithms to measure the speed of the pixels based on comparisons of frames, creating a field that describes the displacement that occurred between two consecutive frames of a video sequence. In other words, the optical flow consists of a dense field of velocity where each pixel in the image plane is associated with a single velocity vector [85,86]. The Kalman method and the Lucas Kanade pyramidal method were applied to the same sequence of images (cf. Figure 7).



Figure 7. The obtained image when the Lucas Kanade pyramidal method was applied.

The Lucas Kanade pyramidal method shows a better approach to the objective, but the real dimension of the object and a continuous track along the image sequence are still under development. There is a great potential in this technique to follow moving objects, such as the RBCs flowing through a glass capillary, however, due to the complexity of the method and the need for multiple variables, further investigation is required.

4.1.4. Results

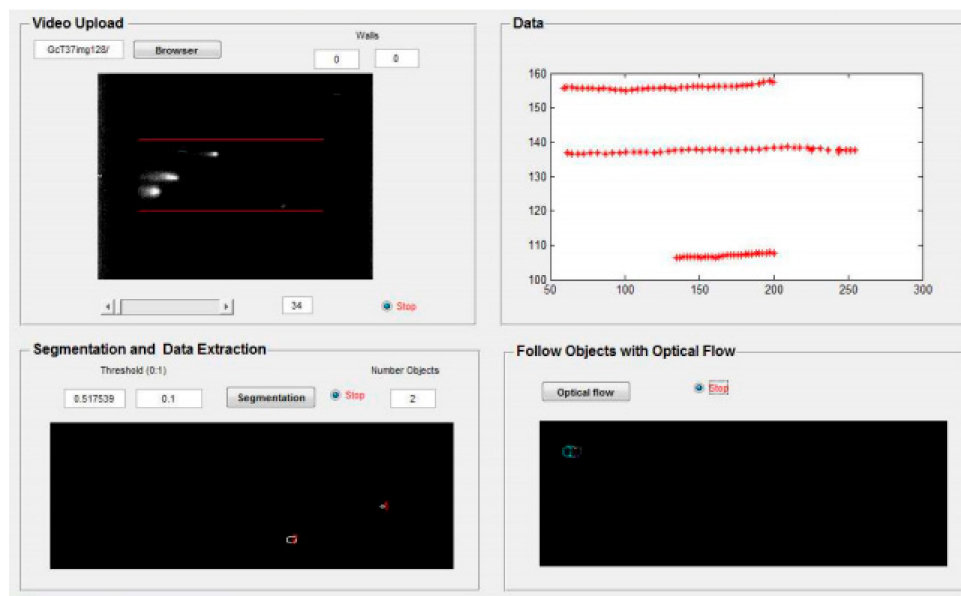
Figure 8 shows the developed graphical user interface (GUI) in MATLAB performing the image processing described in the upper sections and the trajectories of individual labeled RBCs flowing in the center plane of a microchannel, determined by the manual tracking and the proposed automatic tracking method.

The present study indicates that the data obtained from the proposed automatic method significantly matches the data obtained from the manual method. This data, x-y positions, can be used to calculate the means square deviation (MSD) and the radial dispersion (D_{yy}) to analyze the behavior of the RBC through a microchannel.

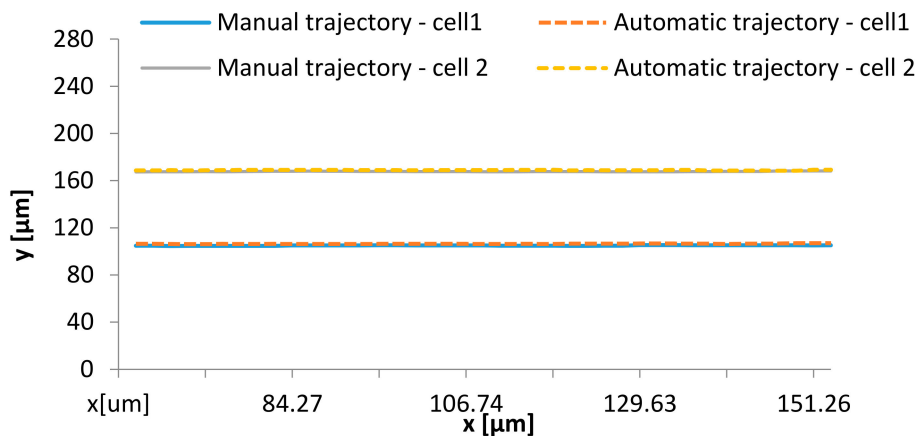
4.2. Cell-Free Layer Thickness in a Bifurcation and Confluence Microchannel

4.2.1. Set-Up and Working Fluids

The series of x-y images were captured with a resolution of 600×800 pixels. All images were recorded at the center plane of the microchannels at a rate of 200 frames/second, transferred to the computer and then evaluated by using an image analysis software. The microscope system used in the present study consisted of an inverted microscope (IX71, Olympus, Tokyo, Japan) combined with a high-speed camera (i-SPEED LT, Olympus, Tokyo, Japan). The blood samples used were collected from a healthy adult sheep, and ethylenediaminetetraacetic acid (EDTA) was added to prevent coagulation. The RBCs were separated from the blood by centrifugation and washed twice with physiological saline. The washed RBCs were suspended in Dextran 40 to make up the required RBCs concentration by volume.



(a)



(b)

Figure 8. Automatic method results: (a) developed graphical user interface (GUI) in MATLAB and (b) trajectories of individual labeled RBCs determined by the manual and automatic method.

4.2.2. Manual Methods

The MTrackJ plugin was used to automatically compute the centroid of the selected RBC. After obtaining x and y positions, the data was exported for the determination of each individual RBC trajectory (cf. Figure 9).

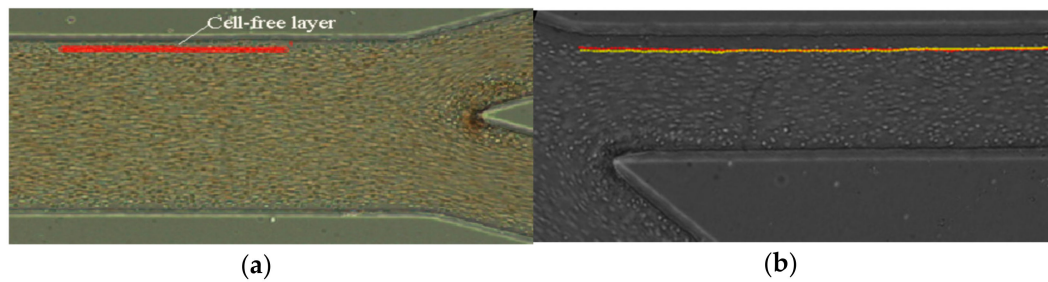


Figure 9. Manual method showing the trajectories of RBC defining the region of the CFL: (a) for an expansion geometry and (b) for a bifurcation geometry.

A semi-automatic method was also applied based on the use of the ZProject plugin [78]. This plugin projects an image stack along the axis perpendicular to the image plane (the so-called “z” axis) and has six different projection types.

- **Average intensity projection** outputs an image where each pixel stores the average intensity over all images in the stack at the corresponding pixel location (cf. Figure 10a);
- **Sum Slices** creates a real image that is the sum of the slices in the stack (Figure 10b).
- **Standard Deviation** creates a real image containing the standard deviation of the slices (cf. Figure 11a);
- **Median** creates an image containing the median value of the slices (cf. Figure 11b).
- **Minimum intensity projection (Min)** creates an output image where each of the pixels contains the minimum value over all images in the stack at the particular pixel location (cf. Figure 12a).
- **Maximum intensity projection (Max)** creates an output image where each of the pixels contains the maximum value over all images in the stack at the particular pixel location (cf. Figure 12b).

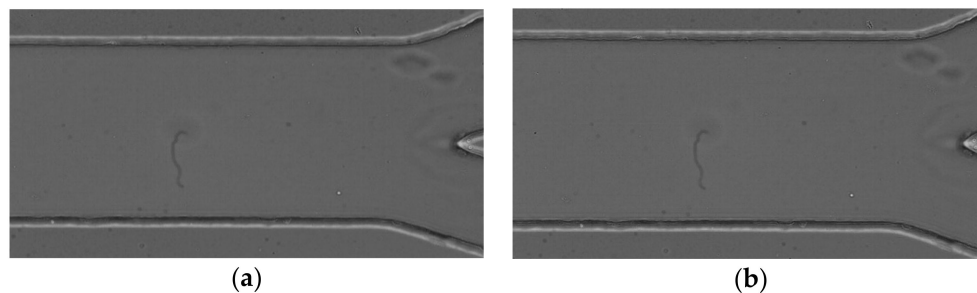


Figure 10. (a) The obtained image by applying the projection average intensity and (b) the obtained image by applying the projection sum slices.

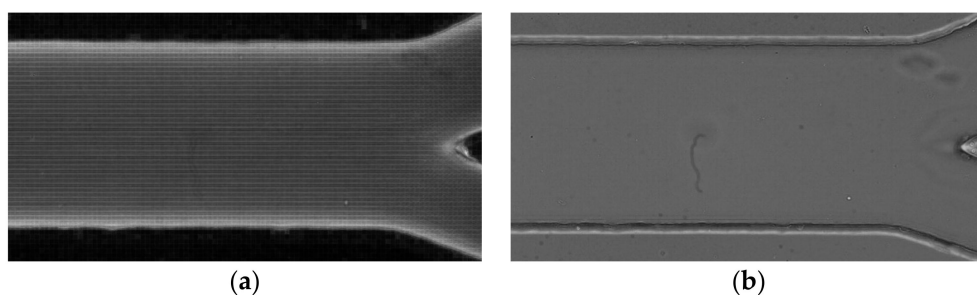


Figure 11. (a) Image obtained by applying the standard deviation projection and (b) image obtained by applying the median projection.

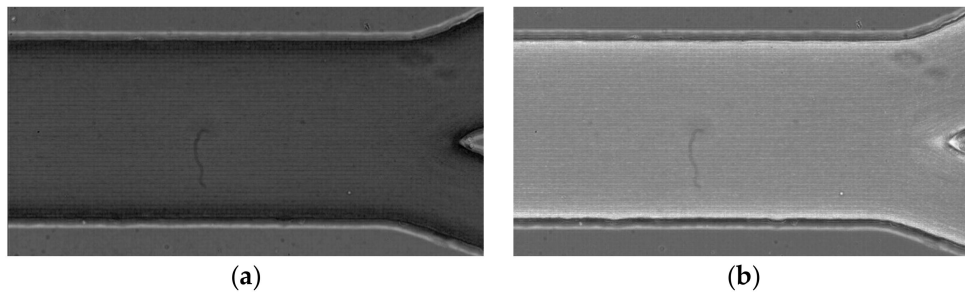


Figure 12. (a) The obtained image with the projection minimum intensity, and (b) the obtained image with the projection maximum intensity.

After applying an appropriate projection to a stack, the resulting image is obtained, and it is then converted to a binary image (see Figure 13). The thresholding in ImageJ can be done automatically or by applying the level that the user requires.

$$threshold = \frac{(average\ background + average\ objects)}{2} \quad (1)$$

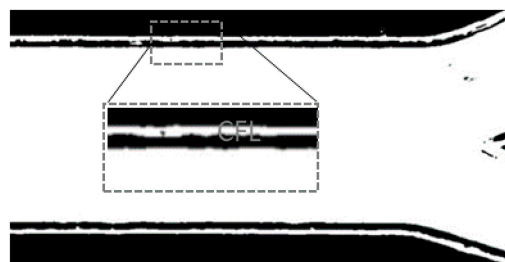


Figure 13. The obtained image from the ZProject method with the projection maximum intensity to extract the data. It shows a well defined CFL thickness.

This method works well for a good image quality and for simple geometry of the channels and represents the data accurately. Nevertheless, for more complex image data the method has some difficulties to get the correct data, so it will be necessary to specifically develop a method able to represent the data accurately.

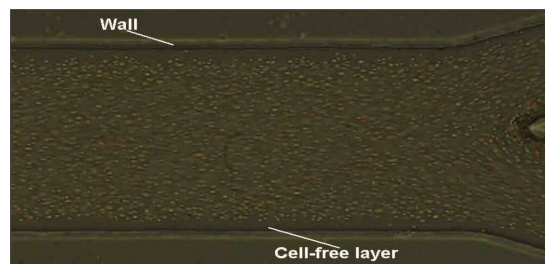
To obtain the data, the tool *Wand* is used, which creates a selection by tracing objects of uniform color or thresholded objects. To trace an object with the *Wand* tool, it is necessary to click inside near the right edge, or outside to the left of the object. Once it finds the edge, it follows it until it returns to the starting point. The *Wand* takes the pixel value where you click as an initial value. Then, it selects a contiguous area under the condition that all pixel values in that area must be in the range initial value—tolerance to initial value + tolerance. Then the selected area will be analyzed to measure the CFL thickness.

4.2.3. Automatic Method

The method is based on the binarization of the sequence image. The general steps of the method are:

- Preprocessing to smooth the image and eliminate the artifacts;
- Evaluation of the intensity of all image sequences;
- Apply the binarization to the resulting image;
- Select the area to obtain the required data;

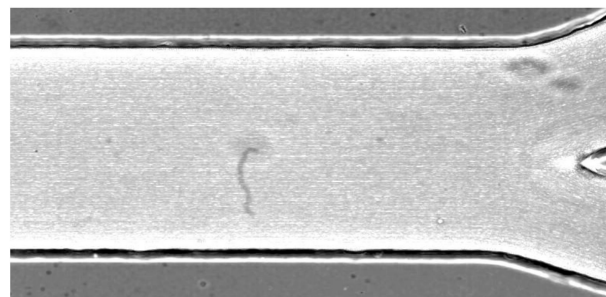
All image sequences were processed using the image processing toolbox available in MATLAB [45]. The sequence of images was loaded (cf. Figure 14), and a median filter with a 3×3 pixel mask was applied to each frame to reduce the noise of the images.



```
I=imread(t);
J = rgb2gray(I);
I = imadjust(J);
B=medfilt2(I);
```

Figure 14. An image from the original sequence of images.

Then, the intensity of each pixel in the frame sequence was evaluated to obtain an image with the maximum intensity. With this step, it was possible to identify the region with the highest concentration of blood cells and the region where blood cells do not exist, the cell-free layer (CFL). The regions that represent the CFL have the highest intensity (white) near the microchannel walls (cf. Figure 15).



```
[m,n]=size(I);
for a=1:m
    for b=1:n
        T=I(a,b);
        F=A(a,b);

        if T>=F
            A(a,b)=I(a,b);
        else
            A(a,b)=A(a,b);
        end
    end
end
```

Figure 15. Image with the maximum intensity evaluation.

As a final step, the image was converted into a binary image, the regions of interest were selected and the upper CFL trajectories were automatically measured. Figure 16 shows the image processing result for the developed method.

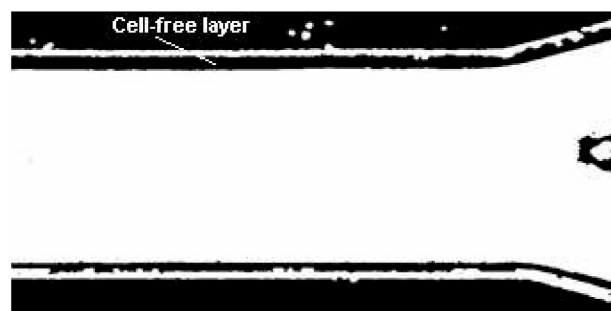


Figure 16. The obtained image from the automatic method.

The area to take the data is defined by the user selecting the wall of the channel and the limit area from the cell-free layer.

4.2.4. Results

Figure 17 shows the results obtained by the manual method using the MtrackJ plugin and the automatic method presented in this work to measure the CFL thickness. A

microchannel with bifurcation and confluence shown in Figure 15 was used for the measurements. The values obtained with both methods can be seen also in Figure 15. Data was taken in the regions represented by A to F.

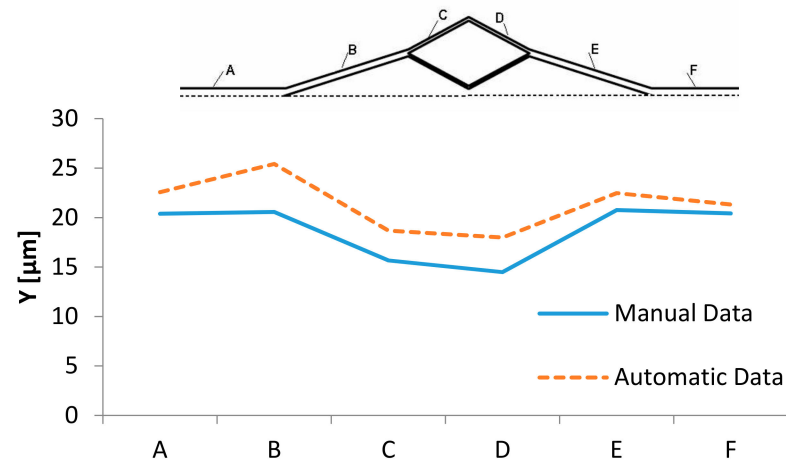


Figure 17. Comparison between the manual and the automatic data, taken in the regions A to F.

It is possible to note that the data obtained by the automatic method have similar behavior with the manual data. However, the values have some discrepancies. The quality of the image and also the level of the threshold can influence this type of measurements.

5. Conclusions and Future Work

The present work presents not only a review on blood cells tracking methods but also comparisons of a manual method and an automatic method for two different blood flow studies. Regarding the study where RBCs were tracked through a 100 μm glass capillary, the automatic method based on a threshold algorithm was used to provide an accurate and automated process to track and as a result, it measured the RBCs flowing in microchannels. The automatic results were in good agreement with the manual method. Further work aims to implement an image analysis application able to track flowing RBCs and, consequently, extract multiple features of the RBCs that can be used in other applications, such as measuring the RBC deformability. Another method based on optical flow was also tested but it is still under development, so that it can be further improved in the future for data collection.

To study the CFL phenomenon in microchannels, the method developed based in the binarization of the image with the maximum intensity evaluation presents some discrepant results when compared to the manual data. Nonetheless, a similar qualitative tendency was observed. In this type of study, the quality of the image sequence plays a crucial role. Hence, by acquiring a sequence of images with higher quality and resolution, we believe that this automatic method can be improved and as a result, it will be able to obtain more accurate results, which should be closer to the ones obtained manually.

Author Contributions: The authors have contributed equally to the work. All authors have read and agreed to the published version of the manuscript.

Funding: This project has been funded by Portuguese national funds of FCT/MCTES (PIDDAC) through the base funding from the following research units: UIDB/00532/2020 (Transport Phenomena Research Center—CEFT), UIDB/04077/2020 (Mechanical Engineering and Resource Sustainability Center—MEtRICs), UIDB/00690/2020 (CIMO). The authors are also grateful for the partial funding of FCT through the projects, NORTE-01-0145-FEDER-029394 (PTDC/EMD-EMD/29394/2017) and NORTE-01-0145-FEDER-030171 (PTDC/EMD-EMD/30171/2017) funded by COMPETE2020, NORTE2020, PORTUGAL2020 and FEDER. D. Bento acknowledges the PhD scholarship SFRH/BD/91192/2012 granted by FCT.

Conflicts of Interest: The authors declare no conflict of interest.

References

1. Lima, R.; Ishikawa, T.; Imai, Y.; Takeda, M.; Wada, S.; Yamaguchi, T. Measurement of Individual Red Blood Cell Motions Under High Hematocrit Conditions Using a Confocal Micro-PTV System. *Ann. Biomed. Eng.* **2009**, *37*, 1546–1559. [CrossRef] [PubMed]
2. Lima, R.; Saadatmand, M.; Ishikawa, T. Microfluidic Devices Based on Biomechanics. In *Integrated Nano-Biomechanics*; Yamaguchi, T., Ishikawa, T., Imai, Y., Eds.; Micro and Nano Technologies; Elsevier: Boston, MA, USA, 2018; pp. 217–263. ISBN 978-0-323-38944-0.
3. Catarino, S.O.; Rodrigues, R.O.; Pinho, D.; Miranda, J.M.; Minas, G.; Lima, R. Blood Cells Separation and Sorting Techniques of Passive Microfluidic Devices: From Fabrication to Applications. *Micromachines* **2019**, *10*, 593. [CrossRef] [PubMed]
4. Goldsmith, H.L.; Turitto, V.T. Rheological Aspects of Thrombosis and Haemostasis: Basic Principles and Applications. *Thromb. Haemost.* **1986**, *55*, 415–435. [CrossRef] [PubMed]
5. Rodrigues, R.O.; Sousa, P.C.; Gaspar, J.; Bañobre-López, M.; Lima, R.; Minas, G. Organ-on-a-Chip: A Preclinical Microfluidic Platform for the Progress of Nanomedicine. *Small* **2020**, *16*, e2003517. [CrossRef] [PubMed]
6. Lima, R.; Ishikawa, T.; Imai, Y.; Yamaguchi, T. Blood Flow Behavior in Microchannels: Past, Current and Future Trends. In *Single and Two-Phase Flows on Chemical and Biomedical Engineering*; Lima, R., Ishikawa, T., Imai, Y., Yamaguchi, T., Eds.; Bentham Science Publishers: Sharjah, United Arab Emirates, 2012; pp. 513–547. ISBN 9781608053476.
7. Brunetti, A.; Carnimeo, L.; Trotta, G.F.; Bevilacqua, V. Computer-assisted frameworks for classification of liver, breast and blood neoplasias via neural networks: A survey based on medical images. *Neurocomputing* **2019**, *335*, 274–298. [CrossRef]
8. Voorneveld, J.; Saaid, H.; Schinkel, C.; Radeljic, N.; Lippe, B.; Gijzen, F.J.; Van Der Steen, A.F.; De Jong, N.; Claessens, T.; Vos, H.J.; et al. 4-D Echo-Particle Image Velocimetry in a Left Ventricular Phantom. *Ultrasound Med. Biol.* **2020**, *46*, 805–817. [CrossRef] [PubMed]
9. Nyrnes, S.A.; Fadnes, S.; Wiggen, M.S.; Mertens, L.; Lovstakken, L. Blood Speckle-Tracking Based on High-Frame Rate Ultrasound Imaging in Pediatric Cardiology. *J. Am. Soc. Echocardiogr.* **2020**, *33*, 493–503.e5. [CrossRef]
10. Nakano, A.; Sugii, Y.; Minamiyama, M.; Niimi, H. Measurement of red cell velocity in microvessels using particle image velocimetry (PIV). *Clin. Hemorheol. Microcirc.* **2003**, *29*, 445–455. [PubMed]
11. Machin, M.; Santomaso, A.; Mazzucato, M.; Cozzi, M.R.; Battiston, M.; De Marco, L.; Canu, P. Single Particle Tracking Across Sequences of Microscopical Images: Application to Platelet Adhesion Under Flow. *Ann. Biomed. Eng.* **2006**, *34*, 833–846. [CrossRef]
12. Bento, D.; Rodrigues, R.O.; Faustino, V.; Pinho, D.; Fernandes, C.S.; Pereira, A.I.; Garcia, V.; Miranda, J.M.; Lima, R. Deformation of Red Blood Cells, Air Bubbles, and Droplets in Microfluidic Devices: Flow Visualizations and Measurements. *Micromachines* **2018**, *9*, 151. [CrossRef]
13. Lima, R.; Wada, S.; Tsubota, K.-I.; Yamaguchi, T. Confocal micro-PIV measurements of three-dimensional profiles of cell suspension flow in a square microchannel. *Meas. Sci. Technol.* **2006**, *17*, 797–808. [CrossRef]
14. Niu, L.; Qian, M.; Yan, L.; Yu, W.; Jiang, B.; Jin, Q.; Wang, Y.; Shandas, R.; Liu, X.; Zheng, H. Real-Time Texture Analysis for Identifying Optimum Microbubble Concentration in 2-D Ultrasonic Particle Image Velocimetry. *Ultrasound Med. Biol.* **2011**, *37*, 1280–1291. [CrossRef]
15. Voorneveld, J.; Keijzer, L.B.; Strachinaru, M.; Bowen, D.J.; Goei, J.S.; Ten Cate, F.T.; Van Der Steen, A.F.; De Jong, N.; Vos, H.J.; Van Den Bosch, A.E.; et al. High-Frame-Rate Echo-Particle Image Velocimetry Can Measure the High-Velocity Diastolic Flow Patterns. *Circ. Cardiovasc. Imaging* **2019**, *12*, e008856. [CrossRef]
16. Gates, P.E.; Gurung, A.; Mazzaro, L.; Aizawa, K.; Elyas, S.; Strain, W.D.; Shore, A.C.; Shandas, R. Measurement of Wall Shear Stress Exerted by Flowing Blood in the Human Carotid Artery: Ultrasound Doppler Velocimetry and Echo Particle Image Velocimetry. *Ultrasound Med. Biol.* **2018**, *44*, 1392–1401. [CrossRef] [PubMed]
17. Lu, J.; Lu, W.-Q. Blood flow velocity and ultra-filtration velocity measured by CT imaging system inside a densely bundled hollow fiber dialyzer. *Int. J. Heat Mass Transf.* **2010**, *53*, 1844–1850. [CrossRef]
18. Onwuzu, S.; Ugwu, A.; Mbah, G.; Elo, I. Measuring wall shear stress distribution in the carotid artery in an African population: Computational fluid dynamics versus ultrasound doppler velocimetry. *Radiography* **2020**. [CrossRef] [PubMed]
19. Moreau, H.D.; Blanch-Mercader, C.; Attia, R.; Maurin, M.; Alraies, Z.; Sanséau, D.; Malbec, O.; Delgado, M.-G.; Bousso, P.; Joanny, J.-F.; et al. Macropinocytosis Overcomes Directional Bias in Dendritic Cells Due to Hydraulic Resistance and Facilitates Space Exploration. *Dev. Cell* **2019**, *49*, 171–188.e5. [CrossRef]
20. Lima, R.; Ishikawa, T.; Imai, Y.; Takeda, M.; Wada, S.; Yamaguchi, T. Radial dispersion of red blood cells in blood flowing through glass capillaries: The role of hematocrit and geometry. *J. Biomech.* **2008**, *41*, 2188–2196. [CrossRef] [PubMed]
21. Lima, R.; Oliveira, M.S.N.; Ishikawa, T.; Kaji, H.; Tanaka, S.; Nishizawa, M.; Yamaguchi, T. Axisymmetric polydimethylsiloxane microchannels for in vitro hemodynamic studies. *Biofabrication* **2009**, *1*, 035005. [CrossRef] [PubMed]
22. Saadatmand, M.; Ishikawa, T.; Matsuki, N.; Abdekhodaie, M.J.; Imai, Y.; Ueno, H.; Yamaguchi, T. Fluid particle diffusion through high-hematocrit blood flow within a capillary tube. *J. Biomech.* **2011**, *44*, 170–175. [CrossRef]
23. Fujiwara, H.; Ishikawa, T.; Lima, R.; Matsuki, N.; Imai, Y.; Kaji, H.; Nishizawa, M.; Yamaguchi, T. Red blood cell motions in high-hematocrit blood flowing through a stenosed microchannel. *J. Biomech.* **2009**, *42*, 838–843. [CrossRef]

24. Yaginuma, T.; Oliveira, M.; Lima, R.; Ishikawa, T.; Yamaguchi, T. Red Blood Cell Deformation in Flows through a PDMS Hyperbolic Microchannel. In Proceedings of the Microtech Conference & Expo 2011, TechConnect World 2011, Boston, MA, USA, 14–16 June 2011.
25. Leble, V.; Fernandes, C.; Dias, R.; Lima, R.; Ishikawa, T.; Imai, Y.; Yamaguchi, T. Flow visualization of trace particles and red blood cells in a microchannel with a diverging and converging bifurcation. In *Computational Vision and Medical Image Processing: VipIMAGE 2011, Proceedings of the 3rd ECCOMAS Thematic Conference on Computational Vision and Medical Image Processing, Olhão, Portugal, 12–14 October 2011*; CRC Press: Boca Raton, FL, USA, 2012; pp. 209–211.
26. Di Ruberto, C.; Loddo, A.; Putzu, L. Detection of red and white blood cells from microscopic blood images using a region proposal approach. *Comput. Biol. Med.* **2020**, *116*, 103530. [CrossRef]
27. The MathWorks. *MatLab*; The MathWorks: Natick, MA, USA, 2010.
28. Carter, B.C.; Shubeita, G.T.; Gross, S.P. Tracking single particles: A user-friendly quantitative evaluation. *Phys. Biol.* **2005**, *2*, 60–72. [CrossRef]
29. Crocker, J.C.; Grier, D.G. Methods of Digital Video Microscopy for Colloidal Studies. *J. Colloid Interface Sci.* **1996**, *179*, 298–310. [CrossRef]
30. Eddins, S.L.; Gonzalez, R.C.; Woods, R.E. *Digital Image Processing Using MATLAB*; Gatesmark Publishing: Knoxville, TN, USA, 2002; ISBN 978-0-9820854-0-0.
31. Monteiro, F. Region-Based Spatial and Temporal Image Segmentation. Ph.D. Dissertation, Universidade do Porto, Porto, Portugal, 2008.
32. Chang, H.-H.; Valentino, D.J. An electrostatic deformable model for medical image segmentation. *Comput. Med. Imaging Graph.* **2008**, *32*, 22–35. [CrossRef]
33. Aly, A.A.; Bin Deris, S.; Zaki, N. Research Review for Digital Image Segmentation Techniques. *Int. J. Comput. Sci. Inf. Technol.* **2011**, *3*, 99–106. [CrossRef]
34. Shashi, P.; Suchithra, R. Review Study on Digital Image Processing and Segmentation. *Am. J. Comput. Sci. Technol.* **2019**, *2*, 68. [CrossRef]
35. Tripathy, B.; Mittal, D. Hadoop based uncertain possibilistic kernelized c-means algorithms for image segmentation and a comparative analysis. *Appl. Soft Comput.* **2016**, *46*, 886–923. [CrossRef]
36. Pham, D.L.; Xu, C.; Prince, J.L. Current Methods in Medical Image Segmentation. *Annu. Rev. Biomed. Eng.* **2000**, *2*, 315–337. [CrossRef] [PubMed]
37. Anilkumar, K.; Manoj, V.; Sagi, T. A survey on image segmentation of blood and bone marrow smear images with emphasis to automated detection of Leukemia. *Biocybern. Biomed. Eng.* **2020**, *40*, 1406–1420. [CrossRef]
38. Sharif, H. A numerical approach for tracking unknown number of individual targets in videos. *Digit. Signal Process.* **2016**, *57*, 106–127. [CrossRef]
39. Rogers, S.S.; Waigh, T.A.; Zhao, X.; Lu, J.R. Precise particle tracking against a complicated background: Polynomial fitting with Gaussian weight. *Phys. Biol.* **2007**, *4*, 220–227. [CrossRef]
40. Emami, N.; Sedaei, Z.; Ferdousi, R. Computerized cell tracking: Current methods, tools and challenges. *Vis. Inform.* **2021**, *5*, 1–13. [CrossRef]
41. Rangayyan, R.M. *Biomedical Image Analysis. Biomedical Engineering Series*; Calgary, U., Ed.; University of Calgary: Calgary, AB, Canada, 2005.
42. Adollah, R.; Mashor, M.Y.; Mohd Nasir, N.F.; Rosline, H.; Mahsin, H.; Adilah, H. Blood cell image segmentation: A review. *IFMBE Proc.* **2008**, *21*, 141–144. [CrossRef]
43. Zamani, F.; Safabakhsh, R. An unsupervised GVF snake approach for white blood cell segmentation based on nucleus. In Proceedings of the 2006 8th international Conference on Signal Processing, Guilin, China, 16–20 November 2006; Volume 2, pp. 1–4.
44. Montseny, E.; Sobrevilla, P.; Romani, S. A fuzzy approach to white blood cells segmentation in color bone marrow images. In Proceedings of the 2004 IEEE International Conference on Fuzzy Systems, Budapest, Hungary, 25–29 July 2004; Volume 1, pp. 173–178.
45. Jiang, K.; Liao, Q.-M.; Dai, S.-Y. A novel white blood cell segmentation scheme using scale-space filtering and watershed clustering. In Proceedings of the 2003 International Conference on Machine Learning and Cybernetics, Xi'an, China, 5 November 2003; Volume 5, pp. 2820–2825. [CrossRef]
46. Wu, J.; Zeng, P.; Zhou, Y.; Olivier, C. A novel color image segmentation method and its application to white blood cell image analysis. In Proceedings of the 2006 8th international Conference on Signal Processing, Guilin, China, 16–20 November 2006; Volume 2.
47. Kumar, R.S.; Verma, A.; Singh, J. Color Image Segmentation and Multi-Level Thresholding by Maximization of Conditional Entropy. *Int. J. Signal Process.* **2007**, *1*, 1633–1641.
48. Huang, D.-C.; Hung, K.-D.; Chan, Y.-K. A computer assisted method for leukocyte nucleus segmentation and recognition in blood smear images. *J. Syst. Softw.* **2012**, *85*, 2104–2118. [CrossRef]
49. Willenbrock, F.; Zicha, D.; Hoppe, A.; Hogg, N. Novel Automated Tracking Analysis of Particles Subjected to Shear Flow: Kindlin-3 Role in B Cells. *Biophys. J.* **2013**, *105*, 1110–1122. [CrossRef]

50. How, K.; Bin, A.; Siong, N.; Soo, K. Red Blood Cell Segmentation Utilizing Various Image Segmentation Techniques. In Proceedings of the International Conference on Man-Machine Systems, Langkawi, Malaysia, 15–16 September 2006.
51. Wang, M.; Zhou, X.; Li, F.; Huckins, J.; King, R.W.; Wong, S.T. Novel cell segmentation and online learning algorithms for cell phase identification in automated time-lapse microscopy. In Proceedings of the 2007 4th IEEE International Symposium on Biomedical Imaging: From Nano to Macro, Arlington, VA, USA, 12–15 April 2007; pp. 65–68.
52. Li, Q.; Wang, Y.; Liu, H.; Wang, J.; Guo, F. A combined spatial-spectral method for automated white blood cells segmentation. *Opt. Laser Technol.* **2013**, *54*, 225–231. [CrossRef]
53. Pan, C.; Park, D.S.; Yoon, S.; Yang, J.C. Leukocyte image segmentation using simulated visual attention. *Expert Syst. Appl.* **2012**, *39*, 7479–7494. [CrossRef]
54. Sadeghian, F.; Seman, Z.; Ramli, A.R.; Kahar, B.H.A.; Saripan, M.-I. A Framework for White Blood Cell Segmentation in Microscopic Blood Images Using Digital Image Processing. *Biol. Proced. Online* **2009**, *11*, 196–206. [CrossRef] [PubMed]
55. Ritter, N.; Cooper, J. Segmentation and border identification of cells in images of peripheral blood smear slides. *Conf. Res. Pract. Inf. Technol. Ser.* **2007**, *62*, 161–169.
56. Ongun, G.; Halici, U.; Leblebicioglu, K.; Atalay, V.; Beksac, M.; Beksac, S. Feature extraction and classification of blood cells for an automated differential blood count system. In Proceedings of the IJCNN'01. International Joint Conference on Neural Networks, Washington, DC, USA, 15–19 July 2001; Volume 4, pp. 2461–2466.
57. Al-Dulaimi, K.; Tomeo-Reyes, I.; Banks, J.; Chandran, V. Evaluation and benchmarking of level set-based three forces via geometric active contours for segmentation of white blood cell nuclei shape. *Comput. Biol. Med.* **2020**, *116*, 103568. [CrossRef] [PubMed]
58. Maitra, M.; Gupta, R.K.; Mukherjee, M. Detection and Counting of Red Blood Cells in Blood Cell Images using Hough Transform. *Int. J. Comput. Appl.* **2012**, *53*, 13–17. [CrossRef]
59. Banik, P.P.; Saha, R.; Kim, K.-D. An Automatic Nucleus Segmentation and CNN Model based Classification Method of White Blood Cell. *Expert Syst. Appl.* **2020**, *149*, 113211. [CrossRef]
60. Kawaguchi, H.; Masamoto, K.; Ito, H.; Kanno, I. Image-based vessel-by-vessel analysis for red blood cell and plasma dynamics with automatic segmentation. *Microvasc. Res.* **2012**, *84*, 178–187. [CrossRef] [PubMed]
61. Yilmaz, A.; Javed, O.; Shah, M. Object tracking: A Survey. *ACM Comput. Surv.* **2006**, *38*, 13. [CrossRef]
62. Miura, K. Tracking Movement in Cell Biology. *Adv. Biochem. Eng. Biotechnol.* **2005**, *95*, 267–295. [CrossRef]
63. Dobbe, J.G.G.; Streekstra, G.J.; Atasever, B.; Van Zijderveld, R.; Ince, C. Measurement of functional microcirculatory geometry and velocity distributions using automated image analysis. *Med. Biol. Eng. Comput.* **2008**, *46*, 659–670. [CrossRef]
64. Iqbal, M.S.; Khan, T.; Hussain, S.; Mahmood, R.; El-Ashram, S.; Abbasi, R.; Luo, B. Cell Recognition of Microscopy Images of TPEF (Two Photon Excited Florescence) Probes. *Procedia Comput. Sci.* **2019**, *147*, 77–83. [CrossRef]
65. Aly, A.A.; Bin Deris, S.; Zaki, N. A New Algorithm for Cell Tracking Technique. *Adv. Comput. Int. J.* **2011**, *2*, 13–20. [CrossRef]
66. Pan, Y.; Xia, Y.; Zhou, T.; Fulham, M. Cell image segmentation using bacterial foraging optimization. *Appl. Soft Comput.* **2017**, *58*, 770–782. [CrossRef]
67. Möller, M.; Burger, M.; Dieterich, P.; Schwab, A. A framework for automated cell tracking in phase contrast microscopic videos based on normal velocities. *J. Vis. Commun. Image Represent.* **2014**, *25*, 396–409. [CrossRef]
68. Kirisits, C.; Lang, L.F.; Scherzer, O. Optical Flow on Evolving Surfaces with an Application to the Analysis of 4D Microscopy Data. In *Scale Space and Variational Methods in Computer Vision*; Kuijper, A., Bredies, K., Pock, T., Bischof, H., Eds.; Springer: Berlin/Heidelberg, Germany, 2013; Volume 7893. [CrossRef]
69. Niazi, E.; McDonald, J.G.; Fenech, M. An automated method for size and velocity distribution measurement in a particle-laden flow. *Adv. Eng. Softw.* **2019**, *134*, 10–21. [CrossRef]
70. Park, J.H.; Choi, W.; Yoon, G.Y.; Lee, S.J. Deep Learning-Based Super-resolution Ultrasound Speckle Tracking Velocimetry. *Ultrasound Med. Biol.* **2020**, *46*, 598–609. [CrossRef]
71. Carboni, E.J.; Bognet, B.H.; Bouchillon, G.M.; Kadilak, A.L.; Shor, L.M.; Ward, M.D.; Ma, A.W. Direct Tracking of Particles and Quantification of Margination in Blood Flow. *Biophys. J.* **2016**, *111*, 1487–1495. [CrossRef]
72. Varga, L.; Kovács, A.; Grósz, T.; Thury, G.; Hadarits, F.; Dégi, R.; Dombi, J.; Dégi, R. Automatic segmentation of hyperreflective foci in OCT images. *Comput. Methods Programs Biomed.* **2019**, *178*, 91–103. [CrossRef] [PubMed]
73. Chen, T.; Zhang, Y.; Wang, C.; Qu, Z.; Wang, F.; Syeda-Mahmood, T. Complex local phase based subjective surfaces (CLAPSS) and its application to DIC red blood cell image segmentation. *Neurocomputing* **2013**, *99*, 98–110. [CrossRef]
74. Siegmund, B.J.; Kasten, A.; Kühn, J.-P.; Winter, K.; Grüttner, C.; Frerich, B. MRI-tracking of transplanted human ASC in a SCID mouse model. *J. Magn. Magn. Mater.* **2017**, *427*, 151–155. [CrossRef]
75. Muller, R.; Stranik, O.; Schlenk, F.; Werner, S.; Malsch, D.; Fischer, D.; Fritzsche, W. Optical detection of nanoparticle agglomeration in a living system under the influence of a magnetic field. *J. Magn. Magn. Mater.* **2015**, *380*, 61–65. [CrossRef]
76. Kucukal, E.; Man, Y.; Hill, A.; Liu, S.; Bode, A.; An, R.; Kadambi, J.; Little, J.A.; Gurkan, U.A. Whole blood viscosity and red blood cell adhesion: Potential biomarkers for targeted and curative therapies in sickle cell disease. *Am. J. Hematol.* **2020**, *95*, 1246–1256. [CrossRef]
77. Kucukal, E.; Man, Y.; Gurkan, U.A.; Schmidt, B.E. Blood Flow Velocimetry in a Microchannel during Coagulation Using PIV and wOFV. In Proceedings of the ASME 2020 International Mechanical Engineering Congress and Exposition, Virtual, Online, 16–19 November 2020.

78. Abràmoff, M.D.; Magalhães, P.J.; Ram, S.J. Image processing with image]. *Biophotonics Int.* **2004**, *11*, 36–41. [CrossRef]
79. Bento, D.; Pereira, A.I.; Lima, J.; Miranda, J.M.; Lima, R. Cell-free layer measurements of in vitro blood flow in a microfluidic network: An automatic and manual approach. *Comput. Methods Biomech. Biomed. Eng. Imaging Vis.* **2018**, *6*, 629–637. [CrossRef]
80. Bento, D.; Lopes, S.; Maia, I.; Lima, R.; Miranda, J.M. Bubbles Moving in Blood Flow in a Microchannel Network: The Effect on the Local Hematocrit. *Micromachines* **2020**, *11*, 344. [CrossRef]
81. Sbalzarini, I.; Koumoutsakos, P. Feature point tracking and trajectory analysis for video imaging in cell biology. *J. Struct. Biol.* **2005**, *151*, 182–195. [CrossRef]
82. Pinho, D.; Rodrigues, R.O.; Faustino, V.; Yaginuma, T.; Exposto, J.; Lima, R. Red blood cells radial dispersion in blood flowing through microchannels: The role of temperature. *J. Biomech.* **2016**, *49*, 2293–2298. [CrossRef]
83. Lima, R. Analysis of the Blood Flow Behavior through Microchannels by a Confocal Micro-PIV/PTV System. Ph.D. Thesis, Tohoku University, Sendai, Japan, 2007; pp. 1–215.
84. Meijering, E.; Smal, I.; Danuser, G. Tracking in molecular bioimaging. *IEEE Signal Process. Mag.* **2006**, *23*, 46–53. [CrossRef]
85. Horn, B.K.; Schunck, B.G. Determining optical flow. *Artif. Intell.* **1981**, *17*, 185–203. [CrossRef]
86. Barron, J.L.; Thacker, N.A. *Tutorial: Computing 2D and 3D Optical Flow*; Imaging Science and Biomedical Engineering Division, Medical School, University of Manchester: Manchester, UK, 2005; pp. 1–12.



Article

New Method for Preparing Small-Caliber Artificial Blood Vessel with Controllable Microstructure on the Inner Wall Based on Additive Material Composite Molding

Junchao Hu, Zhian Jian, Chunxiang Lu, Na Liu, Tao Yue , Weixia Lan and Yuanyuan Liu *

School of Mechatronics Engineering and Automation, Shanghai University, Shanghai 200444, China; hujunchao@shu.edu.cn (J.H.); jianzhian@shu.edu.cn (Z.J.); 20721813@shu.edu.cn (C.L.); liuna_sia@shu.edu.cn (N.L.); tao_yue@shu.edu.cn (T.Y.); weixia_lan@shu.edu.cn (W.L.)

* Correspondence: yuanyuan_liu@shu.edu.cn

Abstract: The diameter of most blood vessels in cardiovascular and peripheral vascular system is less than 6 mm. Because the inner diameter of such vessels is small, a built-in stent often leads to thrombosis and other problems. It is an important goal to replace it directly with artificial vessels. This paper creatively proposed a preparation method of a small-diameter artificial vascular graft which can form a controllable microstructure on the inner wall and realize a multi-material composite. On the one hand, the inner wall of blood vessels containing direct writing structure is constructed by electrostatic direct writing and micro-imprinting technology to regulate cell behavior and promote endothelialization; on the other hand, the outer wall of blood vessels was prepared by electrospinning PCL to ensure the stability of mechanical properties of composite grafts. By optimizing the key parameters of the graft, a small-diameter artificial blood vessel with controllable microstructure on the inner wall is finally prepared. The corresponding performance characterization experimental results show that it has advantages in structure, mechanical properties, and promoting endothelialization.

Keywords: small caliber blood vessel; composite molding; micro-nano structure; tissue repair; 3D printing



Citation: Hu, J.; Jian, Z.; Lu, C.; Liu, N.; Yue, T.; Lan, W.; Liu, Y. New Method for Preparing Small-Caliber Artificial Blood Vessel with Controllable Microstructure on the Inner Wall Based on Additive Material Composite Molding. *Micromachines* **2021**, *12*, 1312. <https://doi.org/10.3390/mi12111312>

Academic Editors: Rui A. Lima, Susana Catarino and Graça Minas

Received: 8 October 2021
Accepted: 23 October 2021
Published: 26 October 2021

Publisher's Note: MDPI stays neutral with regard to jurisdictional claims in published maps and institutional affiliations.



Copyright: © 2021 by the authors. Licensee MDPI, Basel, Switzerland. This article is an open access article distributed under the terms and conditions of the Creative Commons Attribution (CC BY) license (<https://creativecommons.org/licenses/by/4.0/>).

1. Introduction

The incidence and mortality of cardiovascular diseases have been showing an upward trend year by year, which seriously affects human health [1]. Although a large number of vascular stents have been used clinically, most of them are built-in stent products for large blood vessels, and the treatment of small-diameter vascular diseases and functional defects is still a challenge [2,3]. Most of the blood vessels in the cardiovascular and peripheral vascular system are less than 6 mm in diameter [4]. Due to the small inner diameter of such blood vessels and the slow blood flow rate, built-in stents often lead to problems such as thrombosis. Direct replacement with artificial blood vessels is an important potential method [5,6].

The small-caliber blood vessels in the human body are not only small in diameter and thin in wall, but also have a complex layered structure, including an inner layer that supports cells and induces platelet adhesion and aggregation, as well as a middle layer and an outer layer that provide mechanical support [7–10]. In order to allow the artificial blood vessel to fuse with the host blood vessel after being transplanted into the body, and to quickly achieve the metabolic function of the natural blood vessel, the construction of a small-caliber artificial blood vessel must not only meet the bionic structure and mechanical properties, but also achieve rapid and effective endothelialization. This poses a challenge to both the material design and preparation process [11,12]. A large number of studies have shown that specific microstructures can guide the behavior and arrangement of cells. However, there are few studies that combine this type of research

with the construction of small-caliber blood vessels. At the same time, it must be able to take into account the multiple requirements of bionic small-caliber blood vessels in terms of structure and mechanical properties. In addition, in order to obtain a perfect small-caliber artificial blood vessel, the choice of materials is also very important [13–16]. Because a single material often cannot effectively take into account both biological functions and mechanical properties, natural biological materials combined with polymer composites have become a hot spot in current research [17–19]. However, there is still a lack of systematic composite molding process research, and the research on achieving controllable composites of different materials and structures is still very imperfect.

In this context, this research proposes an additive composite molding method that combines electrospinning [20–22] and electrostatic direct writing [23] micro-imprint technology. The specific process is as follows. As shown in Figure 1, the first major link includes the following three steps: First, the film structure is obtained by micro-imprinting the material, and, considering the needs of cell adhesion and growth, the film structure can also be imprinted into a surface with a specific microstructure. Then, electrostatically direct wiring forms an orderly arranged fiber structure and transfers the orderly arranged fiber structure to the film structure prepared in advance by embossing. On this basis, the second major link is the process of dynamically shaping the formed two-dimensional film structure into a tube through a tubular mold, which specifically includes the following two steps: one is based on a pre-designed and prepared tubular mold, using thin long tweezers extended from the tail of the mold, and the head stretches out to clamp the previously prepared base film and drag it into the tube. The film will be passively rolled into a tube due to the friction with the tube wall and the boundary effect. The diameter of the tube formed is the inner diameter of the mold. Second, under the drive of the three-axis motion platform, the nanofiber film is directly wrapped on the surface of the above-mentioned dynamically crimped tube through the electrospinning process, which can realize the shape of the dynamically formed tube, and it can also realize the on-demand optimization of the mechanical properties and biological properties of the overall pipe structure.

It should be pointed out that the effective realization of the process method proposed above is closely related to the materials selected and the structural parameters of the pipe to be prepared. First of all, in order to realize that the imprinted film is dynamically shaped into a tube, the mechanical properties of the material and the imprinted film thickness parameters need to be weighed and optimized. For this reason, this article chose a polyether ether ketone (PPDO) material with good biocompatibility, good melting characteristics, and ductility. It is a biodegradable and biocompatible aliphatic polyether ester. It has been approved by the FDA for use, and its degradation is mainly hydrolytic cleavage, which can form low-molecular-weight substances consistent with human metabolites, which can be metabolized or bioabsorbed by the human body [24,25]. Considering the need for cell adhesion growth in the later stage, the PPDO film prepared by imprinting can be surface functionalized by plasma treatment and dopamine soaking. Secondly, the ordered fibers of electrostatic direct writing can be effectively transferred to the imprinted two-dimensional film structure, and it is necessary to comprehensively consider the interface energy competition between the direct writing material, the receiving interface, and the imprinting film. In order to solve this problem, this article proposes that the material selected for electrostatic direct writing and the embossed film material need to have different thermal melt ductility, so that effective transfer can be achieved by adjusting the temperature around the transfer device during the transfer process. In this paper, based on the temperature characteristics of PPDO, combined with the requirements of the electrostatic direct writing process, polycaprolactone (PCL) is selected for electrostatic direct writing. Taking into account the needs of cell adhesion and growth in the later stage, PCL materials can also be compounded with materials with good cell affinity such as gelatin.

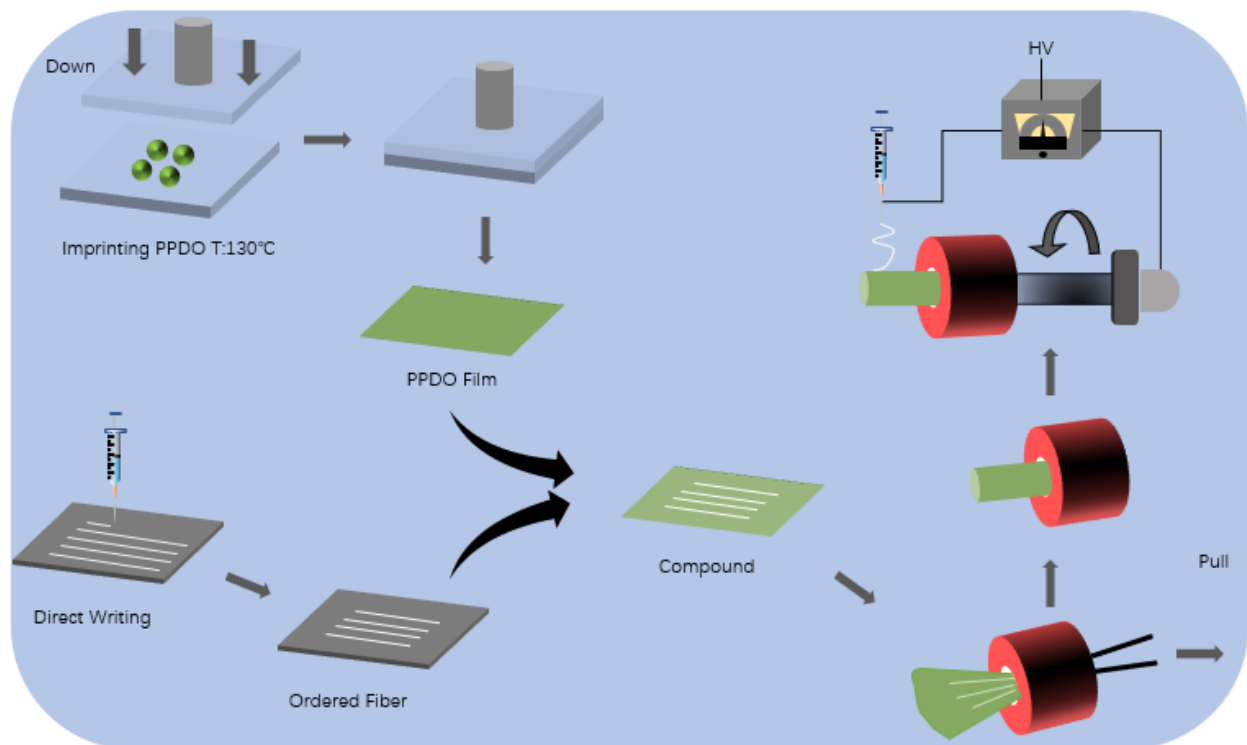


Figure 1. Process flow chart of preparation of small-diameter blood vessels.

It is not difficult to find that the process method proposed in this paper has good processing flexibility and can be controlled in the form of inner wall microstructure, pipe diameter, and wall thickness. The corresponding material selection and specific ratio can also be controlled, adjusted, and designed as needed.

2. Materials and Methods

2.1. Solution Preparation

Preparation of pcl solution: 2.25 g pcl (Average Mn 80000, Sigma-Aldrich, Co., Haverhill, UK) particles were dissolved in 10 mL dichloromethane (Molecular weight 84.93, XiYaShiji, Shanghai, China) and 5 mL dimethylformamide DMF (99.5%, Shanghai Aladdin Biochemical Technology Co., Ltd., Shanghai, China), and stirred under a magnetic stirrer (Shanghai MeiYingPu Instrument Manufacturing Co., Ltd., Shanghai, China) for 2 h at a concentration of 15% (*w/v*).

Preparation of pcl-gelatin solution: 0.8 g of pcl particles were dissolved in 10 mL of trifluoroethanol (99.5%, Shanghai Aladdin Biochemical Technology Co., Ltd.), and stirred under a magnetic stirrer for 2 h. Subsequently, 0.2 g of gelatin (Vetec™ reagent grade, Type A, Sigma-Aldrich, Co., St. Louis, MO, USA) was added and stirred for two hours at 37 degrees, and finally 38 μ L of crosslinking agent was added and stirred for 2 h at a concentration of 10% (*w/v*).

Dopamine solution preparation: 0.02 g dopamine (Shanghai KeLaMan Reagent Co., Ltd., Shanghai, China) powder was dissolved in 10 mL Tris buffer to prepare a dopamine solution with a concentration of 2 mg/mL.

PPDO: Poly(p-dioxanone) PPDO (Suzhou JIAYE Biotechnology Co., Ltd., Suzhou, China) material is granular. It is a kind of aliphatic polyester ether with good biodegradability and biocompatibility. Its unique ether ester structure gives the material high strength and good flexibility. The melting point is 109 °C. In this experiment, PPDO film was prepared under a hot machine (Qingdao Jinggang hot stamping equipment Co., Ltd., Qingdao, Shandong, China).

2.2. Film Fabrication Approaches

2.2.1. Embossed Film Structure Preparation

A plan view of the groove structure is drawn on the drawing software CAD, and the mask plate is processed and prepared. First, a silicon wafer substrate containing a patterned structure is prepared, and the silicon wafer is cleaned then heated on a heating plate at 200 °C for 5 min to remove surface water molecules, followed by spin-coating su-8 2000 glue on the substrate with thick glue spin glue technology. The specific parameters of the rotation speed are: first accelerate to 500 r at an acceleration of 100 r/s and continue for 5 s, then adjust the speed to 2000 r for 30 s, and place it at 95 °C Heating on a hot plate at 95 °C for 1 min, the thickness of the su-8 2000 adhesive layer is about 0.6 mm.

The mask plate is attached to the adhesive layer and exposed with a lithography machine for 7 s, then heated on a 95 °C heating plate for 1 min, and finally immersed in a developer for 1 min for development and then dried to obtain a pattern-containing mold. The mold is placed in a petri dish, and 28 gpdms (SYLGARDTM 184) and 3 gpdms curing agent are mixed in a beaker and stirred with a glass rod for 3–5 min until milky white and the bubbles are small and uniform. Then it is poured into the petri dish and placed in a vacuum machine for 15 min, then placed in a fume hood for 8 h, and finally baked in an oven at 60 °C for 2 h to obtain a pdms mold with grooved microstructure. Same as above, the steps are repeated to prepare multiple ordinary pdms molds without patterns as auxiliary devices for the imprinting process.

Then, 1 g of PPDO (BaiMuDa, Nanjing, China) particles are placed evenly on the ordinary pdms mold, which are moved to the heating plate with the temperature kept at 120 degrees Celsius. They are heated for 5 min until the PPDO particles melt into a liquid state, and then the whole is transferred to the bottom of the imprinting machine. The PDMS mold containing the groove structure is put on the top to fit it, the air pump control valve adjusted to 0.3 MPa, the imprinting machine control switch turned on, and the hot plate squeezes the PPDO material downwards to adjust the temperature control and time module. The temperature is 120 °C and the duration is 30 min. After cooling, the PPDO base film containing the groove microstructure can be obtained.

2.2.2. Ordered Fiber Structure Preparation

In order to be able to effectively analyze the influence of different material components on subsequent cell behavior, this paper designed two sets of samples, namely the pcl group and the pcl-gelatin group.

The prepared PCL solution is loaded into the syringe piston barrel and connected with the syringe on the micro pump actuator through a catheter. The spinning collector is fixed on the XY-axis platform of the three-axis motion platform and the syringe needle and the panel of the spinning collector are made to perpendicularly intersect, adjusting the Z-axis slider so that the distance between the end of the syringe needle and the collector is 5 mm. The positive pole of the high-voltage power supply is connected to the metal part of the syringe needle, the negative pole is connected to the metal part of the spinning collector, and the voltage between the two poles is set to 3200 V. The feed flow rate of the micro pump controller is set to 1 mL/h, the reciprocating speed of the needle with the X-axis platform of the three-axis motion platform is 0.25 m/s and the single stroke in the positive direction of the X-axis is 80 mm. Then, the positive Y-axis moves 50 μm in the direction, and then moves in the negative direction of the X-axis. The distance is 50 μm, and the reciprocating movement is repeated many times. With the deposition of pcl on the tin foil of the collector, the tin foil is finally removed to obtain the PCL direct writing fiber structure.

Loading the prepared PCL-gelatin solution into the syringe piston barrel, the flow rate of the micro pump solution is 1 mL/h, the distance between the end of the spinning syringe needle and the collector is 2 mm, and the needle size used is 23 g. The subsequent steps are similar to the previous PCL direct writing steps, and the pcl-gelatin direct writing fiber structure can be obtained.

2.2.3. Preparation of Composite Film

Similar to the steps for preparing the embossed film, firstly, the PPDO base film is prepared by embossing with pdms chips that do not contain microstructures, and the preparation parameters remain the same as above. The PCL direct writing structure is placed together with the tin foil on the base of the imprinting machine. Covering the PPDO base film on the direct writing structure, the air pump control valve is adjusted to 0.3 MPa and the control switch of the imprinting machine is turned on. At this time, the hot plate will squeeze the PPDO film and the direct writing structure downwards. The temperature control and time module are adjusted to 40 °C and the duration is 30 min, and then it is taken out to obtain a composite film of PPDO and direct writing structure.

2.2.4. Preparation of Artificial Blood Vessel

First, a cylindrical through hole with an inner diameter of 4 mm, an outer diameter of 5 mm, and a length of 20 mm is drawn in the solidworks three-dimensional drawing software, and the FDM software is imported to prepare the corresponding mold. Secondly, slender tweezers are used to insert from one end of the mold and extend the other end to clamp the middle of one end of the prepared film and drag it into the tube. Due to the inner wall of the tube, the film spontaneously curls and eventually rolls into a tube. In order to fully discuss the effects of microstructure and materials on cell behavior, the composite films constructed by the above three types of direct-write fibers were respectively crimped, and the film with only embossed groove structure was also selected for crimping. Finally, the three sets of tubular structures prepared above and the mold are connected with a shaft slightly less than 4 mm in diameter, are assembled on a rotating motor, and placed under a three-axis platform for electrospinning. Loading the prepared PCL solution into the syringe piston barrel, it is connected to the micro pump actuator, and the Z-axis slider is adjusted so that the distance between the end of the syringe needle and the collector is 100 mm. The voltage between the two poles is set to 7 kV. The feed flow rate of the micro pump controller is set to 1 mL/h, and the internal tubular structure is drawn out by 5 mm for every 5 min of spinning. When all of them are taken out, the blood vessel stent can be obtained; that is, the pcl, pcl-gelatin and PPDO with a groove structure inside the stent.

2.3. Characterization of Vascular Grafts

2.3.1. Morphology Observation

In order to observe the guiding structure of the film sample and the macroscopic layered structure of the composite blood vessel, the blood vessels prepared in the imprint group, the pcl direct writing composite group film, and the pcl direct writing composite group were prepared respectively. The morphology of the film sample was detected by an optical microscope to observe the surface structure and morphology. The observation of blood vessels was mainly to observe the layered structure and overall size.

2.3.2. Mechanical Properties

The prepared imprinted film, the film compounded with pcl direct writing fiber, the artificial blood vessel prepared with the imprinted film, and the artificial blood vessel prepared with the film compounded with pcl direct writing fiber were respectively subjected to an axial pull-up test. The prepared film has a size of 20 × 16 mm and a thickness of 0.3 mm, and the corresponding tube is prepared on the basis of the two films of the above specifications. All samples were covered with a pcl electrospun film after preparation, and the electrospinning parameters were all kept the same as described above.

The film and the tube sample are clamped on the universal testing machine. Taking the distance between the two clamps as the initial length, at room temperature, the test piece is stretched at a crosshead speed of 20 mm/min until it breaks. Assuming the incompressibility of the material, and considering the length and cross-sectional area, the load-displacement curve is calculated to determine the stress-strain relationship, using the formula $\varepsilon = (LF - L1)/L1$ to calculate the strain based on the initial length of the specimen

(L1) and the tensile specimen length when the force (F) is applied to the specimen (LF). The tensile stress is calculated using $\sigma = F/S$, where S is the cross-sectional area of the sample. In this case, the cross-sectional area is calculated as $S = tw$, where t is the thickness of the stent and w is the width of the sample. Here, when stretched, it is divided into the film group (including the imprinted film and the pcl direct writing composite film) and the tubular graft group (including the imprinted blood vessel and the pcl direct writing composite blood vessel). At the same time, when the film group is stretched, it is divided into straight groove or direct writing structure stretch, and the corresponding tubular components are axial stretch and radial stretch.

2.3.3. Suture Maintains Strength

Suture retention strength (SRS) is commonly used to measure the ability of a suture to adhere a graft to surrounding tissues. A universal testing machine is used to test the suture retention strength. Each is cut to obtain a film sample (length = 20 mm, width = 16 mm). Each sample is clamped in the test device at the edge of the film sample originally located. Using a 5-0 nylon surgical suture (Yangzhou Yuankang Medical Instruments Co., Ltd., Yangzhou, China), the other end of the sample is sutured to a distance of 2 mm from the end. The distance between the two needles is 2 mm. The suture is fixed on the hole in the self-made orifice plate, which is connected to the fixture of the test equipment. The suture is pulled out at an extension rate of 2 mm/s. SRS is calculated by dividing the maximum force recorded before the suture is pulled out by the number of sutures.

2.3.4. In Vitro Cytocompatibility

The cells were selected from the same batch of endothelial cells (Human Umbilical Vein Endothelial Cells, HUVEC), and resuscitated in four bottles. After resuscitation, they were added to each sample dish for culture. Each culture sample dish was pre-added with 3 mL of culture medium (Lifeline Cell Technology, LLC, Lonza, Walkersville, MD, USA). Finally, it was placed in a 37 degree incubator the culture medium changed every three days. During cell culture, the culture flask is pretreated first; that is, 50 mL gelatin solution with a concentration of 0.1% *w/v* is prepared, filtered with a syringe filter (0.22 μ), and then used. Finally, the culture flask is filled with the filtered gelatin solution (10 cm diameter petri dish requires 2 mL of solution), until the bottom of the bottle is covered and left at room temperature for 5 min, and then suck gelatin solution is sucked from the petri dish, which can be used for endothelial cell resuscitation.

In the endothelial cell inoculation experiment, four groups were prepared: the PPDO film group without microstructure, PPDO imprint film group, pcl direct writing compound group, and pcl gelatin direct writing compound group. The sample preparation method of the composite group is as shown in the previous section, which is a composite of pcl or pcl gelatin direct writing structure and unpatterned PPDO base film. The sample size of each group is four, of which the unstructured PPDO film group is mainly used as a control group to compare and observe the influence of groove structure on cell behavior. The pcl direct writing compound group and the pcl gelatin direct writing compound group can be used for comparison and the influence of the material components forming the microstructure on the cell behavior can be analysed.

Before cell inoculation, the four groups of samples were treated with plasma for 90 s, and then the four groups of samples were immersed in dopamine solution, kept in the dark at room temperature for 24 h, then rinsed with deionized water three times, and finally placed in room temperature to air dry. Before cell seeding, all samples were irradiated with ultraviolet light on both sides for 30 min, and sealed and stored in a refrigerator at $-20\text{ }^{\circ}\text{C}$.

The above-mentioned processed samples were inoculated and cultured with cells according to the groups, and the growth of cells on the samples at 1, 3, 7, and 14 days was recorded for each group of cells. The samples that need to observe the results of cell growth were stained with crystal violet to observe the staining and growth of the cells. The specific staining steps are as follows: first, the waste liquid of the sample is aspirated and DPBS

buffer is added for washing; then, the DPBS buffer is aspirated, 1 mL of paraformaldehyde solution is added, and it is left for 10–15 min. Then, the paraformaldehyde solution is aspirated and washed using the DPBS solution. Finally, crystal violet solution was added and the sample was immersed, placed on a shaker for 10 min, and finally the crystal violet solution was sucked out and cleaned, and the processed sample was placed under a microscope to observe the cell growth results.

3. Results

3.1. Morphology of Vascular Grafts

Figure 2 shows the morphological observation results of the vascular graft. Figure 2A is the imprinted film, Figure 2B,C are the observation results under different magnification microscopes, Figure 2D is the pcl direct writing composite group film, Figure 2E,F are the observation results under different magnification microscopes, Figure 2G is the pcl Gelatin direct writing composite film, and Figure 2H,I are the observation results under different magnification microscopes. The inner diameter of the tubular structure is about 4 mm, as shown in Figure 2J. The layered structure of the stent remains intact, and the inner and outer membranes can be clearly seen, as shown in Figure 2K. Figure 2L is a macroscopic view of the composite tube. It can be seen that there is a composite direct writing structure on the inner wall. The thickness of the whole membrane is about 0.3 mm, which is close to the average thickness of human veins of $346 \pm 121 \mu\text{m}$.

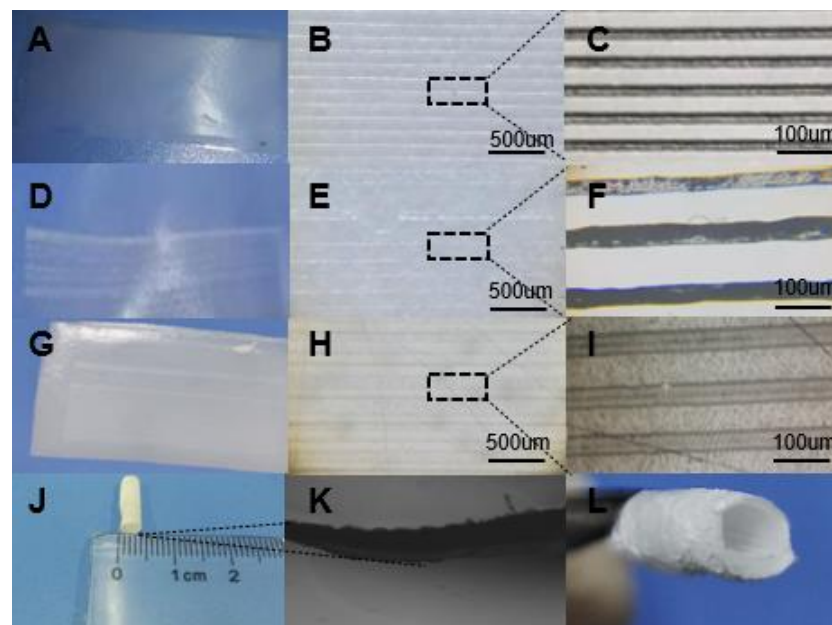


Figure 2. Artificial blood vessel size and film structure: (A) is the PPDO imprinting group film structure prepared by imprinting with the pdms chip containing microstructures at 120°C for 30 min at 120°C . (B,C) is the imprinting group film at different magnifications. The microstructure diagram under the microscope (D) is a sample film composed of PPDO base film and PCL direct writing structure imprinted with a pdms chip that does not contain microstructures in an imprinting machine at 120°C for 30 min. The temperature is 40°C , and the printing time is 30 min. (E,F) is the microstructure of the PCL direct-write composite film under different magnification microscopes. (G) is the imprinting with the pdms chip without microstructure at 120°C . The sample film composed of the PPDO base film prepared in 30 min and the PCL-gelatin direct writing structure meets the parameters of a temperature of 40°C and an imprinting time of 30 min (H,I) for the PCL-gelatin direct writing composite film under different magnification microscopes. The microstructure diagram (J) is the overall size of the vascular graft (K) is the magnified diagram of the layered structure of the blood vessel (L) is the composite diagram of the direct writing structure of the inner wall of the vascular graft.

3.2. Mechanical Properties

The tensile test was carried out on the tensile machine to obtain the stress-strain curve of tensile strength and elongation at break, as shown in Figure 3. Since the difference between the pcl composite group and the pcl gelatin group is mainly in affecting cell growth, they are regarded as the same group for mechanical performance testing. In this experiment, the pcl composite group was selected for testing; the imprinting group with or without microstructures is similar. The situation is regarded as the same group for mechanical performance testing. In this experiment, a sample group with a micro-groove structure was selected for testing. Figure 3A,B are, respectively, the radial tensile and tubular axial tensile stress-strain curves of the film sample, and Figure 3D,E are the radial tensile and tubular axial tensile stress-strain curves of the tubular sample, respectively.

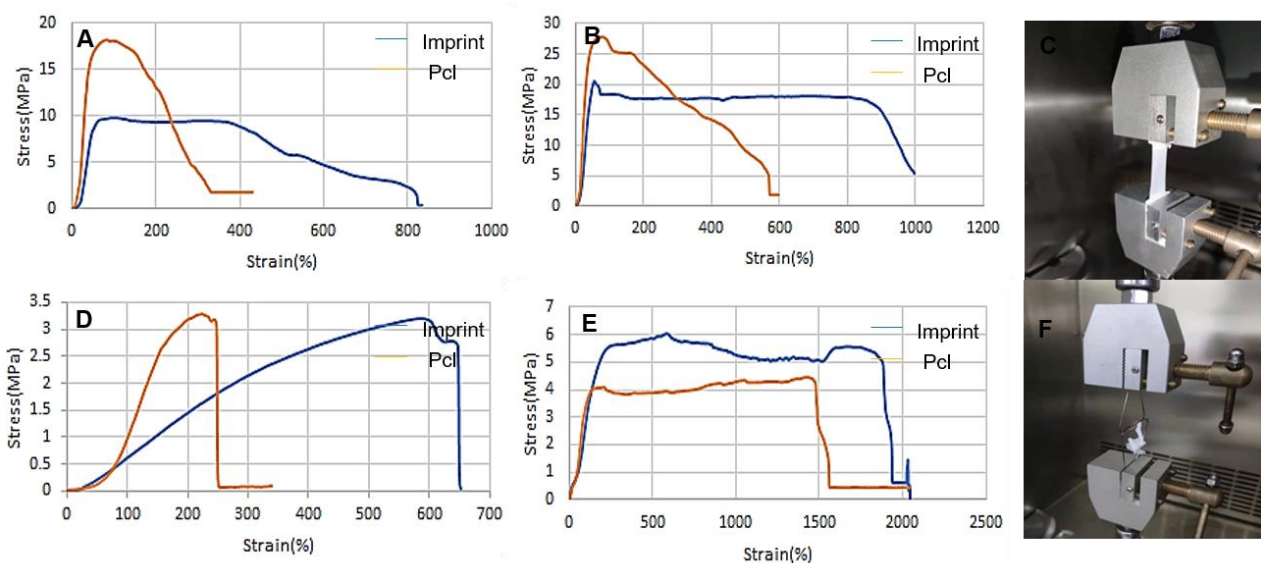


Figure 3. Tensile mechanics test: (A) is the drawing of the imprinted film and the pcl direct writing composite film in the vertical groove direction. The tensile strength of the composite stent is 18.154 MPa, and the tensile strength of the imprinted stent is 9.800 Mpa. (B) is the drawing of the imprinted film and the pcl direct-writing composite film stretching in the direction of the groove, the tensile strength of the composite stent is 27.784 MPa, and the tensile strength of the imprinted stent is 20.516 Mpa. (C) is the film tensile test graph. (D) is the drawing of the embossed tubular sample and the pcl direct-write composite tubular sample in the radial direction. The tensile strength of the composite stent is 3.279 MPa, and the tensile strength of the imprinted stent is 3.189 Mpa. (E) is the embossed tube. The sample and pcl direct-write composite tubular sample stretched along the axial direction, the tensile strength of the composite stent was 4.476 MPa, and the tensile strength of the imprinted group stent was 6.026 Mpa (F) for the tubular tensile experiment.

For the film samples, the results of Figure 3A,B show that the tensile strength of the pcl composite group is worse than that of the imprinting group, and the corresponding elongation is not as good as the imprinting group. In the direction perpendicular to the groove, the tensile strength of the pcl composite stent is 18.154 MPa, and the tensile strength of the imprinted stent is 9.800 Mpa; in the direction of the groove, the tensile strength of the pcl composite stent is 27.784 MPa, and the tensile strength of the imprinted stent is 20.516 Mpa. Therefore, it can be found that both sets of samples meet the mechanical performance requirements of natural blood vessels, however, whether it is the stretching of the straight writing (imprinting) structure or the stretching of the vertical writing (imprinting) structure, the corresponding elongation of the composite group will be larger.

For the tubular sample, the results of Figure 3C,D show that the pcl composite stent and the PPDO imprinted stent have similar mechanical properties, and the imprinting group also has a larger elongation. In the radial direction, the tensile strength of the pcl composite stent is 3.279 MPa, and the tensile strength of the imprinted stent is 3.189 Mpa;

in the axial direction, the tensile strength of the pcl composite stent is 4.476 MPa, and the tensile strength of the imprinted stent. The intensity is 6.026 Mpa. Since the mechanical performance parameters of the ideal blood vessel are 2–3 Mpa in the radial direction and 4–6 Mpa in the axial direction, it can be found that the samples of the composite group and the imprint group basically meet the requirements of the ideal blood vessel. Comparing the mechanical properties of the film stretch, a comprehensive comparison shows that the composite blood vessel has a slight increase in mechanical properties while maintaining the mechanical requirements of the natural blood vessel.

The suture force of the graft is used to evaluate the sutureability of the graft implanted in the body. As can be seen in Figure 4, the stitching performance of the pcl composite stent is better than that of the imprinting group. The results show that: the maximum load of the pcl composite group sample is 23.552 N, and a total of four strands of nylon thread are used for testing during the experiment, so the final suture force is 5.89 N; the maximum load of the imprint group sample is 19.420 N, and the final suture force is 4.855 N.

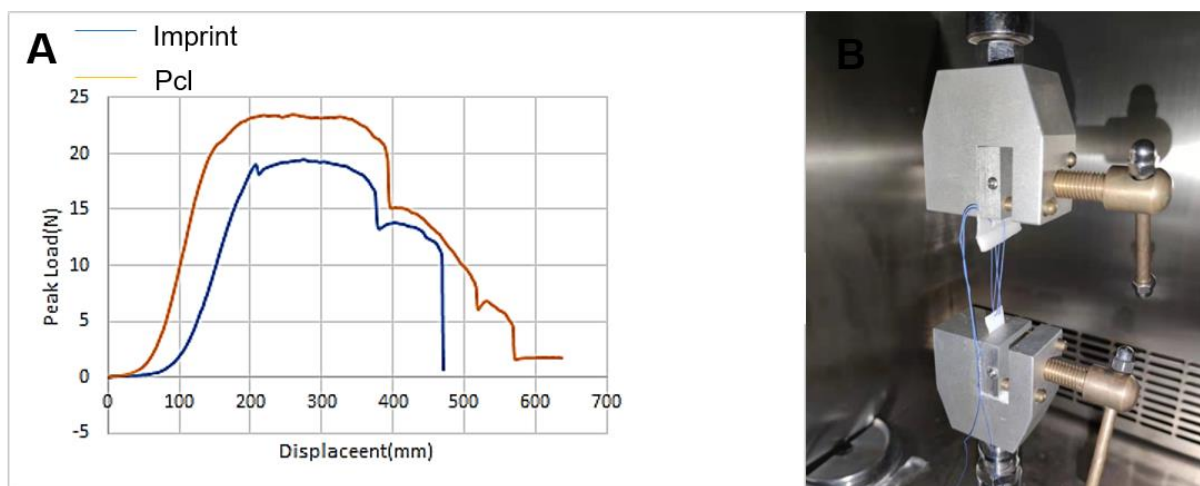


Figure 4. Suture retention experiment: (A) is the force_displacement curve of the embossed film and the pcl direct_write composite film suture retention experiment. (B) is the schematic diagram of the suture experiment.

Comprehensively looking at the stretch and stitching data, the composite group and the imprint group have similar mechanical performance test results. In fact, the basic film PPDO plays a major role. In terms of stitching, film-like stretch, and tubular stretch properties, it can be seen that composite stents have certain advantages.

3.3. Hydrophilic Results

The contact angle is defined as the intersection of the material, water, and air along the surface of the material and the surface of the water droplet. The angle formed by the line, if the contact angle is greater than 90° , the material is judged to be hydrophobic, the larger the angle, the higher the hydrophobicity; if the contact angle is less than 90° , the material is judged to be hydrophilic, and the smaller the angle is, the material is judged to be hydrophilic. Before the four groups of samples were inoculated with cells, the PPDO base film was plasma treated. It can be seen from Figure 5 that before plasma treatment, the contact angle of the sample was 83° , but after plasma treatment, the hydrophilicity of the sample changed to 62° . The results show that the plasma treatment experiment can effectively improve the hydrophilicity of the PPDO film. Therefore, for cell seeding, such results are positive.

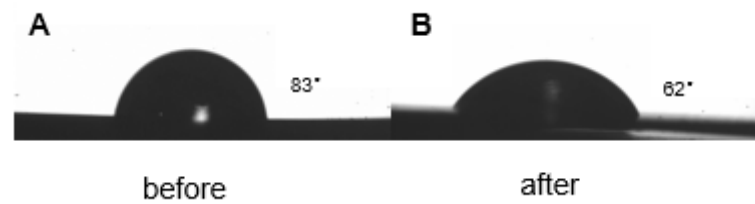


Figure 5. Hydrophilicity of PPDO film before and after plasma treatment: (A) before treatment (B) after treatment.

3.4. Cell Viability

In order to study the stratified vascular inner layer membrane designed to be suitable for cell growth and cling, and thus its potential use as a component of vascular grafts, we evaluated the inner membranes of four groups of samples *in vitro*, and evaluated the cells on their respective substrates for activity, proliferation, and morphology. These four groups of samples were plasma treated and immersed in dopamine solution. In the experimental results on the first day, the orientation of the cells was observed (Figure 6). Secondly, in the 14-day experiment, the metabolic activity and proliferation of endothelial cells was observed (Figure 7). The results in Figure 6 show that there is no obvious regularity in cell growth in the unstructured PPDO film group. From the results of the other three groups of experiments, they have a certain effect on cell growth (Figure 6B). The cells in the pcl direct writing composite group have clinging growth in the direction perpendicular to the direct writing structure. Figure 6C,D has a certain direction in the direction of cell growth, and this kind of orientation is the prerequisite for the regular arrangement of cells in various tissues; it also plays an important role in maintaining specific functions [26].

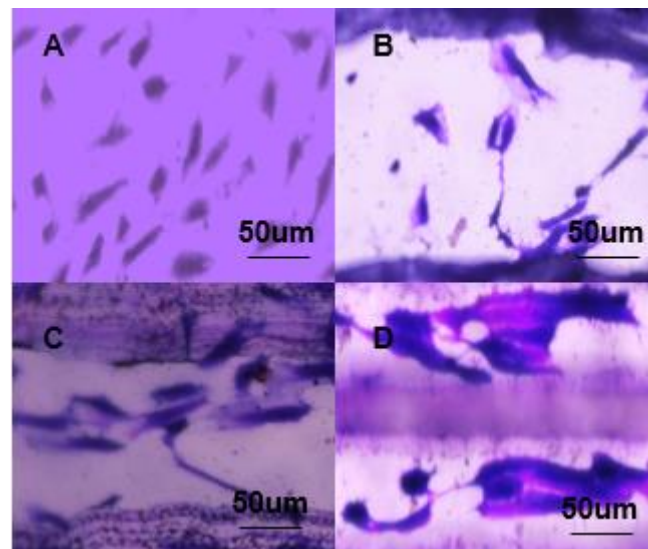


Figure 6. Cell growth on the first day: (A) unstructured PPDO film group, (B) pcl direct writing compound group, (C) pcl gelatin direct writing compound group, and (D) PPDO imprinted film group.

In addition, a macroscopic view of cell growth is shown in Figure 7. After the first day of inoculation, staining, and observation showed that the cells in the unstructured PPDO film group grew densely, while the other three groups also had cell attachment. On the third day, the number of cells in group A decreased, and the cells in group BCD were in a growing state. The results on the 7th day showed that the number of cells in the AD group continued to decline, while the number of cells in the BC group was larger. This difference may be due to the use of gelatin composite materials in group B, which is conducive to cell growth and clinging [27,28]; while group C has more groove structures than group A, which indicates that the introduced microstructure is conducive to cell

growth; comparing group D samples with group B, there is less gelatin material, and the number of cells is significantly reduced, which indicates that the gelatin composite material has better biocompatibility. The results on the 14th day showed that the growth of the three groups of ACD cells was not as ideal as that of group B, which also verified the inferences made above.

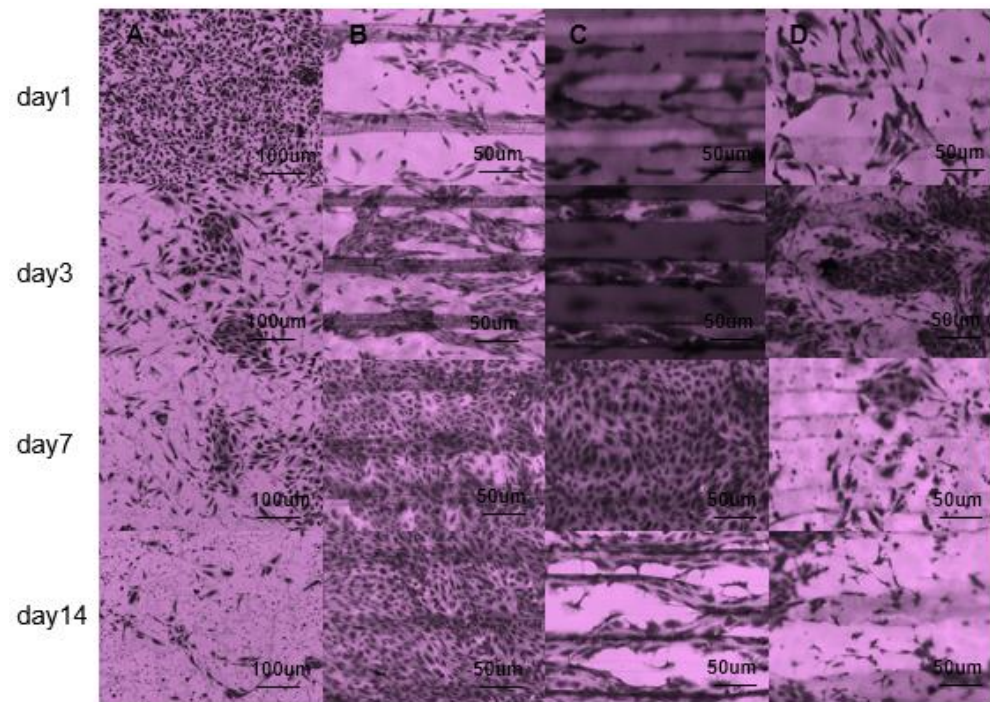


Figure 7. Growth of cells inoculated in two weeks: (A) unstructured PPDO film group, (B) pcl gelaTable, (C) pcl gelatin direct writing compound group, and (D) pcl direct writing compound group.

4. Discussion

The preparation of small-diameter vascular grafts remains a challenge. Simulating natural blood vessels should not only consider the requirements of small-diameter and tubular structures when constructing the microstructure surface, but also the flexibility requirements. On the other hand, the preparation of microstructures needs to take into account the thin-walled, layered, and other structures of natural blood vessels. These are essential for simulating natural blood vessels. To solve this problem, we designed a layered small-diameter vascular graft that mimics the structure of human blood vessels: an inner layer suitable for cell adhesion and an outer layer that provides mechanical properties. Here, the inner layer is made by micro-imprinting and electrostatic direct writing technology. The plasma and dopamine treatment of the PPDO base film and the groove structure of the inner wall provide the necessary growth conditions for cell attachment. The outer layer is obtained by electrospinning, which is a technology that can produce a shape and structure similar to the natural extracellular matrix (ECM), which provides mechanical properties for the overall vascular graft. The choice of pcl, gelatin, etc. as raw materials is based on their bioactive compatibility and electrospinning properties. In addition, these two materials have been tested to have good effects as vascular grafts.

In addition to the morphology of the basic structure, good mechanical properties are also necessary for small-diameter vascular grafts. The mechanical properties of an ideal blood vessel are 2–3 Mpa in the radial direction and 4–6 Mpa in the axial direction, and the tensile strength of the vascular graft prepared by us meets the requirements in this respect. Another important mechanical property to consider is suture retention. The experiments in this article show that the mechanical properties of the composite group and the imprint group are similar to each other. In fact, the basic film PPDO plays a major role. It can be

seen that composite stents have certain advantages in terms of stitching and film-like tensile properties. In terms of biocompatibility, in vitro cell culture experiments showed good cell compatibility. By recording the cell morphology under different experimental groups and different growth periods, it is shown that the samples with PPDO-based film combined with pcl-gelatin direct writing structure are more in line with the expected cell growth effect. In short, in terms of mechanical properties, the composite group has advantages in stretchability and suture performance, so a comprehensive comparison of composite blood vessels is a prerequisite for preparation. In the in vitro cell culture experiment, additional pcl gelatin direct writing composite group samples were added for control. The experimental results show that the pcl-gelatin group has better biocompatibility. In summary, the pcl gelatin direct writing composite group samples meet our expectations.

5. Conclusion and Future Work

In this paper, a small-diameter graft is prepared by a combination of electrostatic spinning, electrostatic direct writing and micro-imprinting, which is mainly divided into imprinting group and composite group. The macroscopic structure of blood vessels is similar to that of natural blood vessels, and the microscopic structure can also achieve the expected effects of cell experiments. In terms of mechanical properties, for tensile properties (including axial and radial), the samples of the composite group and the imprint group basically meet the requirements of ideal blood vessels, and the tensile performance of the composite group is slightly enhanced. In terms of suturing performance, the composite group also has a slight advantage, so a comprehensive comparison of composite blood vessels is a prerequisite for preparation. In the HUVEC in vitro cell culture experiment, additional pcl gelatin direct writing composite group samples were added for control. HUVEC in vitro cell culture experiments, apoptosis and staining showed the compatibility of the graft, indicating that the pcl-gelatin group has better biocompatibility. To sum up, the pcl gelatin direct writing composite group samples meet our expectations, but there are still content that can be supplemented. For example, a variety of different patterns can be prepared on the inner wall of blood vessels to observe cell growth. Or, possibilities include preparing the outer wall of the blood vessel to control its thickness, observing the optimal mechanical properties, etc., which will become part of the continued research work in the future.

Author Contributions: Conceptualization, J.H. and Y.L.; methodology, J.H.; software, Z.J.; validation, C.L., N.L. and J.H.; formal analysis, C.L.; investigation, T.Y.; resources, W.L.; data curation, J.H.; writing—original draft preparation, J.H.; writing—review and editing, J.H. and Y.L.; visualization, W.L.; supervision, T.Y.; project administration, Y.L. All authors have read and agreed to the published version of the manuscript.

Funding: This work was supported by the grants from the National Natural Science Foundation of China (No. 61973206,61703265, 61803250,61933008), Shanghai Science and Technology Committee Rising-Star Program No. 19QA1403700.

Conflicts of Interest: The authors declare no conflict of interest.

References

1. Gao, Q.; Liu, Z.; Lin, Z.; Qiu, J.; Liu, Y.; Liu, A.; Wang, Y.; Xiang, M.; Chen, B.; Fu, J.; et al. 3D Bioprinting of Vessel-like Structures with Multilevel Fluidic Channels. *ACS Biomater. Sci. Eng.* **2017**, *3*, 399–408. [CrossRef]
2. Lovett, M.; Eng, G.; Kluge, J. Tubular silk scaffolds for small diameter vascular grafts. *Organogenesis* **2010**, *6*, 217–224. [CrossRef] [PubMed]
3. Carrabba, M.; Madeddu, P. Current Strategies for the Manufacture of Small Size Tissue Engineering Vascular Grafts. *Front. Bioeng. Biotechnol.* **2018**, *6*, 41. [CrossRef]
4. Kumar, V.A.; Brewster, L.P.; Caves, J.M.; Chaikof, E.L. Tissue Engineering of Blood Vessels: Functional Requirements, Progress, and Future Challenges. *Cardiovasc. Eng. Technol.* **2011**, *2*, 137–148. [CrossRef]
5. Hann, S.Y.; Cui, H.; Esworthy, T.; Miao, S.; Zhou, X.; Lee, S.-J.; Fisher, J.P.; Zhang, L.G. Recent advances in 3D printing: Vascular network for tissue and organ regeneration. *Transl. Res.* **2019**, *211*, 46–63. [CrossRef] [PubMed]

6. Park, S.J.; Lee, J.; Choi, J.W.; Yang, J.H.; Lee, J.H.; Lee, J.; Son, Y.; Ha, C.W.; Lee, N.-K.; Kim, S.H.; et al. Additive manufacturing of the core template for the fabrication of an artificial blood vessel: The relationship between the extruded deposition diameter and the filament/nozzle transition ratio. *Mater. Sci. Eng. C* **2020**, *118*, 111406. [CrossRef]
7. Hasan, A.; Memic, A.; Annabi, N.; Hossain, M.; Paul, A.; Dokmeci, M.R.; Dehghani, F.; Khademhosseini, A. Electrospun scaffolds for tissue engineering of vascular grafts. *Acta Biomater.* **2013**, *10*, 11–25. [CrossRef]
8. Ratcliffe, A. Tissue engineering of vascular grafts. *Matrix Biol.* **2000**, *19*, 353–357. [CrossRef]
9. Grandi, C.; Martorina, F.; Lora, S.; Dalzoppo, D.; Amistà, P.; Sartore, L.; Di Liddo, R.; Conconi, M.T.; Parnigotto, P.P. ECM-based triple layered scaffolds for vascular tissue engineering. *Int. J. Mol. Med.* **2011**, *28*, 947–952. [CrossRef] [PubMed]
10. Jang, S.R.; Kim, J.I.; Park, C.H.; Kim, C.S. Development of Y-shaped small diameter artificial blood vessel with controlled topography via a modified electrospinning method. *Mater. Lett.* **2019**, *264*, 127113. [CrossRef]
11. Simitzi, C.; Ranella, A.; Stratakis, E. Controlling the morphology and outgrowth of nerve and neuroglial cells: The effect of surface topography. *Acta Biomater.* **2017**, *51*, 21–52. [CrossRef]
12. Greiner, A.M.; Sales, A.; Chen, H.; Biela, S.A.; Kaufmann, D.; Kemkemer, R. Nano- and microstructured materials for in vitro studies of the physiology of vascular cells. *Beilstein J. Nanotechnol.* **2016**, *7*, 1620–1641. [CrossRef] [PubMed]
13. Cai, S.; Smith, M.E.; Redenti, S.M.; Wnek, G.E.; Young, M.J. Mouse Retinal Progenitor Cell Dynamics on Electrospun Poly (ϵ -Caprolactone). *J. Biomater. Sci. Polym. Ed.* **2012**, *23*, 1451–1465. [CrossRef] [PubMed]
14. Siddiqui, N.; Asawa, S.; Birru, B. PCL-Based Composite Scaffold Matrices for Tissue Engineering Applications. *Mol. Biotechnol.* **2018**, *60*, 506–532. [CrossRef] [PubMed]
15. Purohit, S.D.; Bhaskar, R.; Singh, H.; Yadav, I.; Gupta, M.K.; Mishra, N.C. Development of a nanocomposite scaffold of gelatin–alginate–graphene oxide for bone tissue engineering. *Int. J. Biol. Macromol.* **2019**, *133*, 592–602. [CrossRef] [PubMed]
16. Sattary, M.; Khorasani, M.T.; Rafienia, M.; Rozve, H.S. Incorporation of nanohydroxyapatite and vitamin D3 into electrospun PCL/Gelatin scaffolds: The influence on the physical and chemical properties and cell behavior for bone tissue engineering. *Polym. Adv. Technol.* **2017**, *29*, 451–462. [CrossRef]
17. Naghieh, S.; Foroozmehr, E.; Badrossamay, M. Combinational processing of 3D printing and electrospinning of hierarchical poly(lactic acid)/gelatin–forsterite scaffolds as a biocomposite: Mechanical and biological assessment. *Mater. Des.* **2017**, *133*, 128–135. [CrossRef]
18. Liu, S.; Zhang, H.; Hu, Q.; Shen, Z.; Rana, D.; Ramalingam, M. Designing vascular supportive albumen-rich composite bioink for organ 3D printing. *J. Mech. Behav. Biomed. Mater.* **2020**, *104*, 103642. [CrossRef]
19. Wang, Y.; Yi, S.; Lu, R.; Sameen, D.E.; Ahmed, S.; Dai, J.; Qin, W.; Li, S.; Liu, Y. Preparation, characterization, and 3D printing verification of chitosan/halloysite nanotubes/tea polyphenol nanocomposite films. *Int. J. Biol. Macromol.* **2020**, *166*, 32–44. [CrossRef]
20. McClure, M.; Wolfe, P.; Rodriguez, I.; Bowlin, G. Bioengineered vascular grafts: Improving vascular tissue engineering through scaffold design. *J. Drug Deliv. Sci. Technol.* **2011**, *21*, 211–227. [CrossRef]
21. Barnes, C.P.; Sell, S.A.; Boland, E.D.; Simpson, D.G.; Bowlin, G.L. Nanofiber technology: Designing the next generation of tissue engineering scaffolds. *Adv. Drug Deliv. Rev.* **2007**, *59*, 1413–1433. [CrossRef] [PubMed]
22. He, W.; Nieponice, A.; Soletti, L. Pericyte-based human tissue engineered vascular grafts. *Biomaterials* **2010**, *31*, 8235–8244. [CrossRef] [PubMed]
23. Zhang, B.; Chung, S.H.; Barker, S. Direct ink writing of polycaprolactone/polyethylene oxide based 3D constructs. *Prog. Nat. Sci. Mater. Int.* **2020**, *31*, 180–191. [CrossRef]
24. Harrison, M.R.; Golbus, M.S.; Filly, R.A. Management of the Fetus with a Correctable Congenital Defect. *JAMA* **1981**, *246*, 774–777. [CrossRef]
25. Bahadur, K.R.; Bhattarai, S.R.; Aryal, S.; Khil, M.S.; Dharmaraj, N.; Kim, H.Y. Novel amphiphilic triblock copolymer based on PPDO, PCL, and PEG: Synthesis, characterization, and aqueous dispersion. *Colloids Surf. A Physicochem. Eng. Asp.* **2007**, *292*, 69–78. [CrossRef]
26. Lu, K.; Qian, Y.; Gong, J.; Zhu, Z.; Yin, J.; Ma, L.; Yu, M.; Wang, H. Biofabrication of aligned structures that guide cell orientation and applications in tissue engineering. *Bio-Des. Manuf.* **2021**, *4*, 258–277. [CrossRef]
27. Mhatre, A.; Bhagwat, A.; Bangde, P.; Jain, R.; Dandekar, P. Chitosan/gelatin/PVA membranes for mammalian cell culture. *Carbohydr. Polym. Technol. Appl.* **2021**, *2*, 100163. [CrossRef]
28. Tillman, B.W.; Yazdani, S.K.; Lee, S.J.; Geary, R.L.; Atala, A.; Yoo, J.J. The in vivo stability of electrospun polycaprolactone–collagen scaffolds in vascular reconstruction. *Biomaterials* **2009**, *30*, 583–588. [CrossRef] [PubMed]

Article

A Novel Microfluidic Device for Blood Plasma Filtration

Zaidon T. Al-aqbi ^{1,*}, Salim Albukhaty ^{2,*} , Ameerah M. Zarzoor ³, Ghassan M. Sulaiman ⁴ , Khalil A. A. Khalil ^{5,6}, Tareg Belali ⁵ and Mohamed T. A. Soliman ⁵ 

¹ College of Agriculture, University of Misan, Al-Amara, Misan 62001, Iraq

² Department of Chemistry, College of Science, University of Misan, Maysan 62001, Iraq

³ Middle Technical University, Technical Institute, Kut 52001, Iraq; ameerah.zaroor@mtu.edu.iq

⁴ Department of Applied Sciences, University of Technology, Baghdad 10066, Iraq; 100135@uotechnology.edu.iq

⁵ Department of Medical Laboratory Sciences, Faculty of Applied Medical Sciences, University of Bisha, 255, Al Nakhil, Bisha 67714, Saudi Arabia; kaahmad@ub.edu.sa (K.A.A.K.); Blaly@ub.edu.sa (T.B.); mohamedtalaat25@yahoo.com (M.T.A.S.)

⁶ Department of Medical Laboratory Sciences, Faculty of Medicine and Health Sciences, University of Hodeidah, Hodeidah 3114, Yemen

* Correspondence: zaidon.alaqbi@uomisan.edu.iq (Z.T.A.-a.); albukhaty.salim@uomisan.edu.iq (S.A.); Tel.: +964-(0)-771-879-3753 (S.A.)

Abstract: The use of whole blood and some biological specimens, such as urine, saliva, and seminal fluid are limited in clinical laboratory analysis due to the interference of proteins with other small molecules in the matrix and blood cells with optical detection methods. Previously, we developed a microfluidic device featuring an electrokinetic size and mobility trap (SMT) for on-chip extract, concentrate, and separate small molecules from a biological sample like whole blood. The device was used to on-chip filtrate the whole blood from the blood cells and plasma proteins and then on-chip extract and separate the aminoglycoside antibiotic drugs within 3 min. Herein, a novel microfluidic device featuring a nano-junction similar to those reported in the previous work formed by dielectric breakdown was developed for on-chip filtration and out-chip collection of blood plasma with a high extraction yield of 62% within less than 5 min. The filtered plasma was analyzed using our previous device to show the ability of this new device to remove blood cells and plasma proteins. The filtration device shows a high yield of plasma allowing it to detect a low concentration of analytes from the whole blood.

Keywords: microfluidics; blood plasma filtration; chip extract; blood molecules



Citation: Al-aqbi, Z.T.; Albukhaty, S.; Zarzoor, A.M.; Sulaiman, G.M.; Khalil, K.A.A.; Belali, T.; Soliman, M.T.A. A Novel Microfluidic Device for Blood Plasma Filtration. *Micromachines* **2021**, *12*, 336. <https://doi.org/10.3390/mi12030336>

Academic Editors: Rui A. Lima and Nam-Trung Nguyen

Received: 22 February 2021

Accepted: 19 March 2021

Published: 22 March 2021

Publisher's Note: MDPI stays neutral with regard to jurisdictional claims in published maps and institutional affiliations.



Copyright: © 2021 by the authors. Licensee MDPI, Basel, Switzerland. This article is an open access article distributed under the terms and conditions of the Creative Commons Attribution (CC BY) license (<https://creativecommons.org/licenses/by/4.0/>).

1. Introduction

Human blood plasma is one of the most convenient and the most important circulating biomarkers sources. Since this free-blood cells matrix has numerous clinically relevant analytes like metabolites, nucleic acids, and proteins, it has become a standard sample for the exclusion or diagnosis of several diseases [1,2]. Moreover, blood plasma is utilized in drug development trials, e.g., for drug monitoring and their metabolites, since it has the drug fraction most relevant to study the pharmacodynamic and pharmacokinetic influences of the drug [3,4]. Plasma transcriptome, proteome, and metabolome studies have increased the spectrum of the diagnostic target for different types of diseases from sepsis to cancer to Alzheimer's [5–7]. Further, foreign nucleic acids as well as antigens and antibodies present in plasma, allow the diagnosis of serious infectious diseases. Additionally, when carrying out plasma analysis in laboratories, blood plasma is useful in the analysis of glucose, total cholesterol, electrolyte concentration, lactate, etc. In clinical chemistry, blood plasma isolation is a necessary step performed, and for the development of miniaturized clinical diagnostic devices, beneficial sample preparation techniques are required [8]. Filtration of plasma from whole blood is very desirable in most cases. Venous blood samples centrifugation is the usual technique to prepare blood plasma with volumes that can be analyzed

using highly sensitive methods like LC-MS/MS (liquid chromatography–tandem mass spectrometry). The expansion of blood plasma separation (BPS) based on microfluidics, dealing only with small sample volumes, has rapidly grown in the field of clinical laboratory medicine [9]. This not only increases patient compliance, convenience, and comfort by reducing the amount of blood required to be pulled allowing point of care (POC) sample collection but also permits the analysis to be performed properly at a part of the duration and cost. Moreover, the potential of on-time repetitive sampling, automated parallelization, and portability are other benefits of performing different procedures at the microscale. Microsampling is a procedure for capturing small volumes of biological samples like whole blood from the human body to be analyzed in a minimally invasive method [10]. To deliver sample volumes sufficient to faithfully detect low concentration analytes from limited sample volumes is still the main challenge with microsampling, so a plasma sampling method must be in a high yield to arrive at reasonable levels in the detection of target analytes at low-concentrations and must give pure plasma without blood cells hemolysis or leakage to be clinically pertinent. Furthermore, extraction time is important to reduce the effect of coagulation, particularly when working with fresh samples, e.g., standard finger pricks. To achieve all these requirements, microfluidics is a favorable technology for manufacturing microminiaturized devices that studies fluids' behavior through micro-channels. There are two types of plasma separation techniques using microfluidics, passive and active. Passive separation techniques demand no external tools, making the devices smaller in size, easier to use, cheaper, and therefore suitable for POC uses [11] while active separation requires exertion of an exterior energy source, e.g., inertial, electric, or acoustic forces [12]. Passive separation techniques can be stored under pressure or driven by capillary forces [13–15]. Using capillary forces in plasma separation is more desirable, since it demands neither vacuum packaging, nor degassing of a suction material [16]. The mechanism of separation is generally based on sedimentation, size exception, or a combination of them [17]. Performing plasma separation using sedimentation gives a pure plasma at the time expense. Plasma separation during size-exclusion avoids the time limitation and permits a quick separation. It could be based on porous media like a filter membrane linked to a capillary channel or a membrane stack [18]. Other microfluidic devices for plasma separation have been demonstrated based on diffusion filter/microfilter [19], bends in micro-channels [20], acoustic waves [21], crossflow filtration [22], and dielectrophoresis [23,24]. Major research projects in recent decades have focused on microfluidics, drug, and gene nano delivery systems, tissue engineering, and biosensors due to cost-effectiveness and high performance [25–29]. Recently, we developed a microfluidic device featuring two nano-junctions with different sizes to form a size and mobility trap (SMT) for on-chip filtrate the whole blood from blood cells and plasma proteins, then on-chip extract, concentrate, and separate small molecules from whole blood [30]. The capability of the device was demonstrated for on-site therapeutic drug monitoring (TDM) of aminoglycoside antibiotic drugs within 3 min. However, this device was fabricated for on-chip filtration and analysis of small molecules from whole blood where the ability to collect the filtered blood for use in other applications is not possible through this device. Here, a novel microfluidic device with a nano-junction created by dielectric breakdown is developed for on-chip filtration and out-chip collection of whole blood to be used in other applications as a pure plasma.

2. Materials and Methods

2.1. Chemicals and Sample Preparation

Fluorescein from Sigma-Aldrich (Sydney, Australia) was prepared in Milli-Q water to get 200 µg/mL solution. Fluorescamine from Sigma-Aldrich was prepared in acetone to obtain 3 mg/mL as a stock solution. Bovine Serum Albumin (BSA) from Sigma-Aldrich was prepared in Milli-Q water 2 mg/mL stock solution and then labeled with Fluorescamine in a ratio 3:1 in borate buffer at pH = 9. Polydimethylsiloxane (PDMS) curing agent and elastomer were purchased from Dow Corning (Michigan, MI, USA). Sodium phosphate monobasic, disodium hydrogen phosphate, and sodium tetraborate were purchased from

Sigma-Aldrich (Sydney, Australia) and used for buffer preparation. All solutions were prepared by using Milli-Q water (18 M Ω , Millipore, North Ryde, Australia) purification system. The fresh finger-prick blood used in the experiments was obtained from healthy volunteers approved by the Tasmanian Health and Medical Human Research Ethics Committee, Office of Research Services, the University of Tasmania (Ethics Approval Ref is H0016575).

2.2. Device Fabrication

Figure 1A presents an AutoCAD design of the device which was then 3D printed using an Eden 3D printer (Figure 1B) to produce a negative template of the device using the previously described process [31]. Then, PDMS was utilized to give the positive master embossing stamp by mixing 210 g in a mass ratio of 5:1 polymer to the elastomer. The PDMS mixture degassed for 15 min and left out for 30 min at room temperature and then poured onto the negative 3D printed template, and then allowed for curing in an oven at 70 °C for at least 12 h. The PDMS positive stamp was cut off and then taken away from the 3D printed template and allowed for thermal age in an oven for 30 min at 250 °C. Then, it used to hot emboss the poly (methyl methacrylate) (PMMA) channel plates (1.5 mm \times 50 mm \times 75 mm). The final PMMA chips were produced using a hot embossing procedure as reported in our previous work [30]. Briefly, PDMS positive stamp and the blank PMMA plate were placed between two 50 mm \times 50 mm \times 6 mm glass plates and place into the hot embosser (MTP-8, Tetrahedron, San Diego, CA, USA). Three steps were used in the embossing process. Step 1 was done by increasing the temperature from a rate of (92 °C/min) until the temperature reached (130 °C) and involved maintaining the pressure at 100 lbs. the next step was performed by enhancing the pressure up to 380 lbs at a rate of 75 lbs/min and maintaining the temperature at (130 °C). When the pressure goes up to 380 lbs, those conditions were held for 20 min. In the final step, the temperature was reduced at a rate of 15 °C /min until the temperature reached (60 °C) and involved maintaining the pressure at 380 lbs. The hot-embossed PMMA microchip device was subsequently bonded with single-sided adhesive tape (Tesa SE, Charlotte, NC, USA). An office laminator (Peach 3500, Peach, Switzerland) was then used and the PMMA channel plate and the adhesive tape were sandwiched between two 1 mm stainless steel plates at 20 °C temperature and 5 speed at 4 orientation, with 90-degree clockwise rotation at each pass.

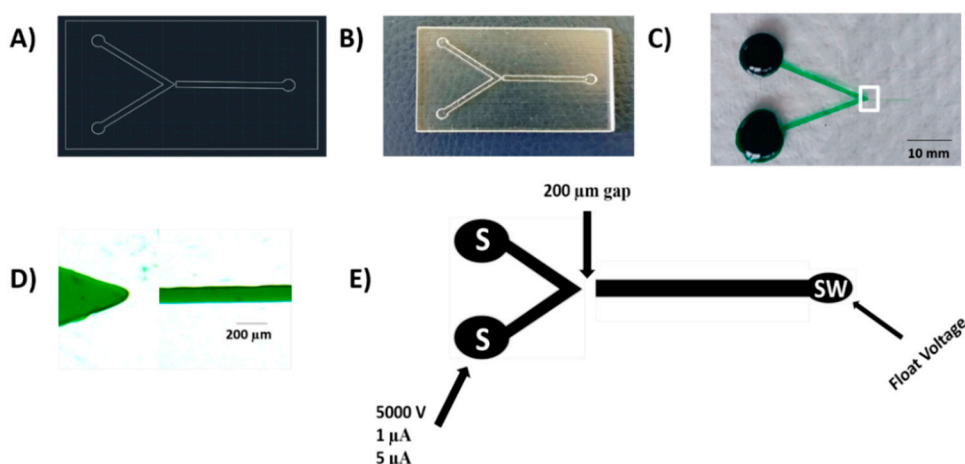


Figure 1. (A) An AutoCAD design of the filtration device (B) photograph image of the negative 3D printed portable device using an Eden 3D printer (C) Photograph image of the hot embossed filtration poly (methyl methacrylate) (PMMA)/adhesive tape device filled with green food dye. Scale bar = 10 mm. (D) Zoomed-in image of the V channel and the filtration channel (white box in panel C) filled with green food dye. Scale Bar = 200 μ m. (E) Schematic of the microfluidic device (dimension not to scale) indicating terminating current and voltages used for generation of the nano-junction Sample (S), and Sample Waste (SW).

2.3. Creation of a Nano-Junction

The complete microchip device is a hybrid hot-embossed PMMA/adhesive tape with a photo of the device shown in Figure 1C and a zoomed-in image of the V-channel and the filtration channel in Figure 1D. The V-channel was 500 μm wide and the filtration channel was 50 μm . The V-channel tip was separated from the filtration channel by a 200 μm gap of PMMA to form the filtration nano-junction. This gap was chosen to allow for lengthy use of higher voltages through the filtration without the secondary breakdown's danger. To form the nanochannel, the V-channel and filtration channel were filled with the breakdown electrolyte, be composed of 10 mM phosphate buffer, pH 11. The filtration nano-junction was created by applying a high voltage of 5000 V to the V-channel whilst the filtration channel was kept grounded Figure 1E. Previously, the high voltage breakdown was 4000 V instead of 5000 V in this work, lower than what was performed in this work. This different voltage in the filtration PMMA devices could be regarding the difference in the gap distance between the separation channel in the double V device and the filtration channel here. The current limit was varied from 1 μA to 5 μA by utilizing an in-house adjustable power supply, controlling by LabView HV V.6 program (National Instrument, Austin, TX, USA) to realize the best repeatability. The V-channel and the filtration channel were cleaned and refilled with the experimental solutions.

2.4. Device Operation and Experimental Practice

Figure 2A,B show the operation of the filtration device, where the blood volume from a fresh finger prick was controlled by pipetting 50 μL of whole blood to the devices to ensure result comparability and evaluate the filtration method. Pipetting was carried out using an autopipette, and the experiments were performed at room temperature to reduce blood evaporation through the filtration process. A simple technique was used in this approach by pushing the whole blood using the autopipette from the V-channel to the filtration channel through the nanochannel and then a hand syringe-vacuum was used to collect the filtered plasma blood in a high yield. All experiments were performed with a Nikon Eclipse Ti-U inverted fluorescence microscope (Nikon Instruments Inc.) worked with NIS-Elements BR 3.10 software (Melville). A filter cube (Semrock, Rochester) composed of an excitation band-pass filter ($488 \pm 10 \text{ nm}$), emission filter ($520 \pm 10 \text{ nm}$), and dichroic mirror to deflect the broadband light source to a 20 \times objective was used to perform all the experiments. Fluorescence images were carried out using a high-definition color charge-coupled device camera (Digital Sight DS. Filc, Nikon, Japan). A photon multiplier tube (PMT) (Hamamatsu Photonics KK, Hamamatsu, Japan) linked to the microscope was used to record the electropherograms. The PMT was linked to an Agilent 35900E A/D box to allow data collection with the Chemstation software (Agilent Technologies, Waldbronn, Germany). An electrical potential was applied by using an in-house 4-channel (0–5 kV) dc power supply to each reservoir using a custom-designed interface connected to 2 platinum electrodes.

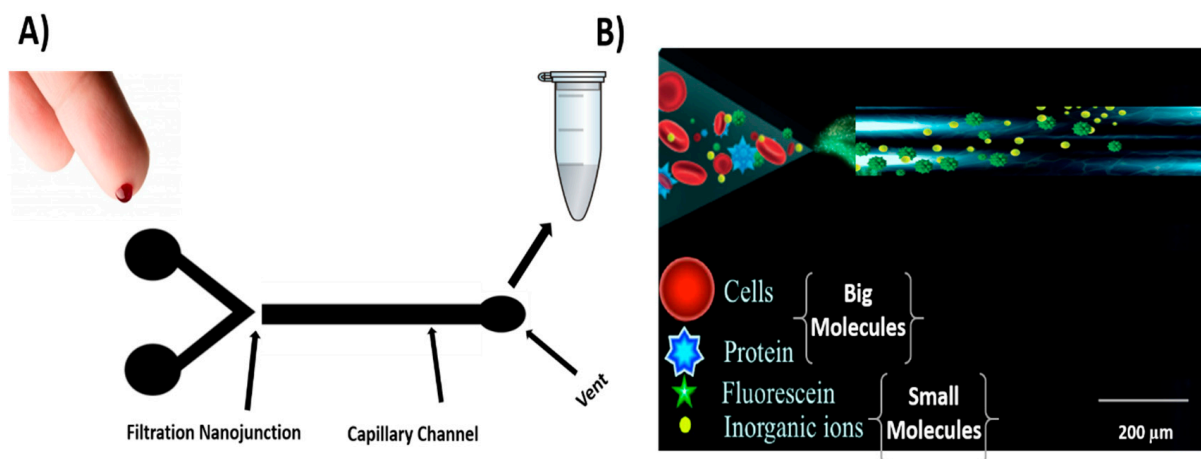


Figure 2. (A) Schematic of the operation of the microfluidic device (dimension not to scale) indicating the filtration process and (B) illustration of the filtration device concept. Nanochannel was formed by controlled dielectric breakdown of the tip of the V-channel and the filtration channel. Large molecules are blocked (Cells and Proteins) while small molecules pass the filtration channel.

3. Results and Discussion

3.1. Filtration and Permeability Studies

Previously, we examined the relevance between the current limit and nano-junction permeability in the double V hot-embossed PMMA device through different breakdown experiments using different charge and size analytes. Briefly, using a current limit of $5 \mu\text{A}$, the resulted nanochannels restricted blood cells ($6\text{--}8 \mu\text{m}$) [32], and R-phycoerythrin (RPE) ($<10 \text{ nm}$ in size) [33] from passing the separation channel while bovine serum albumin (BSA) ($2\text{--}4 \text{ nm}$) [34] labeled-fluorescamine allowed to pass the separation channel. Reducing the current limit to $1 \mu\text{A}$, blocked the BSA, but allowed the transport of anionic small molecules, such as fluorescein (1 nm) [34] and drugs. The SMT in our previous work is based on ions' favorable electrokinetic transport through the resulting nanochannels. The extraction nanochannel was created by applying for a $1 \mu\text{A}$ permit the transport small ions ($<1000 \text{ Da}$) during the nano-junction, whilst blocking the transport of plasma proteins and blood cells. The concentration nanochannel between the V-sample channel and the separation channel was created by applying a $0.1 \mu\text{A}$ current limit to avoid target analytes transport but allows the transfer of small inorganic ions to make a sample desalting. Both the extraction and concentration nanochannels make the SMT in target analytes which can purify, concentrate, desalt, and separate the sample. Here, we build on our previous breakdown work and implement our new design. The results were similar to those reported in our previous work and summarized in Figure 3. We have formed two types of nano-junctions for the filtration process. First, since the current limit was set at $5 \mu\text{A}$ (Figure 3A), the produced nanochannels blocked blood cells from infiltrating the filtration channel, while allowing the transport of proteins like BSA into the filtration channel. For protein recovery assessment, the termination current was reduced to $1 \mu\text{A}$ (Figure 3B) which blocked the BSA but permitted the electrophoretic transport of small molecules ($<1000 \text{ Da}$) such as fluorescein and drugs. Based on the transport results of different sized molecules (fluorescein 1 nm , BSA $2\text{--}4 \text{ nm}$, and Blood cell $4\text{--}6 \mu\text{m}$), the size of fabricated nanochannels can be estimated with this method.

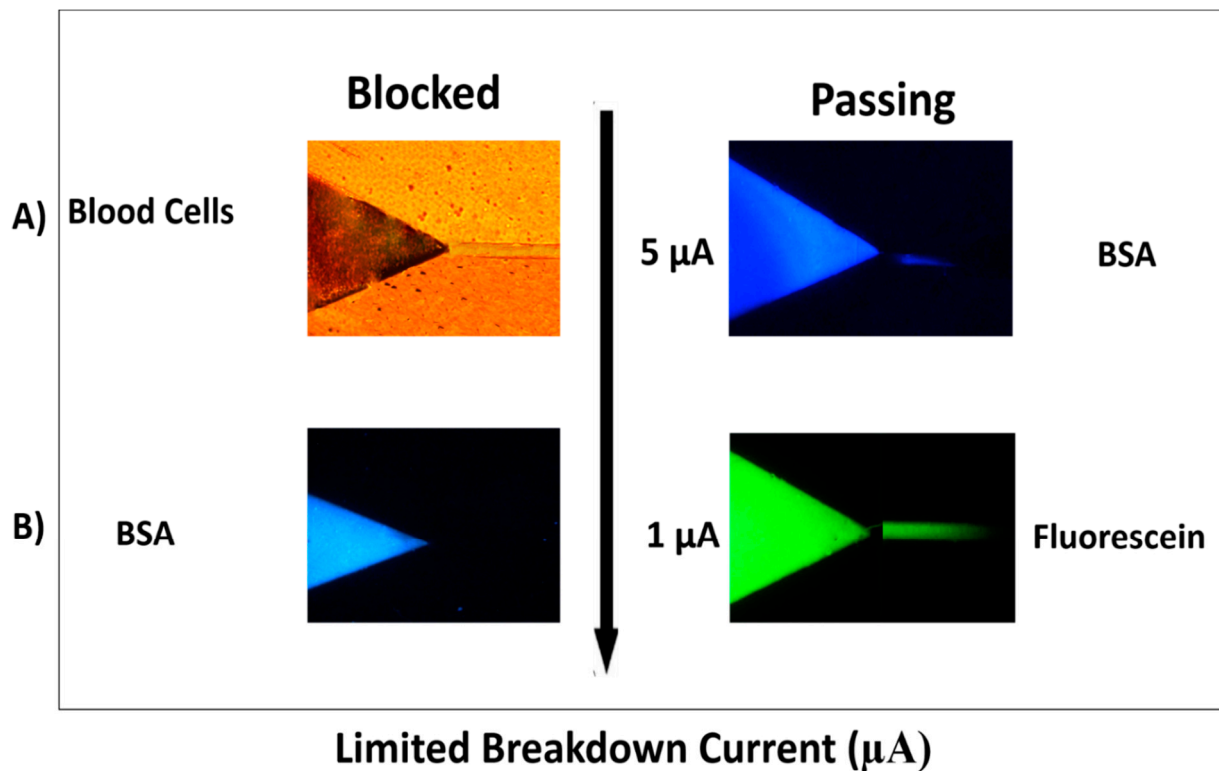


Figure 3. Screenshots presenting the restriction (left column) and passing (right column) of different molecules through nano-junctions formed under different conditions. (A) shows the use of $5 \mu\text{A}$ to create nanochannels which transported Bovine Serum Albumin (BSA) (blue, right) and restricted Blood Cells (left); (B) shows the use of $5 \mu\text{A}$ to create nanochannels which restricted BSA (blue, left) and transported fluorescein (green, right). The nanochannels formed using a breakdown electrolyte of 10 mM phosphate buffer, pH = 11, and terminating currents of 5 and $1 \mu\text{A}$. Images on the left show blocked transport, while those on the right show the permeability of different molecules. Scale Bar = $200 \mu\text{m}$.

3.2. Analysis of Filtered Blood Plasma

The color of the plasma was properly similar to centrifuged plasma treated with EDTA, seemed clear without a pink trace in all filtered blood plasma samples which mentioned that the separation of plasma caused no or a little lysis of erythrocytes as clearly seen in Figure 3A. The purpose of the PMMA hot-embossed filtration device is to purify the whole blood from cells and plasma proteins and allow to pass small molecules like pharmaceuticals with filtered plasma. To evaluate the protein recovery assessment, centrifuged plasma relative to filtered plasma spiked with 5 ppm gentamicin and BSA was assessed for both venous blood samples treated with EDTA and filtered finger-prick blood. Two types of filtered plasma using our filtration device were used after applying $5 \mu\text{A}$ and $1 \mu\text{A}$ termination currents to create different sized nano-junctions comparing to an EDTA-treated centrifuged plasma. These all were analyzed using our previous SMT device after labeling the plasma with fluorescamine reagent and followed by their separation using electrophoresis. Electrophoresis is a separation approach in which particles, molecules, and ions are separated in a conducting liquid medium using an electric field. All primary amines found in the plasma including those on proteins, amino acids, urea, etc., will be reacted with fluorescamine to produce a fluorescent complex within seconds. Figure 4 shows the electrophoretic separation of filtered blood plasma labeled with fluorescamine after using two different nano-junctions. Filtering whole blood using a device with a termination current of $5 \mu\text{A}$ and analyzed with the double V-device gives a pure peak for gentamicin, but plasma proteins and BSA are observed. This indicates plasma proteins can pass through the nano-junctions, while blood cells cannot. In contrast, using a termination current of $1 \mu\text{A}$ gives pure separations due to the observing of small molecules without interfacing and also the removal of some larger proteins, allowing full quantitation of

some small molecules in the blood, with a relative standard deviation (RSD%) = 7.5% for gentamicin ($n = 3$ devices) and with a high recovery efficiency for Gentamicin 94%, and a linear calibration curve of gentamycin from blood is shown in Figure 5. In comparison to other microfluidic devices, the presented device display that the microchip enables the low-cost, rapid, and operationally straightforward separation of plasma from whole blood; also, it demands a small amount of blood to give results within less than 5 min. Therefore, the device provides a favorable solution for biochemical assays.

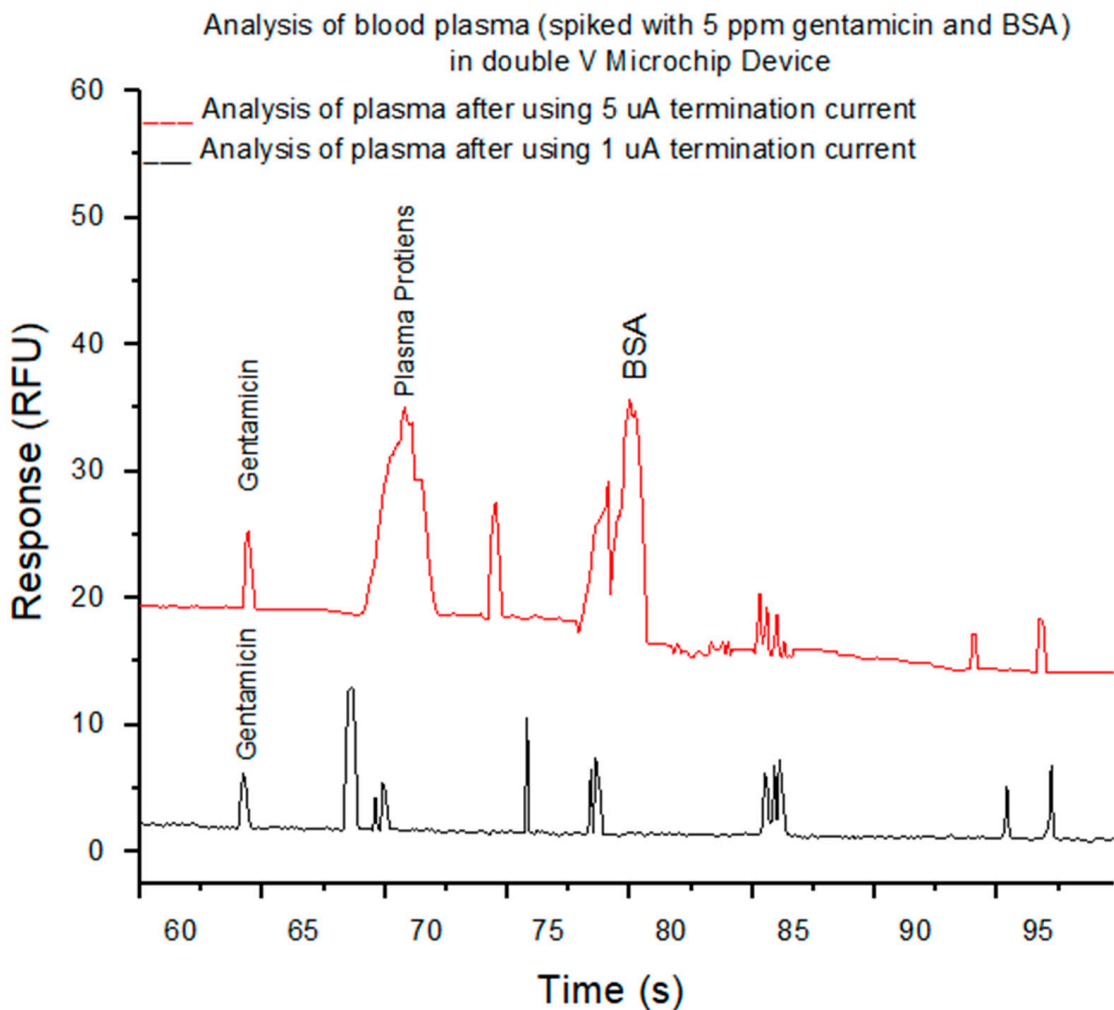


Figure 4. Electropherograms show the analysis of filtered blood spiked with 5 ppm gentamicin and BSA after labeling with fluorescamine in size and mobility trap (SMT) device after using a current limit of 5 uA (red trace) and 1uA current limit (black trace). The background electrolyte (BGE) in the separation channel, was 100 mM phosphate buffer, pH 11.5, with 0.5% HPMC, while V-sample waste channel was 10 mM phosphate buffer, pH 11.5. Applied voltages used in SMT device for extraction and concentration were -200 , -850 , -600 , and $+650$ V for 60s, and separation process were -250 , $+250$, $+2200$, and -500 V at reservoirs B, S, BW, and SW, respectively.

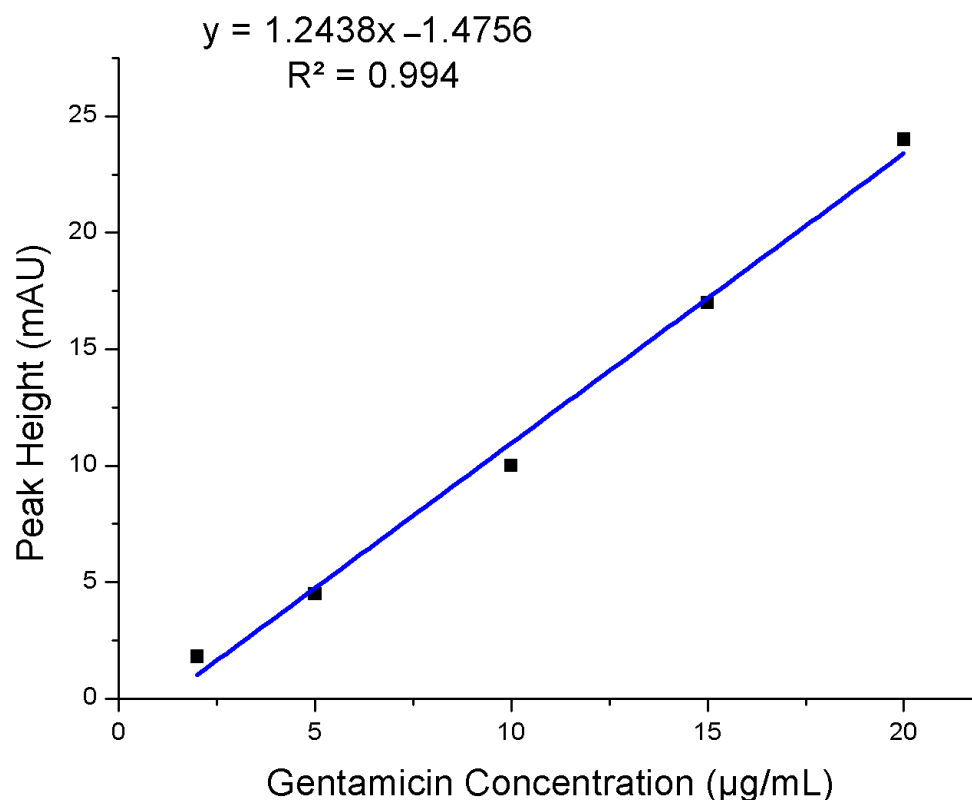


Figure 5. The linear calibration curve for Gentamicin from whole blood.

4. Conclusions

In this work, we have introduced a new device for blood plasma separation using a piece of PMMA microfluidic device. The PMMA filtration device dominant dielectric breakdown enabling the pore size tuning of nano-junctions and thus their permeability for different sized molecules. The creation of nanochannels using dielectric breakdown is fast, simple, and does not depend on valves or pumps. This manner enabled the analysis of the filtered blood which was labeled with fluorescamine. The device is portable and can be offered for the implementation of blood plasma instead of centrifugation process and in POC devices as the device could be engineered into a hand-held portable device and integrated with a hand-held reader for on-site testing and can tackle issues regarding sample storage, stability, and shipping and could be a fully separate plasma sampling device for POC.

Author Contributions: Conceptualization and methodology, Z.T.A.-a. and S.A.; formal analysis, A.M.Z., S.A. and G.M.S.; investigation and data curation, Z.T.A.-a., S.A. and G.M.S.; validation G.M.S., A.M.Z. and K.A.A.K.; visualization, T.B. and M.T.A.S.; writing—original draft preparation, G.M.S. and K.A.A.K.; writing—review and editing, K.A.A.K., T.B. and M.T.A.S.; supervision, Z.T.A.-a. and G.M.S.; project administration, S.A. All authors have read and agreed to the published version of the manuscript.

Funding: This research received no external funding.

Acknowledgments: The authors extend their appreciation to the University of Misan, and University of Technology, Baghdad for their technical support.

Conflicts of Interest: The authors declare no conflict of interest.


References

- Kersaudy-Kerhoas, M.; Sollier, E. Micro-scale blood plasma separation: From acoustophoresis to egg-beaters. *Lab Chip* **2013**, *13*, 3323–3346. [CrossRef]
- Mielczarek, W.S.; Obaje, E.; Bachmann, T.; Kersaudy-Kerhoas, M. Microfluidic blood plasma separation for medical diagnostics: Is it worth it? *Lab Chip* **2016**, *16*, 3441–3448. [CrossRef] [PubMed]
- Sturm, R.; Henion, J.; Abbott, R.; Wang, P. Novel membrane devices and their potential utility in blood sample collection prior to analysis of dried plasma spots. *Bioanalysis* **2015**, *7*, 1987–2002. [CrossRef]
- Emmons, G.; Rowland, M. Pharmacokinetic considerations as to when to use dried blood spot sampling. *Bioanalysis* **2010**, *2*, 1791–1796. [CrossRef]
- Neugebauer, S.; Giamarellos-Bourboulis, E.J.; Pelekanou, A.; Marioli, A.; Baziaka, F.; Tsangaris, I.; Bauer, M.; Kiehntopf, M. Metabolite profiles in sepsis: Developing prognostic tools based on the type of infection. *Crit. Care Med.* **2016**, *44*, 1649–1662. [CrossRef] [PubMed]
- Cheng, G. Circulating miRNAs: Roles in cancer diagnosis, prognosis and therapy. *Adv. Drug Deliv. Rev.* **2015**, *81*, 75–93. [CrossRef]
- Olsson, B.; Lautner, R.; Andreasson, U.; Öhrfelt, A.; Portelius, E.; Bjerke, M.; Hölttä, M.; Rosén, C.; Olsson, C.; Strobel, G. CSF and blood biomarkers for the diagnosis of Alzheimer’s disease: A systematic review and meta-analysis. *Lancet Neurol.* **2016**, *15*, 673–684. [CrossRef]
- Crowley, T.A.; Pizziconi, V. Isolation of plasma from whole blood using planar microfilters for lab-on-a-chip applications. *Lab Chip* **2005**, *5*, 922–929. [CrossRef]
- Kim, J.-H.; Woenker, T.; Adamec, J.; Regnier, F.E. Simple, miniaturized blood plasma extraction method. *Anal. Chem.* **2013**, *85*, 11501–11508. [CrossRef] [PubMed]
- Lei, B.U.; Prow, T.W. A review of microsampling techniques and their social impact. *Biomed. Microdevices* **2019**, *21*, 81. [CrossRef] [PubMed]
- Sollier, E.; Cubizolles, M.; Faivre, M.; Fouillet, Y.; Achard, J.L. A passive microfluidic device for plasma extraction from whole human blood. *Annu. Int. Conf. IEEE Eng. Med. Biol. Soc.* **2009**, *2009*, 7030–7033. [CrossRef] [PubMed]
- Berlanda, S.F.; Breitfeld, M.; Dietsche, C.L.; Dittrich, P.S. Recent Advances in Microfluidic Technology for Bioanalysis and Diagnostics. *Anal. Chem.* **2021**, *93*, 311–331. [CrossRef]
- Thorslund, S.; Klett, O.; Nikolajeff, F.; Markides, K.; Bergquist, J. A hybrid poly (dimethylsiloxane) microsystem for on-chip whole blood filtration optimized for steroid screening. *Biomed. Microdevices* **2006**, *8*, 73–79. [CrossRef] [PubMed]
- Kim, Y.C.; Kim, S.-H.; Kim, D.; Park, S.-J.; Park, J.-K. Plasma extraction in a capillary-driven microfluidic device using surfactant-added poly (dimethylsiloxane). *Sens. Actuators B Chem.* **2010**, *145*, 861–868. [CrossRef]
- Homsy, A.; van der Wal, P.D.; Doll, W.; Schaller, R.; Korsatko, S.; Ratzer, M.; Ellmerer, M.; Pieber, T.R.; Nicol, A.; De Rooij, N.F. Development and validation of a low cost blood filtration element separating plasma from undiluted whole blood. *Biomicrofluidics* **2012**, *6*, 012804. [CrossRef]
- Zhang, H.; Li, G.; Liao, L.; Mao, H.; Jin, Q.; Zhao, J. Direct detection of cancer biomarkers in blood using a “place n play” modular polydimethylsiloxane pump. *Biomicrofluidics* **2013**, *7*, 034105. [CrossRef] [PubMed]
- Albukhaty, S.; Al-Musawi, S.; Abdul Mahdi, S.; Sulaiman, G.M.; Alwahibi, M.S.; Dewir, Y.H.; Soliman, D.A.; Rizwana, H. Investigation of Dextran-Coated Superparamagnetic Nanoparticles for Targeted Vinblastine Controlled Release, Delivery, Apoptosis Induction, and Gene Expression in Pancreatic Cancer Cells. *Molecules* **2020**, *25*, 4721. [CrossRef]
- Li, X.; Chen, W.; Liu, G.; Lu, W.; Fu, J. Continuous-flow microfluidic blood cell sorting for unprocessed whole blood using surface-micromachined microfiltration membranes. *Lab Chip* **2014**, *14*, 2565–2575. [CrossRef] [PubMed]
- Beebe, D.J.; Mensing, G.A.; Walker, G.M. Physics and applications of microfluidics in biology. *Annu. Rev. Biomed. Eng.* **2002**, *4*, 261–286. [CrossRef]
- Blatter, C.; Jurischka, R.; Schoth, A.; Kerth, P.; Menz, W. Separation of Blood Cells and Plasma in Microchannel Bend Structures. In Proceedings of the International Society for Optical Engineering 5591, Lab-on-a-Chip: Platforms, Devices, and Applications, Philadelphia, PA, USA, 8 December 2004; pp. 143–151.
- Nilsson, A.; Petersson, F.; Jönsson, H.; Laurell, T. Acoustic control of suspended particles in micro fluidic chips. *Lab Chip* **2004**, *4*, 131–135. [CrossRef] [PubMed]
- Chen, X.; Liu, C.C.; Li, H. Microfluidic chip for blood cell separation and collection based on crossflow filtration. *Sens. Actuators B Chem.* **2008**, *130*, 216–221. [CrossRef]
- Gascoyne, P.R.; Vykoukal, J. Particle separation by dielectrophoresis. *Electrophoresis* **2002**, *23*, 1973–1983. [CrossRef]
- Nakashima, Y.; Hata, S.; Yasuda, T. Blood plasma separation and extraction from a minute amount of blood using dielectrophoretic and capillary forces. *Sens. Actuators B Chem.* **2010**, *145*, 561–569. [CrossRef]
- Cheng, S.J.; Hsieh, K.Y.; Chen, S.L.; Chen, C.Y.; Huang, C.Y.; Tsou, H.I.; Kumar, P.V.; Hsieh, J.C.; Chen, G.Y. Microfluidics and Nanomaterial-based Technologies for Circulating Tumor Cell Isolation and Detection. *Sensors* **2020**, *20*, 1875. [CrossRef] [PubMed]
- Jabir, M.; Sahib, U.I.; Taqi, Z.; Taha, A.; Sulaiman, G.; Albukhaty, S.; Al-Shammari, A.; Alwahibi, M.; Soliman, D.; Dewir, Y.H.; et al. Linalool-Loaded Glutathione-Modified Gold Nanoparticles Conjugated with CALNN Peptide as Apoptosis Inducer and NF- κ B Translocation Inhibitor in SKOV-3 Cell Line. *Int. J. Nanomed.* **2020**, *15*, 9025–9047. [CrossRef]

27. Albukhaty, S.; Naderi-Manesh, H.; Tiraihi, T.; Sakhi Jabir, M. Poly-L-lysine-coated superparamagnetic nanoparticles: A novel method for the transfection of pro-BDNF into neural stem cells. *Artif. Cells Nanomed. Biotechnol.* **2018**, *46* (Suppl. S3), S125–S132. [CrossRef]
28. Al-Musawi, S.; Albukhaty, S.; Al-Karagoly, H.; Sulaiman, G.M.; Alwahibi, M.S.; Dewir, Y.H.; Soliman, D.A.; Rizwana, H. Antibacterial Activity of Honey/Chitosan Nanofibers Loaded with Capsaicin and Gold Nanoparticles for Wound Dressing. *Molecules* **2020**, *25*, 4770. [CrossRef]
29. Albukhaty, S.; Al-Bayati, L.; Al-Karagoly, H.; Al-Musawi, S. Preparation and characterization of titanium dioxide nanoparticles and in vitro investigation of their cytotoxicity and antibacterial activity against *Staphylococcus aureus* and *Escherichia coli*. *Anim. Biotechnol.* **2020**, *28*, 1–7. [CrossRef]
30. Al-aqbi, Z.T.; Yap, Y.C.; Li, F.; Breadmore, M.C. Integrated Microfluidic Devices Fabricated in Poly (Methyl Methacrylate)(PMMA) for On-site Therapeutic Drug Monitoring of Aminoglycosides in Whole Blood. *Biosensors* **2019**, *9*, 19. [CrossRef]
31. Macdonald, N.P.; Currivan, S.A.; Tedone, L.; Paull, B. Direct production of microstructured surfaces for planar chromatography using 3D printing. *Anal. Chem.* **2017**, *89*, 2457–2463. [CrossRef] [PubMed]
32. Shalan, A.I.; Gaudry, A.J.; Guijt, R.M.; Breadmore, M.C. Tuneable nanochannel formation for sample-in/answer-out devices. *Chem. Commun.* **2013**, *49*, 2816–2818. [CrossRef] [PubMed]
33. Li, F.; Guijt, R.M.; Breadmore, M.C. Nanoporous membranes for microfluidic concentration prior to electrophoretic separation of proteins in urine. *Anal. Chem.* **2016**, *88*, 8257–8263. [CrossRef] [PubMed]
34. Cervera, J.; Ramírez, P.; Manzanares, J.A.; Mafé, S. Incorporating ionic size in the transport equations for charged nanopores. *Microfluid. Nanofluid.* **2010**, *9*, 41–53. [CrossRef]

Article

Microfluidic-Based Biosensor for Blood Viscosity and Erythrocyte Sedimentation Rate Using Disposable Fluid Delivery System

Yang Jun Kang 

Department of Mechanical Engineering, Chosun University, 309 Pilmun-daero, Dong-gu, Gwangju 61452, Korea; yjkang2011@chosun.ac.kr; Tel.: +82-62-230-7052; Fax: +82-62-230-7055

Received: 9 January 2020; Accepted: 18 February 2020; Published: 20 February 2020



Abstract: To quantify the variation of red blood cells (RBCs) or plasma proteins in blood samples effectively, it is necessary to measure blood viscosity and erythrocyte sedimentation rate (ESR) simultaneously. Conventional microfluidic measurement methods require two syringe pumps to control flow rates of both fluids. In this study, instead of two syringe pumps, two air-compressed syringes (ACSs) are newly adopted for delivering blood samples and reference fluid into a T-shaped microfluidic channel. Under fluid delivery with two ACS, the flow rate of each fluid is not specified over time. To obtain velocity fields of reference fluid consistently, RBCs suspended in 40% glycerin solution (hematocrit = 7%) as the reference fluid is newly selected for avoiding RBCs sedimentation in ACS. A calibration curve is obtained by evaluating the relationship between averaged velocity obtained with micro-particle image velocimetry (μ PIV) and flow rate of a syringe pump with respect to blood samples and reference fluid. By installing the ACSs horizontally, ESR is obtained by monitoring the image intensity of the blood sample. The averaged velocities of the blood sample and reference fluid ($\langle U_B \rangle$, $\langle U_R \rangle$) and the interfacial location in both fluids (α_B) are obtained with μ PIV and digital image processing, respectively. Blood viscosity is then measured by using a parallel co-flowing method with a correction factor. The ESR is quantified as two indices (t_{ESR} , I_{ESR}) from image intensity of blood sample ($\langle I_B \rangle$) over time. As a demonstration, the proposed method is employed to quantify contributions of hematocrit ($Hct = 30\%$, 40% , and 50%), base solution ($1\times$ phosphate-buffered saline [PBS], plasma, and dextran solution), and hardened RBCs to blood viscosity and ESR, respectively. Experimental Results of the present method were comparable with those of the previous method. In conclusion, the proposed method has the ability to measure blood viscosity and ESR consistently, under fluid delivery of two ACSs.

Keywords: blood viscosity; Erythrocyte sedimentation rate (ESR); T-shaped microfluidic channel; air-compressed syringe (ACS); micro-particle image velocimetry

1. Introduction

Microcirculation plays a substantial role in regulating blood flows and exchanging substances (gases, nutrients, and waste) between blood samples and peripheral tissues. Impaired microcirculation commonly leads to organ failures or mortality [1]. There is a need for comprehensive research that offers an insight that intrinsic properties and flow characteristics of blood samples share with microcirculatory disorders such as hypertension, sickle cell anemia, and diabetes [2]. The previous study has reported that biophysical properties of blood samples (hematocrit (Hct), viscosity, and erythrocyte sedimentation rate (ESR)) are strongly correlated with coronary heart diseases [3]. Thereafter, the biophysical properties of the blood sample have been studied extensively for the effective monitoring of circulatory disorders [4–9].

Under normal physiological conditions, red blood cells (RBCs) occupy 40–50% of blood volume. As RBCs are the most abundant cells in the blood sample, the biophysical properties of the blood sample are determined dominantly by properties of RBCs. The characteristics of RBCs, including morphology, membrane viscoelasticity, and RBCs count, are evaluated by quantifying several biophysical properties of blood samples, including viscoelasticity (or viscosity), deformability, and hematocrit. In that regard, plasma proteins in blood samples induce RBC aggregation, which occurs at an extremely low shear rate (i.e., $\dot{\gamma} = 1\sim 10\text{ s}^{-1}$) [10] or stasis. Among the biophysical properties of blood samples, blood viscosity is determined by several factors, including hematocrit, plasma viscosity, RBCs deformability, and RBCs aggregation. Thus, their properties of blood samples are employed to monitor variations in the characteristics of blood samples. At lower shear rates, RBC aggregation causes to increase blood viscosity. At high shear rates, the deformation and alignment of RBCs lead to a decrease in blood viscosity. In other words, blood viscosity provides information on aggregation and deformability simultaneously. However, at extremely low shear rates, a syringe pump (SP) exhibits fluidic instability and RBC sedimentation continuously occurs. A microfluidics-based viscometer does not provide consistent values of blood viscosity. Conventionally, blood viscosity has been measured at sufficiently high shear rates (i.e., $\dot{\gamma} > 10\text{ s}^{-1}$ [11,12] or $\dot{\gamma} > 50\text{--}100\text{ s}^{-1}$ [13,14]), especially in microfluidic environments. For the reason, blood viscosity obtained with a microfluidic device does not give sufficient information on the contributions of plasma proteins to RBC aggregation. To evaluate variations in plasma proteins consistently, it is additionally necessary to quantify RBCs aggregation or ESR.

A microfluidic device has several advantages, including small volume consumption, fast measurement, easy sample handling, high sensitivity, and disposability. Thus, it has been widely used to measure various biophysical properties of blood samples (i.e., blood viscosity [15], RBCs aggregation [16], RBCs deformability [17,18], and hematocrit [19]).

The previous methods for measuring blood viscosity are conveniently divided into three categories (i.e., driving sources, devices, and quantification techniques). First, extrinsic driving sources such as SPs [20], pressure sources, and hand-held pipettes [13] have been suggested for delivering a blood sample into a specific device. Additionally, intrinsic driving sources such as capillary force (or surface tension) [21,22] and gravity force [23] have been applied to supply blood samples into a device. Second, various devices such as a microelectromechanical system (MEMS)-based microfluidic device, a 3D-printed microfluidic device [13,24], and a paper-based device [25] have been suggested for inducing blood flow in a specifically constrained direction. Third, quantification techniques such as advancing meniscus (i.e., variations of a blood column over time) [15,22,26,27], the falling time of a metal sphere in a tube [28], electric impedances (i.e., resistance, capacitance) [29,30], droplet length [31], digital flow compartment with a microfluidic channel array [11,12], interface detection in co-flowing streams [32,33], and reversal flow switching in a Wheatstone bridge analog of a fluidic circuit [14] have been suggested to measure blood viscosity.

To measure RBCs aggregation in microfluidic environments, a blood sample is placed into a microfluidic channel. By applying shear stress to the blood sample with external driving systems (i.e., an SP [34], pinch valve [16], or stirring motor [35]), the RBCs in the blood sample are aggregated or disaggregated, depending on the shear rate. Several quantification methods, such as light intensity (i.e., transmission, and back-scattering) [16], electrical conductivity [36,37], microscopic RBC images [38–40], ultrasonic images [41], and optical tweezers [42] have been suggested for obtaining temporal variations of RBCs aggregation. As another approach, RBC aggregation can be quantified by measuring the sedimentation distances of RBCs in a blood sample during a specific duration (i.e., ESR). Unlike the conventional Westergren ESR method, a microfluidic-based ESR measurement is quantified by measuring the conductivity of the blood sample in a PDMS chamber with a square cross-section (i.e., each side = 4 mm, depth = 5 mm) [43]. Owing to the continuous ESR in the driving syringe, RBC-free regions (or depleted regions) expand from the top layer with an elapse of time. The blood sample is supplied into a microfluidic device from the top layer of the driving syringe. To monitor blood flows in the microfluidic channel, microscopic images are sequentially captured with a high speed

camera. Image intensity of each microscopic image is calculated over time by conducting digital image processing. The ESR is then evaluated by quantifying temporal variations of the image intensity [44].

To measure blood viscosity and RBC aggregation inexpensively, two SPs should be replaced with an inexpensive and disposable delivery system. To remove the syringe pump, single ACS is suggested to infuse the blood sample into a microfluidic device for measuring pressure and RBCs aggregation over continuously varying flow rates [45]. In this study, the ultimate goal of this study is to measure blood viscosity and RBC aggregation (or ESR), without two SPs.

In this study, a simple method for measuring blood viscosity and ESR is proposed. It involves the quantification of the interfacial location in a co-flowing channel and microscopic image intensity of blood sample flowing in a microfluidic device. Two air-compressed syringes (ACSs) are employed to simultaneously deliver the blood sample and reference fluid. Based on an ACS for delivering blood samples as suggested in previous studies [46,47], two ACSs are suggested to deliver blood samples and reference fluid simultaneously. Since the flow rates of both fluids are not specified under fluid delivery with the ACSs, it is necessary to quantify them with a time-resolved micro-particle image velocimetry (μ -PIV) technique. Based on a parallel co-flowing method with a correction factor [32], the blood viscosity is measured by monitoring the interfacial location in a co-flowing channel. Unlike the previous studies [46,47], two ACSs are installed horizontally to measure ESR effectively. Continuous sedimentation in the ACS causes an expansion of an RBC-free layer from the top layer. When blood samples are delivered to the blood channel from the ACS, the populations of RBCs (or hematocrit) are reduced over time. Since a continuous ESR contributes to increasing microscopic image intensity of blood flows, the ESR can be quantified by monitoring the image intensity of the blood sample.

When compared to previous methods that have the ability to measure blood viscosity under fluid delivery with syringe pumps, two syringe pumps are replaced by two ACSs as a novelty of this method. Here, a 40% glycerin solution is newly selected as the reference fluid. RBCs as fluid tracers are added into reference fluid. Velocity fields of both fluids are obtained consistently over time by conducting a time-resolved micro-PIV technique.

By installing the ACSs horizontally, the continuous ESR inside the ACS is filled with the blood sample causing it to expand RBC-free regions. As RBCs aggregation tends to increase substantially at lower hematocrit or lower velocity, it contributes to increasing the image intensity of blood samples. Thus, it is possible to evaluate the ESR by monitoring the microscopic image intensity of the blood sample.

2. Materials and Methods

2.1. Fabrication of Microfluidic Device and Experimental Procedure

A microfluidic device for measuring blood viscosity and ESR consisted of two inlets (a, b), one outlet (a), and a T-shaped channel (width = 250 μm , depth = 20 μm), as shown in Figure 1A-a. The T-shaped channel was composed of a blood channel, a reference channel, and a co-flowing channel. When analyzing the velocity fields of each fluid, the T-shaped channel does not require to align each microscopic image in the horizontal direction. Conventional micro-electromechanical-system techniques, such as photolithography and deep reactive ion etching (DRIE), were employed to fabricate 4-inch silicon mold. To peel off PDMS block from the master mold easily, plasma surface treatment was conducted after the DRIE process [48]. PDMS elastomer (Sylgard 184, Dow Corning, Midland, MI, USA) was mixed with a curing agent at a ratio of 10:1. After positioning the mold on a petri dish, the PDMS mixture was poured into the mold. Air bubbles dissolved in the PDMS were removed by operating a vacuum pump (WOB-L Pump, Welch, Gardner Denver, Milwaukee, WI, and USA) for 1 h. After curing the PDMS in a convective oven at 70 $^{\circ}\text{C}$ for 1 h, a PDMS block was peeled off from the mold. It cut with a razor blade. Two inlets and outlets were punched with a biopsy punch (outer diameter = 1.0 mm). After treating the surfaces of the PDMS block and a glass slide with an oxygen plasma system (CUTE-MPR, Femto Science Co., Gyeonggi-do, Korea), the PDMS block was bonded on

a glass substrate. A microfluidic device was finally prepared by placing it on a hotplate at 120 °C for 10 min.

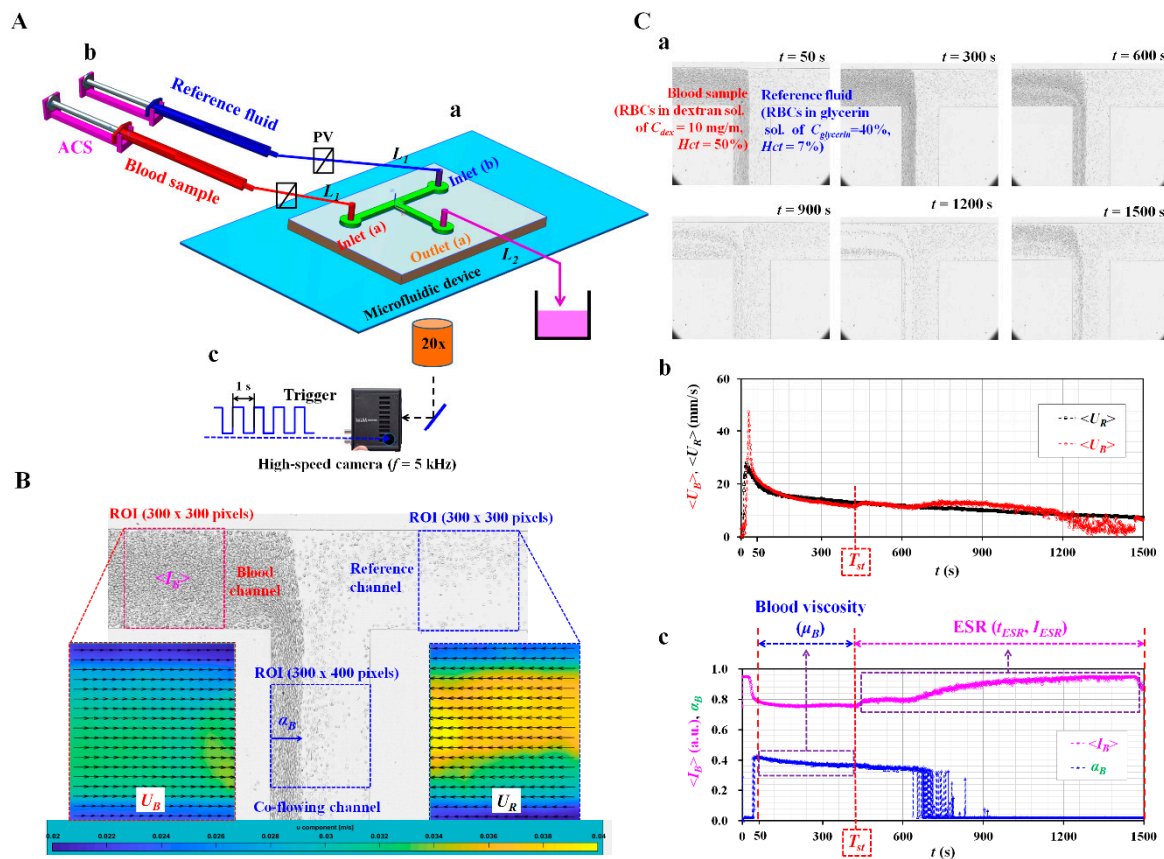


Figure 1. Proposed method for measuring blood viscosity and erythrocyte sedimentation rate (ESR) under fluid delivery of two air-compressed syringes (ACSs). (A) Schematic diagram of the proposed technique, including a microfluidic device, two ACSs, and an image acquisition system. (a) A microfluidic device consisting of two inlets (a,b), one outlet (a), and a T-shaped channel (i.e., blood channel, reference channel, and co-flowing channel). (b) Two ACSs for delivering blood samples and reference fluid. Each ACS was composed of a disposable syringe (~1 mL), a fixture, and a pinch valve. (c) The microfluidic device is located in an optical image acquisition system composed of optical microscopy with a 20× objective lens (NA = 0.4), and a high-speed camera. The camera had a frame rate of 5 kHz and captured sequential snapshots at an interval of 1 s. (B) Three regions-of-interest (ROIs) were selected for evaluating four parameters ($\langle I_B \rangle$, U_B , U_R , and α_B). $\langle I_B \rangle$ and α_B were obtained by conducting digital image processing. U_B and U_R were obtained by conducting a micro-particle image velocimetry (PIV) technique. (C) As a preliminary demonstration, blood sample (normal RBCs in 10 mg/mL dextran solution (Hct = 50%)) and reference fluid (RBCs in 40% glycerin solution (Hct = 7%)) were delivered to each inlet with two ACSs. (a) Microscopic images captured at a specific time (t) (t = 50, 300, 600, 900, 1200, and 1500 s). (b) Temporal variations of $\langle U_B \rangle$ and $\langle U_R \rangle$. (c) Temporal variations of $\langle I_B \rangle$ and α_B . Separation time (T_{st}) was obtained as the time when $\langle I_B \rangle$ started to increase. First, blood viscosity was evaluated from three parameters (U_B , U_R , and α_B) obtained within T_{st} . Second, the ESR of the blood sample was evaluated from $\langle I_B \rangle$ obtained above T_{st} .

As shown in Figure 1A-b, two polyethylene tubes (L_1) (length = 300 mm, inner diameter = 500 μm , and thickness = 500 μm) were tightly fitted into two inlets (a, b). The end of each tube was connected to the individual syringe needle of the ACS. The outlet of each ACS was clamped with a pinch valve. The other tube (L_2) (length = 200 mm, inner diameter = 500 μm , and thickness = 500 μm) was tightly fitted into outlet (a). The end of the tube (L_2) was connected to a waste dish. To remove air bubbles and avoid non-specific binding of plasma proteins to the inner surface of the channels, the channel was

filled with bovine serum albumin (BSA) solution ($C_{BSA} = 2 \text{ mg/mL}$) through outlet (a). After an elapse of 10 min, the microfluidic channel was newly filled with $1\times$ PBS.

Based on the concept of ACS as reported in a previous study [45], two ACSs were employed to deliver the blood sample and reference fluid into the microfluidic device. Figure A1A (Appendix A) showed two ACSs filled with the blood sample ($Hct = 50\%$) and reference fluid (RBCs suspended in 40% glycerin solution ($Hct = 7\%$)). Each ACS was composed of a disposable syringe ($\sim 1 \text{ mL}$), a fixture, and a pinch valve. Two pinch valves were used to stop or allow the fluid flow of each fluid. Each ACS was placed horizontally on the stage of the optical microscope and fixed with an adhesive tape. Here, an angle of inclination of the ACS only depended on an individual fixture. It was certain that the installation angle of the ACS remained identical because the same fixture of the ACS was used for all experiments.

As shown in Figure A1B (Appendix A), the operation of each ACS was classified into five steps: (1) piston movement at the lowest position forward at $t = t_1$, (2) air suction by moving the piston to 0.7 mL backward at $t = t_2$, (3) blood suction by moving the piston to 0.3 mL backward at $t = t_3$, (4) air compression by moving the piston to 0.3 mL forward at $t = t_4$, and (5) blood delivery by removing the pinch valve at $t = t_5$. As the air cavity inside the ACS was compressed to 0.3 mL, internal pressure increased substantially above atmospheric pressure. Similarly, the reference fluid was sucked into the syringe. The remainder of the procedure was the same as blood delivery. By removing two pinch valves, blood sample and reference fluid were delivered to the corresponding inlets because pressure difference increased inside the ACS.

The microfluidic device was positioned on an optical microscope (BX51, Olympus, Tokyo, Japan) equipped with a $20\times$ objective lens ($NA = 0.4$). As shown in Figure 1A-c, a high-speed camera (FASTCAM MINI, Photron, Tokyo, Japan) was used to obtain sequential microscopic images of the blood sample and reference fluid flowing in the microfluidic channels. The camera offered a spatial resolution of 1280×1000 pixels. Each pixel corresponded to $10 \mu\text{m}$ physically. A function generator (WF1944B, NF Corporation, Yokohama, Japan) triggered the high-speed camera at an interval of 1 s. Then, two microscopic images were captured at a frame rate of 5 kHz.

To minimize the effect of temperature on blood viscosity, all experiments were conducted at a room temperature of $25 \text{ }^\circ\text{C}$. Contributions of two factors (i.e., humidity, and atmospheric pressure) to the present method were neglected. After the blood sample was injected into an ACS, the blood sample did not contact with environment air. Additionally, the ACS was operated by pressure difference (ΔP) between pressure inside ACS (P_{ACS}) and atmosphere pressure (P_{atm}) (i.e., $\Delta P = P_{ACS} - P_{atm}$) [47]. The pressure difference depended on air volume inside the ACS (i.e., gauge pressure), rather than atmospheric pressure.

2.2. Quantification of Microscopic Image Intensity, Blood Velocity Fields, and Interfacial Location

First, blood viscosity was obtained by quantifying the velocity fields of blood sample flowing in the blood channel, the velocity fields of reference fluid flowing in the reference channel, and the interface location between two fluids flowing in the co-flowing channel.

RBCs as fluid tracers were added into reference fluid to obtain the velocity fields of the reference fluid. To measure velocity fields of reference fluid consistently, RBCs should be distributed uniformly in reference fluid during experiments. According to previous studies [1,2], when reference fluid was prepared by adding RBCs into $1\times$ PBS and filled into the ACS, sedimentation of RBCs in ACS occurred continuously over time. RBCs in reference fluid did not flow uniformly over time. After a certain lapse of time, there were no fluid tracers in reference fluid. It was then impossible to obtain the velocity fields of the reference fluid. To resolve the critical issue, a 40% glycerin solution was carefully selected as a base solution in reference fluid. Additionally, to minimize contributions of RBCs to velocity fields and viscosity, hematocrit of RBCs added into reference fluid was fixed at $Hct = 7\%$.

As shown in Figure 1B, an ROI (300×300 pixels) was selected to obtain the velocity fields of the blood sample flowing in the blood channel. Another ROI with 300×300 pixels was selected to obtain

the velocity fields of the reference fluid flowing in the reference channel. By conducting a time-resolved μ PIV technique, the velocity fields of the blood sample (U_B) across the blood channel width were obtained over time. Additionally, velocity fields of the reference fluid flow (U_R) across the reference channel width were obtained over time. The size of the interrogation window was selected as 64×64 pixels. The window overlap was set to 75%. The velocity fields were validated and corrected with a median filter. The averaged velocities ($\langle U_B \rangle$, $\langle U_R \rangle$) of both fluids were calculated as an arithmetic average over the specific ROI. To obtain the interface (i.e., blood sample-filled width) in the co-flowing channel (α_B), an ROI with 300×400 pixels was selected in the co-flowing channel. A gray-scale microscopic image was converted into a binary image by adopting Otsu's method [49]. By conducting an arithmetic average over the ROI, variations of the interfacial location in the co-flowing channel (α_B) were obtained over a period of time.

Second, the ESR was evaluated by quantifying the microscopic image intensity of the blood sample flowing in the blood channel. To evaluate the microscopic image intensity of blood flows, and ROI with 300×300 pixels was selected in the blood channel. The image intensity of the blood sample flowing in the blood channel was obtained by conducting digital image processing with a commercial software package (Matlab 2019, Mathworks, Natick, MA, USA). An averaged value of microscopic image intensity ($\langle I_B \rangle$) was obtained by performing an arithmetic average of image intensity over the specific ROI.

2.3. Quantification of Blood Viscosity and ESR

As a preliminary demonstration, blood samples (normal RBCs suspended in specific dextran solution (10 mg/mL), $Hct = 50\%$) and reference fluid were delivered to the corresponding inlets (a, b) under the fluid delivery with two ACSs. To visualize the velocity fields of the reference fluid flowing in the reference channel, the reference fluid was prepared by adding normal RBCs ($Hct = 7\%$) into a 40% glycerin solution.

Figure 1C-a showed microscopic images captured at specific times (t) ($t = 50, 300, 600, 900, 1200, \text{ and } 1500 \text{ s}$). Above $t = 600 \text{ s}$, the populations of RBCs flowing in the blood channel decreased substantially over time. As shown in Figure 1C-b, temporal variations of U_B and U_R were obtained by conducting the μ PIV technique. As the pressure difference between the inner pressure and atmospheric pressure tended to decrease over time in the ACS, the averaged velocity of the reference fluid ($\langle U_R \rangle$) tended to decrease stably over time. However, owing to the continuous ESR inside the ACS, an RBC-free liquid was observed in a tube, as shown in Figure A1C (Appendix A). The averaged velocity of the blood sample ($\langle U_B \rangle$) varied unstably above $t = 400 \text{ s}$. Figure 1C-c showed the temporal variations in the image intensity of the blood sample flowing in the blood channel ($\langle I_B \rangle$), and the interface between the two fluids in the co-flowing channel (α_B). Similar to U_B , the continuous ESR inside the ACS led to unstable behaviors in $\langle I_B \rangle$ and α_B . In this study, the separation time when unstable behavior began was denoted as T_{st} . At $t < T_{st}$, three factors ($\langle U_B \rangle$, $\langle U_R \rangle$, and $\langle \alpha_B \rangle$) exhibited stable variations over time. Thus, the blood viscosity was quantified from the three factors ($\langle U_B \rangle$, $\langle U_R \rangle$, and α_B). For a rectangular channel with an extremely low aspect ratio, an approximate formula of fluidic resistance was derived approximately as $R = \frac{12 \mu_B L}{w h^3}$. A co-flowing channel was filled with a blood sample and reference fluid, respectively. For simple mathematical representation, both streams were represented as two fluidic resistances connected in parallel. The corresponding fluidic resistance for each fluid was derived as $R_B = \frac{12 \mu_B L}{W \alpha_B h^3}$ for a blood sample, and $R_R = \frac{12 \mu_R L}{W(1-\alpha_B) h^3}$ for reference fluid. Here, μ_R meant the viscosity of the reference fluid. As both fluids had the same pressure drop (i.e., $\Delta P = R_B \cdot Q_B = R_R \cdot Q_R$), blood viscosity formula (μ_B) was derived as $\mu_B = \mu_R \times \left(\frac{\alpha_B}{1-\alpha_B} \right) \times \left(\frac{Q_R}{Q_B} \right)$. Here, Q_B and Q_R represented the flow rate of the blood sample and reference fluid, respectively. The simple mathematical model did not account for real boundary conditions in co-flowing flows. Thus, to compensate for the deviation from the real boundary condition, the previous study included a correction factor in the analytical formula of blood viscosity. According to the blood viscosity formula reported in a parallel co-flowing method with a correction factor [32], the blood viscosity formula (μ_B) was modified as $\mu_B = C_f \times \mu_R \times \left(\frac{\alpha_B}{1-\alpha_B} \right) \times \left(\frac{Q_R}{Q_B} \right)$.

Since the correction factor (C_f) was varied depending on the channel size, a numerical simulation was conducted to determine the correction factor. Based on a procedure discussed in a previous study [32], a numerical simulation using commercial computational fluid dynamics (CFD) software (CFD ACE+, ESI Group, Paris, France) for a rectangular channel (width = 250 μm , depth = 20 μm) was conducted to obtain the viscosity of the test fluid with respect to the interface. For convenience, it was assumed that the reference fluid and test fluid behaved as Newtonian fluids. Both fluids had the same value, as $\mu_{ref} = \mu_{test} = 1$ cP. The interface between both fluids was relocated by varying the flow rate ratio of the reference fluid to test fluid. As shown in Figure A2A (Appendix A), when the interface moved from center line ($\alpha_x = 0.5$) to each wall (i.e., $\alpha_x = 0$ or 1), the blood viscosity without the correction factor (i.e., μ_n) showed a large deviation when compared with the viscosity of the test fluid ($\mu_{test} = 1$ cP). Considering that the viscosity of the test fluid should have a constant value of $\mu_{test} = 1$ cP with respect to the interface, the correction factor (C_f) could be obtained by reciprocating μ_n with respect to α_x (i.e., $C_f = 1/\mu_n$). By conducting a regression analysis, the variations of the correction factor with respect to the interface were obtained as $C_f = 9.7212\alpha_x^4 - 19.442\alpha_x^3 + 15.687\alpha_x^2 - 5.9659\alpha_x + 1.8992$ ($R^2 = 0.9968$). As shown in Figure A2B (Appendix A), to validate C_f , the viscosities of the test fluid were given as (a) $\mu_{test} = 1$ cP and (b) $\mu_{test} = 4.08$ cP. The flow rates of both fluids were the same, at 1 mL/h (i.e., $Q_{ref} = Q_{test} = 1$ mL/h). By applying the correction factor, the viscosities of the test fluids were determined as 1 cP and 4.14 cP, respectively. From the results, it was found that the parallel co-flowing method with the correction factor had the ability to measure the viscosity of a test fluid within 1.4% of a normalized difference. However, at $t > T_{st}$, the continuous ESR inside the ACS caused unstable behaviors in blood flows. To quantify the ESR, two indices (i.e., I_{ESR} , T_{ESR}) were suggested from $\langle I_B \rangle$ and T_{st} , as shown in Figure 5. Based on previous studies [45,50], one ESR index (I_{ESR}) was suggested simply by integrating $\langle I_B \rangle$ from $t = T_{st}$ to $t = T_{end}$ (i.e., $I_{ESR} = \int_{t=T_{st}}^{t=T_{end}} \langle I_B \rangle dt$). Here, T_{end} represented the end time of each experiment. Additionally, $T_{ESR} = T_{st} - T_i$. T_i indicated the initial time when the blood sample started to fill the blood channel.

From the preliminary demonstration, four factors ($\langle U_B \rangle$, $\langle U_R \rangle$, α_B , and $\langle I_B \rangle$) could be effectively employed to obtain the blood viscosity and ESR when two ACSs were employed to deliver the blood sample and reference fluid into a microfluidic device.

2.4. Selection of Base Solution in Reference Fluid

To visualize the velocity fields of the reference fluid, RBCs were added into the reference fluid as fluid tracers. Glycerin solution was suggested as a reference fluid to minimize the sedimentation of RBCs inside the ACS. According to a previous study [51], the density (ρ) and viscosity (μ) increased at higher concentrations of glycerin solution as shown in Figure A3A (Appendix A). To evaluate the sedimentation rate of the RBCs added into the reference fluid, a simple ESR tester was prepared by using a disposable syringe (~ 1 mL) as shown in Figure A3C (Appendix A). The disposable syringe was fitted vertically into a hole (outer diameter = 4 mm) of the PDMS block. The outlet of the hole was closed with 3M adhesive tape. The syringe was filled with a specific concentration of glycerin solution (~ 0.5 mL). A 50 μL RBCs droplet was dropped into a specific concentration of glycerin solution. To monitor the sedimentation rate of the RBCs droplet in the simple ESR tester, snapshots were captured at an interval of 1 s with a smartphone camera (Galaxy A5, Samsung, Korea). As shown in Figure A3B (Appendix A), temporal variations of sedimentation height (H) were obtained by varying the concentration of the glycerin solution ($C_{glycerin}$) ($C_{glycerin} = 5\%$, 10% , 20% , 30% , and 40%). Figure A3C (Appendix A) showed sedimentation of the RBCs droplet in 30% glycerin solution over time (t) ($t = 0, 156, 192, 249, 259, 270$, and 275 s). From the results, the RBCs droplet in the 40% glycerin solution remained nearly identical at the upper position, even without sedimentation. Furthermore, considering that the densities of normal RBCs range from 1090 kg/m³ to 1106 kg/m³ [52], the reference fluid was selected as a 40% glycerin solution ($C_{glycerin} = 40\%$), because its density was greater than that of the RBCs.

2.5. Statistical Analysis

The statistical significance was evaluated by conducting statistical analyses with a commercial software package (Statistical Package for the Social Sciences (SPSS) Statistics version 24, IBM Corp., Armonk, NY, USA). Two ESR indices (I_{ESR} , T_{ESR}) and blood viscosity ($\langle\mu_B\rangle$) obtained by the present method were compared with results reported in a previous study (i.e., blood viscosity: μ_B , ESR index: S_{EAI}). An analysis of variance (ANOVA) test was applied to verify significant differences between comparative results. A linear regression analysis was conducted to verify the correlations between two parameters. All experimental results were expressed as mean \pm standard deviation. If the p -value was less than 0.05, the experimental results exhibited significant differences within a 95% confidence interval.

3. Results and Discussion

3.1. Contribution of RBCs Added into Reference Fluid to Viscosity and Velocity Fields

To evaluate the effects of the RBCs added into the reference fluid on fluid viscosity, the viscosity of the reference fluid was measured by varying the volume of the RBCs added to the reference fluid (i.e., hematocrit [Hct]). In that regard, a 1 \times PBS was delivered to the blood channel (i.e., left-side channel) at a constant flow rate of $Q_{PBS} = 1$ mL/h with a syringe pump (SP) (neMESYS, Centoni GmbH, Germany). The hematocrit (Hct) of the reference fluid was adjusted to $Hct = 3\%$, 5% , 7% , and 9% by adding normal RBCs into the 40% glycerin solution. The reference fluid was delivered to the reference channel (i.e., right-side channel) at a constant flow rate of $Q_{glycerin} = 1$ mL/h with an SP. Figure 2A showed microscopic images for evaluating the interfacial location in the co-flowing channel with respect to Hct ((a) $Hct = 0\%$, (b) $Hct = 3\%$, (c) $Hct = 5\%$, (d) $Hct = 7\%$, and (e) $Hct = 9\%$). To verify the contribution of the hematocrit in the reference fluid to the velocity fields (U_R), the velocity fields of the reference fluid were obtained across the reference channel width with respect to Hct . As shown in Figure 2B-a, a variation of the velocity profile (U_R) was obtained across the reference channel width with respect to Hct . The inset showed the microscopic image and velocity profile of the reference fluid with $Hct = 3\%$. From the results, the velocity profile did not show a distinctive difference depending on the hematocrit. Figure 2B-b showed variations of the averaged velocity of the reference fluid ($\langle U_R \rangle$) with respect to Hct . The hematocrit in the reference fluid did not contribute to varying $\langle U_R \rangle$ significantly. As shown in Figure 2C-a, the variations of the interface in the co-flowing channel (α_R) and the viscosity (μ_R) were obtained with respect to Hct . The interface and viscosity remained constant as $\alpha_R = 0.771 \pm 0.003$ and $\mu_R = 3.868 \pm 0.068$ cP for the reference fluid, with up to 9% hematocrit. From the results, it could be observed that providing up to a 9% hematocrit in the reference fluid did not significantly contribute to increasing the viscosity of the reference fluid. In addition, as shown in Figure A3A (Appendix A), an empirical formula [51] indicated that a 40% glycerin solution without any RBCs had a viscosity value of 4.07 cP. Based on the parallel co-flowing method with the correction factor [32], the viscosity of the reference fluid was measured consistently within a 5% difference when compared with the empirical formula. Furthermore, a previous flow-switching method [14] was employed to measure the viscosity of the reference fluid with respect to hematocrit. The inset of Figure 2C-b showed reversal flow-switching in the junction channel for the reference fluid with $Hct = 7\%$. By increasing the flow rate of the 1 \times PBS (Q_{PBS}) from $Q_{PBS} = 1$ mL/h to $Q_{PBS} = 3.1$ mL/h, the hydrodynamic balancing in both side channels caused to reverse flow direction from left direction to right direction (i.e., reversal flow-switching phenomena) [14]. In other words, the junction channel was filled with blood at $Q_{PBS} = 1$ mL/h. However, it was filled with 1 \times PBS at $Q_{PBS} = 3.1$ mL/h. Based on the viscosity formula suggested in the flow-switching method, the viscosity of the reference fluid was quantified as $\mu_R = 3.1 \pm 0.05$ cP. As shown in Figure 2C-b, the viscosity obtained by both methods remained stable, with respect to hematocrit. Similar to the case in the parallel co-flowing method with the correction factor, the results of the flow-switching method indicated that the RBCs added into the reference fluid did not contribute to varying the viscosity within 9% hematocrit. The viscosity obtained by the flow-switching

method was underestimated by approximately 20% when compared with that obtained by the parallel co-flowing method with the correction factor. From these results, in this study, the reference fluid was prepared by adding normal RBCs ($Hct = 7\%$) into a 40% glycerin solution throughout all experiments.

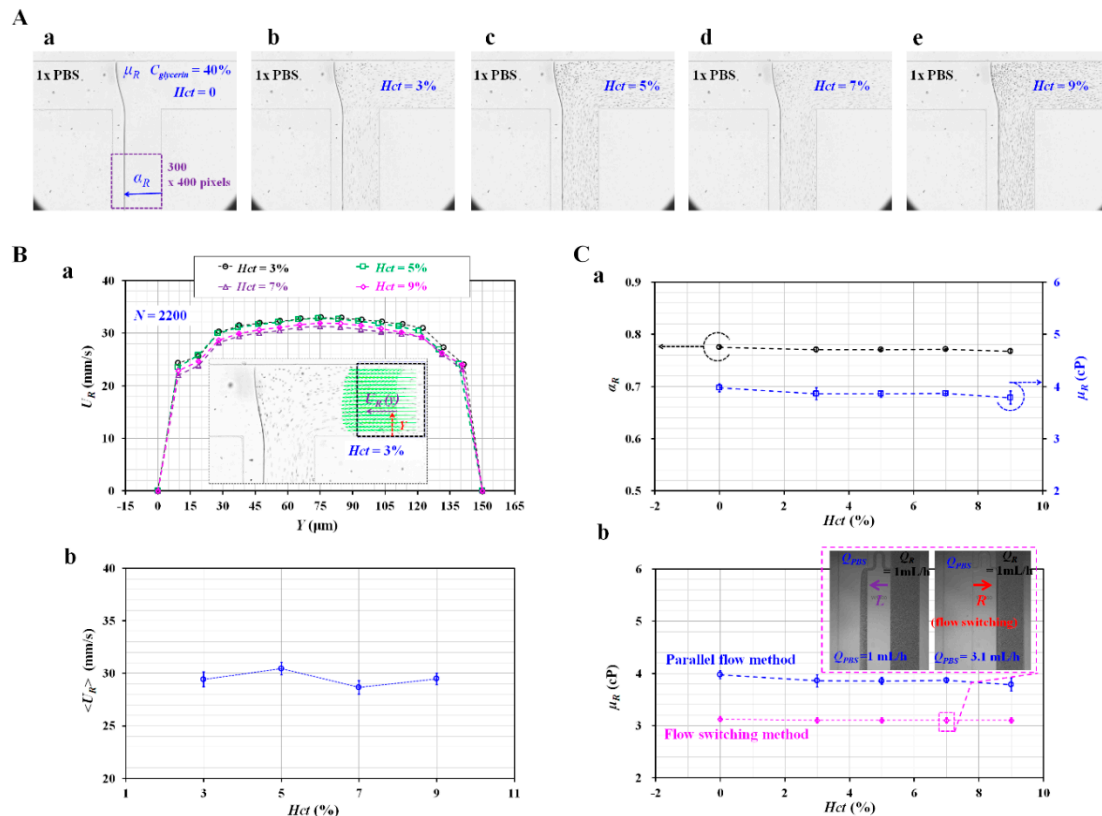


Figure 2. Contributions of RBCs added into the reference fluid to viscosity. 1× PBS was delivered to the blood channel at a constant flow rate of 1 mL/h with a syringe pump (SP). The hematocrit (Hct) of reference fluid was adjusted by adding normal RBCs into 40% glycerin solution ($Hct = 0, 3\%, 5\%, 7\%,$ and 9%). The reference fluid was delivered to the reference channel at a constant flow rate of 1 mL/h with an SP. **(A)** Microscopic images for obtaining interface (α_R) in co-flowing channel with respect to Hct ((a) $Hct = 0$, (b) $Hct = 3\%$, (c) $Hct = 5\%$, (d) $Hct = 7\%$, and (e) $Hct = 9\%$). **(B)** Contributions of hematocrit in reference fluid to velocity fields (U_R). **(a)** Variation of velocity fields (U_R) across reference channel width with respect to Hct . The inset showed a microscopic image and a velocity profile of the reference fluid with $Hct = 3\%$. **(b)** Variations of $\langle U_R \rangle$ averaged over a region of interest (ROI) with respect to Hct . **(C)** Effect of Hct in reference to fluid on viscosity (μ_R). **(a)** Variations of α_R and μ_R with respect to Hct . **(b)** Comparison between the proposed method (i.e., the parallel-flow method with correction factor) and previous method (i.e., flow-switching method) with respect to Hct .

3.2. Relationship between Flow Rate of Syringe Pump and Averaged Velocity Obtained by μPIV

To obtain blood viscosity, the flow rates of the blood sample and reference fluid should be measured from the averaged velocity obtained by conducting the μPIV technique. In other words, there was a need to obtain the relationship between the flow rate delivered by the SP (Q_{sp}) and the averaged velocity obtained by conducting the μPIV technique ($\langle U \rangle$).

The hematocrit of the blood sample was adjusted to $Hct = 30\%$, 40% , and 50% by adding normal RBCs into the base solution ($1\times$ PBS, plasma). Using two SPs, the flow rate of each fluid decreased stepwise from $Q_{sp} = 1.5$ mL/h to $Q_{sp} = 0.1$ mL/h, at an interval of 0.2 mL/h. With respect to each flow rate, the SP had been operated for 8 min. The blood sample was prepared by adding normal RBCs into plasma. As shown in Figure 3A-a, temporal variations of the averaged velocity ($\langle U_B \rangle$) and the flow rate of the SP (Q_{sp}) were obtained by varying the hematocrit. At a higher flow rate of Q_{sp} , the hematocrit contributed to decreasing $\langle U_B \rangle$. At a lower flow rate of Q_{sp} , $\langle U_B \rangle$ remained constant, without contribution from the hematocrit. By changing the base solution from plasma to a $1\times$ PBS, temporal variations of $\langle U_B \rangle$ and Q_{sp} were obtained with respect to Hct . As shown in Figure 3A-b, the variations of $\langle U_B \rangle$, with respect to hematocrit, were very similar to those of a blood sample composed of plasma. By averaging $\langle U_B \rangle$ with respect to Q_{sp} , $\langle U_B \rangle$ was quantified as mean \pm standard deviation with respect to Q_{sp} . To determine the relationship between $\langle U_B \rangle$ and Q_{sp} , a scatter plot was used to plot $\langle U_B \rangle$ on a vertical axis and Q_{sp} on a horizontal axis. Figure 3A-c showed variations of $\langle U_B \rangle$ with respect to Q_{sp} and Hct in a blood sample composed of plasma. For example, $\langle U_B \rangle$ was estimated as about 30 mm/s for $Q_{sp} = 1.3$ mL/h. Based on formula of flow rate (i.e., $Q_{\mu P} = \langle U_B \rangle A_c$, $A_c = w \times h$), flow rate obtained by μ PIV was estimated as $Q_{\mu PIV} = 0.54$ mL/h. When compared with $Q_{sp} = 1.3$ mL/h, the normalized difference between Q_{sp} and $Q_{\mu PIV}$ was estimated as 59% . In this study, instead of the flow rate formula, the flow rate of the blood sample or reference fluid was estimated from the calibration formula obtained in advance. Thus, it was necessary to determine the relationship between velocity ($\langle U_B \rangle$) and Q_{sp} . A regression analysis was conducted by assuming the regression formula as a quadratic model. Regression formulas between $\langle U_B \rangle$ and Q_{sp} with respect to Hct were obtained, as shown inside of Figure 3A-c. The regression formulas for each hematocrit were obtained as $\langle U_B \rangle = -5.027 Q_{sp}^2 + 30.279 Q_{sp}$ ($R^2 = 0.998$) for $Hct = 30\%$, $\langle U_B \rangle = -6.262 Q_{sp}^2 + 30.660 Q_{sp}$ ($R^2 = 0.999$) for $Hct = 40\%$, and $\langle U_B \rangle = -5.916 Q_{sp}^2 + 29.137 Q_{sp}$ ($R^2 = 0.999$) for $Hct = 50\%$. Figure 3A-d showed variations of $\langle U_B \rangle$ with respect to the Q_{sp} and Hct in a blood sample composed of $1\times$ PBS. From the regression analysis, as shown inside Figure 3A-d, the regression formulas for each hematocrit were obtained as $\langle U_B \rangle = -4.850 Q_{sp}^2 + 30.791 Q_{sp}$ ($R^2 = 0.998$) for $Hct = 30\%$, $\langle U_B \rangle = -7.897 Q_{sp}^2 + 33.519 Q_{sp}$ ($R^2 = 1.000$) for $Hct = 40\%$, and $\langle U_B \rangle = -5.717 Q_{sp}^2 + 29.286 Q_{sp}$ ($R^2 = 0.999$) for $Hct = 50\%$. For the same hematocrit, the base solution (i.e., plasma or $1\times$ PBS) did not contribute to varying the coefficients of the quadratic formula (i.e., normalized difference $< 4\%$ except $Hct = 40\%$). However, for the same base solution, the coefficients of a quadratic model varied significantly with respect to hematocrit.

A regression formula between Q_{sp} and $\langle U_R \rangle$ for the reference fluid (i.e., 40% glycerin solution) with RBCs ($Hct = 7\%$) was obtained by using a similar procedure to that used for the blood sample. Figure 3B-a showed the temporal variations of Q_{sp} and $\langle U_R \rangle$ for the reference fluid. $\langle U_R \rangle$ was obtained as a mean \pm standard deviation for a corresponding Q_{sp} . When compared with the blood sample, $\langle U_R \rangle$ increased substantially, owing to the lower value of the hematocrit. As shown in Figure 3B-b, variations of $\langle U_R \rangle$ with respect to Q_{sp} were represented by a scatter plot. From a regression analysis, the regression formula between $\langle U_R \rangle$ and Q_{sp} was obtained as $\langle U_R \rangle = -7.770 Q_{sp}^2 + 37.127 Q_{sp}$ ($R^2 = 0.9875$).

From the results, the coefficients of the quadratic formula were varied significantly with respect to hematocrit. However, the base solution (i.e., $1\times$ PBS, or plasma) did not contribute to changing the coefficients of the regression formula. Using regression formulae between Q_{sp} and $\langle U_R \rangle$ (or $\langle U_B \rangle$) obtained in advance, the $\langle U_R \rangle$ or $\langle U_B \rangle$ obtained by conducting the μ PIV technique was converted into a flow rate (i.e., Q_B , Q_R , respectively).

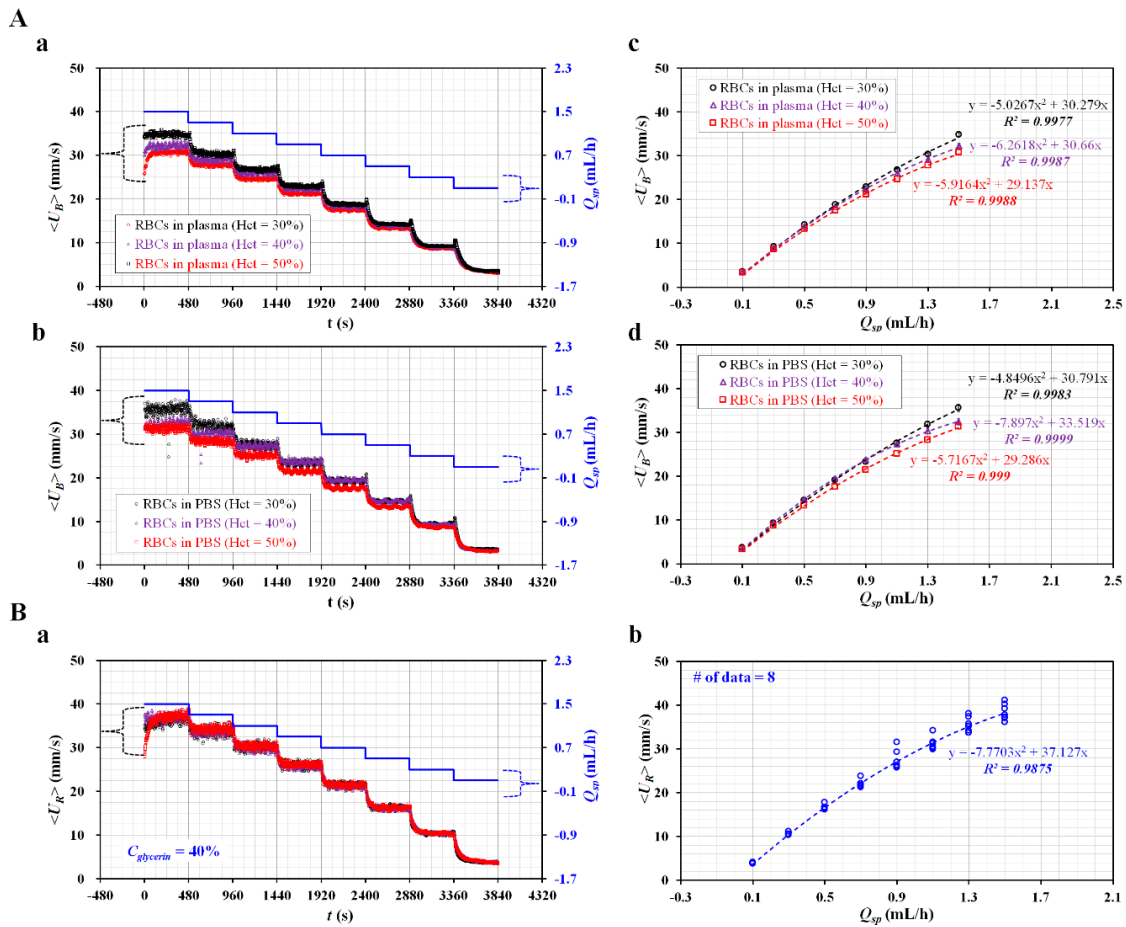


Figure 3. Calibration formula for the relationship between flow rate controlled by SP (Q_{sp}) and averaged velocity obtained by μ PIV technique ($\langle U \rangle$). Hematocrit (Hct) of blood was adjusted to $Hct = 30\%$, 40% , and 50% by adding normal RBCs into a base solution ($1\times$ PBS or plasma). With two syringe pumps, the flow rate of each fluid decreased stepwise from $Q_{sp} = 1.5$ mL/h to $Q_{sp} = 0.1$ mL/h at an interval of 0.2 mL/h. Each flow rate was maintained for 8 min. (A) Relationship between Q_{sp} and $\langle U_B \rangle$ with respect to hematocrit and base solution. (a) Temporal variations in $\langle U_B \rangle$ and Q_{sp} of blood sample (normal RBCs in plasma) with respect to Hct . (b) Temporal variations in $\langle U_B \rangle$ and Q_{sp} of blood sample (normal RBCs in $1\times$ PBS) with respect to Hct . (c) Regression formula between $\langle U_B \rangle$ and Q_{sp} of blood sample (normal RBCs in plasma) with respect to Hct . (d) Regression formula between $\langle U_B \rangle$ and Q_{sp} of blood sample (normal RBCs in $1\times$ PBS) with respect to Hct . (B) Calibration formula of relationship between Q_{sp} and $\langle U_R \rangle$ of reference fluid (40% glycerin solution with RBCs ($Hct = 7\%$)). (a) Temporal variations of Q_{sp} and $\langle U_R \rangle$. (b) Regression formula between $\langle U_B \rangle$ and Q_{sp} .

3.3. Quantitative Comparison of Blood Viscosity with Respect to Fluid Delivery System (ACS, SP)

Since the $\langle U_R \rangle$ and $\langle U_B \rangle$ obtained from the μ PIV technique were converted into flow rates (Q_R and Q_B) from regression formulae obtained in advance, the blood viscosity could be measured by monitoring the interface (α_B) in the co-flowing channel, under fluid delivery with an ACS. The blood viscosity obtained by the ACS was quantitatively compared with one obtained by an SP. Blood samples ($Hct = 30\%$, 40% , and 50%) were prepared by adding normal RBCs into the base solution ($1\times$ PBS, plasma).

Figure 4A-a showed the temporal variations of Q_R , Q_B , and α_B for the blood sample (normal RBCs in $1\times$ PBS, $Hct = 50\%$). In addition, Figure 4A-b depicted the temporal variations of Q_R , Q_B , and α_B for the blood sample (normal RBCs in plasma, $Hct = 50\%$). Using the blood viscosity formula, the blood viscosity was obtained by using the temporal variations of Q_R , Q_B , and α_B . Here, the viscosity of the reference fluid was given as $\mu_R = 4.08$ cP by using measurement results reported in previous

studies [14,51]. For a rectangular channel (width = w , depth = h) with a lower aspect ratio [32], the formula of shear rate ($\dot{\gamma}$) was given as approximately $\dot{\gamma} = \frac{6Q_B}{wh^2}$. The corresponding shear rate of the blood viscosity obtained at a specific blood flow rate (Q_B) was estimated by using the shear rate formula. A scatter plot was employed to plot μ_B on a vertical axis, and $\dot{\gamma}$ on a horizontal axis. As shown in Figure 4B-a, variations of μ_B were obtained with respect to the shear rate under fluid delivery with the two ACSs. Here, the blood sample ($Hct = 50\%$) was prepared by adding normal RBCs into plasma or $1\times$ PBS. The blood sample has behaved as a Newtonian fluid at sufficiently higher shear rates ($\dot{\gamma} > 10^3 \text{ s}^{-1}$). From the experimental results, μ_B remained constant with respect to the shear rate. By conducting an arithmetic average of μ_B over specific shear rates, the blood viscosity was expressed as $\langle \mu_B \rangle = \text{mean} \pm \text{standard deviation}$. The viscosity of the blood sample composed of plasma ($\langle \mu_{B, plasma} \rangle = 2.381 \pm 0.042 \text{ cP}$) was significantly higher than that of the blood sample composed of $1\times$ PBS ($\langle \mu_{B, PBS} \rangle = 1.845 \pm 0.0573 \text{ cP}$). To compare with the blood viscosity obtained under fluid delivery with two ACSs, the same blood samples were employed to measure the blood viscosity under fluid delivery with two SPs. Two fluids (blood sample, reference fluid) were delivered to each inlet of the microfluidic device, at the same flow rate ($Q_B = Q_R$).

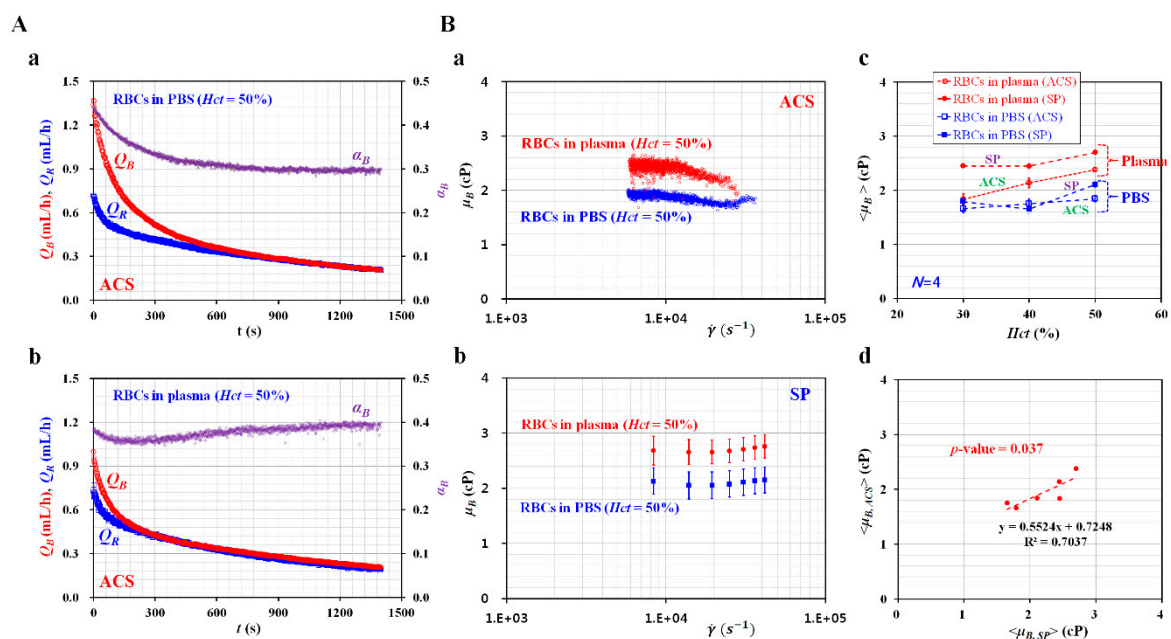


Figure 4. Quantitative comparison of blood viscosity for blood samples (normal RBCs in plasma and PBS, $Hct = 50\%$) with respect to the fluid delivery system (ACS, SP). **(A)** Variations of flow rates (Q_B , Q_R) and interface (α_B) with respect to the base solution ($1\times$ PBS, plasma). **(a)** Temporal variations of Q_B , Q_R , and α_B for a blood sample (normal RBCs in $1\times$ PBS, and $Hct = 50\%$). **(b)** Temporal variations of Q_B , Q_R , and α_B for a blood sample (normal RBCs in plasma, and $Hct = 50\%$). **(B)** Variation of blood viscosity depending on the base solution, hematocrit, and fluid delivery system (ACS and SP). **(a)** Variations of blood viscosity (μ_B) of blood samples with respect to the base solution ($1\times$ PBS, plasma) and shear rate under fluid delivery of ACS. **(b)** Variations of μ_B with respect to the base solution ($1\times$ PBS, plasma) and shear rate under fluid delivery of two SPs. **(c)** Variations of $\langle \mu_B \rangle$ with respect to base solution ($1\times$ PBS, plasma), hematocrit ($Hct = 30\%$, 40% , and 50%), and fluid delivery system (ACS, SP). $\langle \mu_B \rangle$ was quantified as $\langle \mu_B \rangle = \text{mean} \pm \text{standard deviation}$ by conducting an arithmetic average of μ_B obtained over shear rates. **(d)** Correlation between blood viscosity obtained under ACS ($\langle \mu_{B, ACS} \rangle$) and blood viscosity obtained under SP ($\langle \mu_{B, SP} \rangle$).

As represented in Figure 3A-a and Figure 3A-b, the flow rate of the SP (Q_{sp}) decreased stepwise from $Q_{sp} = 1.5 \text{ mL/h}$ to $Q_{sp} = 0.1 \text{ mL/h}$ at an interval of 0.2 mL/h . Each flow rate had been maintained for 8 min. As shown in Figure 4B-b, variations in μ_B of the blood samples (normal RBCs in plasma

and 1× PBS, $Hct = 50\%$) were obtained with respect to the shear rate. The blood viscosity remained constant with respect to the shear rate. The viscosity of the blood sample composed of plasma ($\langle\mu_B, plasma\rangle = 2.728 \pm 0.0918$ cP) was higher than that of the blood sample composed of 1× PBS ($\langle\mu_B, PBS\rangle = 2.109 \pm 0.0429$ cP). When compared with the blood viscosity obtained by the ACS, blood viscosity obtained by the SP increased by approximately 12.5%. To determine the effects of hematocrit on blood viscosity, variations of blood viscosity were obtained by varying the hematocrit ($Hct = 30\%$, 40% , and 50%), base solution (1× PBS, plasma), and fluid delivery system (ACS, SP). Figure 4B-c showed the variations of $\langle\mu_B\rangle$ with respect to Hct , base solution, and the fluid delivery system. Under fluid delivery with an ACS, $\langle\mu_B\rangle$ tended to increase with respect to Hct . Under fluid delivery with an SP, there was no significant difference between $Hct = 30\%$ and $Hct = 40\%$. The blood viscosity increased at $Hct = 50\%$ when compared with $Hct = 30\%$ or 40% . To determine the correlation between the blood viscosity obtained by the ACS ($\langle\mu_B, ACS\rangle$) and the blood viscosity obtained by the SP ($\langle\mu_B, SP\rangle$), a scatterplot was used to plot $\langle\mu_B, ACS\rangle$ on a vertical axis, and $\langle\mu_B, SP\rangle$ on a horizontal axis, as shown in Figure 4B-d. According to a linear regression analysis, $\langle\mu_B, ACS\rangle$ was expressed as $\langle\mu_B, ACS\rangle = 0.5524 \langle\mu_B, SP\rangle + 0.7248$ ($R^2 = 0.7037$, p -value = 0.037). Here, p -value = 0.037 indicated that a linear regression showed sufficient relationship between two viscosity values (i.e., $\langle\mu_B, ACS\rangle$ vs. $\langle\mu_B, SP\rangle$). In addition, R^2 was obtained as a high value of $R^2 = 0.7037$. Although two SPs were effectively used to deliver two fluids during measurement of blood viscosity, the arrangement included challenges, such as a bulky size and a high cost. From the correlation between $\langle\mu_B, ACS\rangle$ and $\langle\mu_B, SP\rangle$, it was found that the ACS can be effectively employed to deliver two fluids in the measurement of blood viscosity. Thus, the blood viscosity can be measured consistently under fluid delivery with two ACSs.

3.4. Quantitative Measurement of ESR with Respect to base Solution and Hematocrit

The ESR of the blood sample was evaluated by quantifying the microscopic image intensity of the blood sample ($\langle I_B \rangle$) flowing in the blood channel. Two ESR indices (t_{ESR} , I_{ESR}) were suggested by quantifying the temporal variations of $\langle I_B \rangle$. The blood samples ($Hct = 30\%$, 40% , and 50%) were prepared by adding normal RBCs into a base solution (1× PBS, plasma).

As shown in Figure 5A-a, variations of $\langle I_B \rangle$ for the blood sample (normal RBCs in plasma) were obtained with respect to Hct . $\langle I_B \rangle$ tended to decrease at higher values of Hct . In addition, T_{st} tended to be shorter at lower values of the hematocrit. To exclude the contribution of plasma protein to the ESR, the plasma was replaced with the 1× PBS. As shown in Figure 5A-b, temporal variations of $\langle I_B \rangle$ for the blood sample (normal RBCs in 1× PBS) were obtained by varying Hct . $\langle I_B \rangle$ tended to decrease at higher values of Hct . With a certain elapse of time, $\langle I_B \rangle$ remained constant. There was no existence of separation time within 2000 s (i.e., $T_{st} > 2000$ s). The results indicated that the 1× PBS did not sufficiently contribute to enhancing ESR when compared with plasma.

To quantify the ESR of the blood sample (normal RBCs in plasma) from $\langle I_B \rangle$ as shown in Figure 5A-a, two ESR indices (t_{ESR} , I_{ESR}) were obtained with respect to the hematocrit. Figure 5B-a showed variations of t_{ESR} and I_{ESR} with respect to Hct . According to the results, t_{ESR} tended to increase significantly with respect to hematocrit (p -value = 0.0004). I_{ESR} tended to decrease substantially with respect to hematocrit (p -value = 0.001). Under blood delivery with the ACS, the RBCs tended to fall down continuously inside the ACS, which was installed horizontally. Owing to the continuous ESR inside the ACS, the populations of RBCs delivered to the blood channel decreased over time. Thus, $\langle I_B \rangle$ increased gradually over time, as shown in Figure 5A-a. However, when the plasma was replaced with the 1× PBS, the blood sample did not exhibit an ESR inside the ACS. For this reason, after a certain period of time, $\langle I_B \rangle$ remained constant over time, as shown in Figure 5A-b. To quantitatively compare with results reported in a previous study, two indices (t_{ESR} , I_{ESR}) and S_{EAI} (previous ESR index) [45] were plotted on a vertical axis and horizontal axis, respectively. S_{EAI} exhibited larger scatters than t_{ESR} or I_{ESR} . From the regression analysis, the linear regression exhibited higher values of $R^2 = 0.7474 \sim 0.7755$. The results indicated that the two ESR indices exhibited consistent variations

with respect to hematocrit when compared with S_{EAI} . Thus, the two ESR indices (t_{ESR} , I_{ESR}) can be effectively used to evaluate the variation of ESR with respect to hematocrit.

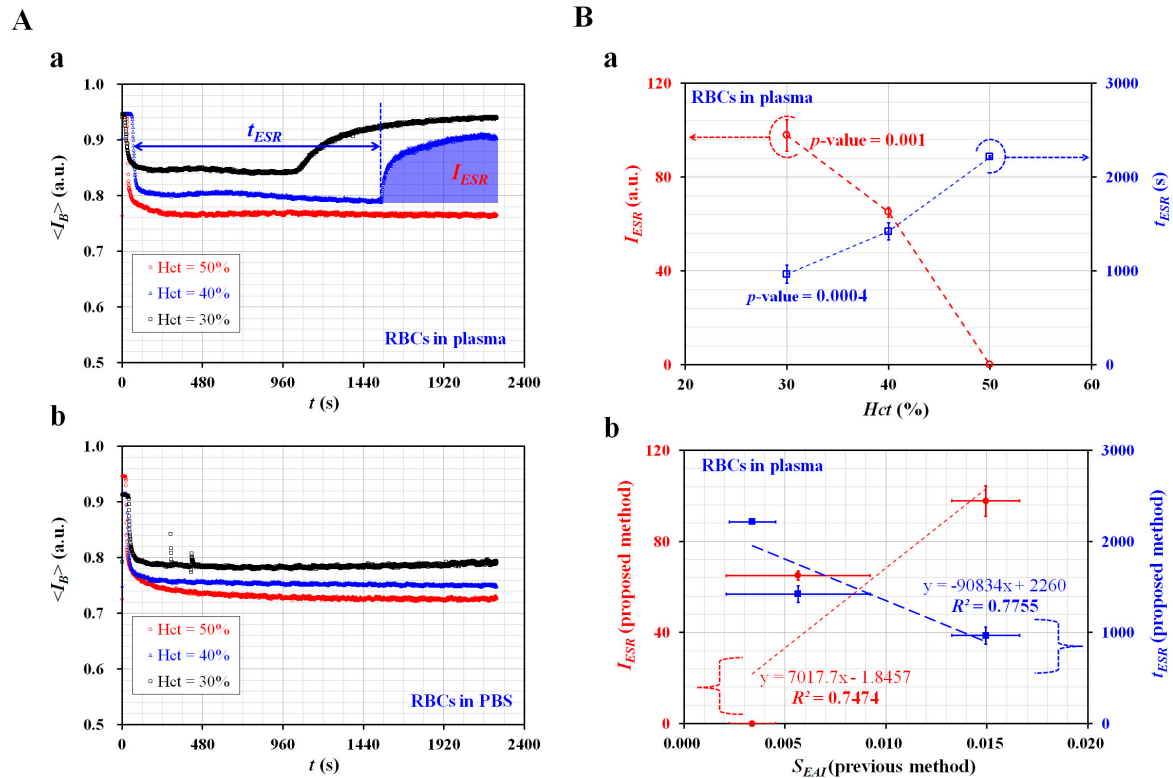


Figure 5. Evaluation of ESR for blood samples with respect to base solutions (1× PBS, and plasma) and hematocrit ($Hct = 30\%$, 40% , and 50%). (A) Variations of $\langle I_B \rangle$ with respect to base solution and hematocrit. (a) Temporal variations of $\langle I_B \rangle$ of blood sample (normal RBCs in plasma) with respect to Hct . (b) Temporal variations of $\langle I_B \rangle$ of blood sample (normal RBCs in 1× PBS) with respect to Hct . (B) Variations of two ESR indices (t_{ESR} , I_{ESR}) for blood sample (normal RBCs in plasma) with respect to Hct . (a) Variations of t_{ESR} and I_{ESR} with respect to Hct . (b) Correlation between proposed ESR indices (t_{ESR} , I_{ESR}) and previous ESR index (S_{EAI}).

3.5. Variations of Blood Viscosity and ESR for Blood Samples Composed of Specific Dextran Solutions

A specific dextran solution as a base solution was prepared to enhance the ESR of the blood sample. To exclude the contributions of hematocrit to ESR, the hematocrit of the blood sample was adjusted to $Hct = 50\%$. The blood samples were prepared by adding normal RBCs into specific concentrations of dextran solution (i.e., $C_{dex} = 0, 5, 10, 15,$ and 20 mg/mL). $C_{dex} = 0$ meant 1× PBS as control. As shown in Figure 6A-a, temporal variations of Q_B were obtained with respect to C_{dex} . From the results, the blood sample composed of dextran solution ($C_{dex} \leq 5$ mg/mL) exhibited stable variations of Q_B over time. However, above $C_{dex} \geq 10$ mg/mL, the separation time (T_{st}) tended to reduce at higher concentrations of the dextran solution. Figure 6A-b showed temporal variations of α_B with respect to C_{dex} . Similar to the case with Q_B , α_B varied unstably above $C_{dex} \geq 10$ mg/mL. T_{st} tended to be shorter at higher concentrations of the dextran solution. By using stable variations of Q_B and α_B obtained at $t < T_{st}$, variations of μ_B were obtained with respect to the shear rate. As shown in Figure 6A-c, blood viscosities were obtained at sufficiently higher shear rates ($\dot{\gamma} > 10^3$ s⁻¹). They remained constant with respect to the shear rate. Additionally, the blood viscosity tended to increase at higher concentrations of the dextran solution. By averaging the μ_B values obtained at shear rates, the blood viscosity was expressed as $\langle \mu_B \rangle = \text{mean} \pm \text{standard deviation}$. Figure 6A-d showed variations of $\langle \mu_B \rangle$ with respect to C_{dex} and the fluid delivery system (ACS, SP). When compared with the results reported in a previous study [45], the present results exhibited sufficiently consistent variations of $\langle \mu_B \rangle$ with respect to C_{dex} .

In addition, there was no significant difference between the ACS and SP. As shown in Figure 6A-e, to determine the correlation between $\langle\mu_B\rangle$ obtained by the proposed method (two ACSs) and μ_B obtained by the previous method (two SPs) [45], a scatter plot was used to plot $\langle\mu_B\rangle$ (proposed method) on a vertical axis and μ_B (previous method) on a horizontal axis. According to linear regression analysis, the high value of $R^2 = 0.9767$ indicated that the proposed method could give comparable results when compared with the previous method. Thus, ACSs could be effectively employed to deliver fluid samples. After measuring the blood viscosity with respect to C_{dex} , the contributions of the dextran solution to the ESR were evaluated by quantifying the image intensity of the blood sample flowing in the blood channel ($\langle I_B \rangle$). As shown in Figure 6B-a, temporal variations of $\langle I_B \rangle$ were obtained with respect to C_{dex} . As a result, T_{st} was reduced at higher concentrations of the dextran solution. Using $\langle I_B \rangle$ with respect to C_{dex} , two ESR indices (t_{ESR} , I_{ESR}) were obtained with respect to C_{dex} . As shown in Figure 6B-b, the ESR indices remained constant up to $C_{dex} = 5$ mg/mL. Above $C_{dex} \geq 10$ mg/mL, t_{ESR} tended to decrease substantially with respect to C_{dex} (p -value = 0.0001). I_{ESR} increased largely at higher concentrations of dextran solution (p -value = 0.0001). To compare with the results reported in a previous study [45], a scatterplot was used to plot t_{ESR} and I_{ESR} (i.e., proposed method) on a vertical axis, and S_{EAI} (i.e., previous method: periodic on-off control with an SP) on a horizontal axis. As shown in Figure 6B-c, a linear regression analysis was conducted to determine the correlation between the proposed method and the previous method. The higher value of $R^2 = 0.8202$ – 0.8548 indicated that the two ESR indices (t_{ESR} , I_{ESR}) gave comparable results when compared with the previous method. Thus, the ESR indices can be effectively used to quantify the ESRs of blood samples.

3.6. Variations of Blood Viscosity and ESR for Blood Samples Composed of Hardened RBCs

As the last demonstration, the proposed method was applied to evaluate the contribution of hardened RBCs to the ESR. As shown in Figure 5A-a, a blood sample ($Hct = 50\%$) composed of plasma did not contribute to variations in the ESR. To stimulate the ESR of a blood sample with a high value of $Hct = 50\%$, the plasma as a base solution was replaced with a specific concentration of dextran solution (i.e., $C_{dex} = 15$ mg/mL). Hardened RBCs were prepared by sufficiently exposing normal RBCs to specific concentrations of GA solution (C_{GA}) (i.e., $C_{GA} = 0, 5, 10,$ and 15 $\mu\text{L/mL}$). $C_{GA} = 0$ indicated normal RBCs as control. The blood samples ($Hct = 50\%$) were then prepared by adding hardened RBCs into the specific dextran solutions.

Figure 7A showed the temporal variations of Q_B with respect to C_{GA} . T_{st} tended to increase at higher concentrations of the GA solution. At $C_{GA} = 15$ $\mu\text{L/mL}$, Q_B tended to decrease stably over time. Figure 7B showed the temporal variations of α_B with respect to C_{GA} . The variations of α_B were very similar to those of Q_B . At $C_{GA} = 15$ $\mu\text{L/mL}$, α_B remained constant after a certain period of time. Figure 7C showed the temporal variations of $\langle I_B \rangle$ with respect to C_{GA} . Except for at $C_{GA} = 15$ $\mu\text{L/mL}$, $\langle I_B \rangle$ tended to increase stably over time. Additionally, T_{st} tended to increase at higher concentrations of the GA solution. By measuring three factors (Q_B , α_B , and $\langle I_B \rangle$) simultaneously, the hardened blood sample composed of hardened RBCs fixed with $C_{GA} = 15$ $\mu\text{L/mL}$ did not exhibit an ESR inside the ACS. Thus, there were no significant variations of Q_B and α_B . As shown in Figure 7D, variations of $\langle\mu_B\rangle$ were obtained with respect to C_{GA} . $\langle\mu_B\rangle$ tended to increase considerably with respect to C_{GA} . As the GA solution contributed to stiffening the RBCs' membranes, it was reasonable that the blood viscosity increased at higher concentrations of the GA solution. Figure 7E showed variations of the two ESR indices (t_{ESR} , I_{ESR}) with respect to C_{GA} . t_{ESR} tended to increase with respect to C_{GA} . I_{ESR} tended to decrease with respect to C_{GA} .

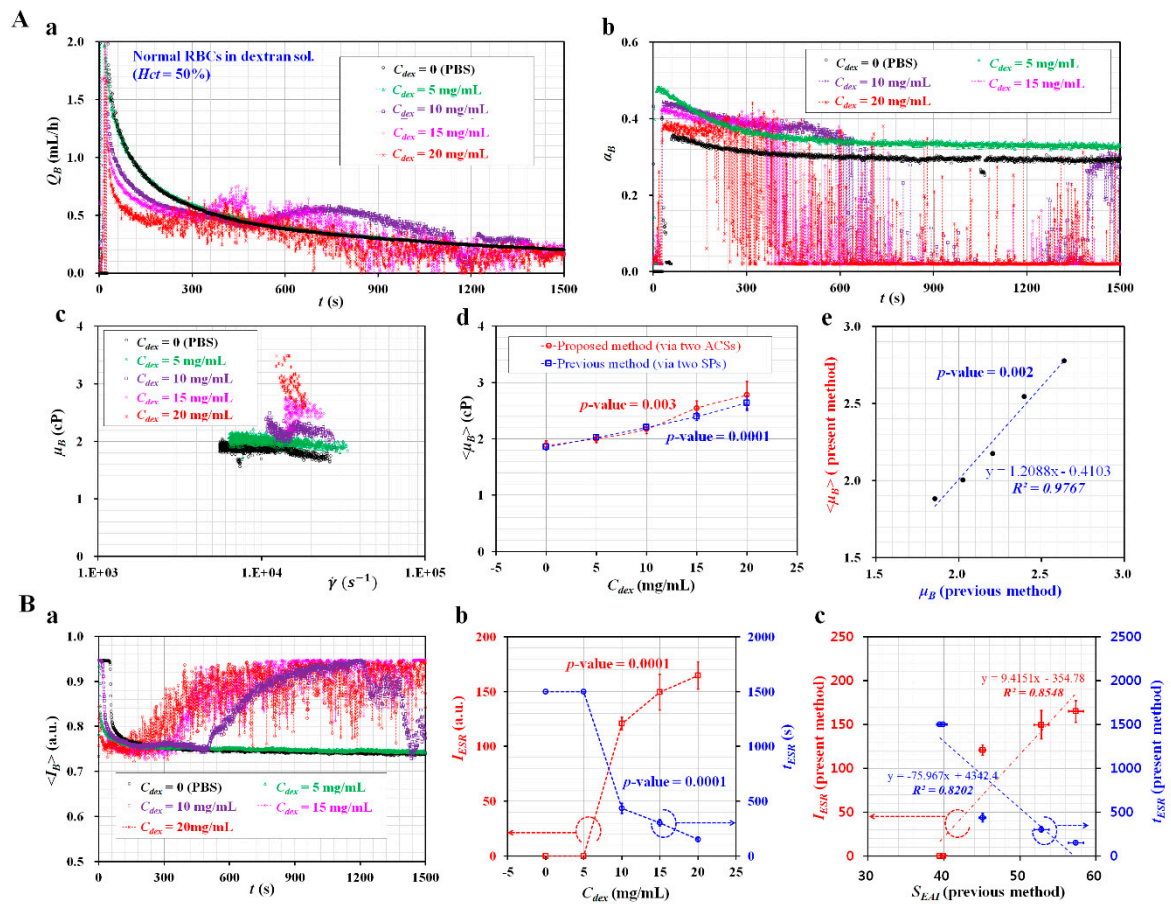


Figure 6. Measurement of blood viscosity and ESR for blood samples composed of specific concentrations of dextran solution. Blood samples ($Hct = 50\%$) were prepared by adding normal RBCs into various concentration of dextran solution (C_{dex}) (i.e., $C_{dex} = 0, 5, 10, 15,$ and 20 mg/mL). $C_{dex} = 0$ meant $1 \times$ PBS as control. **(A)** Variations of blood viscosity with respect to C_{dex} . **(a)** Temporal variations of Q_B with respect to C_{dex} . **(b)** Temporal variations of α_B with respect to C_{dex} . **(c)** Variations of μ_B with respect to shear rate and C_{dex} . **(d)** Variations of $\langle \mu_B \rangle$ with respect to the C_{dex} and fluid delivery system (ACS, SP). **(e)** Correlation between blood viscosity obtained by the proposed method and blood viscosity obtained by the previous method. **(B)** Variations of ESR with respect to C_{dex} . **(a)** Temporal variations of $\langle I_B \rangle$ with respect to C_{dex} . **(b)** Variations of two ESR indices (t_{ESR}, I_{ESR}) with respect to C_{dex} . **(c)** Quantitative comparison between the proposed method (t_{ESR}, I_{ESR}) and previous method (S_{EAI}).

From the experimental results, it was found that the GA solution caused an increase in blood viscosity. Furthermore, the proposed method had the ability to consistently measure blood viscosity and ESR, under simultaneously fluid delivery from two ACSs.

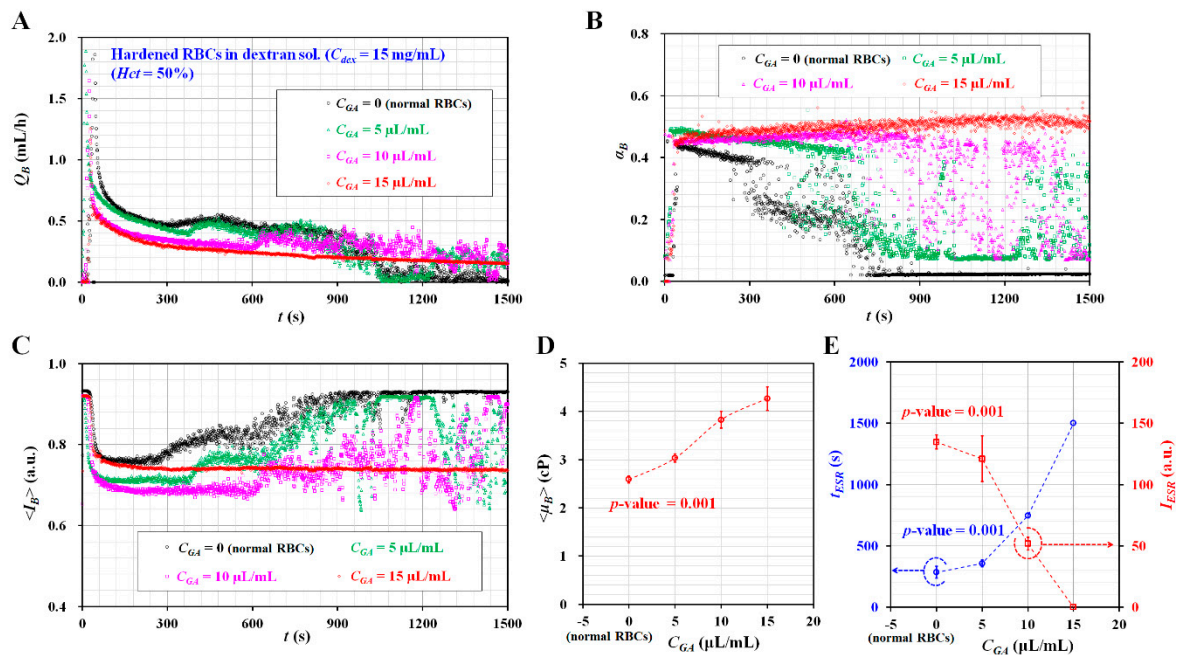


Figure 7. Measurement of blood viscosity and ESR and blood viscosity for blood samples composed of hardened RBCs with glutaraldehyde (GA) solution. To prepare hardened RBCs from normal RBCs, normal RBCs were sufficiently exposed to specific concentrations of GA solution (C_{GA}) ($C_{GA} = 0, 5, 10,$ and $15 \mu\text{L/mL}$). $C_{GA} = 0$ meant normal RBCs as control. Blood sample ($Hct = 50\%$) was prepared by adding hardened RBCs into the dextran solution ($C_{dex} = 15 \text{ mg/mL}$). (A) Temporal variations of Q_B with respect to C_{GA} . (B) Temporal variations of α_B with respect to C_{GA} . (C) Temporal variations of $\langle I_B \rangle$ with respect to C_{GA} . (D) Variations of $\langle \mu_B \rangle$ with respect to C_{GA} . (E) Variations of two ESR indices (t_{ESR}, I_{ESR}) with respect to C_{GA} .

4. Conclusions

In this study, a simple method of measuring blood viscosity and ESR was demonstrated by quantifying averaged velocities of a blood sample and reference fluid, where the blood sample and reference fluid were delivered to a microfluidic device with two ACSs. According to the experimental results, a 40% glycerin solution with RBCs ($Hct = 7\%$) was selected as the reference fluid to obtain velocity fields and avoid sedimentation of RBCs in the ACS. Using a calibration formulae between the flow rate of an SP (Q_{sp}) and the averaged velocity obtained by the μPIV technique ($\langle U_B \rangle$) in advance, $\langle U_B \rangle$ or $\langle U_R \rangle$ was converted into Q_B or Q_R , respectively. As a demonstration, the proposed method was employed to evaluate the contributions of the hematocrit ($Hct = 30\%, 40\%,$ and 50%), base solution ($1\times$ PBS, plasma, dextran solution), and hardened RBCs to the blood viscosity and ESR, respectively. The results of the proposed method were comparable with those reported in previous studies that used two SPs. From the experimental results, it could be concluded that the proposed method had the ability to consistently measure blood viscosity and ESR under simultaneous fluid delivery with two ACSs. However, image acquisition for quantifying blood flows in microfluidic channels was demonstrated from the optical microscope and a high-speed camera. To resolve the issue, the proposed method should be improved substantially by adopting a portable image acquisition system in the near future.

Funding: This work was supported by the Basic Science Research Program through the NRF, funded by the Ministry of Science and ICT (MSIT) (NRF–2018R1A1A1A05020389).

Conflicts of Interest: The authors declare no conflict of interest.

Appendix A.

Appendix A.1. Figure A1

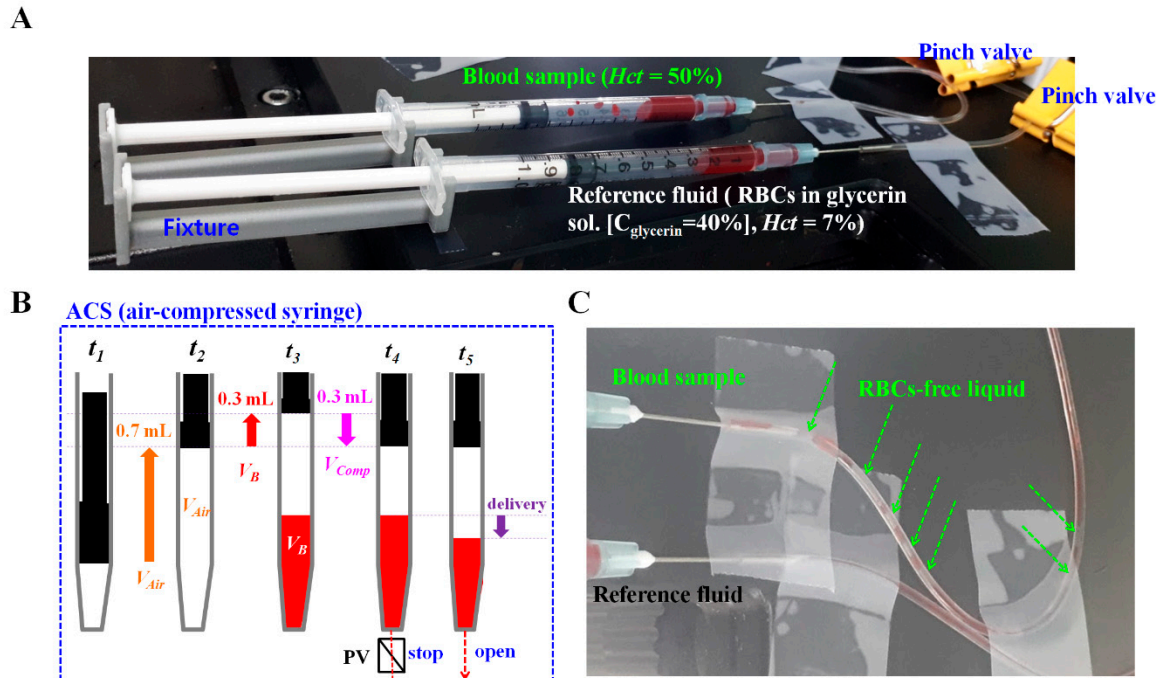


Figure A1. Fabrication and operation of the air-compressed syringe. (A) Two air-compressed syringes (ACSs) filled with blood sample ($Hct = 50\%$) and reference fluid (RBCs in 40% glycerin sol. [$Hct = 7\%$]). Each ACS was composed of a disposable syringe ($\sim 1\text{mL}$), a fixture, and a pinch valve. (B) Operation of ACS: piston movement at the lowest position forward at $t = t_1$, air suction ($V_{Air} = 0.7\text{ mL}$) by moving piston to 0.7 mL backward at $t = t_2$, blood suction by moving piston to 0.3 mL backward ($V_B = 0.3\text{ mL}$) at $t = t_3$, air compression by moving piston to 0.3 mL forward ($V_{comp} = 0.3\text{ mL}$) at $t = t_4$, and blood delivery by removing pinch valve at $t = t_5$. Similarly, the reference fluid was sucked into the syringe instead of blood. The remaining procedure was the same as blood delivery with the ACS. The blood sample and reference fluid were then delivered into the corresponding inlets with two ACSs. (C) Snapshots for showing RBC-free liquid in a tube under blood delivery using an ACS. Owing to the continuous erythrocyte sedimentation rate (ESR) inside the ACS, a red blood cell (RBC)-free liquid was observed in the microfluidic channel after a certain lapse of time.

Appendix A.2. Figure A2

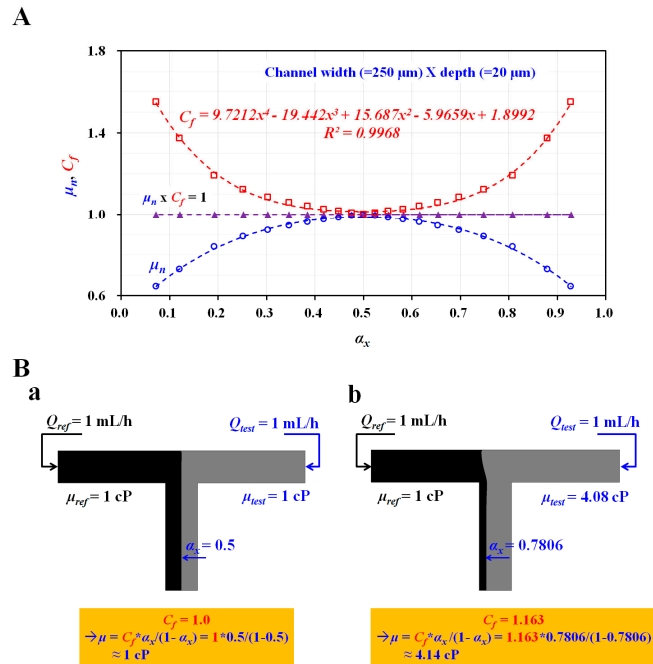


Figure A2. A correction factor of the parallel flow method estimated by conducting a numerical simulation. (A) The polynomial formula of a correction factor (C_f) estimated from a numerical simulation. (B) Numerical simulation results for showing interfacial location depending on the viscosity of test fluid. (a) $\alpha_x = 0.5$ for $\mu_{test} = 1$ cP. Viscosity of test fluid was estimated as 1 cP by considering correction factor of $C_f = 1$. (b) $\alpha_x = 0.7806$ for $\mu_{test} = 4.08$ cP. The viscosity of test fluid was estimated as 4.14 cP by considering the correction factor of $C_f = 1.163$.

Appendix A.3. Figure A3

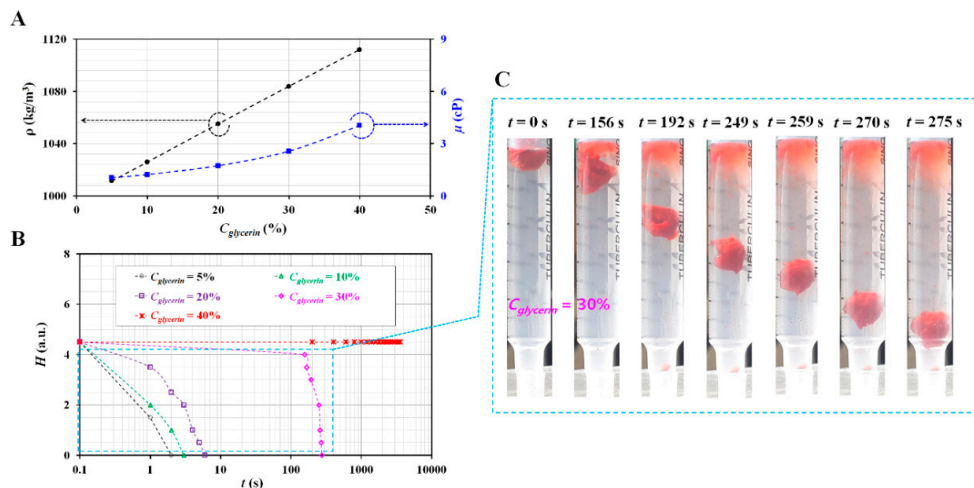


Figure A3. Selection of proper reference fluid by quantifying density (ρ) and sedimentation of RBCs droplet with respect to $C_{glycerin} = 5\%$, 10% , 20% , 30% , and 40% . (A) Variations of ρ and viscosity (μ) with respect to $C_{glycerin}$. (B) Temporal variation of sedimentation height (H) with respect to $C_{glycerin}$. (C) Snapshots for showing sedimentations of RBCs droplet with elapsed time (t) ($t = 0, 156, 192, 249, 259, 270, \text{ and } 275$ s). Here, the syringe was filled with a 30% glycerin solution.

Appendix A.4. Blood Sample Preparation

According to the protocol approved by the Ethics Committee of Chosun University Hospital (CUH) (CHOSUN 2018-05-11), all experimental procedures were conducted after confirming that the procedures involved were appropriate and humane.

Human concentrated RBCs and fresh frozen plasma (FFP) were purchased from the Gwangju-Chonnam blood bank (Gwangju, Korea). The concentrated RBCs and FFP were kept at 4 °C and −20 °C, respectively. The concentrated RBCs were preserved in an anticoagulant solution (i.e., citrate phosphate dextrose adenine [CPDA]). To remove the CPDA from the concentrated RBCs, washing procedures were performed twice. The concentrated RBCs (~20 mL) were mixed with phosphate-buffered saline (PBS) (1×, pH 7.4, Gibco, Life Technologies, New York, NY, USA) (~20 mL) in a 40 mL tube. After inserting the tube in a centrifuge (Allegra X-30R benchtop, Beckman Coulter, Brea, CA, USA), the centrifuge was set to 4000 rpm and was operated for 10 min. Owing to differences in density, the blood sample was distinctively separated into two layers (i.e., upper layer: liquid, and lower layer: RBCs) in the tube. Normal RBCs were collected after removing the liquid positioned in the upper layer. To completely remove the anticoagulant solution, a washing procedure was repeated twice. The FFP was thawed under a room temperature of 25 °C. For removing debris existing in the FFP, pure plasma was collected by passing the FFP through a syringe filter (mesh size = 5 µm, Minisart, Sartorius, and Germany). Finally, the normal RBCs and plasma were stored at 4 °C in a refrigerator before the experiment. Various blood samples were prepared by adding normal or hardened RBCs into a specific base solution. Except for experiments to determine the contributions of hematocrit to blood viscosity or ESR, the hematocrit of the blood sample was fixed at $Hct = 50\%$ for consistent measurement.

First, to evaluate the contributions of hematocrit to blood viscosity and ESR, the hematocrit of the blood sample was adjusted to $Hct = 30\%$, 40% , and 50% by adding normal RBCs into base solution (i.e., 1× PBS, and plasma). Second, to enhance the ESR in ACS, five different concentrations of dextran solution (i.e., $C_{dex} = 0, 5, 10, 15,$ and 20 mg/mL) were prepared by adding dextran powder (*Leuconostoc* spp., MW = 450–650 kDa, Sigma-Aldrich, USA) into 1× PBS. Then, blood samples ($Hct = 50\%$) were prepared by adding normal RBCs into specific concentrations of the dextran solution. Third, four concentrations of glutaraldehyde (GA) solution (i.e., $C_{GA} = 0, 5, 10,$ and 15 µL/mL) were diluted by mixing the GA solution (Grade II, 25% in H₂O, Sigma-Aldrich, USA) with 1× PBS. Homogeneous hardened RBCs were prepared by exposing normal RBCs to each concentration of the GA solution for 10 min. To enhance ESR in blood sample ($Hct = 50\%$) significantly, plasma was replaced with a specific concentration of dextran solution ($C_{dex} = 15$ mg/mL). A hardened blood sample ($Hct = 50\%$) was then prepared by adding homogeneous hardened RBCs into the specific dextran solution.

Appendix A.5. Variation of Velocity, Interface, and Viscosity with Respect to Relocation of Object Plane

Variations of velocity, interface, and viscosity were evaluated by moving an object plane (Z_f) in the depth direction. The object plane (Z_f) relocated from $Z_f = -60$ µm to $Z_f = 60$ µm at intervals of 15 µm. $Z_f = 0$ represented that the microscopic images were captured at the focus plane (i.e., the best conditions for focus). $Z_f > 0$ meant that the microfluidic device moved vertically and that the microscopic images were captured at an out-of-focus plane. $Z_f < 0$ meant that the microfluidic device moved in a gravitational direction and that the microscopic images were captured at the out-of-focus plane. The blood sample ($Hct = 50\%$) was prepared by adding normal RBCs in a 1× PBS. The reference fluid with RBCs ($Hct = 7\%$) was prepared by adding normal RBCs into a 40% glycerin solution. Using two SPs, the reference fluid or blood sample was delivered to the reference channel (i.e., right-side channel). Simultaneously, the 1× PBS was delivered to the blood channel (i.e., left-side channel). The flow rate of each fluid remained at a constant flow rate of 1 mL/h.

First, with respect to the blood sample, the contribution of the object plane to velocity fields and viscosity was evaluated with respect to the relocation of the object plane. As shown in Figure A4-(A-a),

variations of the velocity profile of the blood sample (U_B) across the reference channel width were obtained with respect to $Z_f = -60, -30, 0, 30,$ and $60 \mu\text{m}$. Using data sets of $n = 180$, each velocity was averaged and expressed as a mean \pm standard deviation. The inset of Figure A4-(A-a) depicted the velocity profile of blood flow (U_B) estimated from sequential microscopic images captured at the focal plane ($Z_f = 0$). When Z_f increased from $Z_f = 0$ to an out-of-focus plane, U_B tended to decrease. In other words, the velocity fields varied depending on the object plane.

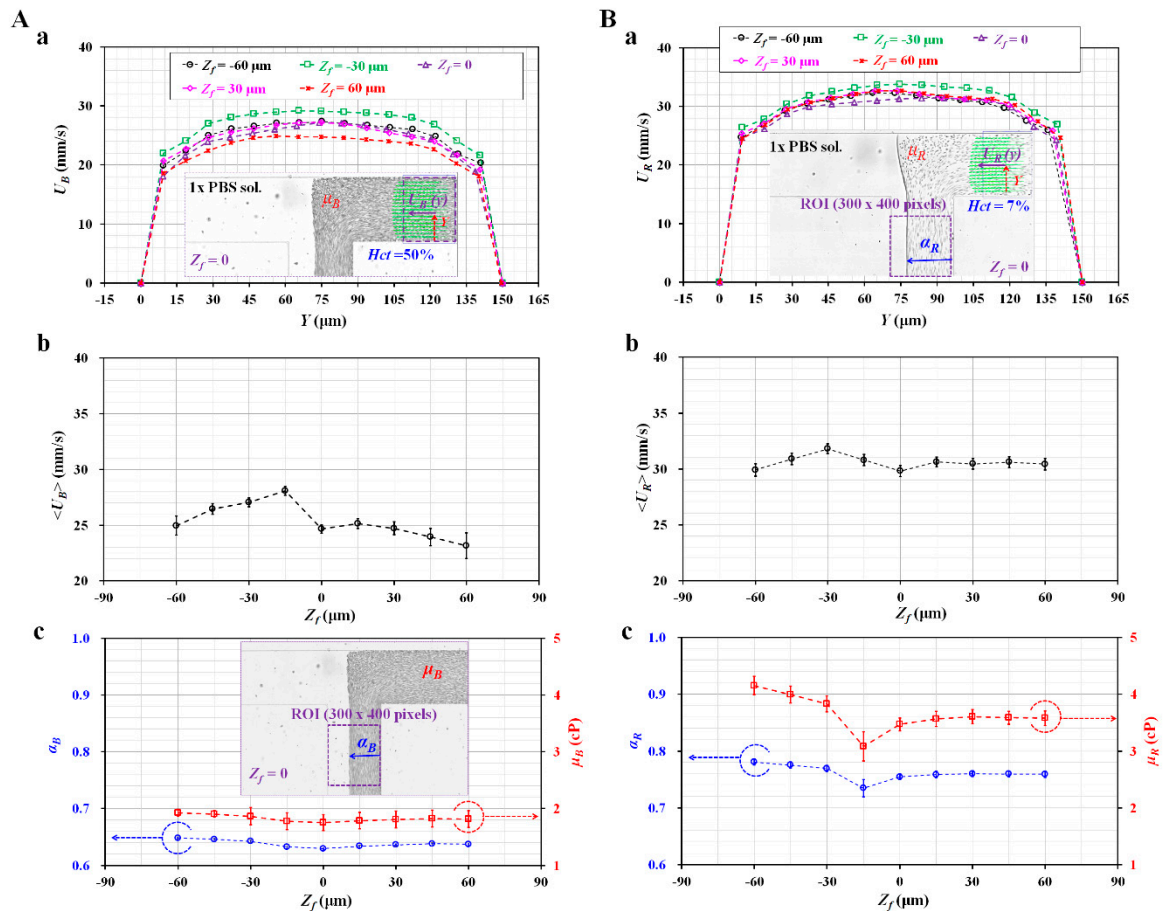


Figure A4. Effect of the relocation of object plane (Z_f) on velocity, interface, and viscosity with respect to the blood sample and reference fluid. A blood sample ($Hct = 50\%$) was prepared by adding normal RBCs into a $1\times$ PBS. A reference fluid with RBCs ($Hct = 7\%$) was prepared by adding normal RBCs into a 40% glycerin solution. Both fluids were delivered to inlets at a constant flow rate of 1 mL/h with two SPs. (A) Effects of the relocation of object plane on velocity, interface, and viscosity for the blood sample. (a) Variations of U_B across reference channel width with respect to $Z_f = -60, -30, 0, 30,$ and $60 \mu\text{m}$. The inset depicted the velocity profile of the blood sample flowing in the reference channel at $Z_f = 0$. (b) Variations of $\langle U_B \rangle$ with respect to Z_f . (c) Variations of α_B and μ_B with respect to Z_f . The inset showed interfacial location (α_B) at $Z_f = 0$. (B) Effect of the relocation of object plane on velocity, interface, and viscosity for reference fluid with RBCs ($Hct = 7\%$). (a) Variations of U_R across reference channel width with respect to $Z_f = -60, -30, 0, 30,$ and $60 \mu\text{m}$. The inset represented U_R and α_R at $Z_f = 0$. (b) Variations of $\langle U_R \rangle$ with respect to Z_f . (c) Variations of α_R and μ_R with respect to Z_f .

Based on an analytical formula for a depth of correlation (DOC) suggested in a previous study [53], the DOC was estimated as $33.9 \mu\text{m}$. Since the DOC was sufficiently higher than the channel depth of $20 \mu\text{m}$ (i.e., $\text{DOC} > \text{depth}$), all RBCs in the microfluidic channel could contribute to calculating the velocity fields uniformly. According to the estimated DOC, the μPIV technique measured averaged velocity

fields in the depth direction at the focal plane ($Z_f = 0$). The averaged velocities of the blood sample and reference fluid ($\langle U_R \rangle$, and $\langle U_B \rangle$) were calculated as an arithmetic average over the specific ROI.

Figure A4-(A-b) showed variations of $\langle U_B \rangle$ with respect to Z_f . When Z_f increased from the focal plane ($Z_f = 0$) to an out-of-focus plane, $\langle U_B \rangle$ tended to gradually decrease. The averaged blood velocity ($\langle U_B \rangle$) remained constant from $Z_f = 0$ to $Z_f = 30 \mu\text{m}$. From the results, $\langle U_B \rangle$ remained constant until the microfluidic device moved vertically with regard to DOC. In that regard, when Z_f decreased from $Z_f = -15 \mu\text{m}$, $\langle U_B \rangle$ tended to gradually decrease.

Figure A4-(A-c) showed variations of α_B and μ_B with respect to Z_f . The inset of Figure A4 (A-c) showed the interfacial location of blood flow (α_B) in a microscopic image captured at the focal plane ($Z_f = 0$). The blood viscosity (μ_B) was obtained by inserting α_B into the viscosity formula as reported in previous studies [32,33]. As α_B and μ_B remained constant with respect to Z_f , the relocation of the object plane did not contribute to varying the blood viscosity.

Second, with respect to the reference fluid with RBCs ($Hct = 7\%$), the effects of the object plane on velocity and viscosity were evaluated by quantifying variations of the velocity fields and viscosity when the object plane moved vertically. As shown in Figure A4-(B-a), variations of velocity profile (U_R) were obtained with respect to $Z_f = -60, -30, 0, 30$, and $60 \mu\text{m}$. The inset of Figure A4-(B-a) represented U_R at the focal plane ($Z_f = 0$). Except for $Z_f = -30 \mu\text{m}$, the relocation of the object plane did not contribute to varying significant variations of $\langle U_R \rangle$. Figure A4-(B-b) showed variations of $\langle U_R \rangle$ with respect to Z_f . When Z_f relocated vertically from the focal plane ($Z_f = 0$), $\langle U_R \rangle$ remained constant with respect to Z_f . From the results, $\langle U_R \rangle$ remained constant, even though the object plane relocated vertically outside the DOC. However, when Z_f relocated in a gravitational direction from the focal plane ($Z_f = 0$), $\langle U_R \rangle$ fluctuated along the object plane. As shown in Figure A4-(B-c), variations of α_R and μ_R were obtained with respect to Z_f . Similar to $\langle U_R \rangle$, α_R and μ_R remained constant when Z_f relocated in the vertical depth direction. However, α_R and μ_R exhibited large fluctuations and increased when relocating Z_f in a gravitational direction.

From these experimental results, it was found that the averaged velocities of the blood sample and reference fluid ($\langle U_B \rangle$, and $\langle U_R \rangle$) remained constant throughout the relocation of the object plane outside the DOC. In other words, when a microfluidic device moved up to the DOC vertically, the averaged velocity and interface remained constant. However, when a microfluidic device moved in the gravitational direction, it contributed to fluctuations of velocity, interface, and viscosity. For consistent measurement of velocity fields and the interfacial location, a microfluidic device was positioned at $Z_f = 0\text{--}30 \mu\text{m}$. In other words, a microscopic image was then captured at the focus plane or at a slightly out-of-focus plane.

References

1. Popel, A.S.; Johnson, P.C. Microcirculation and hemorrheology. *Annu. Rev. Fluid Mech.* **2005**, *37*, 43–69. [CrossRef] [PubMed]
2. Lipowsky, H.H. Microvascular Rheology and Hemodynamics. *Microcirculation* **2005**, *12*, 5–15. [CrossRef]
3. Danesh, J.; Collins, R.; Peto, R.; Lowe, G.D.O. Haematocrit, viscosity, erythrocyte sedimentation rate: Meta-analyses of prospective studies of coronary heart disease. *Eur. Heart J.* **2000**, *21*, 515–520. [CrossRef] [PubMed]
4. Jones, C.M.; Baker-Groberg, S.M.; Cianchetti, F.A.; Glynn, J.J.; Healy, L.D.; Lam, W.Y.; Nelson, J.W.; Parrish, D.C.; Phillips, K.G.; Scott-Drechsel, D.E.; et al. Measurement science in the circulatory system. *Cell Mol. Bioeng.* **2014**, *7*, 1–14. [CrossRef] [PubMed]
5. Oore-ofe, O.; Soma, P.; Buys, A.V.; Debusho, L.K.; Pretorius, E. Characterizing pathology in erythrocytes using morphological and biophysical membrane properties: Relation to impaired hemorrheology and cardiovascular function in rheumatoid arthritis. *Biochim. Biophys. Acta-Biomembr.* **2017**, *1859*, 2381–2391.
6. Kang, Y.J.; Lee, S.-J. In vitro and ex vivo measurement of the biophysical properties of blood using microfluidic platforms and animal models. *Analyst* **2018**, *143*, 2723–2749. [CrossRef]

7. Yeom, E.; Kim, H.M.; Park, J.H.; Choi, W.; Doh, J.; Lee, S.-J. Microfluidic system for monitoring temporal variations of hemorheological properties and platelet adhesion in LPS-injected rats. *Sci. Rep.* **2017**, *7*, 1801. [CrossRef]
8. Kang, Y.J.; Yeom, E.; Lee, S.-J. Microfluidic biosensor for monitoring temporal variations of hemorheological and hemodynamic properties using an extracorporeal rat bypass loop. *Anal. Chem.* **2013**, *85*, 10503–10511. [CrossRef]
9. Kang, Y.J.; Lee, S.-J. Blood viscoelasticity measurement using steady and transient flow controls of blood in a microfluidic analogue of Wheastone-bridge channel. *Biomicrofluidics* **2013**, *7*, 054122. [CrossRef]
10. Schmid-Schonbein, H.; Gaetgens, P.; Hirsch, H. On the shear rate dependence of red cell aggregation in vitro. *J. Clin. Investig.* **1968**, *47*, 1447–1454. [CrossRef]
11. Kim, B.J.; Lee, S.Y.; Jee, S.; Atajanov, A.; Yang, S. Micro-viscometer for measuring shear-varying blood viscosity over a wide-ranging shear rate. *Sensors* **2017**, *17*, 1442. [CrossRef] [PubMed]
12. Kang, Y.J.; Yang, S. Integrated microfluidic viscometer equipped with fluid temperature controller for measurement of viscosity in complex fluids. *Microfluid. Nanofluidics* **2013**, *14*, 657–668. [CrossRef]
13. Oh, S.; Kim, B.; Lee, J.K.; Choi, S. 3D-printed capillary circuits for rapid, low-cost, portable analysis of blood viscosity. *Sens. Actuator B Chem.* **2018**, *259*, 106–113. [CrossRef]
14. Kang, Y.J.; Ryu, J.; Lee, S.-J. Label-free viscosity measurement of complex fluids using reversal flow switching manipulation in a microfluidic channel. *Biomicrofluidics* **2013**, *7*, 044106. [CrossRef]
15. Khnouf, R.; Karasneh, D.; Abdulhay, E.; Abdelhay, A.; Sheng, W.; Fan, Z.H. Microfluidics-based device for the measurement of blood viscosity and its modeling based on shear rate, temperature, and heparin concentration. *Biomedical Microdevices* **2019**, *21*, 80. [CrossRef]
16. Isiksacan, Z.; Erel, O.; Elbuken, C. A portable microfluidic system for rapid measurement of the erythrocyte sedimentation rate. *Lab Chip* **2016**, *16*, 4682–4690. [CrossRef]
17. Zeng, N.F.; Mancuso, J.E.; Zivkovic, A.M.; Smilowitz, J.T.; Ristenpart, W.D. Red blood cells from individuals with abdominal obesity or metabolic abnormalities exhibit less deformability upon entering a constriction. *PLoS ONE* **2016**, *11*, e0156070. [CrossRef]
18. Guo, Q.; Duffy, S.P.; Matthews, K.; Deng, X.; Santoso, A.T.; Islamzada, E.; Ma, H. Deformability based sorting of red blood cells improves diagnostic sensitivity for malaria caused by Plasmodium falciparum. *Lab Chip* **2016**, *16*, 645–654. [CrossRef]
19. Berry, S.B.; Fernandes, S.C.; Rajaratnam, A.; DeChiara, N.S.; Mace, C.R. Measurement of the hematocrit using paper-based microfluidic devices. *Lab Chip* **2016**, *16*, 3689–3694. [CrossRef]
20. Kim, B.J.; Lee, Y.S.; Zhanov, A.; Yang, S. A physiometer for simultaneous measurement of whole blood viscosity and its determinants: Hematocrit and red blood cell deformability. *Analyst* **2019**, *144*, 3144–3157. [CrossRef]
21. Han, Z.; Tang, X.; Zheng, B. A PDMS viscometer for microliter Newtonian fluid. *J. Micromech. Microeng.* **2007**, *17*, 1828–1834. [CrossRef]
22. Srivastava, N.; Davenport, R.D.; Burns, M.A. Nanoliter Viscometer for Analyzing Blood Plasma and Other Liquid Samples. *Anal. Chem.* **2005**, *77*, 383–392. [CrossRef] [PubMed]
23. Kim, H.; Cho, Y.I.; Lee, D.-H.; Park, C.-M.; Moon, H.-W.; Hur, M.; Kim, J.Q.; Yun, Y.-M. Analytical performance evaluation of the scanning tube viscometer for measurement of whole blood viscosity. *Clin. Biochem.* **2013**, *46*, 139–142. [CrossRef] [PubMed]
24. Hong, H.; Song, J.M.; Yeom, E. 3D printed microfluidic viscometer based on the co-flowing stream. *Biomicrofluidics* **2019**, *13*, 014104. [CrossRef] [PubMed]
25. Kang, H.; Jang, I.; Song, S.; Bae, S.-C. Development of a paper-based viscometer for blood plasma using colorimetric analysis. *Anal. Chem.* **2019**, *91*, 4868–4875. [CrossRef]
26. Marinakis, G.N.; Barbenel, J.C.; Tsangaris, S.G. A new capillary viscometer for small samples of whole blood. *Proc. Inst. Mech. Eng.* **2002**, *216*, H1502. [CrossRef]
27. Solomon, D.E.; Abdel-Raziq, A.; Vanapalli, S.A. A stress-controlled microfluidic shear viscometer based on smartphone imaging. *Rheol. Acta* **2016**, *55*, 727–738. [CrossRef]
28. Kim, W.-J.; Kim, S.; Huh, C.; Kim, B.K.; Kim, Y.J. A novel hand-held viscometer applicable for point-of-care. *Sens. Actuator B Chem.* **2016**, *234*, 239–246. [CrossRef]

29. Pop, G.A.M.; Sisschops, L.L.A.; Iliev, B.; Struijk, P.C.; van der Heven, J.G.; Hoedemaekers, C.W.E. On-line blood viscosity monitoring in vivo with a central venous catheter using electrical impedance technique. *Biosens. Bioelectron.* **2013**, *41*, 595–601. [CrossRef]
30. Zeng, H.; Zhao, Y. Rheological analysis of non-Newtonian blood flow using a microfluidic device. *Sens. Actuator A Phys.* **2011**, *166*, 207–213. [CrossRef]
31. Li, Y.; Ward, K.R.; Burns, M.A. Viscosity measurements using microfluidic droplet length. *Anal. Chem.* **2017**, *89*, 3996–4006. [CrossRef] [PubMed]
32. Kang, Y.J. Periodic and simultaneous quantification of blood viscosity and red blood cell aggregation using a microfluidic platform under in-vitro closed-loop circulation. *Biomicrofluidics* **2018**, *12*, 024116. [CrossRef] [PubMed]
33. Kang, Y.J. Microfluidic-based technique for measuring RBC aggregation and blood viscosity in a continuous and simultaneous fashion. *Micromachines* **2018**, *9*, 467. [CrossRef] [PubMed]
34. Kang, Y.J.; Kim, B.J. Multiple and periodic measurement of RBC aggregation and ESR in parallel microfluidic channels under on-off blood flow control. *Micromachines* **2018**, *9*, 318. [CrossRef] [PubMed]
35. Nam, J.-H.; Yang, Y.; Chung, S.; Shin, S. Comparison of light-transmission and -backscattering methods in the measurement of red blood cell aggregation. *J. Biomed. Opt.* **2010**, *15*, 027003. [CrossRef]
36. Baskurt, O.K.; Uykulu, M.; Meiselman, H.J. Time Course of Electrical Impedance During Red Blood Cell Aggregation in a Glass Tube: Comparison with Light Transmittance. *IEEE Trans. Biomed. Eng.* **2010**, *57*, 969–978. [CrossRef]
37. Antonova, N.; Riha, P.; Ivanov, I. Time dependent variation of human blood conductivity as a method for an estimation of RBC aggregation. *Clin. Hemorheolo. Microcir.* **2008**, *39*, 69–78. [CrossRef]
38. Brust, M.; Aouane, O.; Thie'baud, M.; Flormann, D.; Verdier, C.; Kaestner, L.; Laschke, M.W.; Selmi, H.; Benyoussef, A.; Podgorski, T.; et al. The plasma protein fibrinogen stabilizes clusters of red blood cells in microcapillary flows. *Sci. Rep.* **2014**, *4*, 4348. [CrossRef]
39. Kaliviotis, E.; Sherwood, M.; Balabani, S. Partitioning of red blood cell aggregates in bifurcating microscale flows. *Sci. Rep.* **2017**, *7*, 44563. [CrossRef]
40. Tomaiuolo, G.; Lanotte, L.; Ghigliotti, G.; Misbah, C.; Guido, S. Red blood cell clustering in Poiseuille microcapillary flow. *Phys. Fluids* **2012**, *24*, 051903. [CrossRef]
41. Yeom, E.; Lee, S.-J. Microfluidic-based speckle analysis for sensitive measurement of erythrocyte aggregation: A comparison of four methods for detection of elevated erythrocyte aggregation in diabetic rat blood. *Biomicrofluidics* **2015**, *9*, 024110. [CrossRef]
42. Lee, K.; Kinnunen, M.; Khokhlova, M.D.; Lyubin, E.V.; Priezhev, A.V.; Meglinski, I.; Fedyanin, A.A. Optical tweezers study of red blood cell aggregation and disaggregation in plasma and protein solutions. *J. Biomed. Opt.* **2016**, *21*, 035001. [CrossRef]
43. Zhanov, A.; Yang, S. Effects of aggregation on blood sedimentation and conductivity. *PLoS ONE* **2015**, *10*, e0129337. [CrossRef]
44. Kang, Y.J.; Ha, Y.-R.; Lee, S.-J. Microfluidic-based measurement of erythrocyte sedimentation rate for biophysical assessment of blood in an in vivo malaria-infected mouse. *Biomicrofluidics* **2014**, *8*, 044114. [CrossRef]
45. Kang, Y.J. Microfluidic-based biosensor for sequential measurement of blood pressure and RBC aggregation over continuously varying blood flows. *Micromachines* **2019**, *10*, 577. [CrossRef]
46. Kang, Y.J. Simultaneous measurement of blood pressure and RBC aggregation by monitoring on-off blood flows supplied from a disposable air-compressed pump. *Analyst* **2019**, *144*, 3556–3566. [CrossRef]
47. Kang, Y.J. RBC deformability measurement based on variations of pressure in multiple micropillar channels during blood delivery using a disposable air-compressed pump. *Anal. Methods* **2018**, *10*, 4549–4561. [CrossRef]
48. Gao, J.X.; Yeo, L.P.; Chan-Park, M.B.; Miao, J.M.; Yan, Y.H.; Sun, J.B.; Lam, Y.C.; Yue, C.Y. Antistick postpassivation of high-aspect ratio silicon molds fabricated by deep-reactive ion etching. *J. Microelectromech. Syst.* **2006**, *15*, 84–93. [CrossRef]
49. Otsu, N. A threshold selection method from gray-level histograms. *IEEE Trans. Syst. Man. Cybern.* **1979**, *9*, 62–66. [CrossRef]
50. Kang, Y.J. Continuous and simultaneous measurement of the biophysical properties of blood in a microfluidic environment. *Analyst* **2016**, *141*, 6583–6597. [CrossRef]


51. Cheng, N.-S. Formula for the viscosity of a glycerol-water mixture. *Ind. Eng. Chem. Res.* **2008**, *47*, 3285–3288. [CrossRef]
52. Linderkamp, O.; Friederichs, E.; Boehler, T.; Ludwig, A. Age dependency of red blood cell deformability and density: Studies in transient erythroblastopenia of childhood. *Br. J. Haematol.* **1993**, *83*, 125–129. [CrossRef]
53. Bourdon, C.J.; Olsen, M.G.; Gorby, A.D. The depth of correction in micro-PIV for high numerical aperture and immersion objectives. *J. Fluid Eng. Trans. ASME* **2006**, *128*, 883–886. [CrossRef]



© 2020 by the author. Licensee MDPI, Basel, Switzerland. This article is an open access article distributed under the terms and conditions of the Creative Commons Attribution (CC BY) license (<http://creativecommons.org/licenses/by/4.0/>).

Article

Blood Viscoelasticity Measurement Using Interface Variations in Coflowing Streams under Pulsatile Blood Flows

Yang Jun Kang 

Department of Mechanical Engineering, Chosun University, 309 Pilmun-daero, Dong-gu, Gwangju 61452, Korea; jkang2011@chosun.ac.kr; Tel.: +82-62-230-7052

Received: 27 January 2020; Accepted: 26 February 2020; Published: 26 February 2020



Abstract: Blood flows in microcirculation are determined by the mechanical properties of blood samples, which have been used to screen the status or progress of diseases. To achieve this, it is necessary to measure the viscoelasticity of blood samples under a pulsatile blood condition. In this study, viscoelasticity measurement is demonstrated by quantifying interface variations in coflowing streams. To demonstrate the present method, a T-shaped microfluidic device is designed to have two inlets (a, b), one outlet (a), two guiding channels (blood sample channel, reference fluid channel), and one coflowing channel. Two syringe pumps are employed to infuse a blood sample at a sinusoidal flow rate. The reference fluid is supplied at a constant flow rate. Using a discrete fluidic circuit model, a first-order linear differential equation for the interface is derived by including two approximate factors ($F_1 = 1.094$, $F_2 = 1.1087$). The viscosity and compliance are derived analytically as viscoelasticity. The experimental results showed that compliance is influenced substantially by the period. The hematocrit and diluent contributed to the varying viscosity and compliance. The viscoelasticity varied substantially for red blood cells fixed with higher concentrations of glutaraldehyde solution. The experimental results showed that the present method has the ability to monitor the viscoelasticity of blood samples under a sinusoidal flow-rate pattern.

Keywords: viscoelasticity; microfluidic device; coflowing streams; interface; linear differential equation; two approximate factors

1. Introduction

Cardiovascular diseases (CVDs) occur without any symptoms and can lead to unexpected death [1]. In other words, blood clotting or abnormal blood flow contributes to vasculature blockages. Currently, biochemical properties (i.e., biomarkers [2,3] or DNA [4]) are used to diagnose CVDs. However, the biochemical approach has not been considered an effective tool for early detection of CVDs, because it does not provide information on blood flows or blood clotting. Instead of the biochemical approach, a biophysical approach is required to quantify abnormal blood flows in narrow-sized vessels. Blood samples collected from patients with CVDs or disorders exhibit changes in cells (i.e., red blood cells (RBCs) [5] or platelets [6]) or plasma proteins [3,7]. To detect CVDs effectively, it is necessary to quantify the contributions of cells or plasma proteins. Blood flows in microcirculation are determined by the mechanical properties of blood samples. In addition, blood vessel walls (i.e., shape and size) contribute to varying blood flows substantially. These properties include viscosity, elasticity, RBC aggregation, and RBC deformability. According to recent reports, a blood sample collected from a patient with CVD showed significantly different biophysical properties when compared with a normal blood sample [2,8,9]. For this reason, the mechanical properties of blood samples have been used to monitor the status or progress of CVDs. Additionally, the mechanical properties have been quantified under

dynamic blood flows [10]. Under ex vivo closed-circuit conditions, blood flows vary periodically over time. When a flow regulator is integrated into the fluidic circuit, a periodic flow pattern is regulated to a constant flow pattern [11]. The viscosity of the blood sample is then quantified by using reverse flow-switching phenomena under a constant blood flow. Additionally, blood viscosity is obtained by monitoring the interface in coflowing streams, while the flow rates of the blood sample and reference fluid remain constant at the same flow rate with two syringe pumps [12,13]. However, because the blood sample includes viscoelasticity (viscosity and elasticity) under a periodic flow condition, it is necessary to quantify the viscoelasticity of the blood sample without a flow regulator (i.e., periodic flow rate).

Recently, a microfluidic platform has been suggested for effectively manipulating a small volume of blood sample in microfluidic channels. A microfluidic channel has been used to investigate hemorheological properties of blood samples. Under a microfluidic platform, several techniques have been suggested to quantify the viscoelasticity of blood samples. Guido et al. have measured membrane viscoelasticity by measuring the velocity and shape of a single RBC in converging or diverging flow [14]. Kim et al. measured RBC stretching with viscoelastic cell focusing [15]. The method was then used to characterize differences in RBC deformability. Lee et al. measured the viscosity and elasticity of blood samples by infusing steady and transient blood flows sequentially [16]. The viscosity and time constant were obtained sequentially by controlling the flow rate of the reference fluid and blood sample, respectively. Here, the time constant was quantified by monitoring temporal variation of a bridge channel filled with a human blood sample at a transient blood flow. The elasticity of the blood sample was quantified by using the linear Maxwell model (elasticity = viscosity/time constant). Kang reported that viscosity and elasticity of blood samples can be obtained sequentially under a periodic on–off blood flow condition [17]. Monitoring the interface in a coflowing stream enabled blood viscoelasticity to be obtained at an interval of a specific period.

More recently, the author suggested a viscoelasticity measurement method under a sinusoidal blood flow rate ($Q_B(t)$) ($Q_B(t) = Q_\alpha + Q_\beta \sin(\omega t)$, where Q_α is the mean flow rate, Q_β is the alternating flow rate, and ω is the angular frequency of syringe pump) [18]. While the blood sample is infused periodically, the viscoelasticity of the blood sample is obtained by monitoring the interface in coflowing streams and by calculating the pulsatility index (PI) ($PI = 0.5 \times (Q_{max} - Q_{min})/Q_{ave}$, where Q_{max} is the maximum flow rate, Q_{min} is the minimum flow rate, and Q_{ave} is the average flow rate). A first-order differential equation for coflowing streams is derived by constructing a simple discrete fluidic circuit. Here, using a conventional microelectromechanical system technique, a microfluidic device has rectangular shape with an extremely low aspect ratio (aspect ratio = depth/width = 4/250) which is devised to compensate for the boundary condition difference between a real physical model and a mathematical condition. First, the viscosity of the blood sample is calculated by averaging the equation over a single period. Second, instead of an analytical solution of the equation, the time constant is obtained from the expression of PI . Variations of velocity and interface are required simultaneously to find out time constant of interface. The elasticity is then obtained with a linear Maxwell model. However, the differential equation does not include a correction factor (CF), which makes it necessary to compensate for the boundary condition difference between the real model and mathematical model under coflowing streams [19]. Additionally, the previous study did not use the analytical expression to obtain the viscoelasticity of a blood sample. At last, the method required variations of blood velocity over time. Nonetheless, the previous method shows promise for quantifying the viscoelasticity of blood samples under a periodic blood flow-rate pattern. It is extremely difficult to obtain the viscoelasticity of a blood sample circulated under an ex vivo or in vivo condition (i.e., a real and complex situation). As a preliminary study, it is necessary to develop a simple method for measuring viscoelasticity under a single sinusoidal flow patterns with a syringe pump.

In this study, to resolve these issues, a CF is inserted while deriving a differential equation for coflowing streams. Because the differential equation includes nonlinear terms, it is difficult to find an analytical solution. Conducting computational fluid dynamics (CFD) simulation enables an

approximate expression of the CF to be obtained. Then, two approximation factors (F_1, F_2) are suggested and calculated to convert nonlinear terms into linear terms. Analytical expressions of the viscoelasticity of blood samples are obtained by solving the differential equation. Here, viscosity and compliance are derived analytically. To demonstrate the present method, a T-shaped microfluidic channel is used. When measuring velocity fields of blood sample, a T-shaped microfluidic channel is not required to align a microscopic image in the horizontal or vertical direction. It consists two inlets, one outlet, two guiding channels (blood sample channel, reference fluid channel), and one coflowing channel. Using two syringe pumps, a blood sample is infused into the blood sample channel with a sinusoidal flow-rate pattern. A reference fluid is supplied into the reference fluid channel at a constant flow rate. By monitoring the interface of both fluids in the coflowing channel, the viscosity and compliance are obtained at an interval of a specific period. As a performance demonstration, the present method was used to evaluate the contributions of period (T), diluents (plasma, 1x phosphate-buffered saline (PBS)), and hematocrit (Hct) to viscoelasticity. The present method was then employed to quantify the viscoelasticity of a fixed blood sample prepared by adding fixed RBCs into plasma.

2. Materials and Methods

2.1. Blood Sample Preparation

According to the ethics committee of Chosun University Hospital (CHOSUN 2018-05-11), all experiments were conducted after ensuring that the experimental protocols were appropriate and humane.

Human concentrated RBCs and fresh frozen plasma (FFP) were purchased from the Gwangju–Chonnam blood bank (Gwangju, Korea) and were stored at 4 °C and −20 °C, respectively. Because the RBCs were preserved in citrate phosphate dextrose adenine (CPDA) as an anticoagulant solution, it was necessary to remove CPDA from the concentrated RBCs. The concentrated RBCs (~7 mL) were added into 1x PBS (pH 7.4, Gibco, Life Technologies, Carlsbad, CA, USA) (~7 mL) in a 15-mL tube. After the tube was inserted into a centrifugal separator (Allegra X-30R benchtop, Beckman Coulter, Brea, CA, USA), it was set to 4000 rpm and operated for 10 min. The diluted blood was separated into two layers: an upper layer (plasma), and a lower layer (RBCs). Pure RBCs were collected after removing liquid in the upper layer. Additionally, FFP was thawed at room temperature (25 °C). Plasma was filtered to remove cellular debris and unwanted white blood cells with a syringe filter (mesh size = 5 μm, Minisart, Sartorius, Göttingen, Germany). The RBCs and plasma were stored at 4 °C in a refrigerator before the blood test [20].

First, to evaluate the effect of the contribution of Hct and diluents (1x PBS, plasma) on the viscoelasticity of blood samples, blood samples with $Hct = 30\%$, 40% , 50% , and 60% were prepared by adding normal RBCs into 1x PBS or plasma. Except in the experiment for evaluating the contribution of Hct , all blood samples were adjusted to $Hct = 50\%$. Second, to fix normal RBCs chemically, three different concentrations of glutaraldehyde (GA) solution ($C_{GA} = 4, 8, \text{ and } 12 \mu\text{L/mL}$) were diluted by mixing GA solution (Grade II, 25% in H_2O , Sigma-Aldrich, St. Louis, MO, USA) into 1x PBS. Normal RBCs were fixed for consistent measurement because RBCs needed to be unchanged over experimental time. To fix normal RBCs, normal RBCs were mixed with each concentration of GA solution for 10 min prior to washing them. Fixed RBCs were collected after a washing procedure. The fixed blood sample ($Hct = 50\%$) was then prepared by adding the fixed RBCs into plasma. Here, to evaluate the contribution of fixed RBCs to viscoelasticity effectively, it was necessary to remain constant at a level of hematocrit (i.e., $Hct = 50\%$).

2.2. Fabrication on a Microfluidic Device and Experimental Procedure

A T-shaped microfluidic device for measuring blood viscoelasticity consisted of two inlets (a, b), one outlet (a), two guiding channels (blood sample channel (BC), reference fluid channel (RC)), and one coflowing channel (CC), as shown in Figure 1A-a and Figure S1 (Supplementary Materials). The blood

sample channel (width = 250 μm, length = 7500 μm) and reference fluid channel (width = 250 μm, length = 7500 μm) were connected to the coflowing channel (width = 250 μm, length = 9200 μm). Here, dimensions of a microfluidic channel were selected to measure velocity fields and blood viscosity accurately. First, velocity fields of blood flows were obtained accurately with microscopic images captured with at least 10× objective lens. Based on fields of view, channel width and length were selected suitably. Second, a rectangular channel with low aspect to ratio was preferred to measure blood viscosity effectively under coflowing method. The channel depth of the microfluidic device was fixed at 20 μm.

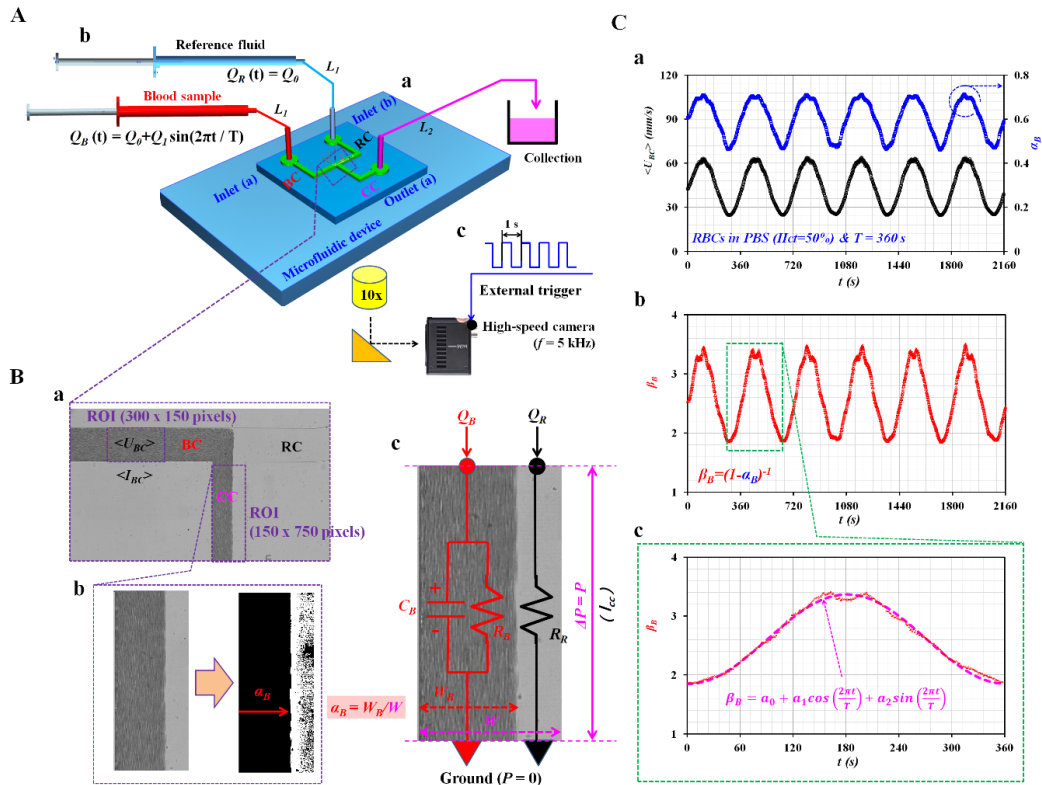


Figure 1. Proposed method for measuring blood viscoelasticity by monitoring the interface of both fluids in coflowing streams under a pulsatile blood flow rate. (A) Schematic diagram of the proposed method, including a microfluidic device, two syringe pumps, and an image acquisition system. (a) Microfluidic device composed of two inlets (a, b), one outlet (a), two guiding channels (blood sample channel (BC) and reference-fluid channel (RC)), and a coflowing channel (CC). (b) Two syringe pumps employed to supply blood sample and reference fluid into the corresponding inlets. (c) High-speed camera with a frame rate of 5 kHz employed to capture microscopic images at an interval of 1 s. (B) Quantification of interface in coflowing channel and its mathematical model with a discrete fluidic circuit. (a) Region of interest (ROI, 150 × 750 pixels) selected in coflowing channel for evaluating interface (α_B) and ROI (300 × 150 pixels) selected in blood sample channel for evaluating averaged blood velocity ($\langle U_{BC} \rangle$) or averaged image intensity ($\langle I_{BC} \rangle$). (b) Image conversion from gray-scale image to binary-scale image by using digital image processing. Interface (α_B) was obtained as $\alpha_B = W_B/W$. W_B and W represent blood-filled width and channel width, respectively. (c) Discrete fluidic circuit for mathematical representation of two fluids flowing in coflowing channel. Ground represented zero value of pressure ($P = 0$). (C) As a preliminary demonstration, a blood sample ($Hct = 50\%$, RBCs suspended in 1x PBS) was supplied into inlet (a) at a sinusoidal flow rate ($Q_B(t) = 1 + 0.5 \sin(2\pi t/360)$ mL/h); 1x PBS was supplied into inlet (b) at a constant flow rate of $Q_R(t) = 1$ mL/h. (a) Temporal variations of $\langle U_{BC} \rangle$ and α_B with an elapse of time. (b) Temporal variations of $\beta_B = (1 - \alpha_B)^{-1}$ over time. (c) Extractions of three constants (a_0, a_1 , and a_2) of $\beta_B(t) = a_0 + a_1 \cdot \cos(\omega \cdot t) + a_2 \cdot \sin(\omega \cdot t)$ by conducting a curve-fitting technique for a single period of 360 s.

Conventional microelectromechanical-system fabrication techniques (photolithography and deep reactive ion etching) were used to fabricate a master mold on a 4-inch silicon wafer. polydimethylsiloxane (PDMS) (Sylgard 184, Dow Corning, Midland, MI, USA) prepolymer and a curing agent were mixed at a ratio of 10:1. After the mold was fixed in a Petri dish, the PDMS mixture was poured on the master mold. Air bubbles in the PDMS were removed with a vacuum pump for 1 h. After curing the PDMS mixture in a convective oven (70 °C for 1 h), a PDMS block was peeled from the master mold. It was cut with a razor blade. Three ports (two inlets and one outlet) were punched with a biopsy punch (outer diameter = 1.2 mm). After oxygen–plasma treatment on the PDMS block and a glass slide with an oxygen–plasma system (CUTE-MPR, Femto Science Co., Gyeonggi, Korea), a microfluidic device was finally prepared by bonding the PDMS block on the glass slide.

As shown in Figure 1A-b, two polyethylene tubes (L_1 , inner diameter = 500 μm , thickness = 500 μm , and length = 300 mm) were connected from two disposable syringes (~ 1 mL) to two inlets (a and b). The other polyethylene tube (L_2 , inner diameter = 500 μm , thickness = 500 μm , and length = 200 mm) was connected from an outlet (a) to a waste collection unit. To remove air bubbles in the channels and avoid nonspecific binding of plasma proteins to the inner surfaces of the channels, all channels were filled completely with bovine serum albumin (BSA) solution of $C_{BSA} = 2$ mg/mL through outlet (a) with a disposable syringe. After 10 min, all channels were rinsed then filled with 1x PBS. After two disposable syringes (~ 1 mL) were filled with blood sample (~ 1 mL) and 1x PBS (~ 1 mL), they were installed into two syringe pumps (neMESYS, Cetoni GmbH, Germany). The blood sample was supplied into inlet (a) at a sinusoidal flow rate ($Q_B(t) = Q_0 + Q_1 \cdot \sin(2\pi t/T)$). Q_0 and Q_1 are the average and amplitude of the sinusoidal flow rate. Additionally, T represents the period. Reference fluid (1x PBS) was supplied into inlet (b) at a constant flow rate ($Q_R(t) = Q_0$).

As shown in Figure 1A-c, the microfluidic device was positioned on an optical microscope (BX51, Olympus, Tokyo, Japan) equipped with a 10 \times objective lens (NA = 0.25). A high-speed camera (FASTCAM MINI, Photron, USA) was used to capture microscopic images of the blood sample and 1x PBS flowing in microfluidic channels. It offered a spatial resolution of 1280 \times 1000 pixels. Each pixel corresponded to 10 μm . With a function generator (WF1944B, NF Corporation, Yokohama, Japan), a pulse signal with a period of 1 s triggered the high-speed camera. Microscopic images were sequentially captured at a frame rate of 5 kHz. All experiments and blood sample preparations were conducted at a room temperature of 25 °C.

2.3. Quantification of Interface (α_B), Averaged Blood Velocity ($\langle U_{BC} \rangle$), and Averaged Image Intensity ($\langle I_{BC} \rangle$)

Variations of the interface in the coflowing channel were used to quantify the viscoelasticity of the blood sample. Additionally, the image intensity and velocity fields of the blood sample flowing in the blood sample channel were obtained to evaluate the erythrocyte sedimentation rate (ESR) that occurred in the driving syringe while the blood flow rate was controlled by the syringe pump. First, to obtain the interface between the blood sample and 1x PBS in the coflowing channel, a specific ROI of 150 \times 750 pixels was selected in the coflowing channel, as shown in Figure 1B-a. To obtain the interface in the coflowing channel effectively, a gray-scale image was converted into a binary-scale image by adopting Otsu's method [21]. As shown in Figure 1B-b, the blood-filled width (W_B) over the ROI was calculated by using a commercial software package (MATLAB 2019, MathWorks, Natick, MA, USA). The interface (α_B) was obtained as $\alpha_B = W_B/W$. Here, W is the channel width of the coflowing channel. Second, to monitor variations of blood flow rate supplied from the syringe pump, velocity fields of the blood sample flowing in the blood sample channel were obtained by conducting a time-resolved micro particle image velocimetry (micro-PIV) technique. A specific ROI of 300 \times 150 pixels was selected in the blood sample channel. The size of the interrogation window was 32 \times 32 pixels. The window overlap was 50%. The obtained velocity fields were validated with a median filter. The averaged velocity ($\langle U_{BC} \rangle$) was calculated as an arithmetic average of U_{BC} distributed over the ROI. Third, to evaluate the ESR that occurred in the driving syringe, it was necessary to quantify the microscopic image intensity of the blood sample flowing in the blood sample channel. A specific ROI with 300 \times 150 pixels was

selected in the blood sample channel. The image intensity of the blood sample flowing in the blood sample channel was obtained by conducting digital image processing with MATLAB. An averaged image intensity ($\langle I_{BC} \rangle$) was obtained by averaging variations of I_{BC} distributed over the ROI.

2.4. Discrete Fluidic Circuit for Representing Viscoelasticity of Blood Sample

Blood samples were assumed to be Newtonian fluids. To evaluate the viscoelasticity of the blood sample, a simple mathematical model was constructed with discrete fluidic circuit elements. As shown in Figure 1B-c, two fluids flowing in the coflowing channel (i.e., blood sample stream, reference fluid stream) are represented with individual discrete fluidic circuit elements. The fluid circuit model is composed of a flow-rate element (Q_B, Q_R), resistance element (R_B and R_R), and compliance element (C_B). Q_B and Q_R are the flow rates of the blood sample and reference fluid, respectively. Ground represented zero value of pressure ($P = 0$).

The blood stream for representing the viscoelasticity of the blood sample was modeled as a resistance element (R_B) and compliance element (C_B) combined in parallel. The C_B was included to account for the compliance effect of the RBCs, the microfluidic channel, and a connected tube. However, because the reference fluid flowed at a constant flow rate in the coflowing channel, the compliance effect of a microfluidic channel and tube filled with reference fluid was negligible. For this reason, the reference stream was simply modeled only as a single resistance element (R_R). The coflowing channel was partially filled with the blood sample stream (W_B) and reference fluid stream ($W - W_B$). Because ground represented zero value of pressure, both streams had the same pressure drop ($P_B = P_R = \Delta P = P$). Based on mass conservation for the blood sample stream and reference fluid stream in the coflowing channel, two equations were derived:

$$Q_B = \frac{P}{R_B} + C_B \frac{dP}{dt} \quad (1)$$

for the blood sample stream, and

$$Q_R = \frac{P}{R_R} \quad (2)$$

for the reference fluid stream. By inserting Equation (2) into Equation (1), a first-order ordinary differential equation was derived:

$$\frac{Q_B}{Q_R} = \frac{R_R}{R_B} + C_B \frac{d}{dt} (R_R) \quad (3)$$

Because a rectangular-shaped channel (width = w , depth = h , and length = l) with a lower aspect ratio (AR) (i.e., $AR = \text{depth}/\text{width} = 20/250$) was filled with fluid (viscosity = μ), the resistance element was modeled approximately as [21]:

$$R = \frac{12 \mu L}{w h^3} \quad (4)$$

Based on the analytical expression of a rectangular channel, the corresponding resistance element for each stream was derived as

$$R_B = \frac{12 \mu_B l_{cc}}{W \alpha_B h^3} \quad (5)$$

for the blood sample stream and

$$R_R = CF \times \frac{12 \mu_R l_{cc}}{W(1 - \alpha_B) h^3} \quad (6)$$

for the reference fluid stream. In Equation (6), the CF was included to compensate for the boundary condition difference between the real physical model and approximate circuit model [17]. When inserting Equations (5) and (6) into Equation (4), the following equation was derived.

$$\frac{Q_B}{Q_R} = C_B \frac{d}{dt} \left(CF \frac{12 \mu_R l_{cc}}{W(1 - \alpha_B) h^3} \right) + CF \left(\frac{\mu_R}{\mu_B} \right) \left(\frac{\alpha_B}{1 - \alpha_B} \right) \quad (7)$$

The first part in the right side of Equation (7) was expressed again in a different form.

$$C_B \frac{d}{dt} \left(CF \frac{12\mu_R l_{cc}}{W(1-\alpha_B)h^3} \right) = C_B \frac{d}{dt} \left(CF \times R_{WB} \times \frac{1}{(1-\alpha_B)} \times \frac{\mu_R}{\mu_B} \right) \quad (8)$$

In Equation (8), R_{WB} , which assumed that the coflowing channel was filled with the blood sample, was given as $R_{WB} = \frac{12\mu_B l_{cc}}{Wh^3}$. According to a previous study, blood viscosity remained constant with respect to the interface [18]. Because R_{WB} and $\frac{\mu_R}{\mu_B}$ were independent of time, Equation (8) became a simple expression of Equation (9).

$$C_B \frac{d}{dt} \left(CF \frac{12\mu_R l_{cc}}{W(1-\alpha_B)h^3} \right) = C_B \times R_{WB} \times \left(\frac{\mu_R}{\mu_B} \right) \times \frac{d}{dt} \left(CF \times \frac{1}{(1-\alpha_B)} \right) \quad (9)$$

When Equation (9) was inserted into Equation (7), Equation (7) was then expressed as Equation (10).

$$\left(\frac{Q_B}{Q_R} \right) \left(\frac{\mu_B}{\mu_R} \right) = C_B R_{WB} \frac{d}{dt} \left(CF \times \frac{1}{1-\alpha_B} \right) + CF \times \left(\frac{\alpha_B}{1-\alpha_B} \right) \quad (10)$$

In Equation (10), CF was varied depending on the interface (α_B) (i.e., $CF = CF(\alpha_B)$). Here, the CF was obtained by conducting numerical simulation. Because Equation (10) had nonlinear terms, it was substantially difficult to find an analytical solution. For this reason, it was necessary to approximate the nonlinear Equation (10) as a simple linear equation. Equation (10) was modified as a simple form.

$$\left(\frac{Q_B}{Q_R} \right) \left(\frac{\mu_B}{\mu_R} \right) = F_1 C_B R_{WB} \frac{d}{dt} \left(\frac{1}{1-\alpha_B} \right) + F_2 \left(\frac{\alpha_B}{1-\alpha_B} \right) \quad (11)$$

In Equation (11), F_1 and F_2 were obtained by obtaining the weighted average of CF (i.e., $CF \times (1 - \alpha_B)^{-1}$ or $CF \times \alpha_B \times (1 - \alpha_B)^{-1}$) within a specific value of the interface. As the interface was relocated periodically within a specific range ($0.1 < \alpha_B < 0.9$), two approximate factors (F_1 and F_2) with constant values were calculated from Equations (12) and (13).

$$\sum_{i=1}^{i=n} CF(\alpha_B[i]) \times \frac{1}{1-\alpha_B(i)} = F_1 \sum_{i=1}^{i=n} \frac{1}{1-\alpha_B(i)} \quad (12)$$

and

$$\sum_{i=1}^{i=n} CF(\alpha_B[i]) \times \frac{\alpha_B(i)}{1-\alpha_B(i)} = F_2 \sum_{i=1}^{i=n} \frac{\alpha_B(i)}{1-\alpha_B(i)} \quad (13)$$

By dividing Equation (11) with F_2 , Equation (11) was changed to a simple linear differential equation.

$$\lambda_B \frac{d}{dt} (\beta_B) + \beta_B = 1 + \left(\frac{1}{F_2} \right) \left(\frac{Q_B}{Q_R} \right) \left(\frac{\mu_B}{\mu_R} \right) \quad (14)$$

In Equation (14), β_B and time constant (τ_B) were derived as $\beta_B = (1 - \alpha_B)^{-1}$ and $\lambda_B = C_B R_{WB} \left(\frac{F_1}{F_2} \right)$, respectively. In this study, the flow rates of the blood sample and reference fluid were controlled as $Q_B(t) = Q_0 + Q_1 \sin(\omega t)$ and $Q_R(t) = Q_0$, respectively. Here, ω was given as $\omega = \frac{2\pi}{T}$. The particular solution of Equation (14) was then derived as

$$\beta_B = \beta_0 + \beta_1 \sin(\omega t - \varphi) \quad (15)$$

In Equation (15), β_0 and β_1 were given as Equations (16) and (17).

$$\beta_0 = 1 + \frac{1}{F_2} \left(\frac{\mu_B}{\mu_R} \right) \quad (16)$$

and

$$\beta_1 = \frac{1}{F_2} \left(\frac{\mu_B}{\mu_R} \right) \left(\frac{Q_1}{Q_0} \right) \frac{1}{\sqrt{1 + \omega^2 \lambda_B^2}} \quad (17)$$

Additionally, time delay (φ) was given as $\varphi = \omega \lambda_B$. From Equation (16), the blood viscosity (μ_B) was given as

$$\mu_B = \mu_R F_2 (\beta_0 - 1) \quad (18)$$

Additionally, from Equation (17), the time constant (λ_B) was derived as

$$\lambda_B = \frac{T}{2\pi} \sqrt{\left(\frac{1}{\beta_1 F_2} \right)^2 \left(\frac{Q_1}{Q_0} \right)^2 \left(\frac{\mu_B}{\mu_R} \right)^2 - 1} \quad (19)$$

According to $\lambda_B = R_{WB} C_B \left(\frac{F_1}{F_2} \right)$, the analytical expression of compliance (C_B) was derived as

$$C_B = \left(\frac{F_2}{F_1} \right) \left(\frac{1}{R_{WB}} \right) \left(\frac{T}{2\pi} \right) \sqrt{\left(\frac{1}{\beta_1 F_2} \right)^2 \left(\frac{Q_1}{Q_0} \right)^2 \left(\frac{\mu_B}{\mu_R} \right)^2 - 1} \quad (20)$$

In other words, if β_0 and β_1 could be obtained from periodic variations of the interface (α_B) in the coflowing channel, μ_B and C_B as blood viscoelasticity could be evaluated from Equations (18) and (20), respectively.

As shown in Figure 1C, as a preliminary study, a blood sample ($Hct = 50\%$) was prepared by adding normal RBCs into 1x PBS. The blood sample was supplied into inlet (a) at a sinusoidal flow rate ($Q_B(t) = 1 + 0.5 \sin(2\pi t/360)$ mL/h). Simultaneously, 1x PBS was supplied into inlet (b) at a constant flow rate of $Q_R(t) = 1$ mL/h. Figure 1C-a showed temporal variations of $\langle U_{BC} \rangle$ and α_B over time. In addition, $\langle U_{BC} \rangle$ and α_B exhibited periodic variations over time. Figure 1C-b showed temporal variations of $\beta_B = (1 - \alpha_B)^{-1}$ over time. Figure 1C-c showed temporal variations of β_B selected for a single period ($T = 360$ s). The expression of $\beta_B(t)$ was assumed to be $\beta_B(t) = a_0 + a_1 \cdot \cos(\omega t) + a_2 \cdot \sin(\omega t)$. Using the orthogonal property of the sinusoidal function ($\sin(\omega t)$ and $\cos(\omega t)$), three unknown constants (a_0 , a_1 , and a_2) were obtained from Equations (21)–(23).

$$a_0 = \frac{1}{T} \int_{t=0}^{t=T} \beta_B(t) dt \quad (21)$$

$$a_1 = \frac{2}{T} \int_{t=0}^{t=T} \beta_B(t) \cos(\omega t) dt \quad (22)$$

and

$$a_2 = \frac{2}{T} \int_{t=0}^{t=T} \beta_B(t) \sin(\omega t) dt \quad (23)$$

According to Equations (21)–(23), three unknown constants (a_0 , a_1 , and a_2) were obtained as $a_0 = 2.61$, $a_1 = -0.758$, and $a_2 = -0.017$. In Equation (15), β_0 and β_1 were obtained as $\beta_0 = a_0 = 2.61$ and $\beta_1 = \sqrt{a_1^2 + a_2^2} = 0.785$, respectively. Using Equations (18)–(20), blood viscosity, time constant, and blood compliance were estimated to be $\mu_B = 1.785$ cP, $\lambda_B = 20.491$ s, and $C_B = 208.492 \frac{\mu m^3}{mPa}$, respectively.

3. Results and Discussion

3.1. Correction Factor (CF) and Approximate Factors (F_1 and F_2) via Numerical Simulation

To find two approximate factors (F_1 , F_2) in Equation (11), it was necessary to obtain the CF by conducting numerical simulation with CFD software (CFD-ACE+, ESI Group, Paris, France). For convenience, the flow rate of the blood sample was assumed to be $Q_B = 1$ mL/h. The viscosities of both fluids (blood sample, reference fluid) were assumed as $\mu_B = 1$ cP and $\mu_R = 1$ cP, respectively.

Figure 2A showed variations of the interface (α_B) through numerical simulation with respect to the flow-rate ratio (Q_R/Q_B) ((a) $Q_R/Q_B = 1$, (b) $Q_R/Q_B = 0.8$, (c) $Q_R/Q_B = 0.6$, (d) $Q_R/Q_B = 0.4$, (e) $Q_R/Q_B = 0.2$, and (f) $Q_R/Q_B = 0.1$). The interfaces (α_B) for the corresponding flow-rate ratio (Q_R/Q_B) were obtained as (a) $\alpha_B = 0.5$ for $Q_R/Q_B = 1$, (b) $\alpha_B = 0.553$ for $Q_R/Q_B = 0.8$, (c) $\alpha_B = 0.619$ for $Q_R/Q_B = 0.6$, (d) $\alpha_B = 0.704$ for $Q_R/Q_B = 0.4$, (e) $\alpha_B = 0.818$ for $Q_R/Q_B = 0.2$, and (f) $\alpha_B = 0.891$ for $Q_R/Q_B = 0.1$.

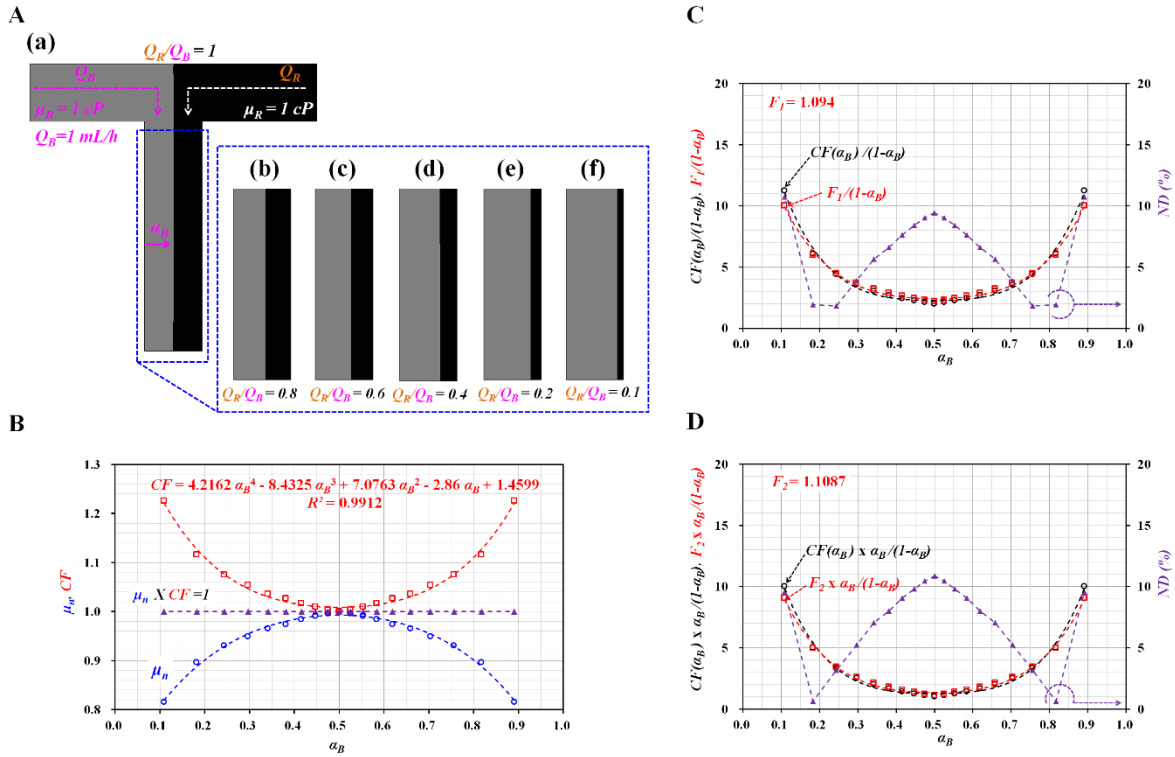


Figure 2. Estimation of correction factor (CF) and two approximate factors (F_1, F_2) with numerical simulation. (A) Variations of interface (α_B) through numerical simulation with respect to flow-rate ratio (Q_R/Q_B): (a) $Q_R/Q_B = 1$, (b) $Q_R/Q_B = 0.8$, (c) $Q_R/Q_B = 0.6$, (d) $Q_R/Q_B = 0.4$, (e) $Q_R/Q_B = 0.2$, and (f) $Q_R/Q_B = 0.1$. For convenience, the flow rate of the blood sample was assumed to be $Q_B = 1$ mL/h. The viscosities of both fluids were given as $\mu_B = 1$ cP and $\mu_R = 1$ cP, respectively. (B) Variations of estimated normalized viscosity (μ_n) of blood sample and CF with respect to interface ($0.1 < \alpha_B < 0.9$). The CF was obtained as $CF = 4.2162 \alpha_B^4 - 8.4325 \alpha_B^3 + 7.0763 \alpha_B^2 - 2.86 \alpha_B + 1.4599$ ($R^2 = 0.9912$). (C) Variations of $CF(\alpha_B)/(1 - \alpha_B)$, $F_1/(1 - \alpha_B)$, and normalized difference (ND) over α_B . (D) Variations of $CF(\alpha_B) \times \alpha_B/(1 - \alpha_B)$, $F_2 \times \alpha_B/(1 - \alpha_B)$, and ND over α_B .

According to the coflowing-streams method [22,23], the viscosity ratio of the blood sample to the reference fluid (μ_B/μ_R) was obtained as $\frac{\mu_B}{\mu_R} = \frac{\alpha_B}{1-\alpha_B}$ by quantifying the interface (α_B) in coflowing streams at the same flow-rate condition ($Q_B = Q_R$). The normalized viscosity of the blood sample was obtained by dividing the estimated viscosity ($\mu_{est} = \mu_R \cdot \alpha_B/(1 - \alpha_B)$) by the given viscosity ($\mu_{given} = 1$ cP) ($\mu_n = \mu_{est}/\mu_{given}$). As shown in Figure 2B, variations of μ_n were obtained by varying the interface ($0.1 < \alpha_B < 0.9$). When the interface was located at the center line ($\alpha_B = 0.5$), μ_n was given as $\mu_n = 1$. In other words, the blood viscosity could be measured accurately when the interface was located at the center line [24]. However, when α_B was relocated from the center line to both walls, μ_n tended to decrease by approximately 0.8. Because the viscosity of the blood sample was given as $\mu_B = 1$ cP, the coflowing-streams method exhibited a large measurement error of approximately 20% when compared with the given viscosity of the blood sample. The reason could be explained by the boundary condition difference between the real physical model and simple mathematical model. Instead of a real and complex model, to construct a simple model of coflowing streams, the coflowing-streams method assumed that the interface of two streams was a virtual wall. In other

words, it assumed that the interface was a virtual-wall boundary. Because the CF varied by channel dimensions (width and depth), the CF was calculated by referring to the general procedure discussed in previous studies [17,19]. The CF was then estimated by the reciprocating μ_n obtained at a specific interface ($CF \cdot (\alpha_n) = \mu_n^{-1}$ for α_n). As shown in Figure 2B, the CF was obtained as $CF = 1$ at the center line ($\alpha_B = 0.5$). However, the CF tended to increase gradually when the interface moved to both walls. According to regression analysis, the CF was obtained as $CF = 4.2162 \alpha_B^4 - 8.4325 \alpha_B^3 + 7.0763 \alpha_B^2 - 2.86 \alpha_B + 1.4599$ ($R^2 = 0.9912$). By inserting the correction factor into the coflowing-streams method, the viscosity of the blood sample was estimated with $\mu_B = \mu_R CF(\alpha_B) \frac{\alpha_B}{1-\alpha_B}$. The coflowing method with correction factor could be used to measure the viscosity of blood with a specific hematocrit. Based on Equation (12), the approximate factor (F_1) was obtained as $F_1 = 1.094$. As shown in Figure 2C, variations of $CF(\alpha_B) \frac{1}{1-\alpha_B}$ and $F_1 \frac{1}{1-\alpha_B}$ were obtained with respect to α_B . The normalized difference (ND) between both terms exhibited its maximum value at the center and both walls. The normalized difference was less than 10%. Additionally, according to Equation (13), the approximate factor (F_2) was obtained as $F_2 = 1.1087$. As shown in Figure 2D, variations of $CF(\alpha_B) \frac{\alpha_B}{1-\alpha_B}$ and $F_2 \frac{\alpha_B}{1-\alpha_B}$ were obtained with respect to α_B . The maximum value of normalized difference was estimated to be approximately 11%. The simulation study showed that the two approximate factors ($F_1 = 1.094$, $F_2 = 1.1087$) could give consistent results when compared with the original expression. Using F_1 and F_2 , the nonlinear Equation (10) was converted into the simple linear Equation (11) for consistency.

3.2. Effect of Period (T) on Viscoelasticity of Blood Sample

To verify the contribution of the period (T) to the viscoelasticity of the blood sample (Equations [18] and [20]), the viscosity and compliance were evaluated by varying the period ($T = 120, 240, 360$, and 480 s). The blood sample ($Hct = 50\%$) was prepared by adding normal RBCs into 1x PBS. Q_0 and Q_1 of the two syringe pumps were controlled at $Q_0 = 1$ and $Q_1 = 0.5$ mL/h, respectively. For a rectangular channel with a lower aspect ratio, the shear rate ($\dot{\gamma}$) was derived as $\dot{\gamma} = \frac{6Q}{wh^2}$ [19]. Based on the shear rate formula, the shear rates of the corresponding flow rate were estimated as $\dot{\gamma} = 8333 \text{ s}^{-1}$ for $Q_B = 0.5$ mL/h and $\dot{\gamma} = 25,000 \text{ s}^{-1}$ for $Q_B = 1.5$ mL/h. Because the shear rate ($\dot{\gamma}$) was much greater than 1000 s^{-1} , it was reasonable that the blood sample behaves as a Newtonian fluid. In other words, the blood viscosity (μ_B) remained constant within the specific flow rates of the blood sample.

As shown in Figure 3A, temporal variations of α_B and $\beta_B = (1 - \alpha_B)^{-1}$ were obtained with respect to the period ((a) $T = 120$ s, (b) $T = 240$ s, (c) $T = 360$ s, and (d) $T = 480$ s). Based on Equations (21)–(23), β_0 and β_1 were obtained at an interval of the corresponding period. Figure 3B-a showed variations of β_0 and β_1 with respect to T , where β_0 and β_1 fluctuated at a shorter period ($T = 120, 360$ s). However, they remained stable at a longer period ($T = 360, 480$ s). Figure 3B-b showed variations of λ_B with respect to T . The λ_B tended to increase linearly for up to $T = 360$ s. However, the slope of λ_B tended to decrease between $T = 360$ and $T = 480$ s. According to Equation (19), the λ_B was linearly proportional to the period (i.e., $\lambda_B \sim T$). The experimental results showed appropriately consistent variations of λ_B with respect to T . Using Equations (18) and (20), the blood viscosity (μ_B) and compliance (C_B) were obtained with respect to T . As shown in Figure 3B-c, μ_B did not exhibit a linear dependency of T . It fluctuated at a shorter period. However, it remained constant at a longer period ($T = 360, 480$ s). The results agreed with Equation (18), which did not relate to the period. It was necessary, however, to set a longer period for consistently measuring the viscosity of the blood sample. Compliance (C_B) tended to increase linearly for up to $T = 360$ s. The slope of C_B tended to decrease between $T = 360$ and $T = 480$ s. According to the mathematical relation, C_B was linearly proportional to λ_B . The experimental results indicated that blood viscosity was independent of period. However, compliance varied linearly depending on the period.

From the results, for consistent measurement of viscoelasticity (blood viscosity and compliance), the period of the syringe pump was set to a longer period of $T = 360$ s throughout all experiments for convenience.

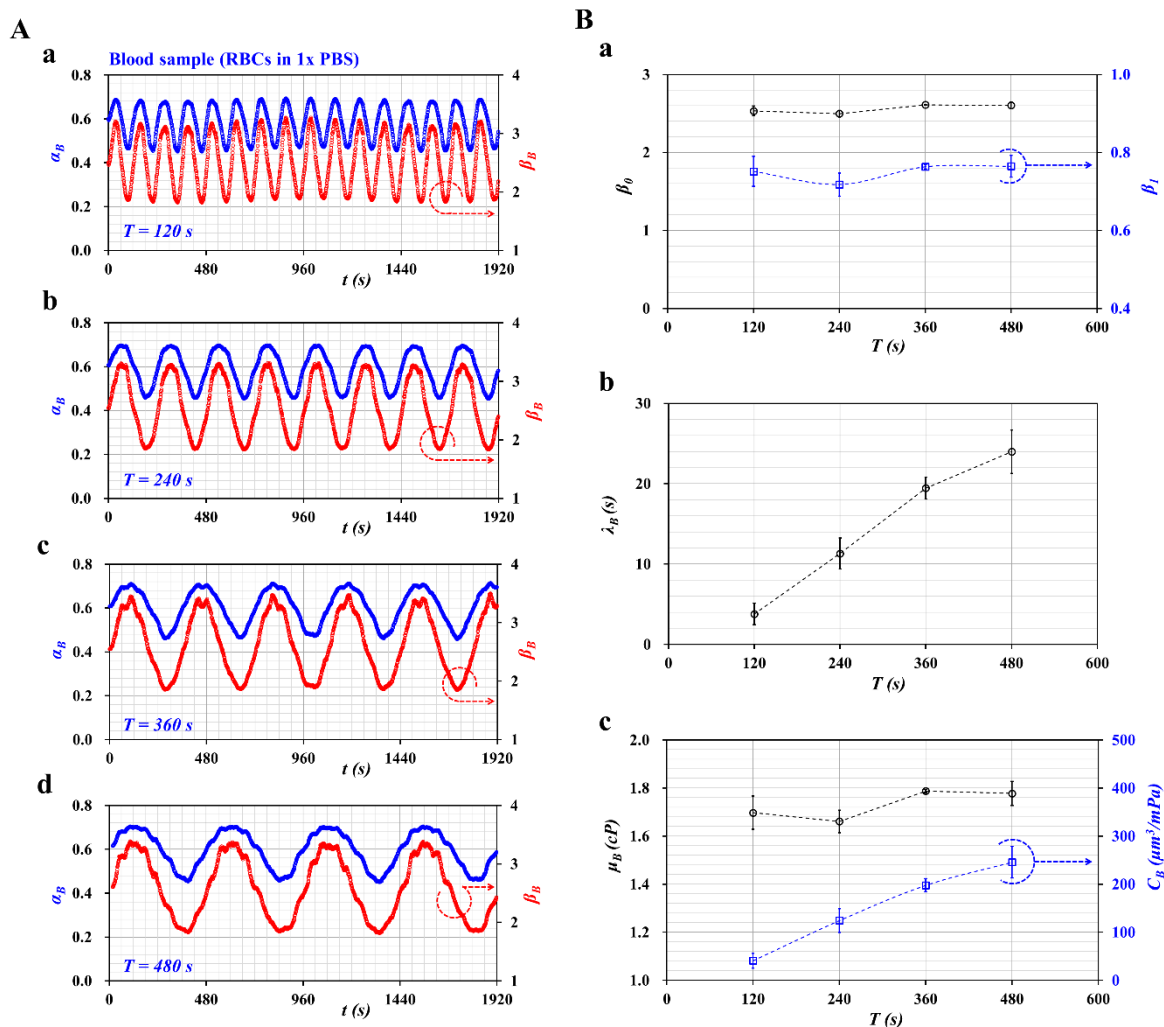


Figure 3. Evaluation of the effect of period (T) on viscoelasticity (blood viscosity and compliance). (A) Temporal variations of α_B and β_B with respect to period (T) ((a) $T = 120$ s, (b) $T = 240$ s, (c) $T = 360$ s, and (d) $T = 480$ s). (B) Quantification of viscosity (μ_B) and compliance (C_B) with respect to period. (a) variations of β_0 and β_1 with respect to T , (b) variations of λ_B with respect to T , and (c) variations of μ_B and C_B with respect to T .

3.3. Quantification of the Effect of Hematocrit on Blood Viscoelasticity

According to a previous study, hematocrit caused an increase in blood viscosity and elasticity [16]. In addition, a blood sample with a low hematocrit ($Hct = 30\%$) exhibited a continuous ESR occurring in a driving syringe [25]. According to the previous study, to increase the ESR significantly, a blood sample was prepared by adding normal RBCs into various concentrations of dextran solution ($C_{dex} = 2, 5, 8,$ and 10 mg/mL). Because the hematocrit of the blood sample flowing in the microfluidic channel varied continuously over time, RBC aggregation or blood viscosity tended to vary continuously [19]. In this study, under blood perfusion with a sinusoidal flow-rate pattern, the contribution of hematocrit to blood viscoelasticity and ESR was quantified by varying the hematocrit. To induce the ESR in a driving syringe, plasma was used as the diluent. In other words, blood samples ($Hct = 30\%, 40\%, 50\%$, and 60%) were prepared by adding normal RBCs into the plasma.

Figure 4A showed temporal variations of β_B with respect to hematocrit ((a) $Hct = 30\%$, (b) $Hct = 40\%$, (c) $Hct = 50\%$, and (d) $Hct = 60\%$). Using temporal variations of β_B , blood viscosity and compliance were obtained at an interval of a specific period. As shown in Figure 4B, temporal variations of μ_B and C_B were obtained with respect to hematocrit ((a) $Hct = 30\%$, (b) $Hct = 40\%$,

(c) $Hct = 50\%$, and (d) $Hct = 60\%$). Both parameters were obtained as mean \pm standard deviation at a specific time ($t = 290, 650, 1010, 1370,$ and 1730 s).

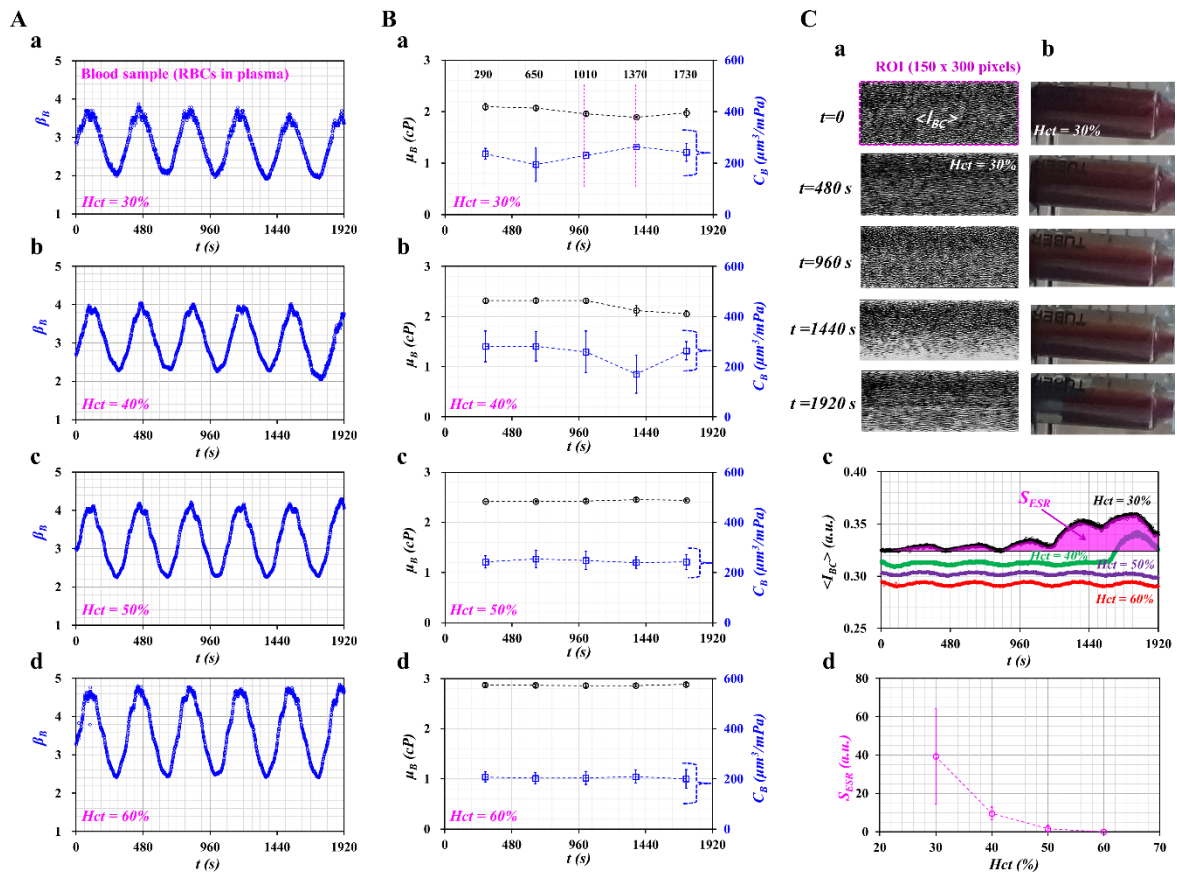


Figure 4. Contribution of hematocrit (Hct) to viscoelasticity and ESR. Blood samples ($Hct = 30\%$, 40% , 50% , and 60%) were prepared by adding normal RBCs into plasma. (A) Temporal variations of β_B with respect to hematocrit ((a) $Hct = 30\%$, (b) $Hct = 40\%$, (c) $Hct = 50\%$, and (d) $Hct = 60\%$). (B) Temporal variations of μ_B and C_B with respect to hematocrit ((a) $Hct = 30\%$, (b) $Hct = 40\%$, (c) $Hct = 50\%$, and (d) $Hct = 60\%$). (C) Evaluation of ESR occurring in driving syringe. (a) Microscopic images of blood sample ($Hct = 30\%$) flowing in blood channels over time ($t = 0, 480, 960, 1440,$ and 1920 s). (b) Side view of a driving syringe over time ($t = 0, 480, 960, 1440,$ and 1920 s). (c) Temporal variations of $\langle I_{BC} \rangle$ with respect to Hct . (d) Variations of S_{ESR} with respect to Hct .

For the blood sample with $Hct = 30\%$, compliance (C_B) fluctuated greatly over time. It tended to decrease after $t = 290$ s, but it tended to increase between $t = 650$ and $t = 1370$ s. After $t = 1370$ s, it remained constant over time. Blood viscosity tended to decrease after $t = 650$ s. In other words, the ESR of RBCs in a driving syringe accelerated over time. In other words, after a certain time, the hematocrit of the blood sample tended to decrease. Thus, μ_B tended to decrease, and C_B tended to increase with an elapse of time. For the blood sample with $Hct = 40\%$, blood viscosity tended to decrease after $t = 1010$ s. Compliance remained constant for up to $t = 1010$ s. After that, it fluctuated over time. When the hematocrit increased from $Hct = 30\%$ to $Hct = 40\%$, the time when C_B had the minimum value tended to increase substantially. However, for the blood samples with high hematocrit ($Hct = 50\%$, 60%), blood viscosity and compliance remained constant over time. The blood viscosity tended to increase at a higher hematocrit. The compliance tended to decrease at a higher hematocrit. According to a previous study, blood elasticity tended to increase with respect to hematocrit [16]. When compared with the previous result, compliance tended to decrease with respect to the hematocrit. The experimental results

can be considered reasonable, because compliance had the reciprocal of elasticity (i.e., compliance $\sim 1/\text{elasticity}$).

To quantify the ESR that occurred in a driving syringe, the microscopic image intensities of the blood sample were obtained over time. A driving syringe was installed horizontally. Because of the ESR in the driving syringe, the hematocrit of the blood sample flowing in a microfluidic channel tended to decrease over time. Here, variations of hematocrit were used by monitoring the image intensity of the blood sample [26]. Figure 4C-a showed microscopic images of the blood sample ($Hct = 30\%$) flowing in the blood sample channel over time ($t = 0, 480, 960, 1440,$ and 1920 s). After $t = 960$ s, the number of RBCs tended to decrease significantly. The image intensity tended to increase. At $t = 1920$ s, the image intensity tended to decrease as RBCs tended to increase significantly. The contrast of each image was enhanced by conducting image processing with the software Image-J (NIH, Maryland, USA). A specific ROI (300×150 pixels) in the blood sample channel was selected to quantify the image intensity ($\langle I_{BC} \rangle$). To visualize the ESR in a driving syringe, a side view of a syringe filled with a blood sample ($Hct = 30\%$) was captured sequentially with a smartphone camera (Galaxy A5, Samsung, Korea). As lower level of hematocrit exhibited higher value of $\langle I_{BC} \rangle$, the results of blood sample ($Hct = 30\%$) was selected and summarized at a specific time. Figure 4C-b showed snapshots of a driving syringe over time (t) ($t = 0, 480, 960, 1440,$ and 1920 s). Before $t = 480$ s, there was no indication of the ESR occurring in a driving syringe, because the RBCs were distributed uniformly. After $t = 960$ s, because of the continuous ESR, the blood sample inside the syringe was separated into two regions: an RBC-rich region (i.e., lower layer) and an RBC-free region (i.e., upper layer). As shown in Figure 4C-a, the ESR in the driving syringe caused a reduced number of RBCs in the microfluidic channel. To quantify the decrease in hematocrit resulting from ESR in the driving syringe, the image intensity of the blood sample ($\langle I_{BC} \rangle$) was obtained over time. Figure 4C-c showed temporal variations of $\langle I_{BC} \rangle$ with respect to $Hct = 30\%, 40\%, 50\%$, and 60% . For a blood sample with $Hct = 30\%$, $\langle I_{BC} \rangle$ tended to increase after $t = 1190$ s. For a blood sample with $Hct = 40\%$, image intensity tended to increase after $t = 1570$ s. For blood samples with a high hematocrit ($Hct = 50\%, 60\%$), the image intensity remained constant over time. This result showed that a lower hematocrit contributed to varying image intensity (or numbers of RBCs) of blood samples flowing in a microfluidic channel. According to a specific parameter (S_{ESR}) suggested in a previous study [20], variations of ESR were quantified with respect to Hct . The S_{ESR} was obtained as $S_{ESR} = \int_{t=0}^{t=1920} (\langle I_{BC} \rangle - I_{min}) dt$. Here, I_{min} represents the minimum value of $\langle I_{BC} \rangle$ within a specific duration, $t = 1920$ s. Figure 4C-d showed variations of S_{ESR} with respect to Hct . The S_{ESR} tended to decrease substantially with respect to Hct . The blood sample with $Hct = 30\%$ showed the maximum value of S_{ESR} . This result indicated that S_{ESR} varied significantly depending on the hematocrit.

From the result, one can conclude that the viscoelasticity of the blood sample suggested by the present method can be varied with the hematocrit. In addition, it can be employed to quantify variations of the ESR occurring in the driving syringe by monitoring temporal variations of viscoelasticity.

3.4. Quantification of the Contribution of Hardened RBCs to Blood Viscoelasticity

Finally, the method was employed to quantify the contribution of hardened RBCs to the viscoelasticity of blood samples. According to previous studies [27,28], normal RBCs were hardened chemically with GA solution. The degree in rigidity increased gradually by varying concentrations of the GA solution. Normal RBCs were hardened chemically with three different concentrations of GA solution (C_{GA}) ($C_{GA} = 4, 8,$ and $12 \mu\text{L}/\text{mL}$). The hardened blood sample ($Hct = 50\%$) was then prepared by adding hardened RBCs into plasma.

Figure 5A showed temporal variations of β_B with respect to C_{GA} . As the concentration of GA solution increased, β_B tended to increase gradually. In addition, the β_B exhibited steady and periodic variations over time. Figure 5B showed temporal variations of $\langle I_{BC} \rangle$ with respect to C_{GA} . The inset showed a microscopic image of the fixed blood sample (i.e., fixed RBCs with $C_{GA} = 12 \mu\text{L}/\text{mL}$) captured at $t = 480$ s. The $\langle I_{BC} \rangle$ tended to decrease slightly at a higher concentration of GA solution. However,

it exhibited steady and periodic variations over time. The result indicated that the fixed blood sample with $Hct = 50\%$ did not induce the ESR in the driving syringe as shown in Figure 4.

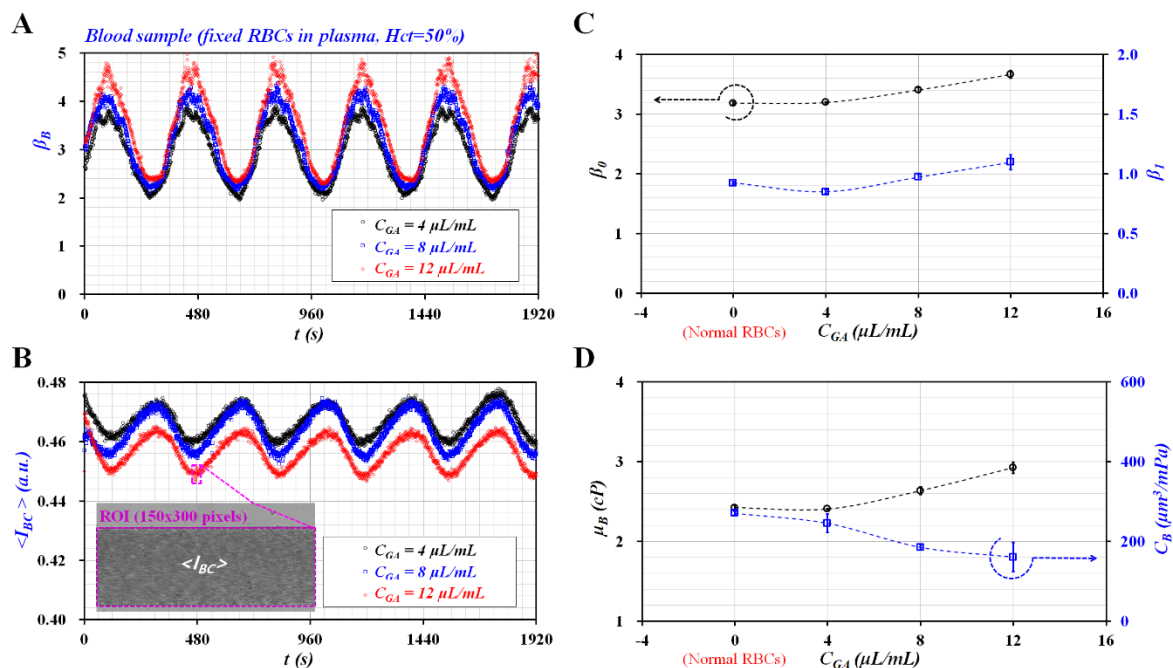


Figure 5. Contribution of fixed blood sample to viscoelasticity of blood sample. Fixed RBCs were prepared chemically with GA solution (C_{GA}) ($C_{GA} = 4, 8, \text{ and } 12 \mu\text{L/mL}$). A fixed blood sample ($Hct = 50\%$) was then prepared by adding fixed RBCs into plasma: (A) temporal variations of β_B with respect to C_{GA} , (B) temporal variations of $\langle I_{BC} \rangle$ with respect to C_{GA} , (C) variations of β_0 and β_1 with respect to C_{GA} , and (D) variations of μ_B and C_B with respect to C_{GA} .

Figure 5C showed variations of β_0 and β_1 with respect to C_{GA} . Both parameters (β_0 and β_1) tended to increase substantially at a higher concentration of GA solution. Because the GA solution was employed to increase the rigidity of RBCs, both parameters presented distinctive variations of hardness. Based on Equations (18)–(20), variations of μ_B and C_B were obtained at an interval of $T = 360 \text{ s}$. As β_B and $\langle I_{BC} \rangle$ showed stable variations over time, μ_B and C_B remained constant over the specific duration of the test as shown in Figure 5A,B. Thus, μ_B and C_B were represented as average \pm standard deviation ($n = 5$). Figure 5D showed variations of μ_B and C_B with respect to C_{GA} . According to previous studies [17,18], blood viscosity and elasticity tended to increase at a higher concentration of GA solution. When compared with the previous results, blood viscosity exhibited consistent variations with respect to the concentration of GA solution. Because compliance was defined as the reciprocal of elasticity, the compliance also showed consistent variations with respect to the concentration of GA solution.

The results lead to the conclusion that the present method could be employed to monitor variations of the viscoelasticity of blood samples while the syringe pump was set to a pulsatile flow-rate pattern.

3.5. Quantificative Comparison of Viscoelasticity Obtained with Present Method and Conventional Viscometer

Using a conventional viscometer, viscoelasticity of cells was modeled with the linear Maxwell model. As shown in Figure 6A-a, the viscoelasticity of each blood sample was modeled as a solid element and a fluid element connected in series. The corresponding constitutive expression of each element was given as $\tau = G\gamma$ (solid element) and $\tau = \mu\dot{\gamma}$ (fluid element), respectively. Here, G and μ represented elasticity and viscosity, respectively. τ and γ denoted shear stress and shear strain. External shear strain was excited periodically as $\gamma(t) = \gamma_0 e^{j\omega t}$. The governing equation was then derived as $\dot{\tau} + \frac{1}{\lambda_{cv}}\tau = G\dot{\gamma}$. Here, the time constant of viscometry (l_{cv}) was expressed as $l_{cv} = \mu/G$.

The viscous effect of the viscometer was considered as negligible since the viscometer did not have an influence on relaxation time of the cells. The viscometer had operated at a wider range of frequency from $\omega = 0.3$ rad/s to $\omega = 700$ rad/s [29]. The previous study indicated that the time constant of whole blood was obtained as $\lambda_{cv} = 1.5\text{--}13.4$ ms for shear flow [29], and $\lambda_{cv} = 114\text{--}259$ ms for extensional flow [30].

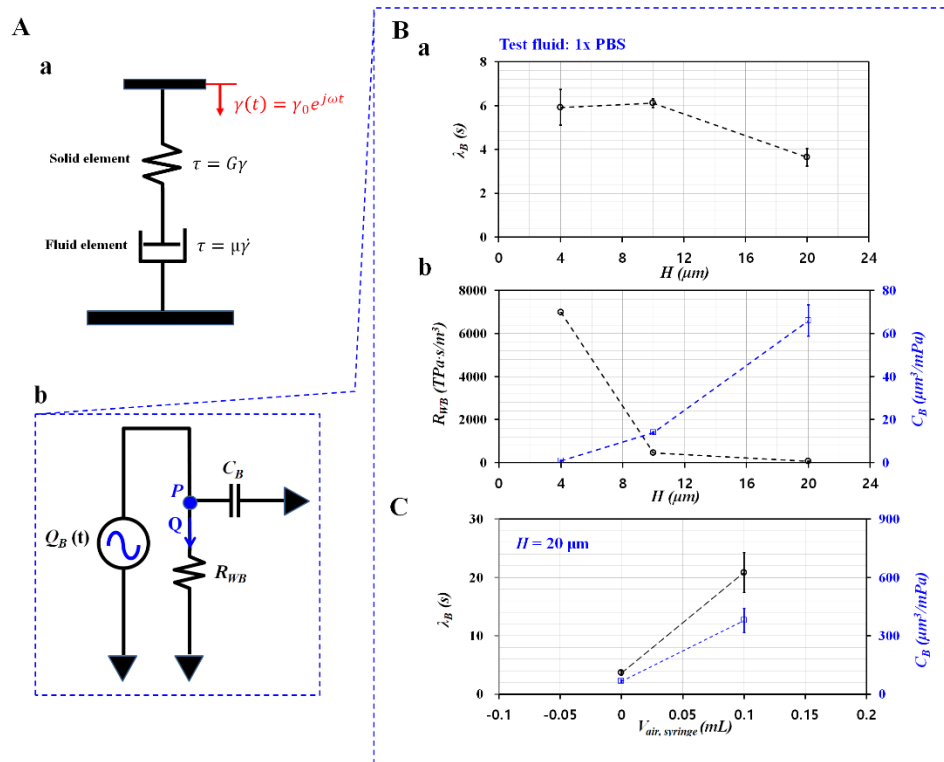


Figure 6. Mathematical representation and quantification of contributions of channel depth and air cavity to compliance. (A) Mathematical representation of conventional viscometer and microfluidic system. (a) Mathematical representation of conventional viscometer. (b) Mathematical representation of microfluidic system. (B) Evaluation of channel depth (H) on compliance. Here, 1x PBS as test fluid was infused into a microfluidic system. (a) Variations of λ_B with respect to H . (b) Variations of R_{WB} and C_B with respect to H . (C) Evaluation of air cavity on compliance.

On the other hand, under periodic blood flow in the microfluidic system, Figure 6A-b showed the simple fluidic circuit model of the microfluidic system. Based on electric circuit analysis, the governing equation of fluidic system was derived as $\lambda_B \dot{Q} + Q = Q_B(t)$. Here, Q represented the flow rate which passed through resistance element. Time constant (λ_B) was derived as $\lambda_B = R_{WB} \cdot C_B$. R_{WB} and C_B represented fluidic resistance of the coflowing channel filled with only blood sample and compliance, respectively. As shown in Figure 6A-b, a microfluidic system behaved as an R-C low pass filter. To effectively infuse alternating components in the periodic flow rate into a microfluidic system, the period of the excitation flow rate should be much longer than the time constant of the microfluidic system (i.e., $T > \lambda_B$). In addition, the syringe pump used in this study did not infuse blood samples during short periods. From the experimental results as shown in Figure 3B, period (T) of the sinusoidal flow rate was fixed as $T = 360$ s.

The λ_B was determined by R_{WB} and C_B . Flexible tubing and the PDMS channels tended to vary the time constant substantially [11]. A microfluidic channel with different channel depths (H) ($H = 4, 10, \text{ and } 20 \mu\text{m}$) was prepared to change R_{WB} . Here, 1x PBS was infused into a microfluidic channel to reduce or remove the viscoelastic effects. As shown in Figure 6B-a, the corresponding time constant for each channel depth was obtained as $\lambda_B = 5.92 \pm 0.81$ s ($H = 4 \mu\text{m}$), $\lambda_B = 6.11 \pm 0.20$ s ($H = 10 \mu\text{m}$), and

$t_B = 3.64 \pm 0.40$ s ($H = 20$ μm). In addition, Figure 6B-b showed variations of R_{WB} and C_B with respect to H . A lower channel depth contributed to increasing R_{WB} , and decreasing C_B . The result indicated that fluidic resistance (R_{WB}) had a strong influence on C_B . To find out the contribution of compliance element (C_B), the compliance of the microfluidic system increased intentionally by securing the air cavity inside the driving syringe. As shown in Figure 6C, variations of λ_B and C_B were obtained with respect to $V_{air} = 0$ and 0.1 mL. When the air cavity of 0.1 mL existed inside the driving syringe, λ_B and C_B increased considerably as $\lambda_B = 20.84 \pm 3.42$ s and $C_B = 378.59 \pm 62.11$ s. From the result, the air cavity tended to increase λ_B and C_B substantially. When compared with viscometry data, the time constant (λ_B) increased about $O(10^2)$ significantly because of the compliance effect of the microfluidic system (i.e., flexible tubing, PDMS channels, and the air cavities existing in the driving syringe). In addition, minimum threshold of C_B (i.e., detection limit) was estimated as 66.05 ± 7.30 $\mu\text{m}^3/\text{mPa}$ at a specific condition (i.e., $V_{air} = 0$, $H = 20$ μm). According to a previous study [17], time constants obtained with two different systems (i.e., λ_{PM} : microfluidic system, λ_{CPV} : conventional viscometer) were obtained and compared with respect to $C_{glycerin} = 10\%$, 20% , 30% and 40% . As glycerin solution did not include viscoelasticity, both time constants remained unchanged with respect to different concentrations of glycerin solution. However, the microfluidic system had a longer time constant with $O(10^0)$. The ratio of time constant between λ_{CPV} and λ_{PM} was obtained as $\lambda_{CPV}/\lambda_{PM} = O(10^2)$. To quantitatively determine elasticity obtained with both methods, a scatter plot was employed by plotting G_{PM} on the vertical axis and G_{CPV} on the horizontal axis. According to linear regression analysis, regression coefficient (R^2) had a higher value ($R^2 = 0.9617$). This result indicated that the elasticity obtained with microfluidic system exhibited consistent variations with respect to $C_{glycerin}$ when compared with elasticity obtained with conventional viscometer. Thus, the microfluidic system could be employed to measure viscoelasticity effectively. The slope of 0.0022 indicated that elasticity obtained with the microfluidic system was much less than that obtained with the conventional viscometer.

According to order analysis, C_B had an order of $O(10^{-13})$ from the analytical expression of time constant. Here, O represented order. According to experimental results as shown in Figure 5, the blood sample (normal RBCs suspended in plasma, $Hct = 50\%$) had $\lambda_B = 36.084 \pm 0.713$ s, $\mu_B = 2.422 \pm 0.028$ cP, and $R_{WB} = 135.148 \pm 2.03$ $\text{TPa}\cdot\text{s}/\text{m}^3$. The compliance (C_B) was then obtained as $C_B = 270.598 \pm 4.63$ $\mu\text{m}^3/\text{mPa}$. The corresponding order of each parameter was calculated as (1) $O(10^1)$ for λ_B , (2) $O(10^0)$ for μ_B , and $O(10^{12})$ for R_{WB} . As the unit of C_B was expressed as $\mu\text{m}^3/\text{mPa}$, the order of C_B was calculated as $O(10^{-18})/O(10^{-3}) = O(10^{-15})$. Thus, C_B obtained for the blood sample had an order of $O(10^{-13})$. In order words, both approaches (i.e., analytical expression, and experimental data) exhibited the same order of $O(10^{-13})$. Thus, the present method could be used to monitor C_B of blood samples sufficiently.

To compare the relationship between G_B and C_B , it was assumed that λ_{cv} of the conventional viscometer had the same λ_B as the microfluidic system (i.e., $\lambda_{cv} = \lambda_B$). The time constant obtained by the microfluidic system was used to evaluate G_B and C_B simultaneously. The following relation was given as $\frac{\mu}{G} = R_{WB} \times C_B$. The analytical expression indicated that G_B and C_B had a reciprocal relationship (i.e., $G \sim 1/C_B$). Using experimental results as shown in Figure 4, G_B and C_B were obtained with respect to $Hct = 30\%$, 40% , 50% , and 60% . Additionally, by referring to the previous study [18], variations of G_B were represented with respect to $Hct = 30\%$, 40% , and 50% . Here, blood samples were prepared by adding normal RBCs into plasma. As shown in Figure 7A, at $Hct > 40\%$, G_B tended to increase with respect to Hct . Inversely, C_B tended to decrease with respect to Hct . When compared with the previous study, the trend of G_B increased similarly with respect to Hct . It can be inferred that different microfluidic systems contributed to differences of G_B between both studies. Additionally, variations of C_B and G_B were summarized with respect to C_{GA} as shown in Figure 7B. Here, in the previous study [4], fixed blood samples were prepared by adding fixed RBCs into 1x PBS instead of plasma. G_B of both studies tended to increase gradually with respect to C_{GA} . From quantitative comparisons between the previous study and the present study, elasticity (G_B) and compliance (C_G) had a reciprocal relationship. Additionally, they varied significantly when the rigidity of RBCs increased substantially.

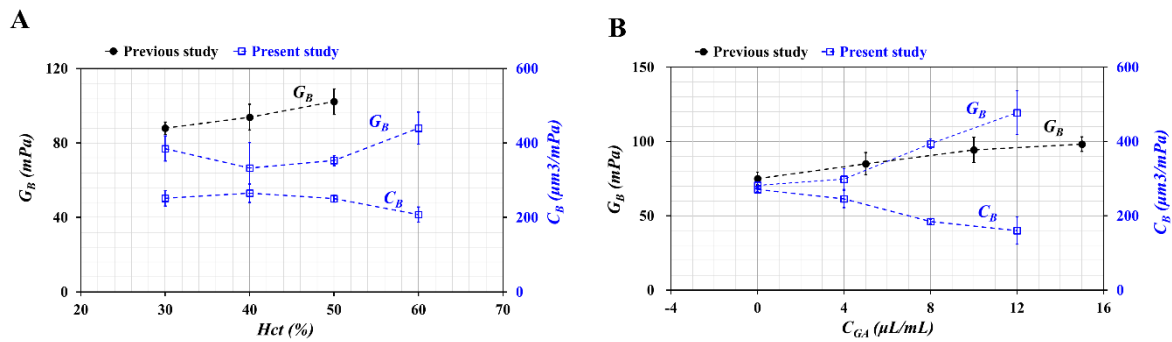


Figure 7. Quantitative compliance of G_B and C_B with respect to previous study [18] and present study. (A) Variation of G_B and C_B with respect to Hct . (B) Variations of G_B and C_B with respect to C_{GA} .

Viscoelasticity (G) was represented as $G = G_1 + j G_2$. Here, G_1 (storing modulus) and G_2 (loss modulus) were expressed as $G_1 = G \left(\frac{\lambda_B^2 \omega^2}{1 + \lambda_B^2 \omega^2} \right)$ and $G_2 = G \left(\frac{\lambda_B \omega}{1 + \lambda_B^2 \omega^2} \right)$. Variations of G_1 and G_2 were represented with respect to radial frequency (ω). G_1 and G_2 tended to vary depending on $\lambda_B \cdot \omega$. However, as $\lambda_B \cdot \omega$ showed a significant difference for both systems, it was apparent that both systems exhibited different variations of G_1 and G_2 with respect to ω . The microfluidic system and conventional viscometer showed different characteristics in terms of angular frequency (or period) and time constants. However, according to experimental results, the microfluidic system could be used effectively to evaluate the viscoelasticity of human blood when compared with conventional viscometers.

4. Conclusions

In this study, a viscoelasticity measurement method for human blood samples (normal blood sample, fixed blood sample) was suggested by quantifying the interface in coflowing streams when a blood sample was infused at a sinusoidal flow rate. Using a discrete fluidic circuit model, a first-order nonlinear differential equation for the interface (α_B) in coflowing streams was derived. Two approximation factors (F_1, F_2) were applied to convert a nonlinear term into a linear term. The viscosity and compliance (as viscoelasticity) were derived analytically from the linear differential equation. From numerical simulation, two approximate factors were obtained: $F_1 = 1.094$ and $F_2 = 1.1087$. The normalized difference between the nonlinear term and linear term was less than 10%. The experimental results showed that compliance varied linearly by period ($T = 120, 240, 360,$ and 480 s). However, the blood viscosity remained constant with respect to period. The hematocrit and diluent contributed to varying viscoelasticity. Finally, viscoelasticity varied substantially depending on the degree in rigidity of RBCs. From the experimental results, it was found that the present method had the ability to monitor variations of viscoelasticity while the syringe pump was set to a pulsatile flow-rate pattern. As a limitation, the microfluidic device used in this study had microfluidic channels that were rectangular shape. However, human or animal blood vessels are not rigid and possess circular shape. When compared with live blood vessels, the rectangular shape of microfluidic device might contribute to varying viscoelasticity of the microfluidic channels within the blood sample. Microfluidic channels with 90° turns can cause live mammalian cells to lyse and aggregate in corners, causing fluid flow disruptions. In our next design, we will evaluate the contributions of channel shape and dimensions to viscoelasticity characteristics of the blood samples. In the near future, the present method will be employed to obtain the viscoelasticity of a blood sample circulated under ex vivo and in vivo conditions. In other words, to measure biomechanical properties of blood circulating under an extracorporeal bypass loop or hemodialysis, the blood sample will be collected from the fluidic circuit at periodic intervals. Biomechanical properties are then evaluated with individual conventional viscometers. However, the repetitive collection tends to reduce blood volume in the circuit substantially. If the present method will be integrated into the future fluidic circuit, viscoelasticity of the blood sample will be obtained at various intervals of time, even without periodic collection of blood samples.

Blood volume loss might be reduced considerably in our microfluidic device when compared with the conventional method. Finally, the data obtained by the novel microfluidic system could be employed effectively to monitor vascular diseases and human health.

Supplementary Materials: The following are available online at <http://www.mdpi.com/2072-666X/11/3/245/s1>, Figure S1: Mask drawing of silicon mold.

Funding: This work was supported by the Basic Science Research Program through the NRF, funded by the Ministry of Science and ICT (MSIT) (NRF-2018R1A1A1A05020389).

Conflicts of Interest: The author declares no conflict of interest.

References

1. Benjamin, E.J.; Muntner, P.; Alonso, A.; Bittencourt, M.S.; Callaway, C.W.; Carson, A.P.; Chamberlain, A.M.; Chang, A.R.; Cheng, S.; Das, S.R.; et al. Heart disease and stroke statistics—2019 update. *Circulation* **2019**, *139*, e56–e528. [CrossRef] [PubMed]
2. Upadhyay, R.K. Emerging risk biomarkers in cardiovascular diseases and disorders. *J. Liquids* **2015**, *2015*, 971453. [CrossRef] [PubMed]
3. Melander, O.; Modrego, J.; Zamorano-Leon, J.J.; Santos-Sancho, J.M.; Lahera, I.; Lopez-Farre, A.J. New circulating biomarkers for predicting cardiovascular death in healthy population. *J. Cell. Mol. Med.* **2015**, *19*, 2489–2499. [CrossRef] [PubMed]
4. Mikeska, T.; Craig, J.M. DNA methylation biomarkers: Cancer and beyond. *Genes* **2014**, *5*, 821–864. [CrossRef] [PubMed]
5. Agrawal, R.; Smart, T.; Nobre-Cardoso, J.; Richards, C.; Bhatnagar, R.; Tufail, A.; Shima, D.; Jones, P.H.; Pavesio, C. Assessment of red blood cell deformability in type 2 diabetes mellitus and diabetic retinopathy by dual optical tweezers stretching technique. *Sci. Rep.* **2016**, *6*, 15873. [CrossRef] [PubMed]
6. Yeom, E.; Byeon, H.; Lee, S.J. Effect of diabetic duration on hemorheological properties and platelet aggregation in streptozotocin-induced diabetic rats. *Sci. Rep.* **2016**, *6*, 21913. [CrossRef]
7. Lygirou, V.; Latosinska, A.; Makridakis, M.; Mullen, W.; Delles, C.; Schanstra, J.P.; Zoidakis, J.; Pieske, B.; Mischak, H.; Vlahou, A. Plasma proteomic analysis reveals altered protein abundances in cardiovascular disease. *J. Transl. Med.* **2018**, *16*, 104. [CrossRef]
8. Lowe, G.; Rumley, A.; Norrie, J.; Ford, I.; Shepherd, J.; Cobbe, S.; Macfarlane, P.; Packard, C. Blood rheology, cardiovascular risk factors, and cardiovascular disease: The west of scotland coronary prevention study. *Thromb. Haemost.* **2000**, *84*, 553–558.
9. Koenig, W.; Sund, M.; Filipiak, B.; Doring, A.; Lowel, H.; Ernst, E. Plasma viscosity and the risk of coronary heart disease results from the MONICA-Augsburg cohort study, 1984 to 1992. *Aetior. Thromb. Vasc. Biol.* **1998**, *18*, 768–772. [CrossRef]
10. Tomaiuolo, G.; Carciati, A.; Caserta, S.; Guido, S. Blood linear viscoelasticity by small amplitude oscillatory flow. *Rheol. Acta* **2016**, *55*, 485–495. [CrossRef]
11. Kang, Y.J.; Yang, S. Fluidic low pass filter for hydrodynamic flow stabilization in microfluidic environments. *Lab Chip* **2012**, *12*, 1881–1889. [CrossRef] [PubMed]
12. Hong, H.; Song, J.M.; Yeom, E. 3D printed microfluidic viscometer based on the co-flowing stream. *Biomicrofluidics* **2019**, *13*, 014104. [CrossRef] [PubMed]
13. Yeom, E.; Kim, H.M.; Park, J.H.; Choi, W.; Doh, J.; Lee, S.-J. Microfluidic system for monitoring temporal variations of hemorheological properties and platelet adhesion in LPS-injected rats. *Sci. Rep.* **2017**, *7*, 1801. [CrossRef] [PubMed]
14. Tomaiuolo, G.; Barra, M.; Preziosi, V.; Cassinese, A.; Rotoli, B.; Guido, S. Microfluidics analysis of red blood cell membrane viscoelasticity. *Lab Chip* **2011**, *11*, 449–454. [CrossRef] [PubMed]
15. Cha, S.; Shin, T.; Lee, S.S.; Shim, W.; Lee, G.; Lee, S.J.; Kim, Y.; Kim, J.M. Cell stretching measurement utilizing viscoelastic particle focusing. *Anal. Chem.* **2012**, *84*, 10471–10477. [CrossRef] [PubMed]
16. Kang, Y.J.; Lee, S.-J. Blood viscoelasticity measurement using steady and transient flow controls of blood in a microfluidic analogue of Wheastone-bridge channel. *Biomicrofluidics* **2013**, *7*, 054122. [CrossRef] [PubMed]
17. Kang, Y.J. Continuous and simultaneous measurement of the biophysical properties of blood in a microfluidic environment. *Analyst* **2016**, *141*, 6583–6597. [CrossRef]


18. Kang, Y.J. Simultaneous measurement of erythrocyte deformability and blood viscoelasticity using micropillars and co-flowing streams under pulsatile blood flows. *Biomicrofluidics* **2017**, *11*, 014102. [CrossRef]
19. Kang, Y.J. Periodic and simultaneous quantification of blood viscosity and red blood cell aggregation using a microfluidic platform under in-vitro closed-loop circulation. *Biomicrofluidics* **2018**, *12*, 024116. [CrossRef]
20. Kang, Y.J. Microfluidic-based biosensor for sequential measurement of blood pressure and RBC aggregation over continuously varying blood flows. *Micromachines* **2019**, *10*, 577. [CrossRef]
21. Otsu, N. A threshold selection method from gray-level histograms. *IEEE Trans. Syst. Man. Cybern.* **1979**, *9*, 62–66. [CrossRef]
22. Lee, J.; Tripathi, A. Intrinsic Viscosity of Polymers and Biopolymers Measured by Microchip. *Anal. Chem.* **2005**, *77*, 7137–7147. [CrossRef]
23. Solomon, D.E.; Vanapalli, S.A. Multiplexed microfluidic viscometer for high-throughput complex fluid rheology. *Microfluid. Nanofluid.* **2014**, *16*, 677–690. [CrossRef]
24. Choi, S.; Park, J.-K. Microfluidic Rheometer for Characterization of Protein Unfolding and Aggregation in Microflows. *Small* **2010**, *6*, 1306–1310. [CrossRef] [PubMed]
25. Kang, Y.J. Microfluidic-based measurement of RBC aggregation and the ESR using a driving syringe system. *Anal. Methods* **2018**, *10*, 1805–1816. [CrossRef]
26. Jalal, U.M.; Kim, S.C.; Shim, J.S. Histogram analysis for smartphone-based rapid hematocrit determination. *Biomed. Opt. Express* **2017**, *8*, 3317–3328. [CrossRef]
27. Kim, B.J.; Lee, Y.S.; Zhanov, A.; Yang, S. A physiometer for simultaneous measurement of whole blood viscosity and its determinants: Hematocrit and red blood cell deformability. *Analyst* **2019**, *144*, 3144–3157. [CrossRef]
28. Kang, Y.J. Simultaneous measurement of blood pressure and RBC aggregation by monitoring on–off blood flows supplied from a disposable air-compressed pump. *Analyst* **2019**, *144*, 3556–3566. [CrossRef]
29. Campo-Deano, L.; Dullens, R.P.A.; Aarts, D.G.A.L.; Pinho, F.T.; Oliveira, M.S.N. Viscoelasticity of blood and viscoelastic blood analogues for use in polydimethylsiloxane in vitro models of the circulatory system. *Biomicrofluidics* **2013**, *7*, 034102. [CrossRef]
30. Sousa, P.C.; Vaz, R.; Cerejo, A.; Oliveira, M.S.N.; Alves, M.A.; Pinho, F.T. Rheological behavior of human blood in uniaxial extensional flow. *J. Rheol.* **2018**, *62*, 447–456. [CrossRef]



© 2020 by the author. Licensee MDPI, Basel, Switzerland. This article is an open access article distributed under the terms and conditions of the Creative Commons Attribution (CC BY) license (<http://creativecommons.org/licenses/by/4.0/>).

Article

Experimental Investigation of Air Compliance Effect on Measurement of Mechanical Properties of Blood Sample Flowing in Microfluidic Channels

Yang Jun Kang 

Department of Mechanical Engineering, Chosun University, 309 Pilmun-daero, Dong-gu, Gwangju 61452, Korea; yjkang2011@chosun.ac.kr; Tel.: +82-62-230-7052; Fax: +82-62-230-7055

Received: 9 April 2020; Accepted: 27 April 2020; Published: 28 April 2020



Abstract: Air compliance has been used effectively to stabilize fluidic instability resulting from a syringe pump. It has also been employed to measure blood viscosity under constant shearing flows. However, due to a longer time delay, it is difficult to quantify the aggregation of red blood cells (RBCs) or blood viscoelasticity. To quantify the mechanical properties of blood samples (blood viscosity, RBC aggregation, and viscoelasticity) effectively, it is necessary to quantify contributions of air compliance to dynamic blood flows in microfluidic channels. In this study, the effect of air compliance on measurement of blood mechanical properties was experimentally quantified with respect to the air cavity in two driving syringes. Under periodic on–off blood flows, three mechanical properties of blood samples were sequentially obtained by quantifying microscopic image intensity ($\langle I \rangle$) and interface (α) in a co-flowing channel. Based on a differential equation derived with a fluid circuit model, the time constant was obtained by analyzing the temporal variations of $\beta = 1/(1-\alpha)$. According to experimental results, the time constant significantly decreased by securing the air cavity in a reference fluid syringe (~ 0.1 mL). However, the time constant increased substantially by securing the air cavity in a blood sample syringe (~ 0.1 mL). Given that the air cavity in the blood sample syringe significantly contributed to delaying transient behaviors of blood flows, it hindered the quantification of RBC aggregation and blood viscoelasticity. In addition, it was impossible to obtain the viscosity and time constant when the blood flow rate was not available. Thus, to measure the three aforementioned mechanical properties of blood samples effectively, the air cavity in the blood sample syringe must be minimized ($V_{air, R} = 0$). Concerning the air cavity in the reference fluid syringe, it must be sufficiently secured about $V_{air, R} = 0.1$ mL for regulating fluidic instability because it does not affect dynamic blood flows.

Keywords: air compliance effect; RBC aggregation; blood viscosity; blood viscoelasticity; blood velocity fields; interface in co-flowing streams; microfluidic device

1. Introduction

A blood sample is composed of cells (i.e., red blood cells (RBCs), white blood cells, and platelets) and plasma. Given that the number of RBCs is much larger than that of the other cells, RBCs have a significant role in determining mechanical properties of blood samples (viscosity, deformability, and aggregation). In addition, plasma proteins substantially contribute to increasing aggregation. Since a strong relationship between cardiovascular diseases and mechanical properties of blood samples was reported [1–4], mechanical properties of blood samples have been suggested as label-free biomarkers for early detection of cardiovascular diseases.

In contrast with bulky viscometers [5,6], a microfluidic-based device can provide numerous advantages including fast response, small volume consumption, and disposability. Currently,

such devices are widely employed for quantifying mechanical properties of blood samples (viscosity [7–10], RBC aggregation [11–14], RBC deformability [3,15], and hematocrit (Hct) [16–18]). A microfluidic device has been also employed to separate RBCs or tumor cells from whole blood sample [19–21].

In microfluidic environments, blood flows must remain unchanged over time to measure blood viscosity accurately. However, during the process of supplying a blood sample into a microfluidic device, the syringe pump causes fluidic instability at low flow rates [22]. To stabilize unstable flows resulting from the syringe pump, several techniques including air cavity in a driving syringe [23] or microfluidic channel [24,25], portable air cavity unit [22,26], and flexible compliance unit [27–32], were demonstrated in microfluidic systems. These methods act on the compliance element in the fluidic circuit model. The compliance was defined as $C = \Delta V / \Delta P$. Here, ΔV and ΔP represents variations of volume and pressure, respectively. This contributes to regulating alternating components and increasing the time constant. Thus, they contribute to removing alternating components of blood flows. Owing to the compliance effect, the fluidic flow remains constant over time. Additionally, the compliance effect tends to delay transient blood flows significantly. Among the aforementioned methods, an air cavity secured inside the syringe is simple and effective because it does not require additional devices. In other words, a disposable syringe (~1 mL) is partially filled with a blood sample (~lower layer) and an air cavity (~upper layer), respectively. Then, the syringe is placed into a syringe pump. Given that the air cavity secured inside the syringe contributes to damping out fluidic fluctuations resulting from the syringe pump [22], the blood flows remain constant over time in the microfluidic channel.

Blood viscosity is measured with a microfluidic device under constant shearing flow condition. After a blood sample and a reference fluid are infused into the microfluidic device at the same flow rate, blood viscosity can be quantified by monitoring the interface in co-flowing streams [8,10]. RBC aggregation is obtained by quantifying the microscopic image intensity of the blood sample under periodic on-off fashion or transient fluidic flows [33,34]. Owing to RBC aggregation in blood samples, the image intensity tends to increase after the blood flow stops suddenly. However, the air cavity secured inside the disposable syringe (i.e., air compliance) has an influence on transient behaviors of blood flows. When turning the syringe pump off suddenly, it takes a longer time to stop blood flows because of the air-compliance effect. Within a specific duration, the blood flow rate does not decrease to sufficiently lower shear rates where RBC aggregation occurs. Thus, it is impossible to quantify RBC aggregation. A simple method to resolve this issue is a pinch valve to stop blood flows immediately [35]. A time constant defining blood viscoelasticity can be obtained by monitoring the interface in co-flowing streams under periodic transient blood flows [33,36]. In other words, after turning the syringe pump off, a time constant is obtained by analyzing the transient behavior of blood flows (i.e., blood velocity). However, when a pinch valve is used to stop blood flows immediately, it is impossible to obtain the time constant throughout transient variations of blood flows. Although air compliance is used effectively for measuring blood viscosity, it hinders the quantification of RBC aggregation or blood viscoelasticity. To quantify the mechanical properties of blood samples (i.e., blood viscosity, RBC aggregation, and viscoelasticity) effectively, it is necessary to quantify contributions of air compliance to dynamic blood flows in microfluidic channels.

In this study, the air compliance effect on measurement of blood mechanical properties was quantified experimentally with respect to the air cavity in two driving syringes. To measure the three aforementioned mechanical properties of the blood sample (i.e., blood viscosity, RBC aggregation, and viscoelasticity), both the blood sample and the reference fluid were filled with individual syringes. The air cavity inside each syringe set a certain volume ranging from 0 to 0.2 mL. After placing them into syringe pumps, the blood sample and reference fluid were infused into a microfluidic channel. The flow rate of the reference fluid remained constant over time. The flow rate of the blood sample was controlled by turning the syringe pump on or off periodically. Three mechanical properties of the

blood sample were obtained sequentially by quantifying the microscopic image intensity of the blood sample and the interface between the two fluids flowing in a co-flowing channel, respectively.

As a demonstration, the time constants of test fluids (i.e., blood sample and glycerin (20%)) were first obtained by varying the air cavity in the reference fluid syringe for up to 0.2 mL. Second, variations of the time constant were obtained with respect to Hct = 30%, 40%, and 50%. Finally, to stimulate RBC aggregation, a blood sample (Hct = 50%) was prepared by adding normal RBCs into different diluents (i.e., 1× PBS (phosphate-buffered saline), plasma, and two dextran solutions). The effect of air compliance on the three mechanical properties of blood samples considered was evaluated by varying the air cavity secured in each syringe (~0.1 mL).

2. Materials and Methods

2.1. Blood Sample Preparation

The Ethics Committee of Chosun University Hospital (CHOSUN 2018-05-11) approved all experimental protocols conducted for this study. Such protocols were deemed appropriate and humane. Gwangju–Chonnam blood bank (Gwangju, Korea) provided concentrated RBCs and fresh frozen plasma (FFP). After conducting washing procedures with a centrifuge twice, pure RBCs were collected from the concentrated RBCs. Additionally, plasma was prepared by thawing FFP at a room temperature of 25 °C. To evaluate the three considered mechanical properties of blood sample with respect to air cavity, various blood samples were prepared by changing hematocrit or diluent. First, to evaluate the contributions of hematocrit or diluent to the time constant (or viscoelasticity), the hematocrit of blood sample was adjusted to Hct = 30%, 40%, and 50% by adding normal RBCs into the diluent (i.e., 1× phosphate-buffered saline (PBS), and plasma). Second, to stimulate RBC aggregation in blood samples, a specific concentration of dextran solution was added into 1× PBS. Dextran powder (*Leuconostoc* spp., MW = 450–650 kDa, Sigma–Aldrich, St. Louis, MO, USA) was diluted with 1× PBS. A blood sample (Hct = 50%) was prepared by adding normal RBCs into two dextran solutions (5, and 10 mg/mL).

2.2. Microfluidic Device and Experimental Setup

As shown in Figure 1A-a, a microfluidic device consisted of two inlets (a, b), one outlet, and two guiding channels (test fluid channel (TC, width (W) = 1000 μm), reference fluid channel (RC, width (W) = 100 μm)), and co-flowing channel (CC, width (W) = 1000 μm). To increase blood volume flowing in test channel, channel depth was set to $h = 100 \mu\text{m}$ if available under micro-electromechanical-system technique (MEMS) fabrication. A four-inch sized silicon mold was fabricated using the MEMS techniques (i.e., photolithography and deep reactive ion etching). Polymer PDMS (polydimethylsiloxane) (Sylgard 184, Dow Corning, Midland, MI, USA) and a curing agent were mixed at a ratio of 10:1. Mixed PDMS was poured onto the silicon mold. After letting it solidify into a convective oven (70 °C for 1 h), the cured PDMS was peeled off from the mold. Two inlets (a, b) and one outlet were punched with a biopsy punch (outer diameter = 0.5 mm). Using an oxygen plasma system (CUTE-MPR, Femto Science Co., Hwaseong-si, South Korea), the PDMS block was strongly bonded to the glass slide.

To squeeze out the air bubble inside the microfluidic channels and avoid adherence of RBCs to the channels, microfluidic channels were filled with a bovine serum albumin of 2 mg/mL through the outlet. After an elapse of 10 min, the microfluidic channels were filled again with 1× PBS. As shown in Figure 1A-b, a reference fluid syringe was filled with 1× PBS (~0.5 mL) and air cavity ($V_{air, R}$), respectively. Likewise, a test fluid syringe was filled with a test fluid (~0.5 mL) and air cavity ($V_{air, T}$), respectively. To supply the reference fluid into the reference fluid channel, a polyethylene tubing (length = 300 mm, inner diameter = 0.25 mm, and thickness = 0.25 mm) was connected from a syringe needle to inlet (a). To infuse the test fluid into the blood sample channel, a polyethylene tubing (length = 300 mm, inner diameter = 0.25 mm, and thickness = 0.25 mm) was connected from a syringe

needle to inlet (b). To collect both samples from the co-flowing channel, a polyethylene tubing (length = 200 mm, inner diameter = 0.25 mm, and thickness = 0.25 mm) was fitted tightly into the outlet. Using two syringe pumps (neMESYS, Cetoni GmbH, Korbussen, Germany), the reference fluid was infused at a constant flow rate of $Q_R = Q_0$. The test fluid was supplied at periodic on-off fashion (period (T) = 240 s, duty ratio = 0.5, and $Q_T = Q_0$). A microfluidic device was placed on an optical inverted microscope (BX51, Olympus, Tokyo, Japan) equipped with a 10× objective lens (NA = 0.25). A high-speed camera (FASTCAM MINI, Photron, Tokyo, Japan) captured two microscopic images sequentially at a frame rate of 500 fps. The image acquisition continued at an interval of 0.5 s with a function generator. All experiments were conducted at a temperature of 25 °C.

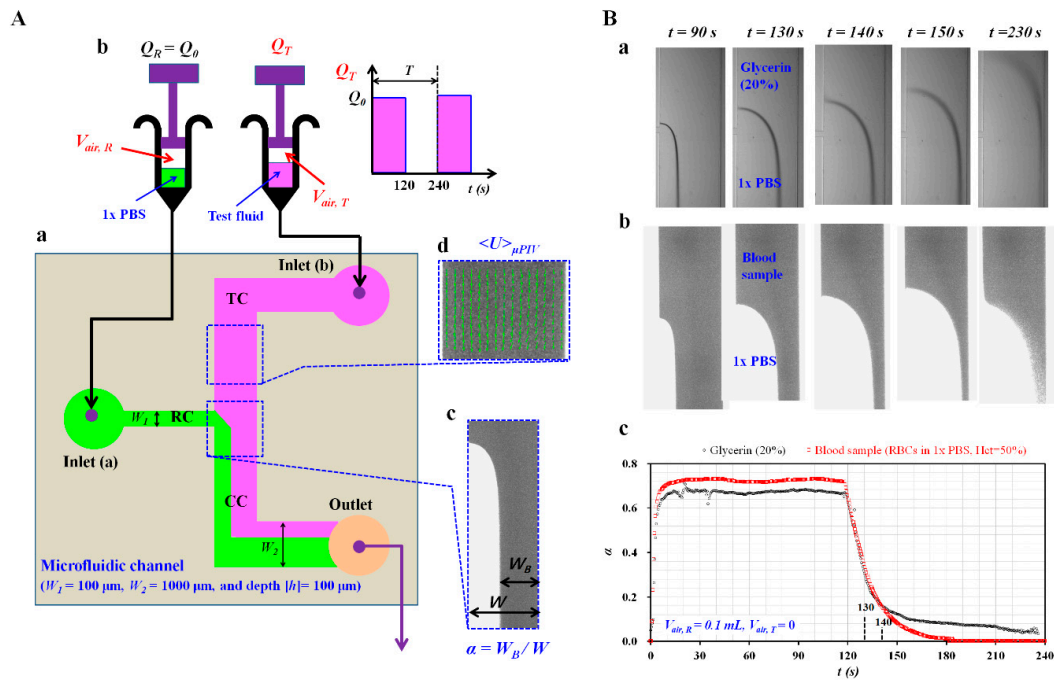


Figure 1. Proposed method for measuring the effect of air compliance on measurement of mechanical properties of blood samples flowing in microfluidic channels. (A) Schematic diagram of experimental setup including a microfluidic device, two syringe pumps, and an image acquisition system. (a) A microfluidic device comprising two inlets (a, b), one outlet, two guiding channels for two fluids (reference channel (RC), test channel (TC)), and a co-flowing channel (CC). (b) Two syringe pumps for delivering reference fluid and test fluid. (c) The interface in the co-flowing channel was quantified as $\alpha = W_B/W$. (d) Velocity fields of blood flows obtained with a micro-particle image velocimetry (PIV) technique. (B) As a preliminary demonstration, a blood sample (normal red blood cells (RBCs) in 1× phosphate-buffered saline (PBS), hematocrit (Hct) = 50%) and glycerin (20%) as a test fluid were prepared to show temporal variations of α . (a) Microscopic images of a blood sample and 1× PBS flowing in the co-flowing channel at specific time instants ($t = 90, 130, 140, 150,$ and 230 s). (b) Microscopic images of glycerin (20%) and 1× PBS flowing in the co-flowing channel at specific time instants ($t = 90, 130, 140, 150,$ and 230 s). (c) Temporal variations of α with respect to the blood sample and glycerin (20%).

2.3. Quantification of Interface, Velocity Fields, and Image Intensity

The right side panel in Figure 1A-c shows a microscopic image taken for estimating the interface in a co-flowing channel. A specific region-of-interest (ROI, 240×200 pixels) was selected within a straight region of the co-flowing channel. Using MATLAB 2019 (MathWorks, Natick, MA, USA), the blood-filled width (W_B) over the ROI was estimated with Otsu’s method [37]. The interface in the co-flowing channel (α) was defined as $\alpha = W_B/W$. As shown in Figure 1A-d, the velocity fields of the blood sample in the test fluid channel were obtained with a micro-particle image velocimetry (PIV)

technique [38]. A specific ROI (240×200 pixels) was selected within the test fluid channel. The size of the interrogation window was 32×32 pixels. The window overlap was 50%. The velocity fields within ROI were validated with a local median filter. The average velocity ($\langle U \rangle_{\mu PIV}$) was obtained by averaging the velocity fields over the ROI. To evaluate the RBC aggregation of the blood sample, the microscopic image intensity of the blood sample flowing in the test fluid channel was quantified with digital image processing. As shown on the right side channel, a specific ROI (240×200 pixels) was selected within the test fluid channel. An average image intensity ($\langle I \rangle$) was obtained by averaging the image intensities distributed over the ROI.

As a preliminary demonstration, three properties of blood sample (i.e., blood viscosity, RBC aggregation, and viscoelasticity) were quantified by analyzing interface in coflowing channel (α) and image intensity of blood flows in test channel ($\langle I \rangle$), respectively. A blood sample (normal RBCs suspended in $1 \times$ PBS, Hct = 50%) and glycerin (20%) as the test fluid were prepared to show temporal variations of the interface (α) depending on the air cavity in a syringe. Two syringes were filled with the test fluid (~ 0.5 mL) and reference fluid (~ 0.5 mL), respectively. Then, the air cavity in the reference fluid syringe was set to 0.1 mL. The air cavity in the test fluid syringe was set to zero. Furthermore, $1 \times$ PBS as reference fluid was injected at a constant flow rate of $Q_0 = 1$ mL/h. The test fluid was injected in a periodic on-off fashion ($T = 240$ s, duty ratio = 0.5, and $Q_0 = 1$ mL/h). Figure 1B-a,b show microscopic images of two test fluids (i.e., blood sample and glycerin (20%)) at specific time instants ($t = 90, 130, 140, 150,$ and 230 s). When capturing microscopic images as shown in Figure 1B-b, light intensity increases significantly in order to clearly see RBCs flowing in the test channel. After turning off the syringe pump of the test fluid at $t = 120$ s, the blood-filled width (W_B) tended to decrease over time. Figure 1B-c shows temporal variations of the obtained α with respect to blood sample and glycerin (20%), respectively. Under the constant blood flow condition (i.e., $t < 120$ s), the value of α of the blood sample was higher than that of glycerin (20%). Under the transient flow condition (i.e., $120 \text{ s} < t < 240 \text{ s}$), the value of α of the blood sample took longer to reach a constant value compared with glycerin (20%). After turning on the syringe pump for the blood sample, the blood flow rate and interface (α) remained constant after an elapse of time constant. Blood viscosity was then quantified with the information of the interface. After an elapse of a half period, the syringe pump for the blood sample was set to turn off. The interface decreased substantially over time. After an elapse of the time constant, RBC aggregation occurred and contributed to increasing image intensity of the blood sample. RBC aggregation was then obtained by analyzing temporal variations of image intensity. In other words, blood viscosity and RBC aggregation were obtained at a constant flow rate and extremely low flow rate, respectively. Thus, to measure both properties effectively, it was necessary to secure sufficient duration of constant flow rate and stationary flow rate under periodic on-off operation of the syringe pump. In other words, time constant should remain much smaller than half period. Air compliance was used widely to eliminate fluidic instability resulting from the syringe pump. However, the air compliance tended to increase time constant substantially. When turning on syringe pump (i.e., $0 < t < 0.5 T$), the air cavity (~ 0.1 mL) inside syringe did not arrive at a constant value of β . When turning off the syringe pump (i.e., $0.5 T < t < T$), β decreased gradually over time. The longer time constant made it difficult to quantify both properties of blood samples. As air compliance hindered in quantifying blood viscosity and RBC aggregation, it is necessary to minimize the time constant by removing the air cavity in the blood syringe pump and securing the air cavity in reference syringe. Thus, the dynamic behavior of two fluids (i.e., time constant) should be considered as a significant factor for effectively quantifying blood viscosity and RBC aggregation under periodic on-off blood flow condition.

3. Results and Discussion

3.1. Variations of Time Constant with Respect to Air Cavity in Reference Fluid Syringe

According to previous studies [22,23,26,29], air compliance was widely used to stabilize fluidic instability resulting from syringe pumps. In this study, a reference fluid was injected at a constant flow

rate with a syringe pump. However, the air cavity in the reference fluid syringe might have an influence on the dynamic variation of the interface in co-flowing channels. For this reason, it was necessary to evaluate the contributions of the air cavity in the reference fluid syringe to time constants of the interface in co-flowing channels. The air cavity in the reference fluid syringe was set to $V_{air,R} = 0, 0.1, \text{ and } 0.2 \text{ mL}$. To separate the effect of the air cavity in the test fluid syringe, such a cavity was set to zero ($V_{air,T} = 0$). Blood samples (normal RBCs suspended in $1\times \text{PBS}$, $\text{Hct} = 50\%$) and glycerin (20%) were prepared as test fluids.

To model the contribution of the air cavity in the syringe to interface, it was required to derive a governing equation for two fluids flowing in a co-flowing channel. As shown in Figure 2A, a fluidic circuit model for two fluids (reference fluid and test fluid) flowing in a co-flowing channel was constructed with discrete circuit elements (i.e., flow rate elements: Q_R, Q_T , resistance elements: R_R, R_T , and compliance element: C_T). Here, C_T denotes the compliance element that was combined with flexible tubing, a microfluidic channel, and an air cavity in the syringe. Additionally, ground (\blacktriangledown) represents pressure set to zero. To keep the mathematical model simple, the interface in the co-flowing channel was modeled as a virtual wall. Different boundary conditions between the real physical model and the mathematical model were compensated by adding a correction factor (C_f) into the governing equation [39]. Thus, both fluids in the co-flowing channel were modeled independently with discrete circuit elements. The governing equation on interface (α) for both fluids flowing in the co-flowing channel is expressed as follows:

$$C_T R_{WT} \frac{d}{dt} \left(\frac{C_f}{1-\alpha} \right) + \frac{C_f \alpha}{1-\alpha} = \left(\frac{Q_T}{Q_R} \right) \left(\frac{\mu_T}{\mu_R} \right) \quad (1)$$

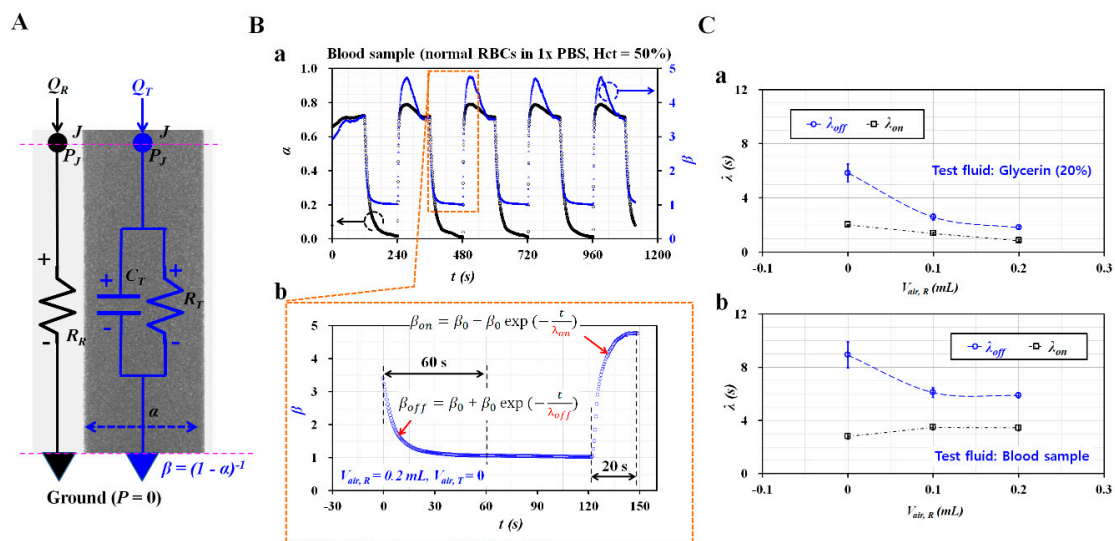


Figure 2. Quantitative evaluations of time constant with respect to the air cavity in the reference fluid syringe ($V_{air,R} = 0, 0.1, \text{ and } 0.2 \text{ mL}$). Here, the air cavity in the test fluid syringe was set to zero. (A) Fluidic circuit model for two fluids (reference fluid, test fluid) flowing in a co-flowing channel. (B) Quantifications of time constants ($\lambda_{off}, \lambda_{on}$) during each period. (a) Temporal variations of α and β with respect to $V_{air,R} = 0.2 \text{ mL}$. (b) Quantifications of λ_{off} and λ_{on} during turn-on and turn-off operation of the syringe pump. (C) Variations of λ_{off} and λ_{on} with respect to the test fluids (blood sample and glycerin (20%)) and air cavity in the reference syringe ($V_{air,R} = 0, 0.1 \text{ and } 0.2 \text{ mL}$). (a) Variations of λ_{off} and λ_{on} with respect to $V_{air,R}$ and glycerin (20%). (b) Variations of λ_{off} and λ_{on} with respect to $V_{air,R}$ and blood sample.

Here, R_{WT} is given by $R_{WT} = 12\mu_T L_{cc} / (W_T h^3)$, where L_{cc} denotes the channel length of the co-flowing channel. Subscript T means test fluid. Instead of subscript T, subscript B is also used

for representing blood sample. According to a numerical simulation using CFD-ACE+ (Ver. 2019, ESI Group, Paris, France), the correction factor could be approximately expressed as $C_f = 6.6908 \alpha^4 - 13.382 \alpha^3 + 10.81 \alpha^2 - 4.1196 \alpha + 1.6206$ ($R^2 = 0.9922$, $0.1 < \alpha < 0.9$) (Figure A1, Appendix A). Because of the nonlinear terms in the left member of Equation (1), the differential equation was difficult to solve substantially. Based on an approximate procedure [39], two approximate coefficients (F_1, F_2) were obtained as $F_1 = 1.112, F_2 = 1.129$, respectively. Consequently, $1/(1-\alpha)$ was converted into β and Equation (1) was transformed into a linear differential equation as follows:

$$\lambda \frac{d}{dt}(\beta) + \beta = 1 + \frac{1}{F_2} \left(\frac{Q_T}{Q_R} \right) \left(\frac{\mu_T}{\mu_R} \right) \quad (2)$$

In Equation (2), the time constant (λ) is expressed as $\lambda = \frac{F_1}{F_2} C_T R_{WT} \cong C_T R_{WT}$. The compliance element (C_T) presents a linear relation with the time constant (λ) and includes the effect of the air cavity in the syringe. Thus, the contribution of the air cavity could be obtained quantitatively by measuring the time constant (λ) with transient behaviors of β .

As shown in Figure 2B-a, temporal variations of α and β were obtained with respect to the blood sample (normal RBCs suspended in $1 \times$ PBS, Hct = 50%). Here, the air cavity in the reference fluid syringe was set to 0.2 mL ($V_{air,R} = 0.2$ mL). Based on Equation (2), the temporal variations of β were represented as shown in Figure 2B-b. When sequentially turning syringe pumps on and off, two time constants ($\lambda_{off}, \lambda_{on}$) could be obtained by analyzing transient variations of β . First, under the turn-off operation of a syringe pump, temporal variations of β_{off} were extracted for 60 s. Based on an exponential model (i.e., $\beta_{off} = \beta_0 + \beta_1 \exp(-t/\lambda_{off})$), λ_{off} was obtained by conducting nonlinear regression analysis with Matlab 2019. Second, under the turn-on operation of a syringe pump, β_{on} converged in a shorter time interval than for β_{off} . Temporal variations of β_{on} were extracted for 20 s. Similarly, based on an exponential model (i.e., $\beta_{on} = \beta_0 + \beta_1 \exp(-t/\lambda_{on})$), λ_{on} was obtained by conducting non-linear regression analysis. Figure 2C-a shows variations of λ_{off} and λ_{on} with respect to $V_{air,R}$ and glycerin (20%). All experimental data were expressed as mean \pm standard deviation. The error bar represented single standard deviation. Note that λ_{off} was much longer than λ_{on} within 0.2 mL of the air cavity. Additionally, λ_{off} decreased substantially when the cavity volume increased from 0 to 0.1 mL. Above $V_{air,R} = 0.1$ mL, it decreased slightly. Figure 2C-b shows variations of λ_{off} and λ_{on} with respect to $V_{air,R}$ and the blood sample. Similar to the glycerin solution, λ_{off} decreased considerably when the air cavity increased from 0 to 0.1 mL. The air cavity in the reference fluid syringe (~ 0.1 mL) contributed to decreasing the time constant (λ_{off}) significantly. However, λ_{on} did not present distinctive variations with respect to the air cavity in the reference fluid syringe. Additionally, two time constants remained unchanged above $V_{air,R} = 0.1$ mL. According to discrete fluidic circuit analysis, air compliance (C) plays a role in regulating the alternating component of the flow rate. In this study, flow rate of the reference fluid remained unchanged over time. It was modeled as direct component of flow rate. Thus, air cavity secured in reference syringe did not contribute to the changing time constant. However, air cavity with 0.1 mL decreased time constant substantially. Taking into account the fact that air compliance caused the time constant to increase generally, the result showed different trends. Above a 0.1 mL air cavity, the time constant varied slightly. The constant value of the time constant was obtained through fluid viscosity and the compliance effect of the tubing and PDMS device. According to these experimental results, the air cavity in the reference fluid syringe (~ 0.1 mL) contributed to decreasing λ_{off} greatly. Note that λ_{off} decreased more significantly than λ_{on} . Above an air cavity volume of 0.1 mL, the time constants did not present substantial variation.

3.2. Valuations of Time Constant with Respect to Hematocrit and Air Cavity in Blood Sample Syringe

First, to evaluate the contribution of hematocrit to the time constant, the blood sample (Hct = 30%, 40%, and 50%) was prepared by adding normal RBCs into $1 \times$ PBS. As shown in Figure 3A-a, variations of λ_{off} and λ_{on} were obtained with respect to Hct. To evaluate the contribution of the air cavity in

the reference fluid syringe, such a cavity was set to $V_{air,R} = 0$ and 0.1 mL. The air cavity in the blood sample syringe was set to $V_{air,B} = 0$. In contrast with λ_{on} , λ_{off} increased largely with respect to Hct. In addition, the air cavity in the reference fluid syringe contributed to decreasing the time constant substantially. As shown in Figure 3A-b, a scatter plot was constructed by plotting λ_{on} on Y-axis and λ_{off} on X-axis. According to linear regression analysis, the following linear regression formula was obtained: $\lambda_{on} = 0.2815 \lambda_{off} + 1.4967$ ($R^2 = 0.8282$). The high regression coefficient (R^2) denotes that λ_{on} and λ_{off} showed a strong linear relationship. From these results, λ_{off} was selected as the representative time constant throughout this study.

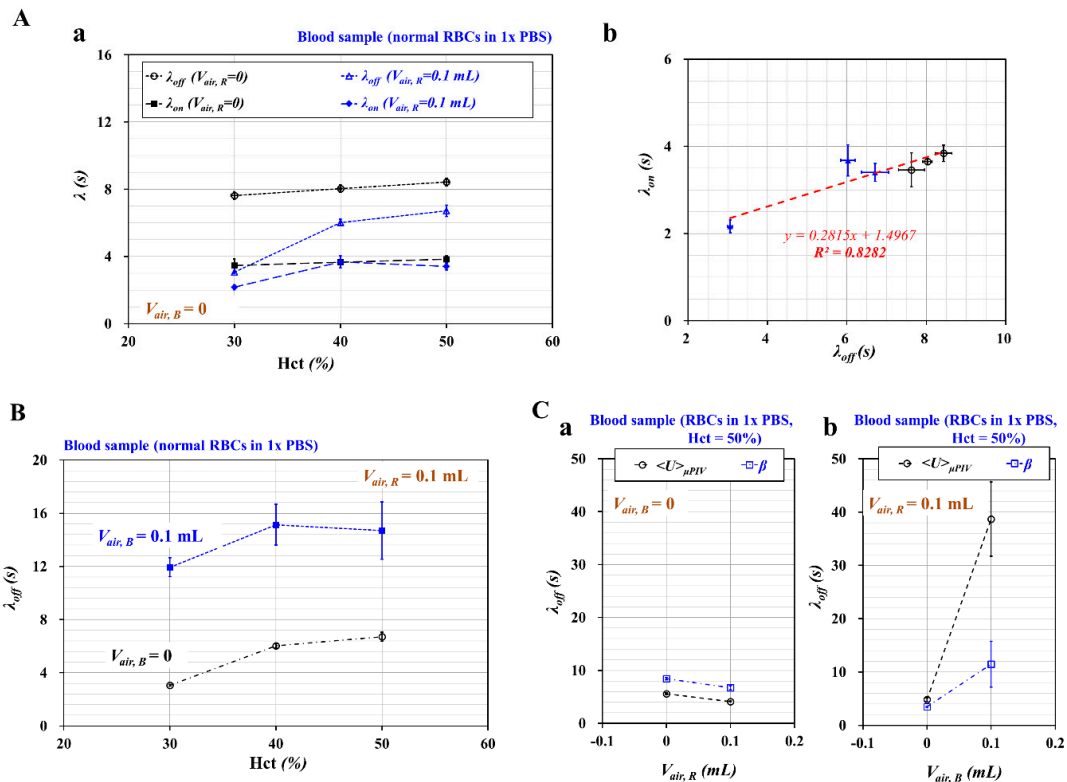


Figure 3. Quantitative evaluations of time constants (λ_{off} , λ_{on}) with respect to hematocrit and air cavity in each syringe. Here, a blood sample was prepared by adding normal RBCs into 1× PBS. (A) The comparison of two time constants with respect to hematocrit and air cavity. (a) Variations of λ_{off} and λ_{on} with respect to Hct = 30%, 40%, and 50% and $V_{air,R} = 0$ and 0.1 mL. (b) Linear relationship between λ_{off} and λ_{on} . Here, the air cavity in the blood sample syringe was set to zero. (B) Variations of λ_{off} and λ_{on} with respect to Hct = 30%, 40%, and 50% with $V_{air,B} = 0$ and 0.1 mL. Here, the air cavity in the reference fluid syringe was set to 0.1 mL. (C) Quantitative comparison of λ_{off} obtained from $\langle U \rangle_{\mu PIV}$ and β . The hematocrit of the blood sample was adjusted to Hct = 50% by adding normal RBCs into 1× PBS. (a) Comparison of λ_{off} obtained from $\langle U \rangle_{\mu PIV}$ and β with respect to $V_{air,R} = 0$ and 0.1 mL. Here, the air cavity in the blood sample syringe was set to zero. (b) Comparison of λ_{off} obtained from $\langle U \rangle_{\mu PIV}$ and β with respect to $V_{air,B} = 0$ and 0.1 mL. Here, the air cavity in the reference fluid syringe was set to 0.1 mL.

Second, to evaluate the effect of the air cavity in the blood sample syringe ($V_{air,B}$) on the time constant (λ_{off}), such cavity was set to $V_{air,B} = 0$, and 0.1 mL. Additionally, to stabilize the fluidic instability resulting from the syringe pump, the air cavity in the reference fluid syringe was set to $V_{air,R} = 0.1$ mL. As shown in Figure 3B, variations of λ_{off} were obtained with respect to Hct = 30%, 40%, and 50% and $V_{air,B} = 0$, and 0.1 mL. The air cavity in the blood sample syringe contributed to increasing the time constant substantially. Theoretically, the size of syringe pump did not contribute to the varying time constant. According to the previous study [22], the time constant tended to increase

linearly with respect to air cavity volume. In other words, air cavity secured in each syringe varied dynamic behaviors of β in coflowing channels (i.e., time constant). Thus, it is necessary to fix air cavity secured in each syringe. Note that, interestingly, the air cavity in the reference fluid syringe contributed to decreasing λ_{off} , as shown in Figure 3A-a. From these results, we inferred that the air cavity increased or decreased the time constant depending on whether it existed in the reference fluid syringe or the blood sample syringe.

Third, to compare the time constant with temporal variations of β , the time constant was additionally obtained with temporal variations of the average velocity of the blood flow in the test fluid channel ($\langle U \rangle_{\mu PIV}$). A blood sample (Hct = 50%) was prepared as the test fluid by adding normal RBCs into 1× PBS. Figure 3C-a shows λ_{off} of $\langle U \rangle_{\mu PIV}$ and λ_{off} of β with respect to $V_{air,R} = 0$ and 0.1 mL. Here, the air cavity in the blood sample syringe was set to zero. Consequently, λ_{off} tended to decrease with respect to $V_{air,R}$. Both $\langle U \rangle_{\mu PIV}$ and β exhibited a similar trend of λ_{off} with respect to $V_{air,R}$. Figure 3C-b shows a comparison of λ_{off} obtained from $\langle U \rangle_{\mu PIV}$ and β with respect to $V_{air,B} = 0$ and 0.1 mL. Here, the air cavity in the reference fluid syringe was set to 0.1 mL. Consequently, λ_{off} tended to increase with respect to $V_{air,B}$. Both $\langle U \rangle_{\mu PIV}$ and β exhibited increase in λ_{off} significantly with respect to $V_{air,B}$. The time constant obtained with β presented a very similar trend with respect to the air cavity compared with the time constant obtained with $\langle U \rangle_{\mu PIV}$. As quantification of $\langle U \rangle_{\mu PIV}$ required an expensive high-speed camera and much time for the micro-PIV procedure, the quantification of β could be considered more effective.

Finally, to evaluate the contribution of the air cavity in the blood sample syringe to blood viscosity (μ_B), the value of μ_B was obtained with respect to $V_{air,B} = 0$ and 0.1 mL. The blood viscosity was quantified under constant flow rate; both fluids were infused at the same flow rate (i.e., $Q_B = Q_R$). By setting $\frac{d\beta}{dt} = 0$ in Equation (2), a formula of blood viscosity was derived as follows:

$$\mu_B = \mu_R \times (\beta - 1) \times F_2 \tag{3}$$

As shown in Figure 4A, μ_B tended to increase with respect to Hct. As expected, the air cavity in the blood sample syringe did not contribute to varying blood viscosity. In addition, it was inferred that the air cavity in the reference fluid syringe (~0.1 mL) was sufficient to maintain a constant flow rate, even at $V_{air,B} = 0$.

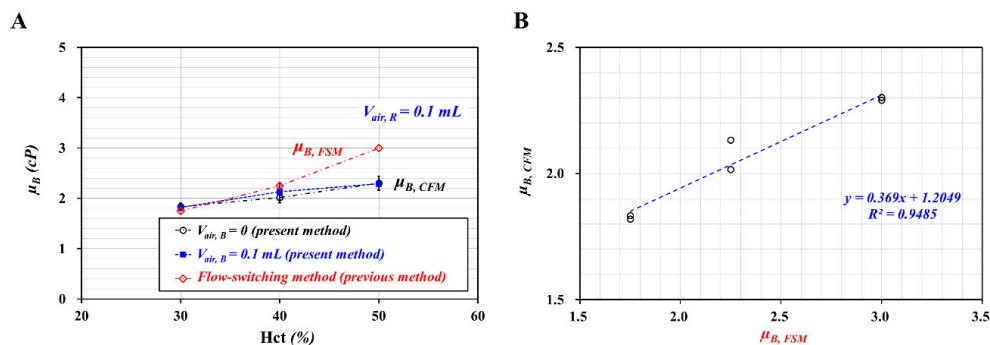


Figure 4. Quantitative comparison of blood viscosity (μ_B) between the co-flowing method (present method) and a flow switching method (previous method). To evaluate the effect of $V_{air,B}$ on μ_B , $V_{air,B}$ was varied from 0 to 0.1 mL. Here, $V_{air,R}$ was set to 0.1 mL. (A) Variations of μ_B obtained with two different methods with respect to Hct. (B) The inset shows the linear relationship between $\mu_{B,CFM}$ (co-flowing method) and $\mu_{B,FSM}$ (flow switching method).

To compare with the blood viscosity obtained with the present method (i.e., co-flowing method), the blood viscosity of the same blood sample was also obtained with a previous method (i.e., flow-switching method) [40]. The previous method produced a higher value of blood viscosity than the present method. The Fåhræus–Lindqvist effect indicated that blood viscosity varied with

respect to channel diameter. In other words, blood viscosity tended to decrease at a smaller channel due to the existence of a cell-free layer. However, blood viscosity remained constant for wider channel with above 300~500 μm . Here, the contribution of a cell-free layer was negligible because it was much smaller than the channel size. As a rectangular channel (width = W , and depth = h) was filled with a blood sample, an equivalent circular diameter (d) was estimated as $d = \sqrt{\frac{4Wh}{\pi}}$ with mass conservation. For the previous method (i.e., switching flow method), a single fluidic channel was filled with blood sample completely when reversal flow in junction occurred. Then, equivalent diameter was estimated as $d = 358 \mu\text{m}$. However, for the present method (i.e., co-flowing method), the corresponding interface of each hematocrit was obtained as $\alpha = 0.65 \pm 0.01$ for Hct = 30%, $\alpha = 0.67 \pm 0.01$ for Hct = 40%, and $\alpha = 0.68 \pm 0.01$ for Hct = 50%. The equivalent diameter was then estimated as $d = 288\text{--}294 \mu\text{m}$. According to the previous study [41], for channel diameter with below $d = 400 \mu\text{m}$, blood viscosity tended to decrease gradually with respect to equivalent diameter. Because the present method had smaller equivalent diameter than the previous method, it was reasonable that blood viscosity obtained by the present method was underestimated substantially when compared with blood viscosity obtained by the previous method. To obtain a linear relationship between both methods, as shown in the inset of Figure 4B, a scatter plot was constructed by plotting the viscosity obtained by the present method (i.e., co-flowing method with $\mu_{B,CFM}$) on Y-axis and the viscosity obtained by previous method (i.e., flow-switching method: $\mu_{B,FSM}$) on X-axis. According to regression analysis, a linear regression formula was obtained: $\mu_{B,CFM} = 0.369 \mu_{B,FSM} + 1.2049$ ($R^2 = 0.9485$). The high value of the regression coefficient (R^2) means that the co-flowing method (i.e., the present method) could be used effectively to monitor blood viscosity compared with the flow-switching method (i.e., the previous method).

3.3. Quantitative Evaluations of Image Intensity, Blood Velocity, and Interface with Respect to Diluent

To evaluate variations of mechanical properties of a blood sample at constant blood flow rate, a blood sample (Hct = 50%) was prepared by adding normal RBCs into two different diluents, namely 1 \times PBS and dextran solution (10 mg/mL). Here, the dextran solution was used as a diluent to enhance the RBC aggregation in the blood sample. The contribution of the dextran solution to the mechanical properties of the blood sample was evaluated by measuring image intensity ($\langle I \rangle$), average velocity ($\langle U \rangle_{\mu\text{PIV}}$), and interface ($\alpha = 1 - \beta^{-1}$) with respect to the blood flow rate (or shear rate). Using two syringe pumps, both fluids were injected at the same flow rate ($Q_R = Q_B = Q_{sp}$). The air cavity in each syringe was set to 0.1 mL (i.e., $V_{air,R} = V_{air,B} = 0.1 \text{ mL}$).

As shown in Figure 5A, the variation of image intensity ($\langle I \rangle$) was obtained with respect to Q_{sp} and the diluent. The right side panel in the figure shows microscopic images captured at specific flow rates (Q_{sp}): (a) $Q_{sp} = 0.075 \text{ mL/h}$, (b) $Q_{sp} = 0.2 \text{ mL/h}$, (c) $Q_{sp} = 0.6 \text{ mL/h}$, (d) $Q_{sp} = 1 \text{ mL/h}$, and (e) $Q_{sp} = 5 \text{ mL/h}$. For the dextran solution as diluent, $\langle I \rangle$ decreased gradually up to $Q_{sp} = 0.4 \text{ mL/h}$. RBC aggregation caused to increase $\langle I \rangle$ at a lower flow rate. However, when the flow rate increased, RBCs tended to disaggregate. Above $Q_{sp} = 0.6 \text{ mL/h}$, $\langle I \rangle$ tended to increase gradually with respect to Q_{sp} . According to a previous study, the orientation and deformability of RBCs contribute to increasing image intensity [42]. Given that RBCs in 1 \times PBS did not include RBC aggregation, $\langle I \rangle$ did not increase, even at lower flow rates. The value of $\langle I \rangle$ tended to increase gradually by increasing the flow rate.

While measuring blood viscosity accurately, it is necessary to evaluate the effect of flow rate on interface ($\alpha = W_B/W$) in the coflowing channel. As shown in Figure 1A-c, blood-filled width (W_B) could be obtained accurately by conducting image processing. However, the channel width was assumed as $W = 1000 \mu\text{m}$. Maximum flow rate was estimated as 2 mL/h when test fluid and reference fluid were set to the same flow rate of 1 mL/h. While infusing the blood sample into single microfluidic channel, the deformed channel width was quantified by increasing flow rate. Variation of W was obtained by varying flow rate ($Q_B = 0.05, 0.1, 0.2, 0.4, 0.6, 0.8, 1, 2, 3, 4,$ and 5 mL/h). As shown in Figure A2 (Appendix A), the channel width of the corresponding flow rate was quantified as $W = 1009 \pm 0.2 \mu\text{m}$ ($Q_B = 1 \text{ mL/h}$), $W = 1012.8 \pm 2.1 \mu\text{m}$ ($Q_B = 2 \text{ mL/h}$), and $W = 1017.5 \pm 1.7 \mu\text{m}$ ($Q_B = 4 \text{ mL/h}$). From the

results, variation of channel width was estimated as less than 2% under the maximum flow rate of 2 mL/h.

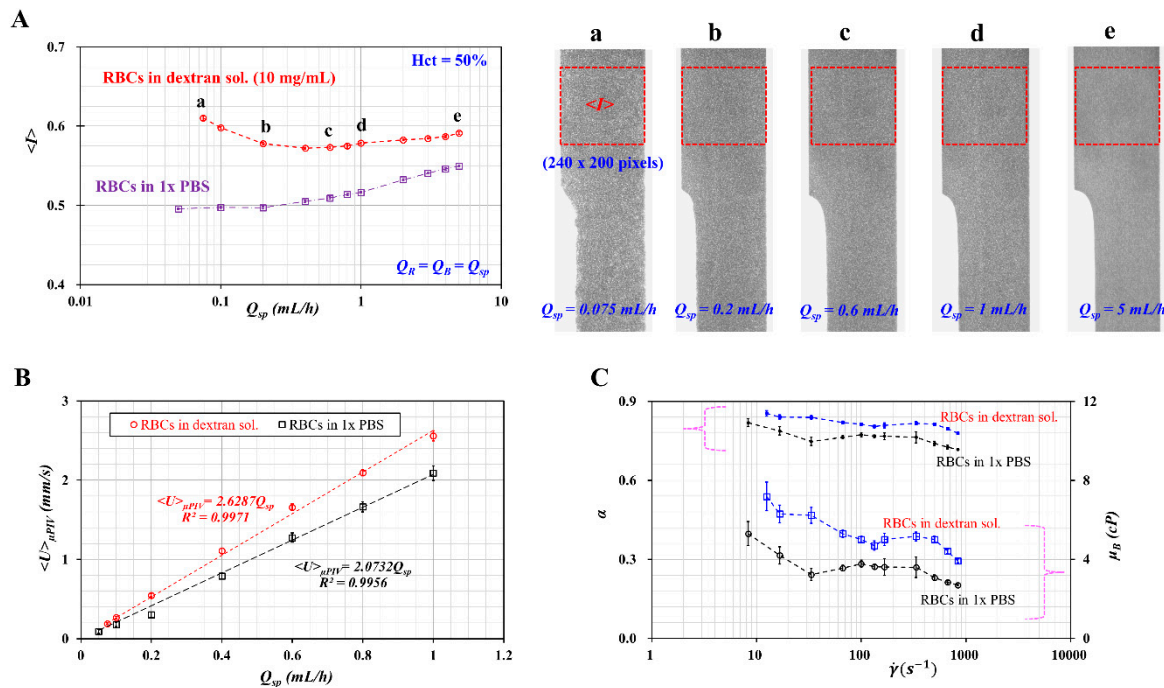


Figure 5. Quantitative evaluations of image intensity ($\langle I \rangle$), blood velocity ($\langle U \rangle_{\mu PIV}$), and interface (α) with respect to diluent. Blood samples (Hct = 50%) were prepared by adding normal RBCs into different diluents, namely 1× PBS and dextran solution (10 mg/mL). The flow rate of each fluid was fixed at the same flow rate ($Q_R = Q_B = Q_{sp}$). (A) Variations of microscopic image intensity ($\langle I \rangle$) with respect to Q_{sp} and diluent. The value of $\langle I \rangle$ was obtained by averaging the image intensity distributed over a specific region-of-interest (ROI) (240×200 pixels) selected within the test fluid channel. The right side panel shows microscopic images captured at a specific flow rate ((a) $Q_{sp} = 0.075$ mL/h, (b) $Q_{sp} = 0.2$ mL/h, (c) $Q_{sp} = 0.6$ mL/h, (d) $Q_{sp} = 1$ mL/h, and (e) $Q_{sp} = 5$ mL/h). (B) Variations of $\langle U \rangle_{\mu PIV}$ with respect to Q_{sp} and diluent. (C) Variations of α and μ_B with respect to $\dot{\gamma}$ and diluent.

Variations of $\langle U \rangle_{\mu PIV}$ with respect to Q_{sp} and diluent were obtained, as shown in Figure 5B. The value of $\langle U \rangle_{\mu PIV}$ tended to increase linearly with respect to Q_{sp} . According to linear regression analysis, a linear regression formula for each diluent was obtained: $\langle U \rangle_{\mu PIV} = 2.6287 Q_{sp}$ ($R^2 = 0.9971$) for dextran solution (10 mg/mL) and $\langle U \rangle_{\mu PIV} = 2.0732 Q_{sp}$ ($R^2 = 0.9956$) for 1× PBS. These results indicated that RBCs suspended in dextran solution reached a higher value of $\langle U \rangle_{\mu PIV}$ (~26.8%) compared with RBCs suspended in 1× PBS.

Finally, to evaluate variations of interface (α) with flow rate and diluent, variations of α and μ_B were obtained with respect to shear rate and diluent. For a rectangular channel (width = W , and depth = h) with low aspect ratio [8], a shear rate for each flow rate (Q_{sp}) is given approximately by $\dot{\gamma} = \frac{6Q_{sp}}{Wh^2}$. Using Equation (3), the blood viscosity of the blood sample was obtained in terms of the shear rate. As shown in Figure 5C, the interface (α) of RBCs suspended in the dextran solution reached a higher value of interface compared with RBCs suspended in 1× PBS. The blood viscosity decreased gradually with respect to the shear rate. The blood sample behaved as a non-Newtonian fluid (or shear-thinning fluid). Furthermore, a dextran solution (10 mg/mL) as diluent contributed to increasing the blood viscosity significantly compared with 1× PBS. When compared with previous results [8], our results showed consistent trends with respect to diluents.

3.4. Variations of Red Blood Cells (RBC) Aggregation, Viscosity, and Viscoelasticity with Respect to Diluent and Air Cavity in Syringe

To quantify three mechanical properties of blood sample (RBC aggregation, viscosity, and viscoelasticity) with respect to air cavity (or air compliance), variations of $\langle I \rangle$, $\langle U \rangle_{\mu PIV}$, and β were simultaneously obtained with respect to diluent and air cavity in each syringe. A blood sample (Hct = 50%) was prepared by adding normal RBCs into four different diluents, namely 1× PBS, two dextran solutions (5, and 10 mg/mL), and plasma. The air cavity in the reference fluid syringe was fixed at $V_{air,R} = 0.1$ mL. Additionally, the air cavity in the blood sample syringe varied from $V_{air,B} = 0$ to $V_{air,B} = 0.1$ mL. Based on experimental results shown in Figure 5A, the flow rate of each fluid was reset to $Q_0 = 0.5$ mL/h for measuring RBC aggregation effectively.

First, as shown in Figure 6A, temporal variations of $\langle I \rangle$ and $\langle U \rangle_{\mu PIV}$ were obtained with respect to diluents. Here, the air cavity in the blood sample syringe was set to $V_{air,R} = 0$. When the syringe pump was turned off periodically, $\langle U \rangle_{\mu PIV}$ decreased suddenly over time. RBC aggregation increased $\langle I \rangle$ gradually over time. Given that 1× PBS did not stimulate RBC aggregation, $\langle I \rangle$ of 1× PBS remain unchanged over time. However, two dextran solutions contributed to increasing $\langle I \rangle$ over time substantially. Given that plasma proteins contributed to RBC aggregation [43,44], $\langle I \rangle$ of plasma increased gradually over time.

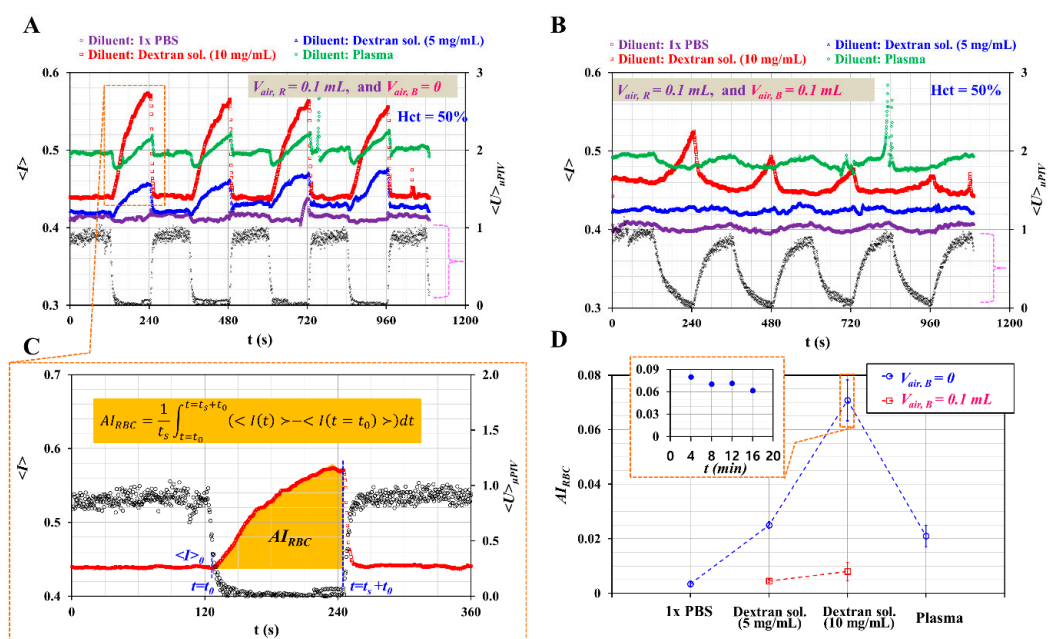


Figure 6. Quantitative evaluations of RBC aggregation with respect to diluent and air cavity in the blood sample syringe. Here, the flow rate of the syringe pump was reset to $Q_0 = 0.5$ mL/h. The air cavity in the reference fluid syringe was set to 0.1 mL. (A) Temporal variations of $\langle I \rangle$ and $\langle U \rangle_{\mu PIV}$ with respect to diluent, i.e., 1× PBS, two dextran solution (5, and 10 mg/mL), and plasma. The air cavity in the blood sample syringe was set to zero. (B) Temporal variations of $\langle I \rangle$ and $\langle U \rangle_{\mu PIV}$ with respect to diluent. The air cavity in the blood sample was set to 0.1 mL. (C) Quantification of RBC aggregation index (AI_{RBC}). The value of AI_{RBC} was obtained as $AI_{RBC} = \frac{1}{t_s} \int_{t=t_0}^{t=t_0+t_s} (\langle I(t) \rangle - \langle I(t=t_0) \rangle) dt$. (D) Variations of AI_{RBC} with respect to diluent and $V_{air,B}$. The inset shows temporal variations of AI_{RBC} with respect to dextran solution (10 mg/mL).

To evaluate the effect of air compliance on RBC aggregation, the air cavity in the blood sample syringe was varied from $V_{air,B} = 0$ to $V_{air,B} = 0.1$ mL. As shown in Figure 6B, temporal variations of $\langle I \rangle$ and $\langle U \rangle_{\mu PIV}$ were obtained with respect to diluent. Even when turning off the syringe pump, $\langle U \rangle_{\mu PIV}$ tended to decrease gradually over time. For this reason, except for a higher concentration of dextran solution (10 mg/mL), $\langle I \rangle$ did not show substantial increase over time. From these results, the air cavity

(~0.1 mL) in the blood sample syringe delayed the transient behaviors of blood velocity considerably. Thus, it was inferred that air compliance hindered the quantification of RBC aggregation. To quantify RBC aggregation with $\langle I \rangle$, it was necessary to define an RBC aggregation index. From Figure 6A, temporal variations of $\langle I \rangle$ and $\langle U \rangle_{\mu PIV}$ were redrawn from $t = 0$ to $t = 360$ s. As shown in Figure 6C, after $t = 120$ s (i.e., turn-off operation of the syringe pump), $\langle U \rangle_{\mu PIV}$ decreased largely over time. Note also that $\langle I \rangle$ tended to increase gradually over time. Here, a specific time instant and minimum value of $\langle I \rangle$ were denoted as $t = t_0$ and $\langle I(t = t_0) \rangle$, respectively. The RBC aggregation index was then obtained by analyzing $\langle I \rangle$ from $t = t_0$ to $t = t_0 + t_s$. According to a previous study [45], an RBC aggregation index (AI_{RBC}) can be defined as follows:

$$AI_{RBC} = \frac{1}{t_s} \int_{t=t_0}^{t=t_0+t_s} (\langle I(t) \rangle - \langle I(t = t_0) \rangle) dt \quad (4)$$

Based on the temporal variations of $\langle I \rangle$ shown in Figure 6A,B, AI_{RBC} was quantified at periodic intervals ($T = 240$ s). Figure 6D shows variations of AI_{RBC} with respect to diluent and $V_{air, B}$. The inset of Figure 6D shows temporal variations of AI_{RBC} with respect to dextran solution (10 mg/mL) and $V_{air, B} = 0$. The RBC aggregation index was quantified with repetitive tests ($n = 8$) and expressed as mean \pm standard deviation. Under no air cavity in the blood sample syringe, the RBC aggregation index for each diluent was obtained as $AI_{RBC} = 0.003 \pm 0.001$ for 1 \times PBS, $AI_{RBC} = 0.025 \pm 0.001$ for dextran solution (5 mg/mL), $AI_{RBC} = 0.071 \pm 0.008$ for dextran solution (10 mg/mL), and $AI_{RBC} = 0.021 \pm 0.003$ for plasma. The dextran solutions and plasma contributed to increasing the RBC aggregation index significantly compared with 1 \times PBS. Additionally, AI_{RBC} tended to increase significantly at higher concentration of dextran solution. When the air cavity in the blood sample syringe was reset to 0.1 mL, the RBC aggregation index for the two dextran solutions was obtained as $AI_{RBC} = 0.004 \pm 0.001$ for the first dextran solution (5 mg/mL) and $AI_{RBC} = 0.008 \pm 0.003$ for the second dextran solution (10 mg/mL). Given that the air cavity (or air compliance) tended to delay the transient behavior of the blood velocity, AI_{RBC} decreased considerably. From these results, the air cavity (~0.1 mL) in the blood sample syringe hindered the quantification of the RBC aggregation substantially.

Second, as shown in Figure 7A-a, the temporal variations of β were obtained with respect to diluent. Air cavities of each syringe were set to $V_{air, R} = 0.1$ mL and $V_{air, B} = 0$, respectively. Among the values of β obtained in Figure 7A-a, to represent how the blood viscosity (μ_B) and the time constant (λ_{off}) were quantified over a single period, temporal variations of β were redrawn at specific durations ranging from $t = 240$ s to $t = 500$ s.

As shown in Figure 7A-b, the value of μ_B was obtained with the Equation (3) under turn-on operation of the syringe pump ($t < 0.5 T$). Afterward, λ_{off} was estimated with regression analysis ($\beta_{off} = \beta_0 + \beta_1 \exp(-t/\lambda_{off})$) under turn-off operation of the syringe pump ($0.5 T < t < T$). As shown in Figure 7A-c, variations of μ_B were obtained at intervals of 240 s with respect to diluent. The value of μ_B for each diluent was obtained as $\mu_B = 2.95 \pm 0.12$ cP for 1 \times PBS, $\mu_B = 3.53 \pm 0.15$ cP for the first dextran solution (5 mg/mL), $\mu_B = 5.89 \pm 0.28$ cP for the second dextran solution (10 mg/mL), and $\mu_B = 4.59 \pm 0.14$ cP for plasma. Under the turn-off operation of the syringe pump, the time constant (λ_{off}) was obtained with respect to diluent. Using a linear Maxwell model (i.e., $\lambda_{off} = \mu_B/G_B$), G_B was obtained by dividing μ_B by λ_{off} . As shown in Figure 7B-b, variations of λ_{off} were represented with respect to diluent and $V_{air, B} = 0$. Additionally, Figure 7A-d shows variations of elasticity (G_B) with respect to diluent. The value of G_B for each diluent was obtained as $G_B = 0.5 \pm 0.02$ mPa for 1 \times PBS, $G_B = 0.62 \pm 0.03$ mPa for the first dextran solution (5 mg/mL), $G_B = 0.79 \pm 0.03$ mPa for the second dextran solution (10 mg/mL), and $G_B = 0.76 \pm 0.05$ mPa for plasma. From these results, blood viscoelasticity (viscosity, elasticity) was quantified consistently with respect to diluent under the air cavity in each fluid syringe ($V_{air, R} = 0.1$ mL, and $V_{air, B} = 0$). The dextran solution as diluent contributed to increasing viscosity and elasticity substantially compared with 1 \times PBS. The plasma reached a higher value of viscosity and elasticity compared with 1 \times PBS. In other words, the plasma proteins led to increased viscosity and elasticity.

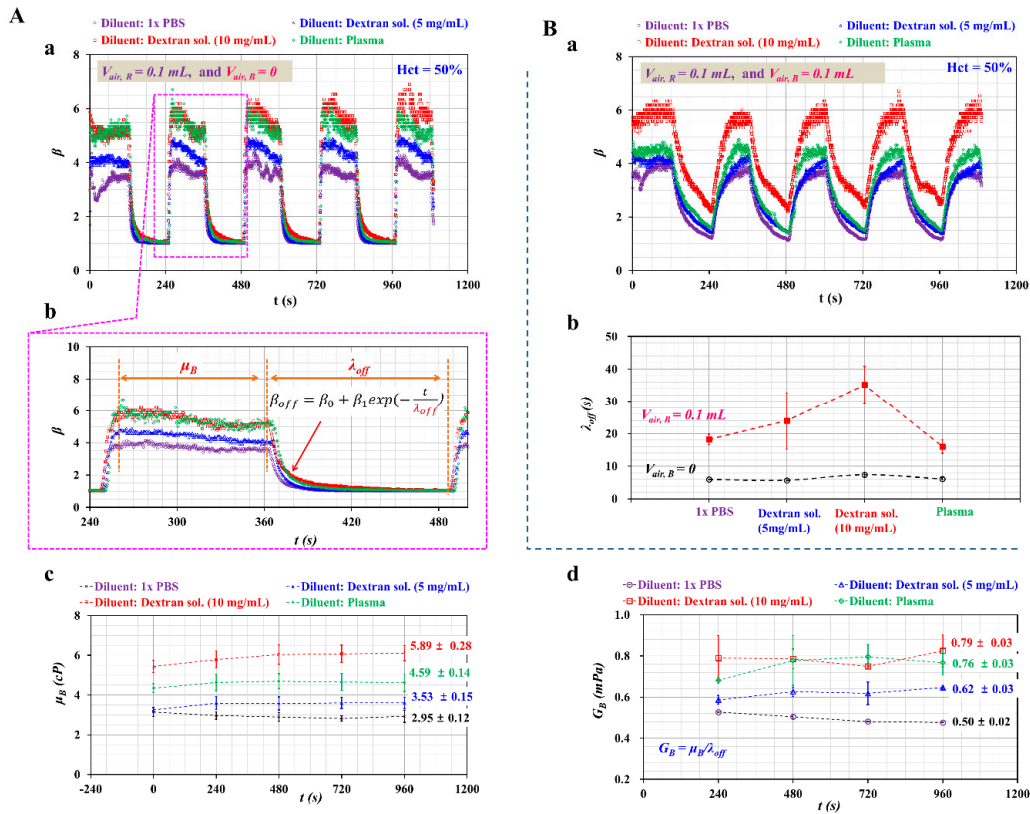


Figure 7. Quantitative evaluations of viscosity (μ_B) and time constant (λ_{off}) with respect to diluent and air cavity in the blood syringe. Here, the flow rate of the individual syringe pump and the air cavity in the reference fluid syringe were fixed at $Q_0 = 0.5$ mL/h and $V_{air,R} = 0.1$ mL, respectively. **(A)** Variations of viscosity (μ_B) and elasticity (G_B) with respect to diluent and $V_{air,B} = 0$. (a) Temporal variations of β with respect to diluent and $V_{air,B} = 0$. (b) Quantification of μ_B and λ_{off} during a single period. Here, μ_B and λ_{off} were obtained sequentially by turning on and off the syringe pump. (c) Variations of μ_B at intervals of 240 s. (d) Variations of G_B with respect to diluent. Here, G_B was obtained by dividing μ_B by λ_{off} . **(B)** Variations of λ_{off} with respect to diluent and $V_{air,B} = 0.1$ mL. (a) Temporal variations of β with respect to diluent. (b) Variations of λ_{off} with respect to diluent and $V_{air,B}$.

To quantify the effect of the air cavity in the blood sample syringe on β , the volume of such air cavities was varied from 0 to 0.1 mL. Additionally, the volume of the air cavity in the reference fluid syringe was set to 0.1 mL. As shown in Figure 7B-a, temporal variations of β were obtained with respect to diluent. The air cavity in the blood sample syringe delayed the transient behavior of β substantially. During turn-on and turn-off operation of the syringe pump, β did not reach a constant value within a specific duration. Given that Equation (3) as blood viscosity was effective for blood viscosity only for constant values of β , it was impossible to obtain the blood viscosity with no information on flow rate (or velocity) at a specific time instant. Figure 7B-b shows variations of λ_{off} with respect to diluent and $V_{air,B}$. Note that the case $V_{air,B} = 0.1$ mL contributed to increasing λ_{off} significantly compared with $V_{air,B} = 0$. When setting $V_{air,B} = 0.1$ mL, λ_{off} was increased largely at a higher concentration of dextran solution.

As shown in Figure 7B-b, while increasing air cavity was secured in the blood syringe from 0 to 0.1 mL, the corresponding time constant of each diluent increased about $\Delta\lambda_{off} = 13.3$ s (1× PBS), $\Delta\lambda_{off} = 18.4$ s (dextran sol. 5 mg/mL), $\Delta\lambda_{off} = 27.8$ s (dextran sol. 10 mg/mL), and $\Delta\lambda_{off} = 10$ s (plasma). As transient time increased largely within a half period, β did not arrive to constant value under periodic on-off operation of syringe pump. As a solution, it is necessary to increase period of blood flow rate. Taking into account the fact that time constant increased about 10~27.8 s for each diluent, half period of blood flow rate should increase at least 27.8 s. When the period of blood flow rate changes from

$T = 240$ s to $T = 300$ s, it will be inferred that β exhibits similar trends as shown in Figure 7A-a. Thus, blood viscosity and RBC aggregation will be obtained without additional information on temporal variations of blood velocity.

To quantify blood viscosity under varying blood flows, it was necessary to obtain β and $\langle U \rangle_{\mu PIV}$ over time. Figure 8A shows temporal variations of β and $\langle U \rangle_{\mu PIV}$ with respect to two diluents, namely 1× PBS and dextran solution (10 mg/mL). As shown in Figure 5B, the relationship between $\langle U \rangle_{\mu PIV}$ and Q_{sp} was obtained in advance as a linear regression formula with respect to each diluent, and the average velocity of the blood sample ($\langle U \rangle_{\mu PIV}$) was converted into the blood flow rate with a regular formula.

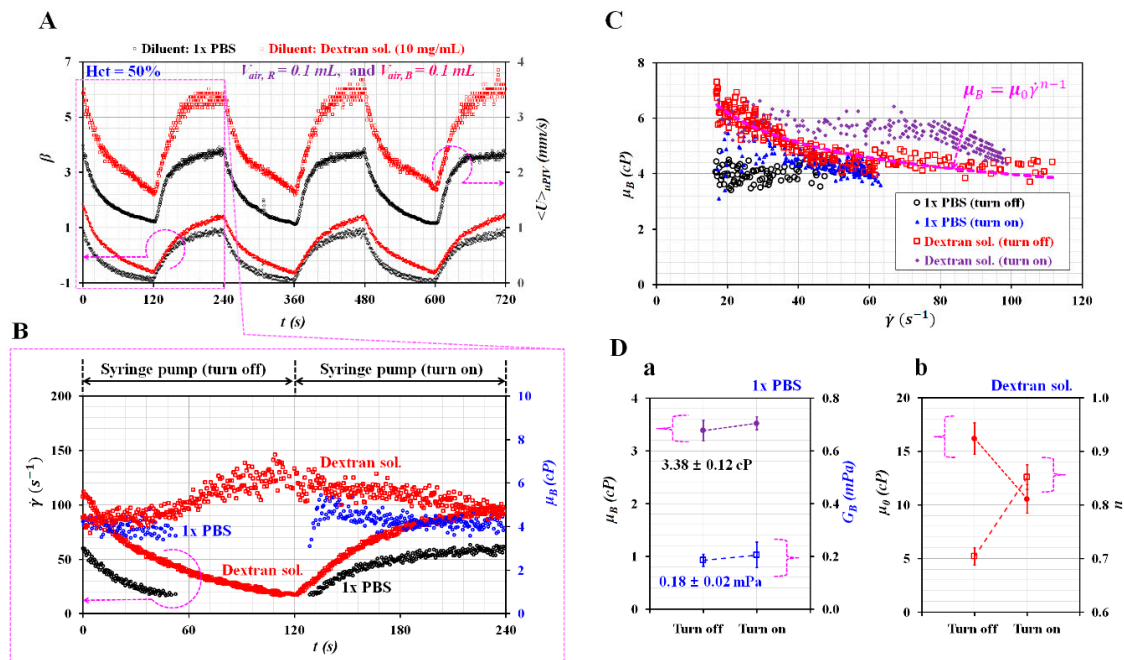


Figure 8. Quantitative evaluation of viscoelasticity with respect to diluent and $V_{air, B} = 0.1$ mL/h. A blood sample (Hct = 50%) was prepared by adding normal RBCs into diluent, i.e., 1× PBS and dextran solution (10 mg/mL). The flow rate of each syringe pump was set to $Q_0 = 0.5$ mL/h. The air cavity of the reference fluid syringe was set to 0.1 mL. (A) Temporal variations of β and $\langle U \rangle_{\mu PIV}$ with respect to diluent. (B) Temporal variations of γ and μ_B with respect to diluent during a single period of 240 s. (C) Variations of μ_B with respect to diluent and syringe operation (turn-off and turn-on). (D) Variations of viscoelasticity with respect to diluent and pump operation. (a) Variations of μ_B and G_B with respect to 1× PBS and syringe operation. (b) Variations of μ_0 and n with respect to dextran solution (10 mg/mL) and syringe operation.

Given that the flow rate of the blood sample varied over time, the formula of blood viscosity was corrected as $\mu_B = \mu_R \times (\beta - 1) \times F_2 \times (Q_R/Q_B)$ by adding a flow rate term into Equation (3). Figure 8B shows temporal variations of γ and μ_B with respect to diluent during a single period of 240 s. Note that μ_B presented large scattering at $Q_{sp} < 0.1$ mL/h. Thus, the minimum value of Q_{sp} was set to 0.1 mL/h. As shown in Figure 8C, variations of μ_B were obtained with respect to γ during the turn-on and turn-off operation of the syringe pump. For 1× PBS as diluent, μ_B remained constant with respect to the shear rate. However, for the dextran solution as diluent, μ_B decreased gradually with respect to the shear rate. As shown in Figure 8D-a, variations of μ_B and G_B were obtained with respect to the syringe operation (i.e., turn-on, turn-off). Given that μ_B remained unchanged over the shear rate, G_B was calculated by dividing μ_B by the time constant (i.e., $G_B = \mu_B/\lambda_{off}$ for turn-off operation, and $G_B = \mu_B/\lambda_{on}$ for turn-on operation). The value of μ_B for each operation was obtained as $\mu_B = 3.38 \pm 0.19$ cP for the turn-off operation, and $\mu_B = 3.52 \pm 0.12$ cP for the turn-on operation. Additionally,

the value of G_B for each operation was obtained as $G_B = 0.18 \pm 0.02$ cP for the turn-off operation, and $G_B = 0.21 \pm 0.05$ cP for the turn-on operation. From these results, μ_B and G_B remained unchanged irrespective of the syringe operation. Compared with the results obtained at $V_{air, B} = 0$ as showed in Figure 7A-c, a 0.1-mL air cavity (~ 0.1 mL) in the blood sample syringe caused to overestimate μ_B . However, it caused G_B to be underestimated. Figure 8D-b shows variations of μ_0 and n with respect to the first dextran solution (10 mg/mL) and syringe operation. The constant μ_0 decreased significantly by switching the syringe pump from turn-off operation to turn-on operation. In addition, the turn-on operation caused to increase the index n substantially compared with the turn-off operation.

In this study, three mechanical properties of blood sample (viscosity, RBC aggregation, and time constant) were quantified with methods suggested in previous studies. First, cone-and-plate viscometer as conventional method has been used to measure blood viscosity. According to the quantitative comparison between conventional viscometer and microfluidic viscometer [40,41,46,47], the previous studies indicated that blood viscosity could be measured consistently in a microfluidic environment. Based on the previous study, as shown in Figure 4A, co-flow method (present method) and flow switching method (previous method) were used to obtain blood viscosity with respect to hematocrit. The present method underestimated blood viscosity when compared with the previous method. However, as shown in Figure 4B, both methods exhibited a high degree of linear relationship (i.e., $R^2 = 0.9485$). Second, RBC aggregation as a conventional method has been quantified by analyzing light intensity [48] or electric impedance [49] of blood sample flowing in slit channel. According to quantitative comparison study [50,51], microscopic image intensity exhibited variations of RBC aggregation in microfluidic channel sufficiently. Thus, without quantitative comparison study, variations of RBC aggregation were quantified by analyzing image intensity of blood flows in the test channel under turn-off blood flows. Finally, under transient flow conditions, time constant has been obtained by analyzing temporal variations of physical parameters including blood velocity, flow rate, and pressure. Based on Equation (2), time constant (l) was obtained by analyzing temporal variations of β . Furthermore, to compare with time constant obtained from information of β , time constant was quantified additionally by analyzing temporal variations of blood velocity ($\langle U \rangle$). As shown in Figure 3C, both time constants exhibited consistent variations with respect to air cavity in reference syringe.

From these experimental results, it leads to the conclusion that the air cavity in the blood sample syringe made the RBC aggregation and blood viscoelasticity vary substantially. The RBC aggregation index decreased largely, even for a 0.1-mL air cavity in the blood sample syringe because of a longer transient behavior of blood flows. Thus, to measure RBC aggregation and viscoelasticity of blood samples consistently, a 0.1-mL air cavity must be secured in the reference fluid syringe as a minimum condition. Additionally, the air cavity in the blood sample syringe must be minimized as much as possible.

4. Conclusions

In this study, the air compliance effect on measurement of blood mechanical properties was quantified experimentally with respect to the air cavity in two driving syringes. Under periodic on-off blood flows, three mechanical properties of blood samples, namely RBC aggregation, blood viscosity, and time constant, were obtained sequentially by quantifying microscopic image intensity of blood samples ($\langle I \rangle$) flowing in the test channel and the interface (α) in a co-flowing channel. Based on a differential equation derived with a fluid circuit model, the time constant was obtained by analyzing temporal variations of $\beta = 1/(1-\alpha)$. First, the air cavity in the reference fluid syringe (~ 0.1 mL) contributed to decreasing λ_{off} greatly. The λ_{off} decreased more significantly than λ_{on} . Above an air cavity volume of 0.1 mL, the time constants did not present substantial variation. The air cavity increased or decreased the time constant depending on whether it existed in the reference fluid syringe or the blood sample syringe. Second, the air cavity did not contribute to varying blood viscosity. From the quantitative comparison study, the co-flowing method (i.e., the present method)

could be used effectively to monitor blood viscosity compared with the flow-switching method (i.e., the previous method). Third, given that the air cavity in the blood sample syringe contributed to delaying transient behaviors of blood flows considerably, this hindered the quantification of the RBC aggregation and blood viscosity. As a solution, when the period of blood flow rate increases about twice time constant (i.e., $\Delta T = 2\lambda_{off}$), blood viscosity and RBC aggregation could be obtained without additional information on temporal variations of blood velocity. From these experimental results, to measure the aforementioned three mechanical properties of blood samples effectively, the air cavity in the blood sample syringe must be minimized ($V_{air, B} = 0$). However, it will be necessary to secure the air cavity in the reference fluid syringe ($V_{air, R} = 0.1$ mL) for stabilizing fluidic instability resulting from the syringe pump.

Funding: This work was supported by the Basic Science Research Program through the NRF, funded by the Ministry of Science and ICT (MSIT) (NRF-2018R1A1A1A05020389).

Conflicts of Interest: The author declares no conflict of interest.

Appendix A

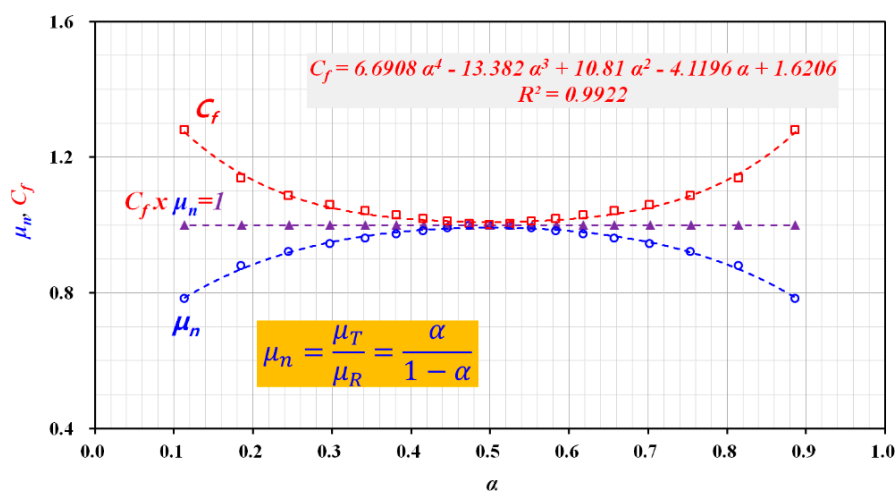


Figure A1. Variations of normalized viscosity (μ_n) with respect to interface (α) in coflowing channel. Based on the principle of parallel streams [47], μ_n was expressed as $\mu_n = \mu_T/\mu_R = \alpha/(1-\alpha)$. μ_T and μ_R represent viscosity of test fluid and reference fluid, respectively. As the viscosity of test fluid is assumed as constant with respect to α , correction factor (C_f) was then obtained as $C_f = 6.6908 \alpha^4 - 13.382 \alpha^3 + 10.81 \alpha^2 - 4.1196 \alpha + 1.6206$ ($R^2 = 0.9922$) by using the following relationship (i.e., $C_f \times \mu_n = 1$).

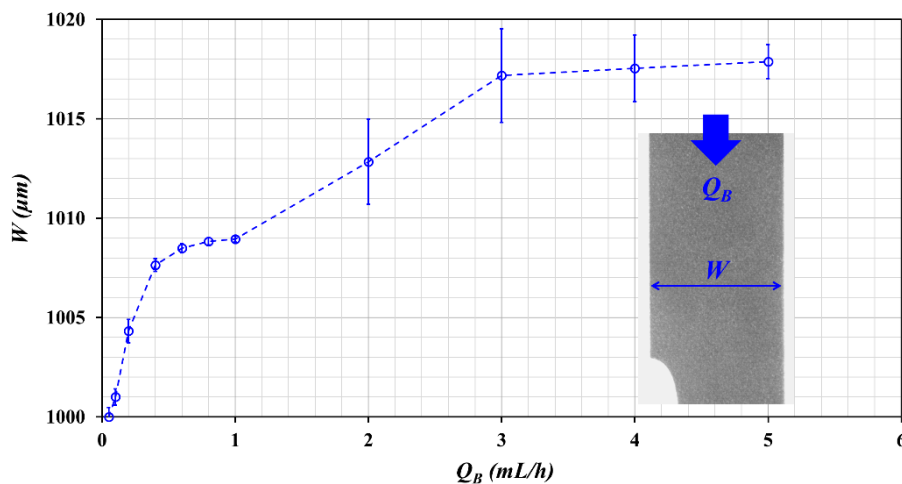


Figure A2. Variations of channel width under blood flow rate (Q_B).

References

1. Danesh, J.; Collins, R.; Peto, R.; Lowe, G.D.O. Haematocrit, viscosity, erythrocyte sedimentation rate: Meta-analyses of prospective studies of coronary heart disease. *Eur. Heart J.* **2000**, *21*, 515–520. [CrossRef] [PubMed]
2. Cho, Y.I.; Mooney, M.P.; Cho, D.J. Hemorheological disorders in diabetes mellitus. *J. Diabetest Sci. Technol.* **2008**, *2*, 1130–1138. [CrossRef] [PubMed]
3. Zeng, N.F.; Mancuso, J.E.; Zivkovic, A.M.; Smilowitz, J.T.; Ristenpart, W.D. Red blood cells from individuals with abdominal obesity or metabolic abnormalities exhibit less deformability upon entering a constriction. *PLoS ONE* **2016**, *11*, e0156070. [CrossRef] [PubMed]
4. Agrawal, R.; Smart, T.; Nobre-Cardoso, J.; Richards, C.; Bhatnagar, R.; Tufail, A.; Shima, D.; Jones, P.H.; Pavesio, C. Assessment of red blood cell deformability in type 2 diabetes mellitus and diabetic retinopathy by dual optical tweezers stretching technique. *Sci. Rep.* **2016**, *6*, 15873. [CrossRef] [PubMed]
5. Kim, H.; Cho, Y.I.; Lee, D.-H.; Park, C.-M.; Moon, H.-W.; Hur, M.; Kim, J.Q.; Yun, Y.-M. Analycal performance evaluation of the scanning tube viscometer for measurement of whole blood viscosity. *Clin. Biochem.* **2013**, *46*, 139–142. [CrossRef]
6. Sousa, P.C.; Vaz, R.; Cerejo, A.; Oliveira, M.S.N.; Alves, M.A.; Pinho, F.T. Rheological behavior of human blood in uniaxial extensional flow. *J. Rheol.* **2018**, *62*, 447–456. [CrossRef]
7. Kim, B.J.; Lee, Y.S.; Zhbanov, A.; Yang, S. A physiometer for simultaneous measurement of whole blood viscosity and its determinants: Hematocrit and red blood cell deformability. *Analyst* **2019**, *144*, 3144–3157. [CrossRef] [PubMed]
8. Kang, Y.J. Microfluidic-based effective monitoring of bloods by measuring RBC aggregation and blood viscosity under stepwise varying shear rates. *Korea-Aust. Rheol. J.* **2020**, *32*, 15–27. [CrossRef]
9. Khnouf, R.; Karasneh, D.; Abdulhay, E.; Abdelhay, A.; Sheng, W.; Fan, Z.H. Microfluidics-based device for the measurement of blood viscosity and its modeling based on shear rate, temperature, and heparin concentration. *Biomed. Microdevices* **2019**, *21*, 80. [CrossRef]
10. Hong, H.; Song, J.M.; Yeom, E. 3D printed microfluidic viscometer based on the co-flowing stream. *Biomicrofluidics* **2019**, *13*, 014104. [CrossRef]
11. Wen, J.; Wan, N.; Bao, H.; Li, J. Quantitative measurement and evaluation of red blood cell aggregation in normal blood based on a modified hanai equation. *Sensors* **2019**, *19*, 1095. [CrossRef] [PubMed]
12. Sherwood, J.M.; Dusting, J.; Kaliviotis, E.; Balabani, S. The effect of red blood cell aggregation on velocity and cell-depleted layer characteristics of blood in a bifurcating microchannel. *Biomicrofluidics* **2012**, *6*, 024119. [CrossRef] [PubMed]
13. Shin, S.; Jang, J.H.; Park, M.S.; Ku, Y.H.; Suh, J.S. A noble RBC aggregometer with vibration-induced disaggregation mechanism. *Korea-Aust. Rheol. J.* **2005**, *17*, 9–13.
14. Zhbanov, A.; Yang, S. Effects of aggregation on blood sedimentation and conductivity. *PLoS ONE* **2015**, *10*, e0129337. [CrossRef] [PubMed]
15. Boas, L.V.; Faustino, V.; Lima, R.; Miranda, J.M.; Minas, G.; Fernandes, C.S.V.; Catarino, S.O. Assessment of the deformability and velocity of healthy and artificially impaired red blood cells in narrow polydimethylsiloxane (PDMS) microchannels. *Micromachines* **2018**, *9*, 384. [CrossRef] [PubMed]
16. Berry, S.B.; Fernandes, S.C.; Rajaratnam, A.; DeChiara, N.S.; Mace, C.R. Measurement of the hematocrit using paper-based microfluidic devices. *Lab Chip* **2016**, *16*, 3689–3694. [CrossRef]
17. Lee, H.Y.; Barber, C.; Rogers, J.A.; Minerick, A.R. Electrochemical hematocrit determination in a direct current microfluidic device. *Electrophoresis* **2015**, *36*, 978–985. [CrossRef]
18. Kim, M.; Yang, S. Improvement of the accuracy of continuous hematocrit measurement under various blood flow conditions. *Appl. Phys. Lett.* **2014**, *104*, 153508. [CrossRef]
19. Zhou, J.; Tu, C.; Liang, Y.; Huang, B.; Fang, Y.; Liang, X.; Ye, X. The label-free separation and culture of tumor cells in a microfluidic biochip. *Analyst* **2020**, *145*, 1706–1715. [CrossRef]
20. Zhou, J.; Papautsky, I. Size-dependent enrichment of leukocytes from undiluted whole blood using shear-induced diffusion. *Lab Chip* **2019**, *19*, 3416–3426. [CrossRef]
21. Zhou, J.; Tu, C.; Liang, Y.; Huang, B.; Fang, Y.; Liang, X.; Papautsky, I.; Ye, X. Isolation of cells from whole blood using shear-induced diffusion. *Sci. Rep.* **2018**, *8*, 9411. [CrossRef] [PubMed]

22. Kang, Y.J.; Yang, S. Fluidic low pass filter for hydrodynamic flow stabilization in microfluidic environments. *Lab Chip* **2012**, *12*, 1881–1889. [CrossRef] [PubMed]
23. Lee, J.; Rahman, F.; Laoui, T.; Karnik, R. Bubble-induced damping in displacement-driven microfluidic flows. *Phys. Rev. E* **2012**, *86*, 026301. [CrossRef] [PubMed]
24. Kasukurti, A.; Eggleton, C.D.; Desai, S.A.; Disharoon, D.I.; Marr, D.W.M. A simple microfluidic dispenser for singlemicroparticle and cell samples. *Lab Chip* **2014**, *14*, 4673–4679. [CrossRef]
25. Araci, I.E.; Agaoglu, S.; Lee, J.Y.; Yepes, L.R.; Diep, P.; Martini, M.; Schmidt, A. Flow stabilization in wearable microfluidic sensors enables noise suppression. *Lab Chip* **2019**, *19*, 3899–3908. [CrossRef]
26. Jiao, Z.; Zhao, J.; Chao, Z.; You, Z.; Zhao, J. An air-chamber-based microfluidic stabilizer for attenuating syringepump-induced fluctuations. *Microfluid. Nanofluid.* **2019**, *23*, 26. [CrossRef]
27. Zhang, X.; Xiang, N.; Tang, W.; Huang, D.; Wang, X.; Yi, H.; Ni, Z. A passive flow regulator with low threshold pressure for high-throughput inertial isolation of microbeads. *Lab Chip* **2015**, *15*, 3473–3480. [CrossRef]
28. Doh, I.; Cho, Y.-H. Passive flow-rate regulators using pressure-dependent autonomous deflection of parallel membrane valves. *Lab Chip* **2009**, *9*, 2070–2075. [CrossRef]
29. Kalantarifard, A.; Haghighi, E.A.; Elbuken, C. Damping hydrodynamic fluctuations in microfluidic systems. *Chem. Eng. Sci.* **2018**, *178*, 238–247. [CrossRef]
30. Zhang, X.; Wang, X.; Chen, K.; Cheng, J.; Xiang, N.; Ni, Z. Passive flow regulator for precise high-throughput flow rate control in microfluidic environment. *RSC Adv.* **2016**, *6*, 31639–31646. [CrossRef]
31. Park, Y.-J.; Yu, T.; Yim, S.-J.; You, D.; Kim, D.-P. A 3D-printed flow distributor with uniform flow rate control for multi-stacked microfluidic systems. *Lab Chip* **2018**, *18*, 1250–1258. [CrossRef] [PubMed]
32. Serra, M.; Gontran, E.; Hajji, I.; Malaquin, L.; Viovy, J.-L.; Descroix, S.; Ferraro, D. Development of a Droplet Microfluidics Device Based on Integrated Soft Magnets and Fluidic Capacitor for Passive Extraction and Redispersion of Functionalized Magnetic Particles. *Adv. Mater. Technol.* **2020**, *5*, 1901088. [CrossRef]
33. Kang, Y.J. Continuous and simultaneous measurement of the biophysical properties of blood in a microfluidic environment. *Analyst* **2016**, *141*, 6583–6597. [CrossRef] [PubMed]
34. Nam, J.-H.; Yang, Y.; Chung, S.; Shin, S. Comparison of light-transmission and -backscattering methods in the measurement of red blood cell aggregation. *J. Biomed. Opt.* **2010**, *15*, 027003. [CrossRef] [PubMed]
35. Kang, Y.J. Simultaneous measurement of blood pressure and RBC aggregation by monitoring on-off blood flows supplied from a disposable air-compressed pump. *Analyst* **2019**, *144*, 3556–3566. [CrossRef]
36. Kang, Y.J. Simultaneous measurement of erythrocyte deformability and blood viscoelasticity using micropillars and co-flowing streams under pulsatile blood flows. *Biomicrofluidics* **2017**, *11*, 014102. [CrossRef]
37. Otsu, N. A threshold selection method from gray-level histograms. *IEEE Trans. Syst. Man. Cybern.* **1979**, *9*, 62–66. [CrossRef]
38. Thielicke, W.; Stamhuis, E.J. PIVlab—Towards user-friendly, affordable and accurate digital particle image velocimetry in MATLAB. *J. Open Res. Softw.* **2014**, *2*, e30. [CrossRef]
39. Kang, Y.J. Blood Viscoelasticity Measurement Using Interface Variations in Coflowing Streams under Pulsatile Blood Flows. *Micromachines* **2020**, *11*, 245. [CrossRef]
40. Kang, Y.J.; Ryu, J.; Lee, S.-J. Label-free viscosity measurement of complex fluids using reversal flow switching manipulation in a microfluidic channel. *Biomicrofluidics* **2013**, *7*, 044106. [CrossRef] [PubMed]
41. Kang, Y.J.; Yang, S. Integrated microfluidic viscometer equipped with fluid temperature controller for measurement of viscosity in complex fluids. *Microfluid. Nanofluid.* **2013**, *14*, 657–668. [CrossRef]
42. Lindberg, L.-G.; Oberg, P.A. Optical properties of blood in motion. *Opt. Eng.* **1993**, *32*, 253–257. [CrossRef]
43. Brust, M.; Aouane, O.; Thie'baud, M.; Flormann, D.; Verdier, C.; Kaestner, L.; Laschke, M.W.; Selmi, H.; Benyoussef, A.; Podgorski, T.; et al. The plasma protein fibrinogen stabilizes clusters of red blood cells in microcapillary flows. *Sci. Rep.* **2014**, *4*, 4348. [CrossRef]
44. Lee, K.; Kinnunen, M.; Khokhlova, M.D.; Lyubin, E.V.; Priezhev, A.V.; Meglinski, I.; Fedyanin, A.A. Optical tweezers study of red blood cell aggregation and disaggregation in plasma and protein solutions. *J. Biomed. Opt.* **2016**, *21*, 035001. [CrossRef] [PubMed]
45. Kang, Y.J. Microfluidic-based biosensor for sequential measurement of blood pressure and RBC aggregation over continuously varying blood flows. *Micromachines* **2019**, *10*, 577. [CrossRef]
46. Kim, B.J.; Lee, S.Y.; Jee, S.; Atajanov, A.; Yang, S. Micro-viscometer for measuring shear-varying blood viscosity over a wide-ranging shear rate. *Sensors* **2017**, *17*, 1442. [CrossRef]

47. Kang, Y.J. Periodic and simultaneous quantification of blood viscosity and red blood cell aggregation using a microfluidic platform under in-vitro closed-loop circulation. *Biomicrofluidics* **2018**, *12*, 024116. [CrossRef]
48. Shin, S.; Nam, J.-H.; Hou, J.-X.; Suh, J.-S. A transient microfluidic approach to the investigation of erythrocyte aggregation: The threshold shear-stress for erythrocyte disaggregation. *Clin. Hemorheol. Microcirc.* **2009**, *42*, 117–125. [CrossRef]
49. Baskurt, O.K.; Uyklu, M.; Meiselman, H.J. Time Course of Electrical Impedance during Red Blood Cell Aggregation in a Glass Tube: Comparison with Light Transmittance. *IEEE Trans. Biomed. Eng.* **2010**, *57*, 969–978. [CrossRef]
50. Yeom, E.; Lee, S.-J. Microfluidic-based speckle analysis for sensitive measurement of erythrocyte aggregation: A comparison of four methods for detection of elevated erythrocyte aggregation in diabetic rat blood. *Biomicrofluidics* **2015**, *9*, 024110. [CrossRef]
51. Kang, Y.J.; Kim, B.J. Multiple and periodic measurement of RBC aggregation and ESR in parallel microfluidic channels under on-off blood flow control. *Micromachines* **2018**, *9*, 318. [CrossRef] [PubMed]



© 2020 by the author. Licensee MDPI, Basel, Switzerland. This article is an open access article distributed under the terms and conditions of the Creative Commons Attribution (CC BY) license (<http://creativecommons.org/licenses/by/4.0/>).

Article

Dielectric Characterization and Separation Optimization of Infiltrating Ductal Adenocarcinoma via Insulator-Dielectrophoresis

Ezekiel O. Adekanmbi, Anthony T. Giduthuri and Soumya K. Srivastava *

Department of Chemical and Materials Engineering, University of Idaho, Moscow, ID 83844-1021, USA; adek5632@vandals.uidaho.edu (E.O.A.); gidu3424@vandals.uidaho.edu (A.T.G.)

* Correspondence: srivastavask@uidaho.edu; Tel.: +1-208-885-7652

Received: 25 February 2020; Accepted: 23 March 2020; Published: 25 March 2020



Abstract: The dielectrophoretic separation of infiltrating ductal adenocarcinoma cells (ADCs) from isolated peripheral blood mononuclear cells (PBMCs) in a ~1.4 mm long Y-shaped microfluidic channel with semi-circular insulating constrictions is numerically investigated. In this work, ADCs (breast cancer cells) and PBMCs' electrophysiological properties were iteratively extracted through the fitting of a single-shell model with the frequency-conductivity data obtained from AC microwell experiments. In the numerical computation, the gradient of the electric field required to generate the necessary dielectrophoretic force within the constriction zone was provided through the application of electric potential across the whole fluidic channel. By adjusting the difference in potentials between the global inlet and outlet of the fluidic device, the minimum (effective) potential difference with the optimum particle transmission probability for ADCs was found. The radius of the semi-circular constrictions at which the effective potential difference was swept to obtain the optimum constriction size was also obtained. Independent particle discretization analysis was also conducted to underscore the accuracy of the numerical solution. The numerical results, which were obtained by the integration of fluid flow, electric current, and particle tracing module in COMSOL v5.3, reveal that PBMCs can be maximally separated from ADCs using a DC power source of 50 V. The article also discusses recirculation or wake formation behavior at high DC voltages (>100 V) even when sorting of cells are achieved. This result is the first step towards the production of a supplementary or confirmatory test device to detect early breast cancer non-invasively.

Keywords: dielectrophoresis; electrophysiological properties; crossover frequency; wake or recirculation formation; dielectric spectra

1. Introduction

Noncommunicable diseases (NCDs) kill more than 36 million people annually representing 63% of global deaths [1]. Breast cancer, a subset of NCDs, accounts for over 500,000 of these deaths [2] with an incidence of about 1.1 million new cases being reported per year [3]. In the United States, as of March 2017, more than 3.1 million women with a history of breast cancer has been reported [4]. About 85% of these breast cancers occur in women who have no family history of breast cancer [4] and one in eight women develop breast cancer in her lifetime. As of now, the main cause of breast cancer cannot be pinned down exactly, but scientists have hypothesized where breast cancer originates. Our bodies consist of many cells, which can be replaced as they age. Old cells tend to copy their DNA before splitting into new ones. However, the copying process could cause mutation which may result in cellular abnormalities called tumors. When tumor cells grow and invade neighboring tissues, they are termed cancerous [5,6]. Breast cancer that starts in the cells of the glands are termed adenocarcinoma

(ADCs), which can be invasive ductal (indicates that the cancer cells present in the milk ducts (Ductal Carcinoma in-situ)) and can begin to infiltrate and replace the normal surrounding tissues of the duct walls (accounts for 80% of breast cancer), also known as invasive lobular. According to the National Cancer Institute, around 90% of breast cancers are adenocarcinomas. If untreated, breast cancers can grow bigger, taking over more surrounding breast tissue. When breast cancer cells break away from the original cancer, they can enter the blood or lymph vessels. Traveling through these vessels, cancer cells may settle in other areas of the breast or in the lymph nodes of the breast tissue, forming new tumors. This is called metastasis. These adenocarcinomas are the most difficult tumor to accurately identify the primary site [7].

Diagnosis of adenocarcinoma is achieved by examining features such as tubular myelin, intranuclear surface apoprotein tubular inclusions, Langerhans cells associated with neoplastic cells, cytoplasmic hyaline globules, glycogen, lipid droplets, and cytoplasmic crystals. The diagnostic is painful since a tissue biopsy is utilized to extract the different types of cells mentioned above making it a cumbersome, time consuming, and costly process since they are ultrastructural features that are needed to be observed through electron microscopes. Another technique to diagnose adenocarcinoma is through the application of immunohistochemistry that has also been explored using estrogen and progesterone receptor proteins, thyroid transcription factor-I and surfactant apoproteins [7]. However, specificity and sensitivity are the main issues associated with this method. An alternative technique including a less invasive route is desirable to address some of the drawbacks of the current diagnostic tools used such that it is rapid, easy-to-use, economical, and sensitive. The combination of peripheral blood mononuclear cells (PBMCs) and microfluidics makes an excellent alternative that is explored through this article.

In this article, we explore the use of PBMCs to detect these cancerous cells since they are known to circulate in the peripheral blood of patients, especially when breast cancer is spread beyond the ducts into other parts of the breast tissues or other organs through blood [8]. PBMCs are typically isolated from whole blood using density gradient centrifugation commonly in Ficoll-Paque PLUS and the Histopaque 1077 media [9]. To discriminate and subsequently separate ADCs from PBMCs, increased interests have been rooted in exploring the utilization of the cell physical properties in lieu of other methods including antibody-conjugation, which is time consuming and can impact ADCs' properties and viability [10]. Leveraging physical characteristics in the form of size-based filtration [11–13], density-gradient separation [14–16], and inertial-hydrodynamic discrimination [17–19] has been explored in the past until Shim et al. reported that size and density distributions of ADCs tend to overlap with those of PBMCs, leading to occasional inefficiency in the separation of ADCs based on size and density. An alternative technique is to utilize the electrophysiological property differences between PBMCs and ADCs in a microfluidic device, termed as dielectrophoresis (DEP).

Dielectrophoresis (DEP), a microfluidic and an electrokinetic technique that could be utilized to detect ADCs from a heterogenous population of PBMCs, utilizes electric signatures like cell capacitance and conductance in a non-uniform electric gradient, and seems to be a novel alternative [20–25]. DEP is a promising technique that is utilized to characterize and manipulate different types of cells like red blood cells, bacteria, virus, yeast, and proteins. It also is capable of detecting subtle changes on the cells based on their state, i.e., alive and dead, healthy and infected. In this article we choose to characterize PBMCs and ADCs utilizing DEP as a detection tool via quantifying the unhealthy or diseased cells, i.e., cancer cells because it employs no moving parts, it is non-destructive for the bioparticles, and utilizes low electric current on a micro-chip without the need of antibody tagging or fluorescent labels making it a portable system. Reduced response time and higher throughput and accuracy makes DEP a promising technique for cancer cell detection.

When a bioparticle is subjected to a non-uniform electric field, the dielectrophoretic forces and the dipole-dipole forces between the particles (dipole moments) are generated based on the differences between the electrical properties (capacitance and conductance) of cells and the surrounding fluid [23]. Traditionally, DEP based cancer cell separations employ metallic electrodes to capture infected cells,

by creating non-uniform electric fields using AC voltage [16,25]. AC DEP device offers a major disadvantage in the form of decreased metal electrode functionality due to fouling when biological samples are manipulated [24,26]. Also, these devices often have high cost associated with the fabrication containing metal parts [24,27]. To address the challenges posed by AC DEP device, we chose to explore DC electric current (insulator-based DEP (iDEP)) as an alternative to electrode-based DEP. iDEP employs insulating objects or structures created by microfabrication embedded in the channel to generate spatial non-uniformities in the field [28,29]. With the electrodes placed in the inlet and outlets, here electroosmotic forces can be utilized for inducing flows, eliminating the need for the pumps for continuous operation [30]. The aim of this work, therefore, is to determine experimentally if there are differences in the electrophysiological properties of normal PBMCs and ADCs and to use these differences, if they exist, to numerically attempt their detection (using DC signals) on a microchip—an important step towards the development of a supplementary diagnostic device for ADCs.

In this article, we develop an *in silico* based COMSOL Multiphysics model for continuously detecting ADCs from a heterogenous population of PBMCs in a microchannel with modified geometry. To create non-uniformity in the electric field, an array of semi-circular insulating obstacles are embedded in the microchannel. First, a PDMS-based microwell was constructed to house a horizontally arranged 100 μm apart platinum electrode (Figure 1) to obtain the characteristic membrane properties of both ADCs and PBMCs. The properties, validated against the available data in the literature, are then utilized to in conjunction with Finite Element Method (FEM) to model and simulate the trajectory of both cells (ADCs and PBMCs) in a semicircular-insulator-based 2D microfluidic channel. While the characterization of the ADCs gives the innate electrical signatures that is characteristic of moderately differentiated infiltrating ductal adenocarcinoma, the utilization of FEM sets a workable model that could serve as a platform for fabricating a novel diagnostic device for ADCs.

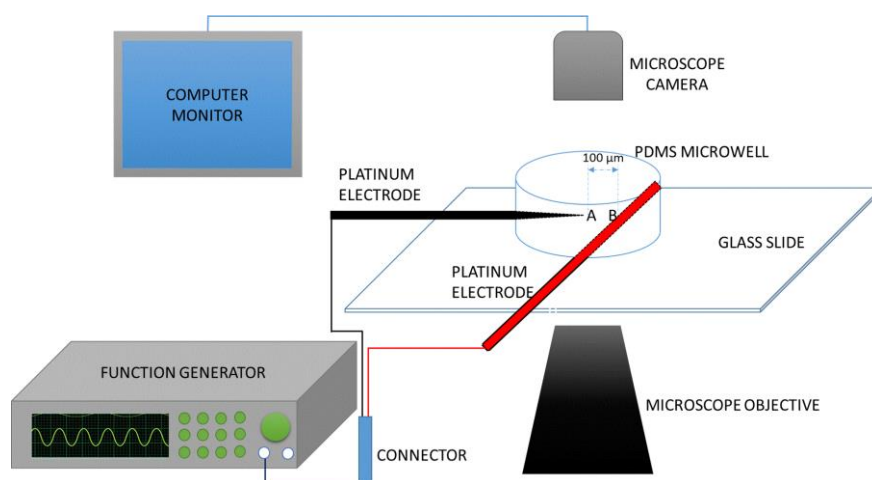


Figure 1. The experimental set-up for the measurement of dielectrophoresis (DEP) crossover frequency using a novel microwell platform to obtain electrophysiological properties, i.e., conductivity and permittivity of peripheral blood mononuclear cell (PBMCs) and adenocarcinoma cells (ADCs) that will aid in designing an early detection platform for breast cancer.

2. Theory of Dielectrophoresis

Crossover frequency measurement is a novel dielectrophoretic-based method of characterizing the dielectric properties of many biological particles. By crossover frequency, we mean the frequency at which cells suspended in a microwell in an osmotic concentration medium, change their direction of motion towards or away from the high field region in an electric-field-gradient-based system. When a bioparticle (i.e., cell) is placed between the two electrodes as shown in Figure 1, the cell can either move to A or B depending on its polarizability relative to the medium in which it is

suspended. Cells move to A (pDEP) if they are more polarizable than the medium and to B (nDEP) if the reverse occurs. At varying conductivity of the suspending medium, various crossover frequency data (f_{xo}) can be generated. In this current work, these data are generated, plotted and fitted with a model (Equation (1)) using least square regression and the confidence of the fit was found through the coefficient of regression analysis. A voltage drop at the electrode boundary is considered to be significant at frequencies below 15 kHz [30]. Also, because the reservoirs of microdevice are typically considered as an enormous source of ions compared with the microchannels themselves, any voltage drop can be neglected between the electrode and the inlet or outlet to the microchannel. In this study, the operating conditions for the crossover frequency quantification are maintained above the reported threshold and thus can neglect the voltage drop at the boundary of the electrodes that are placed in the inlet and outlet reservoirs. According to Pethig [31] or a biological cell whose interfacial polarization between the plasma membrane and the cytoplasm results in a dispersion frequency far below 1 MHz for the cell effective dielectric permittivity and conductivity, the first crossover frequency, f_{xo1} , of the cell membrane is given by:

$$f_{xo1} = f_{xo1}(C_{mem}, G_{mem}, \sigma_m) \tag{1}$$

$$f_{xo1} = \frac{1}{\sqrt{2}} \frac{\sigma_m}{\pi R C_{mem}} \sqrt{1 - \frac{R G_{mem}}{2 \sigma_m} - 2 \left(\frac{R G_{mem}}{2 \sigma_m} \right)^2}$$

$$\forall C_{mem} = \epsilon_{mem} / d \tag{2}$$

$$G_{mem} = \sigma_{mem} / d \tag{3}$$

In terms of total particles and medium properties, f_{xo1} can also be represented as

$$f_{xo1} = \frac{1}{2\pi} \left\{ \frac{(\sigma_m - \sigma_p)(\sigma_p + 2\sigma_m)}{(\epsilon_p - \epsilon_m)(\epsilon_p + \epsilon_m)} \right\}^{1/2} \tag{4}$$

where, C_{mem} is the specific membrane capacitance, G_{mem} the membrane conductance, σ_m the conductivity of the suspending medium, ϵ_{mem} the permittivity of the membrane, σ_{mem} the conductivity of the membrane, d is the characteristic dimension of the cell membrane and R , the radius of the particle. In an iDEP system, the DEP force, \vec{F}_{DEP} , acting on the particles due to the field gradient is a function of the particle and medium characteristics and is given as:

$$\vec{F}_{DEP} = 2\pi\epsilon_m r^3 \left(\frac{\sigma_p - \sigma_m}{\sigma_p + 2\sigma_m} \right) \nabla \left| \vec{E}_{DC} \right|^2 \tag{5}$$

where the quantity $\left(\frac{\sigma_p - \sigma_m}{\sigma_p + 2\sigma_m} \right)$ is the Clausius-Mossotti factor (CM), which is the parameter that determines whether \vec{F}_{DEP} will be positive (as in pDEP) or negative (as in nDEP) and $\nabla \left| \vec{E}_{DC} \right|^2$ is the field distribution parameter that enhances particle polarization and dielectrophoretic separation effect.

This force is usually balanced with the viscous drag within the fluid system. Prior to the utilization of DEP-viscous force balance for particle separation, electrokinetic forces (electroosmotic and electrophoretic forces) would have been utilized to pump the particles to the separation region through the electroosmotic channel wall condition and the electrostatic interaction of the electric field with the particles.

Electroosmotic flow is generated due to the action of the electric field on charged interior surfaces having electrical double-layer (EDL). For the microscale flow, surface charge generated at the solid wall-ionic liquid interface is a significant interfacial property to affect the flow. This is because the surface charge at the solid-liquid interface can redistribute the charged ions in the ionic liquid and forms the electrical double layer (EDL) with local net charge density. However, because of the characteristic

length of the EDL known as Debye length is small and has the typical values from several nanometers to one micrometer (significantly small compared to the dimensions of the channel), thus the effect of EDL on the microscale flow is usually neglectable and it can only produce obvious effect on the nanoscale fluid flow. When an external electric field is applied on the ionic liquid with EDL within a microchannel, the liquid will be driven by the electric field and form the electroosmotic flow (EOF), which is a typical fluidic transport phenomenon over the microscale [32,33]. The nature and magnitude of the charge in EDL is characterized by the Zeta potential [34]. Electroosmotic mobility of fluid is a function of the Zeta potential of the microdevice, i.e., microchannel construction material and is given by [35]:

$$\mu_{EO} = \frac{-\xi \varepsilon_m}{\eta} \quad (6)$$

where, μ_{EO} is the electroosmotic mobility, ε_m is the permittivity of medium, ξ is the Zeta potential of the material and η is the viscosity of suspending medium (buffer). The electrophoretic mobility unlike the electroosmotic mobility that depends on the material, depends on the Zeta potential of the particle itself and is given by [36]:

$$\mu_{EO} = \frac{\xi_p \varepsilon_m}{\eta} \quad (7)$$

where, ξ_p is the Zeta potential of the particle. At the separation region, the particle experiences a dielectrophoretic force that is impacted by the particle mobility. The DEP mobility is a function of CM factor and for a spherical particle it is expressed as [37]:

$$\mu_{DEP} = \frac{\pi d_p^2 \varepsilon_m}{12\eta} CM \quad (8)$$

where, d_p is the particle diameter and η is the medium viscosity.

3. Materials and Methods

3.1. Microwell Fabrication

Silicone elastomer mixed with its curing agent in 10:1 ratio (Sylgard 184, Dow Corning, Midland, MI, USA) was placed in a desiccator chamber under 0.27-mTorr vacuum in order to remove the bubbles formed during the mixing process. After three successive degassing operations lasting for 15 min, at an interval of 5 min between each run, the clear PDMS was poured into a clean petri dish and cured in the oven at 70 °C for 1 h. This step was followed by dicing the PDMS into 1" × 1" squares. A 3-mm hole was punched into each of the diced PDMS to create a well onto which the cell suspension was pipetted. Scotch tape was used to remove any dirt/dust from the PDMS after which it is was irreversibly sealed to a borosilicate glass slide through plasma oxidation of 50 W RF power for 1 min. High purity platinum wire was connected to the microwell as shown in Figure 1. With the aid of an Olympus IX71 inverted microscope (Olympus, Tokyo, Japan), the distance (100 μm) between the electrode tips was set. Loctite's self-mix epoxy was used to keep the electrode spacing intact. The epoxy also prevented any leakage of liquid when the microwell was filled with cell suspension. This was evident when anhydrous copper sulfate was dispensed around the filled microwell, in a regulated environment, did not cause any change in color, i.e., from its natural white to blue color.

3.2. Cell Pretreatment

The DEP suspending medium (dextrose solution) was prepared and characterized as described in our previous article [38]. The prepared 100 mL suspending medium was divided into five separate beakers. Into each beaker, except the first, calculated volume of phosphate buffer saline (PBS) was added to successively change the conductivity of the DEP suspending medium to obtain the following conductivities (in mS/m): 50, 60, 74, 88 and 97. Female normal peripheral mononuclear cells (PBMCs)

and infiltrating ductal adenocarcinoma cells (ADCs) with no identifiable angiolymphatic invasion were obtained from Conversant Bio, Huntsville, AL, USA. Also, the cells obtained did not have any identifiable information about the patient itself except their gender and age (Institutional Review Board - IRB exempt). The cells were prepared for experiment according to the supplier's instructions. Thereafter, a known number of cells were transferred into each of the five DEP suspending medium solution where they were washed twice and diluted in 1:400 cell: suspending medium ratio before being pipetted into the DEP microwell for experiment.

3.3. Measurement of Crossover Frequency

After the assurance that the microwell was leakage-free, the platinum electrodes were connected to the two terminals of an 80 MHz Siglent SDG 2082X Arbitrary Waveform Generator (Siglent Technologies, Solon, OH, USA), which supplied an 8 V peak-to-peak sinusoidal AC signal of shifting frequencies. 5 μ L of the PBMCs suspension prepared as discussed in Section 3.2 was transferred into the microwell and allowed to equilibrate. Then, about 4 μ L was carefully siphoned from the well so that fewer cells (between 4–7 cells) were present in the field-of-view for the experiment. Having fewer cells does not only reduce the influence of particle-particle interaction, but also enhances clarity in visualizing cells for crossover frequency determination. The waveform generator was then switched on to generate electric field gradient around the electrodes. Movement of cells was monitored and captured with a high-speed camera at 30 fps as a function of the changing field frequency until the crossover frequency was found. There was no movement of cells or flow when the waveform generator was turned off. The experiment was repeated four times (technical replicates) and there were two set of biological replicates obtained for the experiments and the crossover frequency was found in each case. More experiments were run using the other modified medium at varying conductivities thus obtaining crossover frequency spectra. The PBMCs are majorly lymphocytes (>80%) \sim 10 μ m in diameter while ADCs are \sim 20 μ m in diameter. Measurements were made at room temperature conditions, i.e., $T = 24 \pm 1$ $^{\circ}$ C.

4. Finite Element Modeling and Simulation

In this section, attention was given to the numerical modelling and simulation performed using the dielectric properties obtained from the crossover frequency measurements in Section 3.3. COMSOL Multiphysics 5.3a (Comsol Inc., Stockholm, Sweden) was used to solve fluid flow, electrostatics, and particle tracing modules in an integrated stationary and time-dependent fashion. The architecture of the separation device (Figure 2) was arrived at after a series of parameter modification that ensured a complete separation of ADCs from its mixture with PBMCs. The design was made in 2D because the width to depth ratio was more than 5:1.

Electric current mode was used to solve, in steady states, the current conservation equation based on Ohm's law and electric displacement relations using the electric potential as the dependent variable. This was solved in steady state because the charge relaxation time for the conducting media (water, in this case 3.6×10^{-6} s) is less than the external time scale for device operation (10 s). Solving this Ohm's law with the charge conservation and electric displacement equations gives the electric field, E , which was used to compute the electroosmotic boundary condition used in the creeping flow analysis according to $u_{EO} = \mu_{EO}E$, where u_{EO} is the electroosmotic velocity- the velocity of the bulk of the fluid flowing in the channel due to electric field effects. In the incompressible creeping flow analysis (as is the usual case in microfluidic channel where the Reynolds number is significantly less than unity and viscous force is dominant), the steady state form Stokes equation together with the continuity equation was solved as the synergistic conservation of momentum and mass, which account for the velocity profile within the fluidic channel. The magnitude of this velocity as a function of the position within the channel was then used to solve the drag force (Table 1) acting on the particles flowing within the channel through numerical coupling. The drag force is then counterbalanced by the dielectrophoretic force, Equation (5), at the region where the magnitude of electric field norm was modified as a

result of the constrictions placed between the inlet and the outlet channels. Each particle moving through the microdevice was tracked using the particle tracing module solved in time-dependent mode. Tracking the particles enabled the statistics through which the device parameters (like voltage, device dimensions, etc.) that generated the desired separation of the particles were noted. Using a free triangular customized mesh, with different sizes, growth rate, and curvature factor for both constrictions and the remaining regions within the channel, the geometry was discretized and made ready for finite element analysis. Multifrontal massively parallel (MUMPS) solver, which performs Gaussian factorization, was used in the stationary mode to obtain the velocity profile and the electric field norms. MUMPS solved for the velocity profile and the electric field norms these values with a relative tolerance of 0.001 and without any recourse to lumping while computing the fluxes. GMRES (generalized minimal residual solver), a solver that approximates solutions by the vector in a Krylov subspace with minimal residual, was used in the transient domain to track the particles with respect to their position in space and velocity magnitude as a function of time. The final geometry of the device where complete separation occurs was 1.4 mm in length with 5 semi-circular constriction of radius 0.1 mm and inter-structural constriction spacing of 85 μm . The distance D (Figure 2) between the constriction end and the upper channel wall was fixed to be 35 μm . This distance forbids two cancer cells to pass through the separation region at any given time. This design was made to prevent any form of shielding that may eventually result in incomplete separation. Table 1 provides a list of parameters, variables, boundary conditions in each type of study utilized in COMSOL, and equations associated with the modeling and simulation. Zeta potential for PDMS was assumed to be -0.1 V and a relative permittivity of 80 was used in the simulation. The flow velocity at the inlet was assumed to be 0.001 m/s.

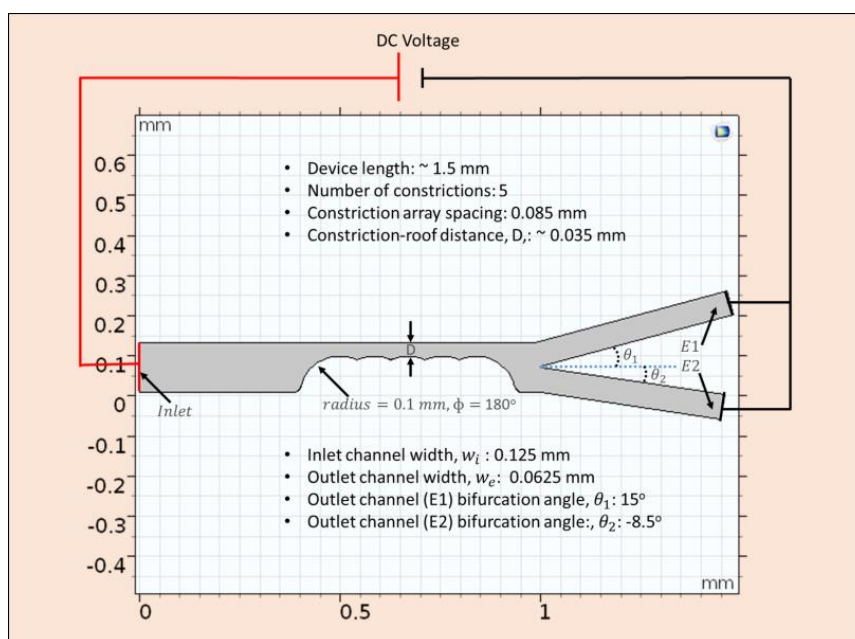


Figure 2. Optimal device design geometry obtained by COMSOL modeling and simulation utilizing the electrophysiological properties of PBMCs and ADCs from the PDMS microwell. Entire microfluidic platform is ~ 1.5 mm with semi-circular constrictions embedded in the channel. Inlet channel is 125 μm wide and the two outlet channel widths are ~ 62.5 μm . Pt electrodes in the inlet and outlet ports is connected to a DC power supply to further sort ADCs from healthy PBMCs.

Table 1. List of parameters, variables, discretization, type of study utilized, and the equations associated that was incorporated into COMSOL package for optimizing the device geometry and sorting of adenocarcinoma (ADCs) from healthy peripheral blood mononuclear cells (PBMCs).

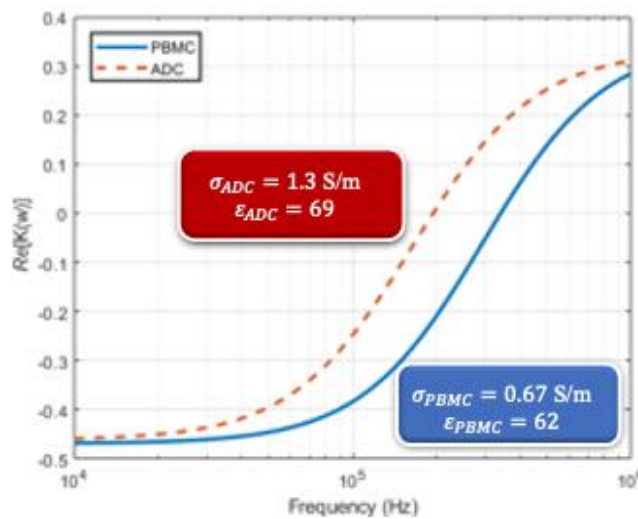
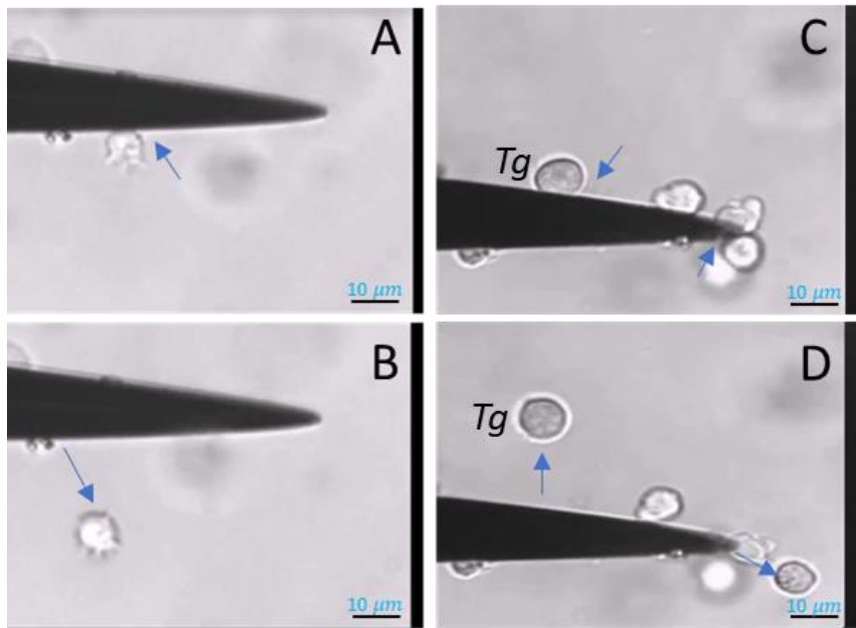
Physics/Parameters	Tag	Dependent Variable	Discretization	Study	Equation
Electric current	ec	V	Lagrange Quadratic	Stationary	$\nabla \cdot \mathbf{J} = Q_{j,v}$ $\mathbf{J} = \sigma \mathbf{E} + \mathbf{J}_e$ $E = -\nabla V$ Wall boundary- insulated $(\mathbf{n} \cdot \mathbf{J} = 0)$
Fluid Flow	spf	u	P2 + P1	Stationary	$\nabla \cdot [-p\mathbf{I} + \mu(\nabla u + (\nabla u)^T)] + \mathbf{F} = 0$ $\rho \nabla \cdot (u) = 0$ Wall boundary- electroosmosis $u = \mu_{eo} E_t$ $\forall \mu_{eo} = \frac{\epsilon_r \epsilon_0}{\mu} \xi; E_t = E - (E \cdot n)n$
Particle tracing	ptf	q, v	Formulation	Transient	$\frac{d(m_p v)}{dt} = \mathbf{F}_t$ $\mathbf{F}_D = \frac{1}{\tau_p} m_p (\mathbf{u} - \mathbf{v})$ $\tau_p = \frac{\rho_p d_p^2}{18\mu}$ $\mathbf{F}_{DEP} = 2\pi r_p^3 \epsilon_0 \text{real}(\epsilon_r^*) \text{real}(K) \nabla \mathbf{E} ^2$ $K = \frac{\epsilon_{r,p}^* - \epsilon_r^*}{\epsilon_{r,p}^* + 2\epsilon_r^*} \forall \epsilon_r^* = \epsilon_r \text{ in stationary field}$ Wall boundary- particles bounce-off walls
			Newtonian		
			Drag law		
			Stokes		
Meshing	Calibration		Mesh Type	Max size	Boundary layer transition
	Fluid dynamics		Free triangular	0.001 mm	Smooth transition to interior mesh
Stationary solver				MUMPS	
Transient Solver				GMRES	

5. Results and Discussion

In this section, we finally discuss and present the important results to prove that breast cancer can be detected early enough using whole blood. This simulation study demonstrating sorting of ADCs from PBMCs will further be validated experimentally (beyond the scope of this article). Our results are categorized into sections demonstrating: (1) experimental evidence of electrophysiological characterization of both healthy PBMCs and breast cancer ADCs, (2) validation of our microwell technique by comparing with studies from literature and (3) modeling and simulation parameters like meshing, stationary analysis, transient analysis.

5.1. Electrophysiological Characterization of PBMCs and ADCs Experimentally

In estimating the properties of both PBMCs and ADCs movement of cells toward or away from high field region was tracked until the crossover frequencies were found in case at changing properties of the suspending medium. Figure 3A,B shows an ADC cell experiencing positive and negative DEP force (pDEP and nDEP) respectively. In Figure 3C,D, we manually tracked the movement of the target cell as previously demonstrated for prostate cancer in Hele-Shaw flow cell by Huang et al. [39]. Figure 3E shows the first crossover frequency behavior when cells experience a switch from nDEP to pDEP. This first crossover frequency, usually in Hz–kHz range is mainly due to the membrane associated proteins, shape, and size of the cell. The first crossover frequency is often enough to study the phenotype of the cells; however, to characterize their genotype, the 2nd crossover frequency value has to be obtained, often in MHz range.



(E)

Figure 3. ADC cells experiencing DEP in the microwell at varying AC frequencies- (A) shows the ADC cells experiencing positive DEP (pDEP) wherein the cells move towards the high-field region or the triangular electrode in here and (B) shows the ADC cells experiencing nDEP behavior wherein the cells move away from the high field region. (C,D) are the images resulting from manual tracking of the target cell (labeled Tg) as demonstrated in [39]. (E) shows a plot of real part of Clausius-Mossotti factor varying with frequency (Hz). Here the cells initially experience nDEP (negative DEP) and as the frequency increases, they switch to pDEP (positive DEP) where the switch is termed as first crossover frequency.

The crossover frequency data for PBMCs and ADCs were fitted using Equation (1). This equation is an ideal model owing to the spherical nature of lymphocytes. Equation (1) is also suitable for ADCs even though they are a little distorted. Kirby and Huang et al. had reported that an isotopically inhomogeneous non-spherical cell can still be analyzed, to a good approximation, with single shell model since the spherical harmonic solutions used in the eigenfunction expansion approximations for DEP force can help define the effective particle properties [39,40]. Since the second crossover frequencies could not be obtained due to the limitation of the measuring equipment, often obtained at

high frequency range (>50 MHz), the cytoplasmic properties used in the simulation were as reported by Qiao et al. using impedance measurement [41]. The total (effective) particle conductivity, σ_p , and permittivity was obtained as described by Adekanmbi et al. [3] and Pethig [31] respectively. Table 2 provides the dielectric properties obtained from our experiments that are compared to the other published literature values in case of PBMCs. It should be noted that the conductivity of the infected ADCs rise sharply compared to the healthy PBMCs that may be attributed to the introduction of new membrane permeation pathways, to membrane peroxidation damage, and to changes in membrane fluidity following infection [42].

Table 2. Dielectric properties, i.e., conductivity and permittivity obtained from our novel electrokinetic technique based on cell response obtained at crossover frequency for ADCs and healthy PBMCs using an osmotic concentration suspending medium maintained at osmotic conductivity and permittivity. Literature reported values has been compared with our novel technique for PBMCs only as a measure of validation [43].

Property	ADCs (Infiltrating Ductal Adenocarcinoma Cells)	PBMCs (Lymphocytes)		Suspending Medium
	Crossover Freq. Technique	Crossover Freq. Technique	Literature Reported [43]	
Conductivity (S/m)	1.3	0.67	0.66	0.055
Permittivity	69	62	59.62	80

The data fitted using MATLAB in Figure 3E were analyzed using chi-square test. The expected value of the crossover frequency is determined from the curves in Figure 3E at $Re(K(\omega)) = 0$ to prove that the fitting is reasonable. The χ^2 critical value at 0.05 significance value is obtained to be 11.07. The χ^2 test statistic value for ADCs and PBMCs are found to be 1.1804 and 2.413 respectively. Since, the calculated test statistic is less than the critical χ^2 value, it signifies a reasonably good fit, i.e., there is no significant difference between the observed (curve) and expected (experimental) values.

However, the authors believe that this is the first time that ADCs were characterized using a novel electrokinetic technique to obtain their dielectric properties i.e., permittivity and conductivity as shown in Table 2.

5.2. Parameters Affecting COMSOL Modeling and Simulation to Obtain High Sorting Efficiencies

In this section, we discuss the factors that affect the optimization of the device geometry to achieve high sorting efficiencies that further influence early breast cancer detection obtained through sorting ADCs from healthy PBMCs.

5.2.1. Meshing of the Device Design in COMSOL

Meshing is one of the factors that strongly affect modelling requirements. Choosing the right mesh element types and sizes is highly pivotal to the accuracy of the simulation results in any finite element problem. Under-meshing can result in solutions that are far less than accurate while over meshing can result in large amount of computational time due to the mesh using too many unnecessary elements. To prevent under meshing, we used mesh elements greater than 40,000. Over meshing was, however, checked and prevented by using meshing sequence with local and global attributes. The local mesh density at the constrictions was sufficiently increased by reducing mesh size while the remaining part of the geometry (where dielectrophoretic force would not have significant effects) was meshed at increased mesh size. This meshing sequence, which was based on Lagrange quadratic representation, reduced the total number of mesh element by 45.17% and computation period by 51.06%. Since the dielectrophoretic force, which causes cells to separate based on their movement away or towards the high field region, acts significantly at the channel constriction zone, it was necessary to verify if the maximum element size (MES) at the constriction would affect the transmission probability of ADCs

and to what extent would that effect be. As shown in Figure 4, the accuracy of the solution (which is a function of the transmission probability) depends on the choice of mesh size. The mesh characteristics that was found to be optimum at the applied effective potential difference is as given in Table 1.

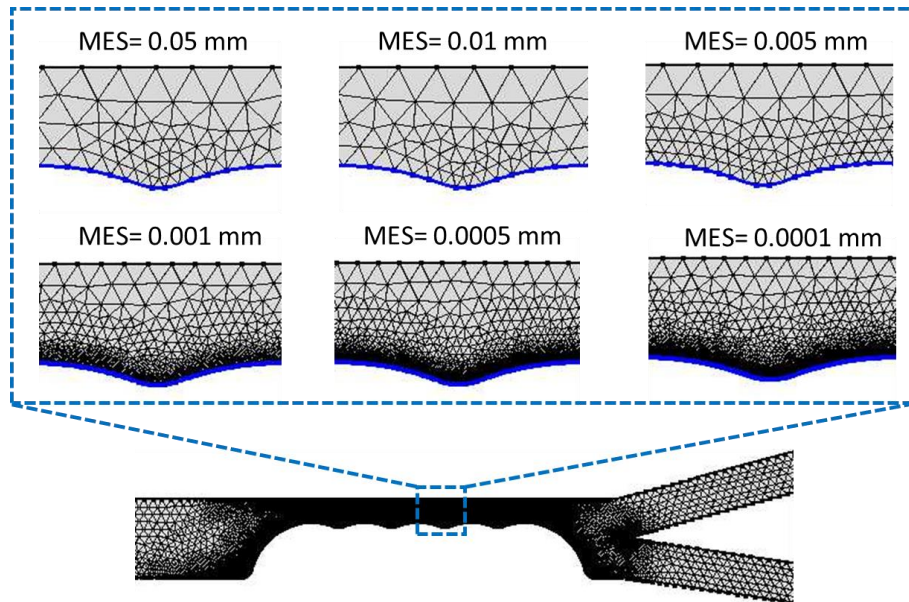


Figure 4. The discretization of the separation region, i.e., along the semicircular constrictions where maximum DEP effect is observed that causes the cells to move into categorized streamlines by adopting variable mesh element size (MES).

Figure 4 demonstrates the gradation of the discretization regime of the constriction zone as the maximum element size (MES) is progressively reduced. At MES = 0.05 mm the density of the triangular mesh is very low indicating that the inter-nodal distance within the discretized zone is large. This large distance depicts an inefficient solution capacity for the gradient of the electric field, which is evident in the low transmission probability (TP) for the ADCs (Figure 5). Transmission Probability, TP, is referred to as the ratio of the number of particles at a specified exit to the total number of the particles at the inlet. In other words, large mesh size at the constriction zone was not able to correctly solve for the electric field gradient which is necessary for dielectrophoretic influence on the particles. When the mesh size was progressively reduced, the number of elements increased correspondingly. This in turn increased the separation efficiency at the constriction zone, hence the dramatic ramping up of the percentage of ADCs that were sorted from healthy PBMCs. It is important to note that the progressive reduction in MES increases the computation time, i.e., with MES at 0.0005 mm and 0.0001 mm requiring 800% and 960% more time than at 0.001 mm. Since the TP value for MES = 0.001 mm, 0.0005 mm and 0.0001 mm are comparatively similar and >97%, the computation was carried out at 0.001 mm with an error margin of $\sim <0.00020\%$. At these values (0.001, 0.0005 and 0.0001 mm), it is safe to conclude that the stationary and transient solutions (within the margin of error) of the coupled physics do not vary with mesh condition as the TP values tend to be approximately constant. MES value beyond 0.0001 mm showed critical error warning sign in COMSOL and was computationally very expensive.

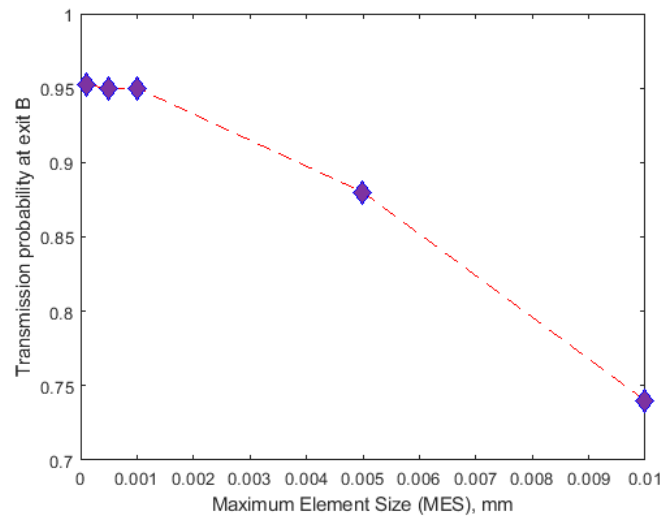


Figure 5. Transmission probability of ADCs as a function of the maximum element size at the separation zone, i.e., around the semicircular constriction region. Since MES at 0.001 mm, 0.0005 mm, and 0.0001 mm are almost similar, the simulation was completed fixing MES at 0.001 mm.

5.2.2. Stationary Field Analysis

The numerical computation comprises of two stationary fields: (a) creeping (fluid) flow and (b) electric current (ec). The electric current was solved in the stationary mode to generate the electric field that not only generated the electro-osmotic effects at the channel wall but also provided the distribution of field strength, E , whose gradient provided the necessary dielectrophoretic force at the constrictions.

As shown in Figure 6A, when DC potential difference was applied across the channel (from the inlet to outlet) and there was a distribution of the electric field as governed by the Laplace equation. The tips of the constrictions within the channel, generated the highest field strength region that was important for dielectrophoretic separation. In Figure 6, the effect of the field gradient is visually more pronounced when the flow field lines were plotted together with the electric field norm. Glaringly, the gradient of the field which was utilized by the dielectrophoretic force acting at the constrictions interfere with the velocity field. The dielectrophoretic velocity introduced at the constrictions added to the already existing electrophoretic and electroosmotic velocities apart from the increase in velocity that was introduced by the continuity equation owing to the reduction in flow area. Figure 6C shows the ripple effects generated from the surface of the constrictions outwards. The resultant effects of this streamline interference could be seen in Figure 6D–F at varying DC voltage, i.e., 10 V, 110 V, and 60 V respectively. The number of constrictions were fixed at 5 and diameter of the constriction was considered to be 100 μm .

Effects of applied potentials and constriction radius on transmission probability: It is important to verify the effects of the electric field strength at various applied potentials and constrictions on the separation efficiency of the microdevice platform. As a result, the radius of the constrictions was varied keeping the number (#) of constrictions fixed at 5 at a given time thus resolving the Laplace equation each time using different applied potential without varying the mesh conditions (Figure 7). The number of constrictions was fixed as an optimization test constraint with respect to the length of the device as well as the exploration of the possibility of initiating cellular separation with minimal insulating constrictions as previously demonstrated by Adekanmbi et al. [38].

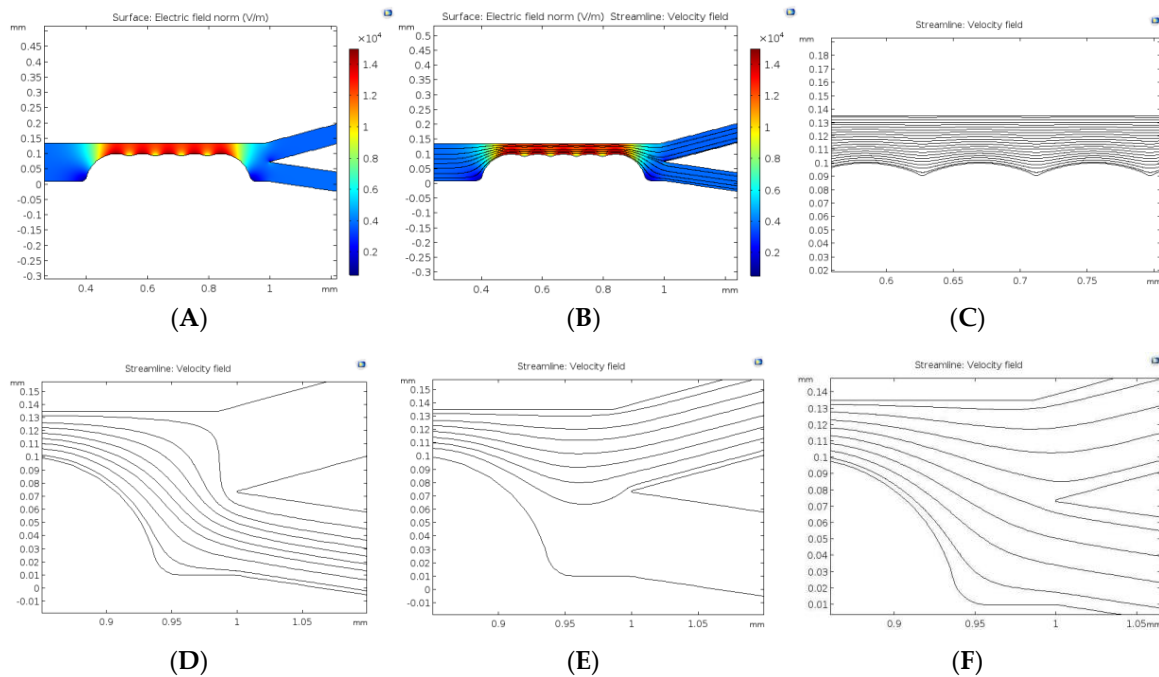


Figure 6. Field and velocity profiles obtained from solving the electrostatics and stokes equations in stationary mode. (A) is the electric field norm, (B) is the combination of the field norm with velocity streamlines, (C) is the zoomed image showing the effect of the constriction zone on velocity streamlines. (D–F) show streamlines based on changing DC voltage at 10 V, 110 V and 60 V respectively. The constriction diameter and number were fixed to be 100 μm and 5 respectively.

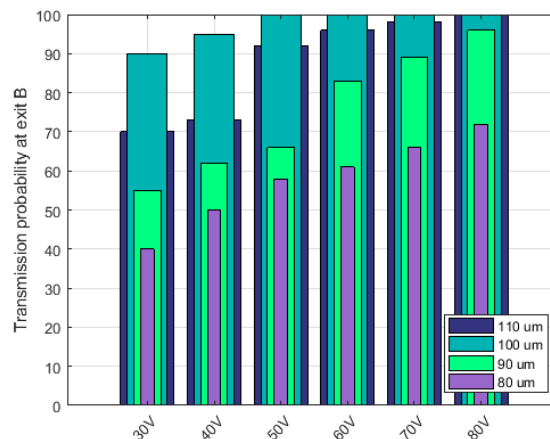


Figure 7. Effects of constriction clearance / size, i.e., diameter and DC voltage on the transmission probability of ADCs. Diameter of the constrictions were varied—80, 90, 100, and 110 μm keeping the number (#) of constrictions fixed, i.e., 5 at a given time. Perfect sorting was observed for constriction diameter of 100 μm at voltages $>50\text{ V}_{\text{DC}}$.

Transmission probability of the total number of PBMCs (from inlet to outlet) as a function of the constriction gap, i.e., D in Figure 2 and applied voltage using a fixed number of constriction entities, i.e., 5 was calculated and plotted as shown in Figure 7. Transmission probability (TP) is congruent to normalizing the amount of PBMCs recovered by the initial amount of PBMCs in the inlet mixture. This means, a TP value of 1 represents 100% separation of the PBMCs from its mixture with ADCs. The essence of calculating the transmission probability was to verify the selectivity of the device and to track operating parameters that would be optimal for the operability of the device. Figure 7 demonstrates the effect of varying the constriction diameter and the applied voltage on the transmission probability

of PBMCs. The TP value for each of the constriction diameter was progressively increased with the changing potential. At a given DC voltage, the recovery of PBMCs was highest when the constriction diameter was 100 μm . More so, from 50 V to 80 V, 100 μm constriction diameter gave a perfect separation of the PBMCs. None of the constriction diameters gave 100% separation except 110 μm at 80 V. These variations in transmission probability could be attributed to the changing electric field strengths as the applied voltage and constriction diameter change. Changing the applied DC potential affected the electrokinetic and dielectrophoretic forces operating within the channel. Electrokinetic contributions within the channel affects the particle velocity and hence the resident time within which the particles are expected to experience strongest DEP force at the constriction zone. At <50 V, the electro-osmotic velocity of the bulk fluid medium was low enough to move the particles slowly to the constriction zone where there is ample residence time for the cells to experience sufficient induced dielectrophoretic force that would cause them to be separated adequately. However, since DEP force depends on square of the field gradient, the low DC potential (<50 V) could not generate the required electric field gradient that is sufficient to induce strong negative dielectrophoretic force necessary for sorting the cells into their respective differential outlets.

Since increasing electric potential could result in increased Joule heating of the microdevice leading to unwholesome modification of the electrokinetic and dielectrophoretic effects, 100 μm constriction diameter was considered to be the ideal dimension for the separation device platform. Furthermore, operating at a lower voltage, i.e., $\sim 60 \text{ V}_{\text{DC}}$ seems to reduce the risk of Joule heating within the insulator-based dielectrophoretic device.

5.2.3. Transient Analysis

Particle tracking analysis was used to trace the movement of both ADCs and PBMCs along the whole microdevice platform. There is no change observed in the particles' trajectory when the particle position is placed either at the center or the edge of the inlet, since a uniform particle distribution is selected in COMSOL within the channel. There is no surface interaction with the particles due to the "bounce-off" condition selected in COMSOL. Particles were seen moving through the channel inlet until they were acted upon by the dielectrophoretic force at the constriction which tend to move the particles either towards or away from the constriction surface depending on the properties of the medium, ADCs, PBMCs, and the generated electric field gradient. From the equation of the dielectrophoretic force (Equation (5)), the force experienced by both PBMCs and ADCs at the constriction depends on the square of the electric field gradient as well as the radius of the particle to the third power. The membrane conductivity of both ADCs and PBMCs are both less than that of the medium. Therefore, it is expected that both of them would experience negative DEP.

Figure 8 demonstrates the scenario where ADCs and PBMCs were partially and completely separated while shifting the applied voltage for a constriction number of 5 and diameter of 100 μm at fixed medium properties. Figure 8A depicts incomplete separation at DC voltage below 50 V. At this applied voltage the strength of the applied electric field was not sufficient enough to push away the PBMCs. At 50 V, the generated field gradient had made the DEP force more negative such that the PBMCs were pushed away enough from the high field region to cause their separation from ADCs (Figure 8B). No separation was observed at higher DC voltages, i.e., >100 V (Figure 8C). However, there was separation at $\sim 100 \text{ V}$ but with some interesting modification to the flow streamlines as shown in Figure 9.

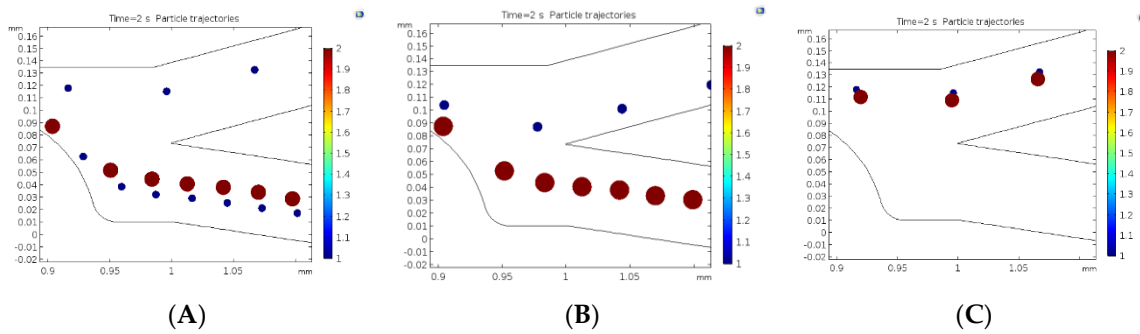


Figure 8. Particle trajectories showing partial (A,C) and complete separation (B) at various voltage conditions. The constriction diameter was fixed at $100\ \mu\text{m}$ along with number of constrictions at 5. (A) shows incomplete separation at $< 50\ V_{DC}$, (B) complete separation at $50\ V_{DC}$, (C) no separation at $> 100\ V_{DC}$.

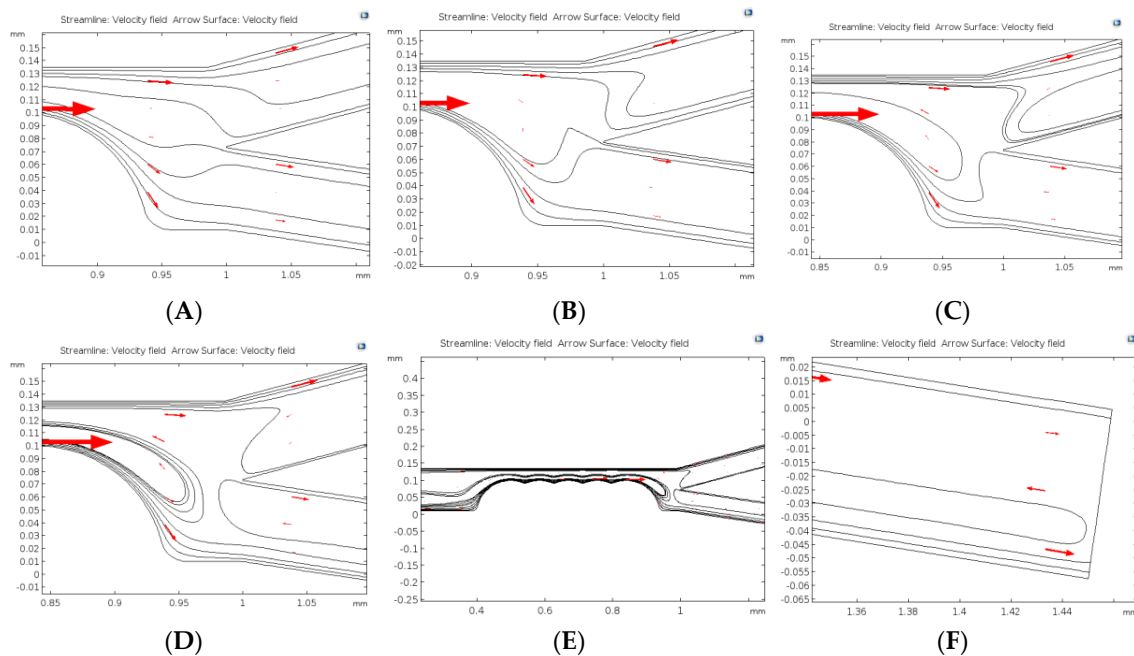


Figure 9. Velocity streamlines at various applied DC voltage conditions at fixed number of constrictions (5) and constriction size ($100\ \mu\text{m}$); (A) and (B) shows streamlines at $60\ V_{DC}$ and $100\ V_{DC}$ respectively; (C) partial recirculation observed at $120\ V_{DC}$; (D) increasing recirculation at $200\ V_{DC}$; (E) shows the recirculation effects that caused non-compliant behavior of cells to the DEP force; and (F) close-up of some cells that tend to reach the exit showing recirculation as well.

In Figure 9A, the operating DC voltage is $60\ \text{V}$ while Figure 9B is at $100\ \text{V}$. At $120\ \text{V}$ (Figure 9C), some streamlines are being recirculated and this recirculation became more and more pronounced as the applied voltage increased to $200\ \text{V}$ (Figure 9D–F). Figure 9D shows the close-up section of the bifurcation zone at $200\ \text{V}$, where in more recirculation of streamlines are being observed. Figure 9E is a close-up representation of the streamline recirculation showing some of the cells that were forced to move in a circular reverse direction to the DEP force. As shown in Figure 9F, some of the cells that were heading towards the exit ports are also forced to move towards the inlet, i.e., recirculated back into the main channel.

This interesting development may be associated with the inter-relation of the high potentials with the electric current within the channel, which, could generate a substantial amount of temperature rise that interferes with the conductivity of the fluid-particle system. Since dielectrophoretic force is a function of conductivity of the fluid-particle system, DEP is hampered as Joule heating becomes more

predominant due to the increased temperature. This simulation neglected particle-particle interaction on the basis of experiments since the cell suspension were to be diluted to an extent where in the cells will substantial be far apart that their interaction can be considered inconsequential.

5.3. Validation of the DEP Microwell Technique

The electrophysiological properties for PBMCs obtained data through our novel microwell platform via DEP crossover frequency measurement were validated by comparing the reported data in literature obtained through DEP electro-rotation measurement as reported by Chan et al. [43]. The samples used in this research and the reported literature values were from non-pregnant young female (<50 years of age) since pregnancy tends to substantially lower the specific membrane conductance of PBMCs [43]. The electrophysiological properties for PBMCs obtained from our experiments and the literature reported values were used to run the simulation independently under the same operating conditions. Figure 10 shows the results of the comparative simulation where a log-log plot of transmission probability (TP) and the progression time were plotted. Statistically, the p-value obtained for this comparison was 0.1 (at 0.01 significance level) implying that we do not have sufficient evidence to reject the null hypothesis of “no significant difference” between the two outcomes.

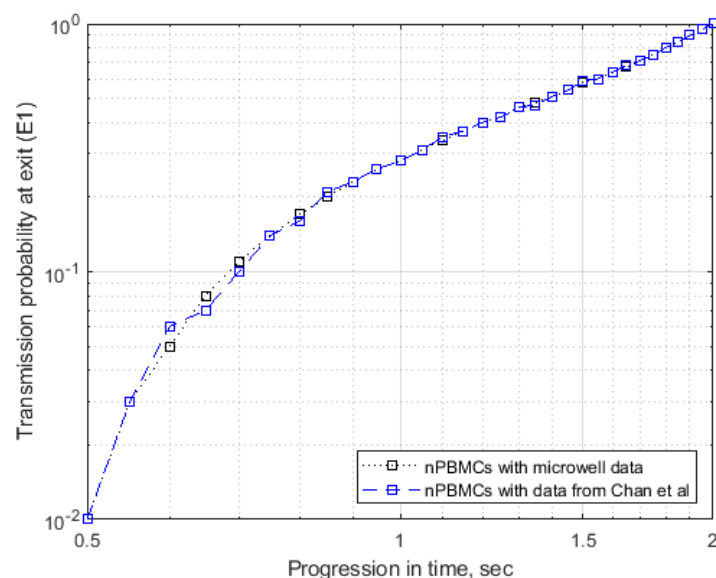


Figure 10. Validation of the electrophysiological properties of healthy PBMCs obtained from the DEP microwell platform using crossover frequency measurement and the literature reported values based on electro-rotation experiments [43]. Both the samples were derived from non-pregnant young women (<50 years of age).

6. Conclusions

Continuous dielectrophoretic separation of infiltrating ductal adenocarcinoma cells (ADCs) from isolated peripheral blood mononuclear cells (PBMCs) using direct current in a semi-circular insulator-based microchannel has been numerically studied. The electrophysiological properties for PBMCs used in simulations were obtained in a novel DEP microwell platform that characterized the behavior of the cells under varying AC frequency by measuring the DEP crossover of the cells. The first and second crossover frequency obtained were curve-fitted using a single shell model to obtain the conductivity and permittivity of the PBMCs. PBMCs vary in size and the sample used in this experiment was majorly small size lymphocytes, i.e., $\sim 10 \mu\text{m}$ in diameter.

Dielectrophoretic force is a function of the gradient of the electric field—a factor that also depend on the applied voltage as well as the constriction radius. In order to induce sufficient field gradient for the dielectrophoretic separation of ADCs from PBMCs, the applied DC potential and the constriction

diameter were dynamically varied until a regime of perfect simulation was obtained at constriction diameter of 100 μm and applied DC potential of ~ 50 V. The number of constrictions in the channel also affects separation efficiency and 5 semi-circular constrictions lead to optimal sorting of ADCs from PBMCs. This insulator-DEP based method of separating infiltrating ductal adenocarcinoma cells (ADCs) from isolated peripheral blood mononuclear cells (PBMCs) using direct current provided a cheaper, less cumbersome, easier-to-use, and yet efficient approach when compare with previous methods that used deformability, magnetism, or dielectric affinity column. Discretization of domain (meshing) in numerical analysis is an important factor that affect the accuracy of the solution obtained from solving any associated physics within a microchannel. In this paper, effort was made to strike a balance between the computational requirements of the mesh size and the desired transmission probability. Mesh size (local and global) was carefully chosen such that the resultant solution of the simulation did not vary with meshing. To aid our understanding of the choice of applied potential and how it relates with the separation efficiency, we found out that increasing the voltage beyond 100 V DC would lead to no separation, i.e., both PBMCs and ADCs moved into one exit channel.

Another interesting phenomenon was observed at higher voltages (>100 V) along with separation was recirculation behavior of cells. Some of the cells that were moving towards the exit channels were forced to change their direction back to the inlet. Recirculation increased especially between the constriction region and the bifurcation into exit channels with increasing DC potential. This behavior or wake formation is due to increased Joule heating as the temperature rises in the microfluidic platform with increasing DC potential since DEP is a function of the conductivity of the medium.

This DEP spectroscopy technique based on crossover measurement allows characterizing the intracellular differences and physical properties of cells, without any labeling, without affecting cell integrity and viability. Finally, this method confirms a high potential of emerging lab-on-chip (LOC) platforms in the early diagnosis and the treatment of breast cancer especially in young women where mammography is ineffective and/or painful.

Author Contributions: Conceptualization, S.K.S.; methodology, E.O.A.; software, E.O.A. and A.T.G.; validation, E.O.A., A.T.G. and S.K.S.; formal analysis, E.O.A. and A.T.G.; investigation, E.O.A.; resources, S.K.S.; data curation, E.O.A.; writing—original draft preparation, E.O.A.; writing—review and editing, S.K.S.; visualization, S.K.S.; supervision, S.K.S.; project administration, S.K.S.; funding acquisition, S.K.S. All authors have read and agreed to the published version of the manuscript.

Funding: This research did not receive any specific grant from funding agencies in the public, commercial, or not-for-profit sectors. However, we would like to acknowledge the partial funding granted by Idaho IDeA Network of Biomedical Research Excellence (Idaho-INBRE) via supporting summer INBRE undergraduate fellow.

Acknowledgments: We would also like to acknowledge the past undergraduate researchers Amanda Vu and Sheila Briggs for their help in DEP microwell experiments.

Conflicts of Interest: The authors have declared no conflict of interest

References

1. Cao, B.; Bray, F.; Ilbawi, A.; Soerjomataram, I. Effect on longevity of one-third reduction in premature mortality from non-communicable diseases by 2030: A global analysis of the sustainable development goal health target. *Lancet Glob. Health* **2018**, *6*, e1288–e1296. [CrossRef]
2. Konigsberg, R.; Obermayr, E.; Bises, G.; Pfeiler, G.; Gneist, M.; Wrba, F.; de Santis, M.; Zeillinger, R.; Hudec, M.; Dittrich, C. Detection of epcam positive and negative circulating tumor cells in metastatic breast cancer patients. *Acta. Oncol.* **2011**, *50*, 700–710. [CrossRef] [PubMed]
3. Adekanmbi, E.; Srivastava, S. Dielectrophoretic applications for disease diagnostics using lab-on-a-chip platform. *Lab Chip* **2016**, *16*, 2148–2167. [CrossRef] [PubMed]
4. Breast Cancer Statistics. Available online: https://www.breastcancer.org/symptoms/understand_bc/statistics. (accessed on 24 March 2020).
5. den Toonder, J. Circulating tumor cells: The grand challenge. *Lab Chip* **2011**, *11*, 375–377. [CrossRef]

6. Karabacak, N.M.; Spuhler, P.S.; Fachin, F.; Lim, E.J.; Pai, V.; Ozkumur, E.; Martel, J.M.; Kojic, N.; Smith, K.; Chen, P.I.; et al. Microfluidic, marker-free isolation of circulating tumor cells from blood samples. *Nat. Protoc.* **2014**, *9*, 694–710. [CrossRef]
7. Hammar, S.P. Metastatic adenocarcinoma of unknown primary origin. *Hum. Pathol.* **1998**, *29*, 1393–1402. [CrossRef]
8. Mego, M. Emerging role of circulating tumor cells in cancer management. *Indian J. Med. Paediatr. Oncol.* **2014**, *35*, 237–238. [CrossRef]
9. Whole Blood is the Best Biospecimen for Isolating Peripheral Blood Mononuclear Cells. Available online: <https://www.dls.com/biopharma/blog/3-reasons-whole-blood-is-necessary-for-pbmc-isolation> (accessed on 5 February 2020).
10. Gascoyne, P.R.; Shim, S. Isolation of circulating tumor cells by dielectrophoresis. *Cancers* **2014**, *6*, 545–579. [CrossRef]
11. Nagrath, S.; Sequist, L.V.; Maheswaran, S.; Bell, D.W.; Irimia, D.; Ulkus, L.; Smith, M.R.; Kwak, E.L.; Digumarthy, S.; Muzikansky, A. Isolation of rare circulating tumour cells in cancer patients by microchip technology. *Nature* **2007**, *450*, 1235–1239. [CrossRef]
12. Deng, G.; Herrler, M.; Burgess, D.; Manna, E.; Krag, D.; Burke, J.F. Enrichment with anti-cytokeratin alone or combined with anti-epcam antibodies significantly increases the sensitivity for circulating tumor cell detection in metastatic breast cancer patients. *Breast Cancer Res.* **2008**, *10*, R69. [CrossRef]
13. Wlodkowic, D.; Cooper, J.M. Tumors on chips: Oncology meets microfluidics. *Curr. Opin. Chem. Biol.* **2010**, *14*, 556–567. [CrossRef]
14. Plouffe, B.D.; Lewis, L.H.; Murthy, S.K. Computational design optimization for microfluidic magnetophoresis. *Biomicrofluidics* **2011**, *5*, 13413. [CrossRef] [PubMed]
15. Liu, Y.; Hartono, D.; Lim, K.M. Cell separation and transportation between two miscible fluid streams using ultrasound. *Biomicrofluidics* **2012**, *6*, 012802. [CrossRef] [PubMed]
16. Gascoyne, P.R.; Wang, X.B.; Huang, Y.; Becker, F.F. Dielectrophoretic separation of cancer cells from blood. *IEEE Trans. Ind. Appl.* **1997**, *33*, 670–678. [CrossRef]
17. Becker, F.F.; Wang, X.B.; Huang, Y.; Pethig, R.; Vykoukal, J.; Gascoyne, P.R. Separation of human breast cancer cells from blood by differential dielectric affinity. *Proc. Natl. Acad. Sci. USA* **1995**, *92*, 860–864. [CrossRef] [PubMed]
18. Moon, H.-S.; Kwon, K.; Kim, S.-I.; Han, H.; Sohn, J.; Lee, S.; Jung, H.-I. Continuous separation of breast cancer cells from blood samples using multi-orifice flow fractionation (MOFF) and dielectrophoresis (DEP). *Lab Chip* **2011**, *11*, 1118–1125. [CrossRef] [PubMed]
19. Yang, F.; Yang, X.; Jiang, H.; Butler, W.M.; Wang, G. Dielectrophoretic separation of prostate cancer cells. *Technol. Cancer Reserach Treat.* **2013**, *12*, 61–70. [CrossRef]
20. Zerbino, D.D. Biopsy: Its history, current and future outlook. *Likars'ka sprava* **1994**, *3–4*, 1–9.
21. An, J.; Lee, J.; Lee, S.H.; Park, J.; Kim, B. Separation of malignant human breast cancer epithelial cells from healthy epithelial cells using an advanced dielectrophoresis-activated cell sorter (DACS). *Anal. Bioanal. Chem.* **2009**, *394*, 801–809. [CrossRef]
22. Alshareef, M.; Metrakos, N.; Juarez Perez, E.; Azer, F.; Yang, F.; Yang, X.; Wang, G. Separation of tumor cells with dielectrophoresis-based microfluidic chip. *Biomicrofluidics* **2013**, *7*, 11803. [CrossRef] [PubMed]
23. Srivastava, S.K.; Daggolu, P.R.; Burgess, S.C.; Minerick, A.R. Dielectrophoretic characterization of erythrocytes: Positive abo blood types. *Electrophoresis* **2008**, *29*, 5033–5046. [CrossRef]
24. Srivastava, S.K.; Gencoglu, A.; Minerick, A.R. Dc insulator dielectrophoretic applications in microdevice technology: A review. *Anal. Bioanal. Chem.* **2011**, *399*, 301–321. [CrossRef]
25. Pethig, R. Review article-dielectrophoresis: Status of the theory, technology, and applications. *Biomicrofluidics* **2010**, *4*, 022811. [CrossRef] [PubMed]
26. Gencoglu, A.; Minerick, A. Chemical and morphological changes on platinum microelectrode surfaces in ac and dc fields with biological buffer solutions. *Lab Chip* **2009**, *9*, 1866–1873. [CrossRef] [PubMed]
27. Ozuna-Chacon, S.; Lapizco-Encinas, B.H.; Rito-Palomares, M.; Martinez-Chapa, S.O.; Reyes-Betanzo, C. Performance characterization of an insulator-based dielectrophoretic microdevice. *Electrophoresis* **2008**, *29*, 3115–3122. [CrossRef] [PubMed]
28. Chou, C.F.; Tegenfeldt, J.O.; Bakajin, O.; Chan, S.S.; Cox, E.C.; Darnton, N.; Duke, T.; Austin, R.H. Electrodeless dielectrophoresis of single- and double-stranded DNA. *Biophys. J.* **2002**, *83*, 2170–2179. [CrossRef]

29. Cummings, E.B.; Singh, A.K. Dielectrophoresis in microchips containing arrays of insulating posts: Theoretical and experimental results. *Anal. Chem.* **2003**, *75*, 4724–4731. [CrossRef]
30. Moncada-Hernandez, H.; Lapizco-Encinas, B.H. Simultaneous concentration and separation of microorganisms: Insulator-based dielectrophoretic approach. *Anal. Bioanal. Chem.* **2010**, *396*, 1805–1816. [CrossRef]
31. Pethig, R.R. *Dielectrophoresis: Theory, Methodology and Biological Applications*; Wiley; Hoboken, NY, USA, 2017.
32. Jing, D.; Zhan, X. Cross-Sectional Dimension Dependence of Electroosmotic Flow in Fractal Treelike Rectangular Microchannel Network. *Micromachines* **2020**, *11*, 266. [CrossRef]
33. Bhattacharyya, S.; Bera, S. Combined electroosmosis-pressure driven flow and mixing in a microchannel with surface heterogeneity. *Appl. Math. Modell.* **2015**, *39*, 4337–4350. [CrossRef]
34. Ghosal, S. Fluid mechanics of electroosmotic flow and its effect on band broadening in capillary electrophoresis. *Electrophoresis* **2004**, *25*, 214–228. [CrossRef] [PubMed]
35. Tandon, V.; Bhagavatula, S.K.; Nelson, W.C.; Kirby, B.J. Zeta potential and electroosmotic mobility in microfluidic devices fabricated from hydrophobic polymers: 1. The origins of charge. *Electrophoresis* **2008**, *29*, 1092–1101. [CrossRef] [PubMed]
36. O'Brien, R.W.; White, L.R. Electrophoretic mobility of a spherical colloidal particle. *J. Chem. Soc. Faraday Trans.* **1978**, *74*, 1607–1626. [CrossRef]
37. Srivastava, S.K.; Baylon-Cardiel, J.L.; Lapizco-Encinas, B.H.; Minerick, A.R. A continuous dc-insulator dielectrophoretic sorter of microparticles. *J. Chromatogr. A* **2011**, *1218*, 1780–1789. [CrossRef]
38. Adekanmbi, E.O.; Ueti, M.W.; Rinaldi, B.; Suarez, C.E.; Srivastava, S.K. Insulator-based dielectrophoretic diagnostic tool for babesiosis. *Biomicrofluidics* **2016**, *10*, 033108. [CrossRef]
39. Huang, C.; Liu, H.; Bander, N.H.; Kirby, B.J. Enrichment of prostate cancer cells from blood cells with a hybrid dielectrophoresis and immunocapture microfluidic system. *Biomed. Microdevices* **2013**, *15*, 941–948. [CrossRef]
40. Kirby, B.J. *Micro- and Nanoscale Fluid Mechanics: Transport in Microfluidic Devices*; Cambridge University Press: Cambridge, UK, 2010.
41. Qiao, G.; Duan, W.; Chatwin, C.; Sinclair, A.; Wang, W. Electrical properties of breast cancer cells from impedance measurement of cell suspensions. *J. Phys. Conf. Ser.* **2010**, *224*, 012081. [CrossRef]
42. Gascoyne, P.; Mahidol, C.; Ruchirawat, M.; Satayavivad, J.; Watcharasit, P.; Becker, F.F. Microsample preparation by dielectrophoresis: Isolation of malaria. *Lab Chip* **2002**, *2*, 70–75. [CrossRef]
43. Chan, K.L.; Morgan, H.; Morgan, E.; Cameron, I.T.; Thomas, M.R. Measurements of the dielectric properties of peripheral blood mononuclear cells and trophoblast cells using ac electrokinetic techniques. *Biochim. Biophys. Acta (BBA) Mol. Basis Disease* **2000**, *1500*, 313–322. [CrossRef]



© 2020 by the authors. Licensee MDPI, Basel, Switzerland. This article is an open access article distributed under the terms and conditions of the Creative Commons Attribution (CC BY) license (<http://creativecommons.org/licenses/by/4.0/>).

Article

Establishment of Colorectal Cancer Organoids in Microfluidic-Based System

Diana Pinho ^{1,*} , Denis Santos ¹, Ana Vila ² and Sandra Carvalho ^{1,*} 

¹ International Iberian Nanotechnology Laboratory, Department of Nanoelectronics Engineering, 4715-330 Braga, Portugal; denis.santos@inl.int

² International Iberian Nanotechnology Laboratory, IP Exploitation and Knowledge Transfer, 4715-330 Braga, Portugal; Ana.Vila@inl.int

* Correspondence: diana.pinho@inl.int (D.P.); carvalho.sandra.santos@gmail.com (S.C.)

Abstract: Colorectal cancer is the second leading cause of cancer death worldwide. Significant advances in the molecular mechanisms underlying colorectal cancer have been made; however, the clinical approval of new drugs faces many challenges. Drug discovery is a lengthy process causing a rapid increase in global health care costs. Patient-derived tumour organoids are considered preclinical models with the potential for preclinical drug screening, prediction of patient outcomes, and guiding optimized therapy strategies at an individual level. Combining microfluidic technology with 3D tumour organoid models to recapitulate tumour organization and in vivo functions led to the development of an appropriate preclinical tumour model, organoid-on-a-chip, paving the way for personalized cancer medicine. Herein, a low-cost microfluidic device suitable for culturing and expanding organoids, OrganoidChip, was developed. Patient-derived colorectal cancer organoids were cultured within OrganoidChip, and their viability and proliferative activity increased significantly. No significant differences were verified in the organoids' response to 5-fluorouracil (5-FU) treatment on-chip and on-plate. However, the culture within the OrganoidChip led to a significant increase in colorectal cancer organoid-forming efficiency and overall size compared with conventional culture on a 24-well plate. Interestingly, early-stage and late-stage organoids were predominantly observed on-plate and within the OrganoidChip, respectively. The OrganoidChip thus has the potential to generate in vivo-like organotypic structures for disease modelling and drug screening applications.

Keywords: microfluidics; patient-derived organoids; colorectal cancer; 3D model; drug screening



Citation: Pinho, D.; Santos, D.; Vila, A.; Carvalho, S. Establishment of Colorectal Cancer Organoids in Microfluidic-Based System. *Micromachines* **2021**, *12*, 497. <https://doi.org/10.3390/mi12050497>

Academic Editor: Iulia M. Lazar

Received: 24 March 2021

Accepted: 26 April 2021

Published: 28 April 2021

Publisher's Note: MDPI stays neutral with regard to jurisdictional claims in published maps and institutional affiliations.



Copyright: © 2021 by the authors. Licensee MDPI, Basel, Switzerland. This article is an open access article distributed under the terms and conditions of the Creative Commons Attribution (CC BY) license (<https://creativecommons.org/licenses/by/4.0/>).

1. Introduction

Colorectal cancer is the second leading cause of cancer death worldwide, and because of population ageing, the global burden is expected to grow to 2.5 million new cases in 2035 [1–3]. Although significant advances in the molecular mechanisms underlying colorectal cancer have been made, the clinical approval of new drugs still faces many challenges [4]. Cancer drug development is characterized by high failure rates in clinical trials, mainly because the preclinical models used in the drug development pipeline do not provide adequate information about drug efficacy or toxicity [5]. Molecular and cellular tumour heterogeneity between and within individual patients represent a landscape and a barrier for effective patient treatment [6–8]. Thus, predictive preclinical cancer models able to precisely replicate the human tumour biology and allow personalized anti-cancer therapy are urgently needed [9,10]. Orthotopic mouse models are considered to be poor human cancer models as they lack the features of the native tissue and do not recreate the human tumour microenvironment [11]. Moreover, conventional 2D cell cultures do not provide information about the complex interactions between the cancer cells, associated stromal components, and the physicochemical microenvironment. Lastly, more complex 3D in vitro models, such as transwell-based cell cultures and spheroids, do not reproduce the complexity observed in the 3D tissue architecture of living organs, and do not retain

the mechanical cues that contribute to the tumour behaviour [12]. Microfluidic cell culture technology has emerged as a promising tool in cancer research as an alternative to animal and traditional cell culture models [13,14]. It is a low-cost technology that handles fluids at a nanoscale, enabling small quantities of samples and providing highly sensitive and high-throughput screening [15,16]. A variety of fabrication methods, aside from soft lithography, vinyl cutters (xurography), laser cutting, 3D printing, and micromilling, among others, are available [17,18]. Microfluidics-based systems have contributed to decreasing manufacturing time and costs by using cheaper materials and tools, allowing for new and advantageous physical behaviour, functionality, and qualities in microfluidic devices. Modelling cancer cell behaviour within the microfluidic device of tumour-on-chip, is highly physiological; enables co-cultures of different cell types; and offer precise control over physical, mechanical, and biochemical properties on the model. However, tumour-on-chip relies on pre-differentiated cells, often cell lines, and cannot emulate the histological and cellular complexity of the tumour and the surrounding microenvironment [19].

Organoid models have been synergistically combined with microfluidic technology [20,21]. Organoids are 3D culture models that recapitulate the organ architecture and *in vivo* counterparts' functional features [22]. The generation of organoids derived from primary and metastatic patient tumours are reported. These patient-derived organoids are distinct from other cancer models in that they conserve the architecture, (epi)genetic, and phenotypic alterations of the original tumour [23,24]. More importantly, patient-derived organoids have been reported to successfully predict a therapy response in cancer patients and facilitate therapeutic decision-making [23,25]. Therefore, establishing patient-derived tumour organoids-on-a-chip may serve as more versatile and predictive preclinical models applicable to cancer drug discovery and personalized therapies. Micro-engineered organoid systems allow for precise control of the space and environment where an organoid is growing. Flow conditions, nutrient supply, shear stress, input–output, and organoid geometry are easily controlled. Furthermore, the complex cellular cross-talk of the native organ can be modelled by organoid-on-chip technology, and the inter-organoid variability is drastically decreased [20].

In this study, a microfluidic device was designed and fabricated through a milling process so as to culture and expand patient-derived colorectal cancer organoids on-chip (OrganoidChip). A culture medium was continuously injected into the distribution channels to provide the proper conditions for organoid growth. Viability assays of organoids cultured within the OrganoidChip were performed and compared with those cultured on conventional well-plates. Our experiments showed a significant increase in organoid viability and proliferation within OrganoidChip, as well as similar sensitivity responses of colorectal cancer organoids to 5-FU on-chip and on-plate. These observations demonstrate the potential of OrganoidChip to provide precise control of drug distribution, similar sensitivity, and improved growth culture conditions of colorectal cancer organoids. Distinct morphology features of colorectal cancer organoids were observed. The culture within OrganoidChip led to a significant increase in colorectal cancer organoid-forming efficiency and organoid size. More importantly, late-stage colorectal cancer organoids were established within OrganoidChip, highlighting the potential for this micro-engineered organoid device to generate *in vivo*-like organotypic structures for disease modelling and drug screening applications.

2. Materials and Methods

2.1. Design and Fabrication of a Microfluidic Platform for Organoid Culture

The molds for the microfluidic device used in this study were fabricated using a high-speed milling machine (FlexiCam Viper, FlexiCam, Eibelstadt, Germany). Micromilling is an alternative, low-cost, non-lithographic top-down technique and a fast method to address some significant microfabrication challenges and allow rapid prototyping. Using rotating cutting tools to remove or cut micro- or milli-scale features in several types of materials (acrylic, aluminium, among others), it is possible to generate molds or directly fabricate

microfluidic channels. Recently, manufacturers have produced milling tools smaller than 100 microns, which have promoted micro-milling machines' ability to fabricate microfluidic devices [18,26].

The device design was created using AutoCAD software (Autodesk AutoCAD 2018, Autodesk, San Rafael, CA, USA) and consists of a bottom layer containing four round wells with 6 mm in diameter and 2.5 mm of depth for cell seeding, and a top layer displaying one inlet channel distributed in four small channels of 1.5 mm × 1 mm (width × depth) and one outlet (2 mm of diameter). The top layer is crucial for the culture medium supply.

The microfluidic devices were fabricated in polydimethylsiloxane (PDMS; Ellsworth Adhesives Iberica, Spain), which was prepared as a two-part system with a mix ratio of 10:1 (*w/w*) or 20:1 (*w/w*) base/curing agent (top and bottom layers, respectively), poured over the molds, degassed, and cured for 1.5 h at 65 °C. The different PDMS ratios were used for the bottom and top layers to generate slight and reversible bonding when both were poured in contact. Following that, the PDMS was unmolded, and the inlet and outlet were made using a puncher of 1.5 mm. Both layers and tubes were sterilized with 70% ethanol (*v/v*) and were then exposed for 30 min to UV light. Afterwards, the bottom layer (20:1 PDMS ratio) was placed on a glass slide, and the top layer (10:1 PDMS ratio) was carefully aligned and placed over the bottom layer. Thus, the layers stuck to each other, creating contact bonding. Tubes were inserted into the inlet and outlet. After organoids seeding, the channels were filled with a culture medium. The microfluidic device was connected to a syringe pump (NE-1000, New Era Pump Systems, Farmingdale, NY, USA) with a working flow rate of 10 µL/h for a continuous medium supply.

2.2. Organoids Culture

Colorectal cancer organoid line Iso-50 was supplied by Cellesce, Ltd., (Cardiff, Wales, UK) and was cultured according to their instructions [27]. These tumour organoids were isolated by Cellesce, Ltd., from surgically-resected colorectal cancer material of patients, as previously described by Sato et al. [24]. The organoid pellet was resuspended in medium 3+, composed by Advanced DMEM/F12 supplemented with 1% GlutaMAX, 1% HEPES buffer solution, and 1% Penicillin/Streptomycin (all Life Technologies, Cramlington, UK). Afterwards, organoids were plated in Matrigel Matrix Basement Membrane Growth Factor Reduced (Corning, NY, USA) in 24-well plates and a microfluidic device (30 µL of blob). Following Matrigel polymerization, the organoids were overlaid with 500 µL of "complete" medium composed of medium 3+ supplemented with 1 × B27 supplement, 1 × N2 supplement (all from Invitrogen), and 1 mM N-acetyl-L-cysteine (Sigma, Darmstadt, Germany). To culture the organoids on-chip, the microfluidic device's bottom layer (previously placed on a glass slide) was first pre-warmed at 37 °C. Iso-50 organoids were then plated in the Matrigel matrix in each microfluidic device's well (30 µL of blob). The bottom layer was placed at 37 °C in an atmosphere of 5% CO₂ to promote Matrigel polymerization. The microfluidic device was assembled with a top layer and tubes, as previously described, and carefully filled with the appropriate culture medium for the organoids' growth. The device was connected to a syringe pump and the flow rate condition was defined as 10 µL/h. For the on-chip control, Iso-50 organoids were cultured within the microfluidic device without a continuous flow of a culture medium.

All of the cultures were maintained in humidified incubators at 37 °C in 5% CO₂, and were monitored daily under a phase-contrast microscope (Nikon Eclipse TS 100, Tokyo, Japan). The culture medium was changed every 2–3 days, and organoids were passaged 1:4 every week.

2.3. Viability Assay

Iso-50 organoids were seeded at a density of 200 structures per well of 24-well plates or microfluidic device (in 30 µL of blob per well), and were cultured until day 8. The viability of the organoids was determined using the CellTiter-Glo 3D Cell Viability Assay (Promega, Madison, WI, USA), as follows: organoids were mixed with 100 µL of

CellTiter-Glo[®] 3D reagent, shaken for 5 min, and incubated for 30 min at room temperature. Luminescence was measured using a Microplate Reader (Synergy H1, Biotek, Winooski, VT, USA). Viability was monitored at days 0, 2, 4, 6, and 8.

2.4. Seeding Density Optimization by ATP Assay

The Iso-50 organoids in the culture were gently dissociated to the near single-cell population using TrypLE (Gibco, Life Technologies, Renfrew, Scotland, UK) before re-suspension within a growth-factor reduced Matrigel. The individual cells were counted using a Trypan blue exclusion test (Gibco, Life Technologies, UK) and were seeded at a range of densities (from 100 to 1000 cells/ μ L of Matrigel dome) into a 24-well plate or microfluidic device (30 μ L blob per well). The ATP measurement of the CellTiter-Glo 3D Cell Viability Assay (Promega, Madison, WI, USA) was then performed to evaluate the organoid proliferative ability according to the manufacturer's instructions.

2.5. Organoid-Forming Efficiency Assays

The organoid-forming efficiency was determined by quantification of the organoid numbers (organoid-colony forming efficiency) and size. The total number of organoid structures per well was manually counted six days after seeding using a phase-contrast microscope at 4 \times magnification. The organoid area was measured by encircling the periphery of each organoid using ImageJ software (NIMH, Bethesda, Rockville, MD, USA). The organoid size was quantified at day 6 of culture by measuring the longest axis.

2.6. Treatment of Iso-50 Organoids with 5-Fluorouracil

Colorectal cancer Iso-50 organoids were treated with chemotherapeutic drug 5-fluorouracil (5-FU) at different concentrations. Briefly, Iso-50 organoids were seeded in a 24-well plate and within the OrganoidChip. Complete media supplemented with 1, 10, and 100 nM 5-FU or 0.1% of dimethyl sulfoxide (DMSO) were replaced onto the organoids on day 4 of culture. DMSO was used as a vehicle for 5-FU. The viability of the organoids was measured after 48 h of treatment (Figure 1).

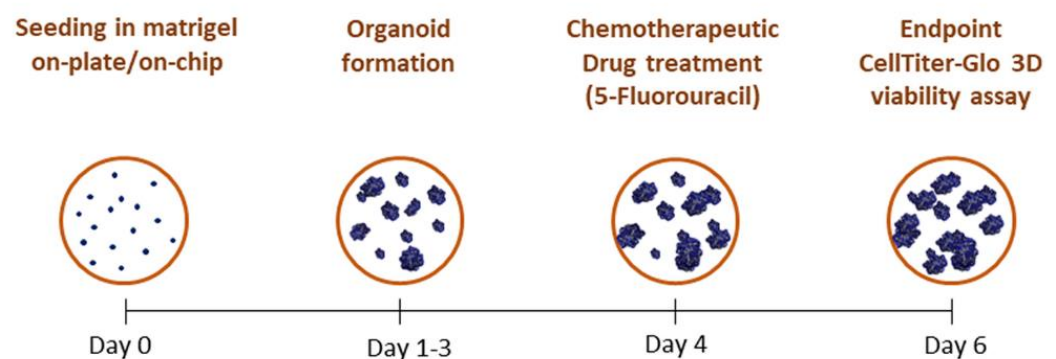


Figure 1. Schematic of the organoid culture timeline.

2.7. Statistical Analysis

Statistical analyses were performed using the Graph Pad program (GraphPad Software, Inc., La Jolla, CA, USA). Student's tests were used to calculate significance with a 95% confidence level (* $p \leq 0.05$; ** $p \leq 0.01$; *** $p \leq 0.001$).

3. Results

3.1. Fabrication of the OrganoidChip Microfluidic Device

The design considerations of the two layers were performed to have the possibility for manual seeding of the organoid structures. In this way, no cell damage and higher control in the seeding procedure could occur. There is also the possibility of downstream testing assays after the culture and maturation under continuous flow conditions.

The layer molds were fabricated in a poly(methyl methacrylate) (PMMA) material with single-flute carbide end-mill tools of 2 mm for the larger steps and 1 mm for the small features of the design and to smooth the surface. The depth of the bottom and top layer was 2.5 and 1 mm, respectively.

In Figure 2A, it is possible to observe the design of the manufactured PMMA molds. The PMMA material proportionated a clear and smooth surface in the PDMS device, essential for the microscope visualizations of 3D structures (Figure 2B). The inlet and outlet in the top layer had a diameter of 2 mm, and the channels for the medium supply had a width of 1.5 mm. The top layer was fabricated with 10:1 PDMS. The bottom layer had 6 mm round wells with a depth of 2.5 mm, and was fabricated with 20:1 PDMS. The PDMS thickness of the bottom and top layer was 4 mm and 2.5 mm, respectively. Thus, the OrganoidChip had a total thickness of 6.5 mm.

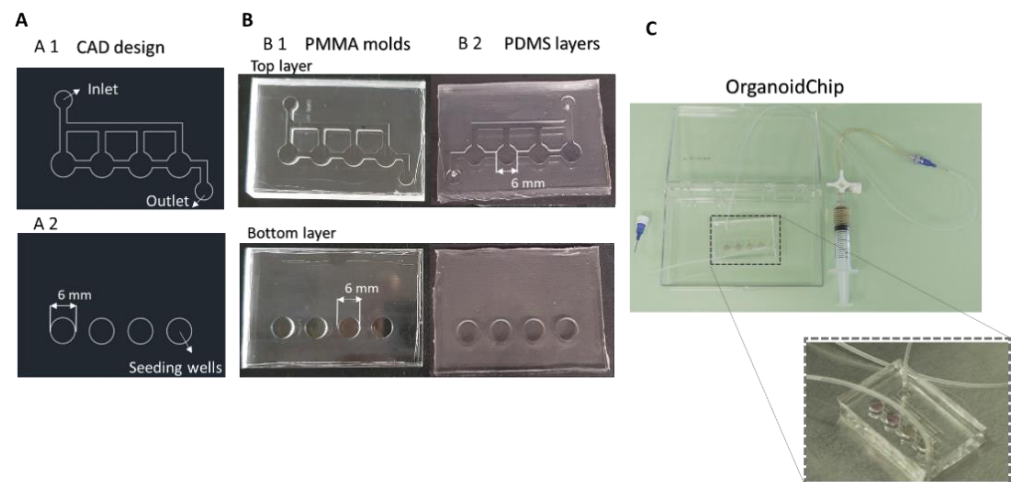


Figure 2. Design and fabrication of the organoid on-chip device. (A) AutoCAD design of the OrganoidChip (A1) top and (A2) bottom layers. The top layer includes one inlet channel distributed in four small channels and one outlet. The bottom layer consists of four round wells of 6 mm in diameter for organoids' seeding and growing. (B) OrganoidChip poly(methyl methacrylate) (PMMA) layers mold fabricated in (B1) the milling machine and the (B2) respective polydimethylsiloxane (PDMS) layers. (C) OrganoidChip setup.

The bonding of both layers was performed by aligning the top layer over the bottom layer. An off-ratio bonding technique occurred (i.e., two layers partially cured with different base-to-crosslinker ratios are brought into contact creating a bonding interface) [28]. This technique enables layer adjustments and a contact bonding strong enough to support the working flow rate of 10 $\mu\text{L}/\text{h}$, giving the possibility of layer detachments and further applications. A flow rate of 10 $\mu\text{L}/\text{h}$ has been used in several tumoroid platforms and reported to generate internal shear stress supported by the Matrigel blob [29,30]. Note that the established flow rate proportionates for 48 h had the same amount of medium added in the on-plate for the comparison tests (500 μL per well). With the inlet connected to a syringe pump via tubing and the outlet connected to a reservoir, the OrganoidChip setup was set, as seen in Figure 2C.

3.2. Establishment of Colorectal Cancer Organoid Line within OrganoidChip

Having designed and fabricated the microfluidic device, the OrganoidChip (Figure 2), we explored its feasibility for culturing organoids. Proper development and maturation of organoids implies a continuous feed of fresh nutrients and waste removal, as they expand in size when they are not vascularized [31,32]. In this study, to evaluate the organoids' growth, colorectal cancer Iso-50 organoids were seeded in Matrigel on-chip and on-plate (around 200 structures/well), and their viability was assessed over eight days of culture. As shown in Figure 3A, the organoids' viability increased, as expected in the first days

of culture. However, a significant decrease in viability was observed after six days of culture, both on-plate and on-chip. This result suggests that the exponential growth of organoids occurs within the first six days of culture. However, comparing the viability of the organoids in the different culture conditions, we observed that the viability of Iso-50 was significantly higher on-chip after day 2.

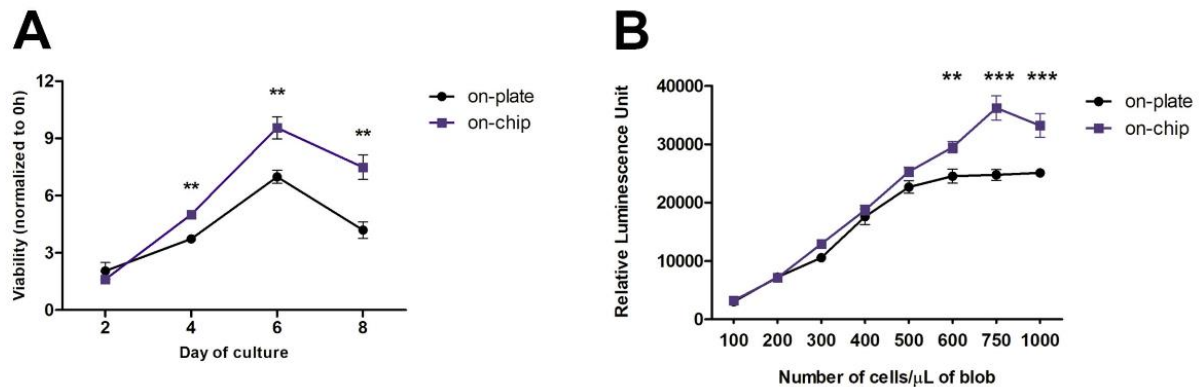


Figure 3. Optimization of Iso-50 organoids culture on-chip. **(A)** Viability of cultured organoids within OrganoidChip (on-chip) and on a traditional plate (on-plate). Viability was monitored at days 0, 2, 4, 6, and 8 using a CellTiter-Glo 3D Cell Viability Assay. The results are described as mean \pm standard deviation (SD) of three independent experiments. The viability of the organoids at days 2, 4, 6, and 8 is expressed as the fold increase, compared with the viability at day 0, taken as 1 (Student's *t*-test: ** $p \leq 0.01$; *** $p \leq 0.001$). **(B)** ATP measurement for proliferation in Iso-50 organoids after six days of culture at different cell seeding densities. Results are described as mean \pm SD of three replicated wells (one independent experiment) for each cell density (Student's *t*-test: ** $p \leq 0.01$; *** $p \leq 0.001$).

Moreover, the significantly decreased viability of the organoids observed from day 6 was more pronounced in the on-plate. These observations indicate that OrganoidChip provides a continuous infusion of nutrients and growth factors, and removes metabolic waste, which are crucial for developing organoids within the microfluidic device. As the organoids viability increases significantly until six days of culture, the endpoint at day six was pointed out all subsequent culture experiments (Figure 1).

We further evaluated the influence of the cell seeding density on the organoids' proliferative ability. Single-cell suspensions were prepared from Iso-50 organoids. The cells were seeded at a range of cell densities within a traditional 24-well plate and microfluidic device, and their proliferation was assessed on day 6 of the culture by measuring the ATP released from the proliferative cells composed of organoids. Regarding the organoids cultured on-plate, an increase in the relative luminescence signal was observed with the ascent of the initial cell seeding on-plate (Figure 3B). Beyond 600 cells/ μ L of blob, a plateau was reached, indicating a slowdown in the organoid proliferation activity, possibly due to restriction to the nutrient and growth factor access and the limited physical space. Interestingly, such a threshold was observed at a seeding density of 750 cells/ μ L of blob on-chip, highlighting that on-chip and under continuous flow conditions, it is possible to have more proliferation. The continuous flow proportionates the constant and renews the culture medium.

3.3. Culture within OrganoidChip Promotes Colorectal Cancer Organoid-Forming Efficiency

The colorectal cancer organoids were characterized to display the morphological and histological features in common with the tumour from which they were derived [27]. The morphological characteristics of the Iso-50 organoids were observed on days 2 and 6 of the culture on-plate versus on-chip (Figure 4A). On day 2 of the culture, colorectal organoid formation was still occurring, as the not late-stage morphology typical of colorectal cancer organoids was not verified. Small and round organoids were observed both on-plate and within OrganoidChip. On day 6 of the culture, distinct morphology features were observed.

Iso-50 organoids cultured on-plate were predominantly mono-cellular structures with a cystic-like shape, exhibiting a visible lumen without projections (arrow). In contrast, structures displaying a thick epithelial cell layer containing glandular structures within the organoid (white arrowhead) or multi-layered organoids with crypt-like projections (black arrowhead) were observed when cultured within OrganoidChip. Because of these different morphological features of Iso-50 organoids cultured on-chip versus on-plate, the organoid-forming efficiency was evaluated. The organoid-forming efficiency was determined by quantifying the organoid numbers (organoid-colony forming efficiency) and size (are and longest axis). The organoid-colony forming efficiency was significantly higher on-chip than on-plate and on-chip control without continuous flow (Figure 4B). In addition, Iso-50 on-chip organoids were significantly higher in diameter and area than for the culture on-plate and on-chip control (Figure 4C). These results highlight the potential of OrganoidChip to provide more physiologically relevant cell culture conditions than the static cell culture, thus contributing to the efficient establishment of cancer organoids.

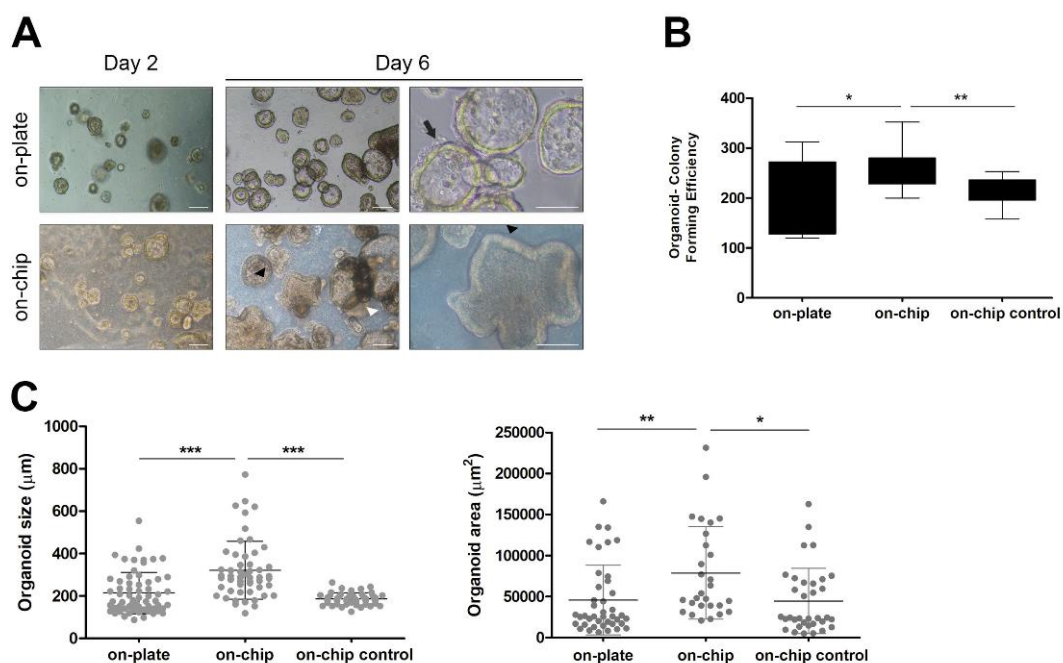


Figure 4. Organoid-forming efficiency within OrganoidChip. (A) Representative images of organoids morphology at days 2 and 6 of culture. On day 6, Iso-50 organoids cultured on-plate exhibited a cystic-like morphology with a visible lumen. In contrast, the organoids cultured on-chip are multi-layered with crypt-like projections or display a thick epithelial cell layer containing glandular structures. Scale bar: 100 μm . (B) Quantification of organoid colony-forming efficiency at day 6 of culture. The results are reported as the mean \pm SD of three independent experiments. (C) Analysis of organoid size and area at day 6 of culture. The results are described as mean \pm SD of a total of 50 organoids in three independent experiments subjected to the analysis (Student's *t*-test: * $p \leq 0.05$; ** $p \leq 0.01$; *** $p \leq 0.001$).

3.4. On-Chip Organoids Drug Sensitivity Testing

To assess the organoids' sensitivity cultured within OrganoidChip to chemotherapeutic drugs, Iso-50 organoids were treated with an increasing dose of 5-fluorouracil (5-FU). 5-FU remains the first-line of treatment for colorectal cancer. Following treatment with 5-FU for 48 h, the organoid viability was determined. According to Figure 5, no significant differences in sensitivity to 5-FU treatment were observed in the colorectal cancer organoids cultured within OrganoidChip and traditional plates. These results suggest the stability and accuracy of colorectal cancer organoids cultured within OrganoidChip as a drug screening model.

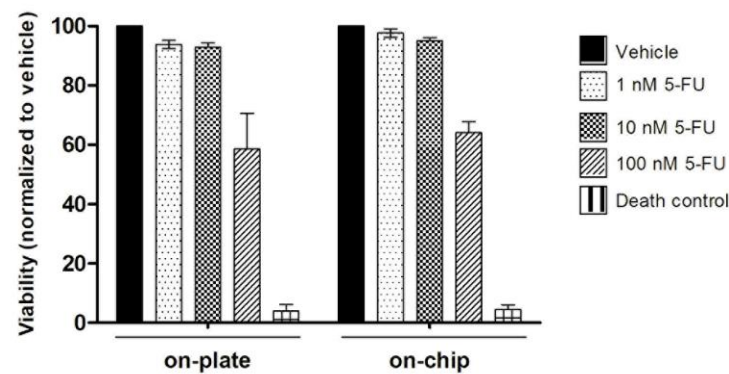


Figure 5. Analysis of organoid viability after treatment with 5-fluorouracil (5-FU). On day 4 of culture, the organoids were treated with 5-FU or 0.1% dimethyl sulfoxide (DMSO; control), and their viability was assessed on day 6. For the dead control, 30% of DMSO was used. The results are described as the mean \pm SD of two wells per condition of two independent experiments. No significant differences were observed (Student's *t*-test: * $p \leq 0.05$; ** $p \leq 0.01$; *** $p \leq 0.001$).

4. Discussion

In the present study, a microfluidic device—OrganoidChip—was fabricated using a milling technique to enable the culture of patient-derived colorectal cancer organoids on-chip. The milling fabrication technique was employed to create the master molds of the microchannels and the main body of the OrganoidChip. In the last decades, milling and micromilling have demonstrated a great potential for lab-on-a-chip and organ-on-a-chip applications, primarily because of their wide selection of working materials, versatile applications, and rapid prototyping, compared with other fabrication procedures [33]. The most common milling application is the fabrication of organ-on-chip platform holders [34] or the direct use of the milled parts combined with other methodologies, such as photolithography and 3D printing, to connect all of the device modules, as Behroodi et al. demonstrated [35]. Another rapid, reliable, and cost-effective microfabrication of microfluidic systems with biomedical applications and lab-on-a-chip devices is the CO₂ laser [chen, wu]. Chen et al. successfully elaborated a versatile protocol of CO₂ laser drilling for the rapid prototyping of various microstructures with different substrate materials to showcase the wide usability range for the proposed method [36]. Wu et al. developed a micro U-well platform with an optimally arranged microwell array using a rapid and straightforward CO₂ laser microfabrication method. This platform has demonstrated their feasibility for developing in vitro 3D multicellular tumour spheroids as a tumour-mimicking model, and as an effective tool for discovering the therapeutic drug screening for cancer treatment [37]. Besides the advantages of CO₂ laser patterning, the milling fabrication for this application is demonstrated to be equally efficient, but cheaper and easier to integrate into the developed device's manufacturing. In this work, the layer molds were fabricated in acrylic to obtain a higher durability, and PDMS replica molding was performed. In this way, a transparent device with an adequate refractive index for microscope visualizations and image acquisition and gas permeability was obtained. Another important application for the developed system is the possibility of downstream studies. The organoids could be recovered intact, as the layers are not bonded permanently, and no holder strategies were needed. Thus, the milling fabrication simplified the manufacturing process of the OrganoidChip: low- cost, high precision, and accuracy in the molds' manufacturing, as well as being user-friendly and applicable for downstream studies.

We further investigated the potential for OrganoidChip as a reliable preclinical cancer model. For this, patient-derived colorectal cancer organoids were cultured within the OrganoidChip. The establishment of patient-derived organoids is crucial for preclinical cancer research and personalized medicine, as they retain patients' genetic and epigenetic aspects. Currently, various patient-derived tumour organoids have been generated. Using microfluidic technology, most reported organoid-on-chips rely on organoids derived from

human induced pluripotent stem cells [38–40]. Tumour organoids derived from patient tissues with lung, mesothelioma, breast, and pancreatic cancer have been generated and cultured within microfluidic devices [41–44]. In our study, colorectal cancer organoids derived from patient tissue established by Cellesce and reported in pilot studies with reproducible data, maintaining the counterpart tissue’s phenotype and genotype, were used [27]. Their viability and proliferation, when cultured within OrganoidChip, was evaluated. Our results revealed significantly increased viability and proliferation rates of colorectal cancer organoids on-chip, compared with traditionally cultured on-plate. Consistent with our observations, previous reports have shown a significant improvement in cell growth and survival within microfluidic devices that can minimize shear stress. In fact, microfluidic technology allows dynamic cell cultures in microperfusion systems to deliver continuous nutrient supplies for long term cell culture [45,46].

Patient-derived organoids preserve the structural architecture of primary tumours [22]. Our results show that colorectal cancer organoids cultured within OrganoidChip exhibit a significant increase in organoid size and organoid colony-forming efficiency, as well as a late-stage morphology, compared with organoids cultured on-plate. Previous reports have shown that as tumour organoids grow in size in conventional culture plates, the diffusion-dependent nutrient and oxygen supplies and waste removal become less efficient. Consequently, organoid viability decreases, and dead cells accumulate in the core region of organoids and undergo fragmentation and necrosis [46,47]. In contrast, microfluidic devices enable the integration of access channels for nutrient supply within organoids, as well as waste removal, mimicking the permeation provided by blood capillaries in vivo [47]. In our study, the OrganoidChip provides a control overflow, shear stress, and biochemical gradient. Nutrients, metabolic, and oxygen are delivered to organoids via laminar flow, reducing the necrotic core’s size and increasing their viability, organoid colony-forming efficiency, and overall size.

The nutrient and oxygen supplies and the removal of waste provided by microfluidic technology also influences organoid maturity. Interestingly, the significant morphological differences observed between colorectal cancer organoids cultured within OrganoidChip and on-plate were closely related to the organoid’s organization stage. The colorectal cancer organoids cultured within OrganoidChip exhibited a late-stage morphology, characterized by a crypt and villi-morphology, thick epithelial cell layer, and oriented and specialized epithelial cells. In contrast, we observed early-stage organoids on-plate as monocellular structures with a cystic-like shape. In fact, the organoid formation process followed a pattern of proliferation, differentiation, cell sorting, lineage commitment, and morphogenesis, resulting in a 3D organoid structure [48,49]. Organoid formation is usually guided by culturing cells in a medium containing soluble factors that promote or inhibit specific signaling pathways. Thus, the culture is directed towards the formation of late-stage organoids, which includes specialized cell types that give rise to organotypic structures and functions [50].

The potential for microfluidic devices for the culture and expansion of patient-derived organoids for personalized drug screening is of the utmost importance. In this study, similar sensitivity responses of colorectal cancer organoids to chemotherapeutic drug 5-FU were observed within OrganoidChip and on-plate. These results highlight the potential for OrganoidChip to provide precise control of drug distribution, sensitivity to chemotherapeutic drugs, and improved growth culture conditions of colorectal cancer organoids. Microfluidic platforms able to culture patient-derived pancreatic and lung tumour organoids and to perform drug sensitivity tests directly on devices have been developed [41,44]. These studies observed significant differences in the responses of individual patient-based organoids to drug treatments.

Taken together, we fabricated a low-cost microfluidic device suitable for the maintenance and expansion of patient-derived colorectal cancer organoids, applicable in downstream studies. The organoids’ morphological and proliferation features were improved when cultured within this microfluidic device. More importantly, a high-fidelity response

to drug treatment was observed compared with the organoid culture in traditional plates. However, device optimizations are needed in order to obtain a higher versatility for the design for other applications. Several outlets can be added; seeding chambers area and flow rates can also be adapted and optimized considering the final application. The individual response of patient-based organoids to 5-FU drug treatment is also necessary. Additionally, further studies, including the genetic profiling of individual patient-based organoids on-chip, are warranted to validate OrganoidChip as a reliable preclinical cancer model.

Overall, these results open new avenues for evaluating phenotypic drug susceptibility tests and disease modelling, as well as for the development of an organoid-on-chip preclinical cancer model with the potential for personalized medicine.

Author Contributions: Device conceptualization, D.P., D.S., A.V. and S.C.; biology experiments conceptualization: S.C.; methodology, D.P. and S.C.; milling process, D.S.; validation, S.C.; formal analysis, S.C.; writing—original draft preparation, S.C.; writing—review and editing, D.P., D.S. and S.C.; supervision, S.C.; project administration, A.V.; funding acquisition, A.V. All authors have read and agreed to the published version of the manuscript.

Funding: The authors would like to thank the funding source for this research: project ATLANTIC-KET-MED (N° Contract EAPA_384/2016), funded by the European Regional Development Fund through the Interreg Atlantic Area Programme (2014–2020), and project InNPec POCI-01-0145-FEDER-031442, funded by Fundação para a Ciência e Tecnologia (FCT).

Acknowledgments: The authors would like to thank Cellesce for providing knowledge about the Iso-50 culture protocol.

Conflicts of Interest: The authors declare no conflict of interest.

References

1. Bray, F.; Ferlay, J.; Soerjomataram, I.; Siegel, R.L.; Torre, L.A.; Jemal, A. Global cancer statistics 2018: GLOBOCAN estimates of incidence and mortality worldwide for 36 cancers in 185 countries. *CA Cancer J. Clin.* **2018**, *68*, 394–424. [CrossRef] [PubMed]
2. Guren, M.G. The global challenge of colorectal cancer. *Lancet Gastroenterol. Hepatol.* **2019**, *4*, 894–895. [CrossRef]
3. Araghi, M.; Soerjomataram, I.; Jenkins, M.; Brierley, J.; Morris, E. Global trends in colorectal cancer mortality: Projections to the year 2035. *Int. J. Cancer* **2019**, *144*, 2992–3000. [CrossRef] [PubMed]
4. Xie, Y.-H.; Chen, Y.-X.; Fang, J.-Y. Comprehensive review of targeted therapy for colorectal cancer. *Signal Transduct. Target. Ther.* **2020**, *5*, 22. [CrossRef] [PubMed]
5. Rubin, E.H.; Gilliland, D.G. Drug development and clinical trials—The path to an approved cancer drug. *Nat. Rev. Clin. Oncol.* **2012**, *9*, 215–222. [CrossRef] [PubMed]
6. Tellez-Gabriel, M.; Ory, B.; Lamoureux, F.; Heymann, M.-F.; Heymann, D. Tumour Heterogeneity: The Key Advantages of Single-Cell Analysis. *Int. J. Mol. Sci.* **2016**, *17*, 2142. [CrossRef]
7. Stanta, G.; Bonin, S. Overview on Clinical Relevance of Intra-Tumor Heterogeneity. *Front. Med.* **2018**, *5*. [CrossRef]
8. Dagogo-Jack, I.; Shaw, A.T. Tumour heterogeneity and resistance to cancer therapies. *Nat. Rev. Clin. Oncol.* **2018**, *15*, 81–94. [CrossRef]
9. Pauli, C.; Hopkins, B.D.; Prandi, D.; Shaw, R.; Fedrizzi, T.; Sboner, A.; Sailer, V.; Augello, M.; Puca, L.; Rosati, R.; et al. Personalized In Vitro and In Vivo Cancer Models to Guide Precision Medicine. *Cancer Discov.* **2017**, *7*, 462–477. [CrossRef]
10. Grandori, C.; Kemp, C.J. Personalized Cancer Models for Target Discovery and Precision Medicine. *Trends Cancer* **2018**, *4*, 634–642. [CrossRef]
11. Day, C.P.; Merlino, G.; Van Dyke, T. Preclinical mouse cancer models: A maze of opportunities and challenges. *Cell* **2015**, *163*, 39–53. [CrossRef]
12. Langhans, S.A. Three-Dimensional in Vitro Cell Culture Models in Drug Discovery and Drug Repositioning. *Front. Pharm.* **2018**, *9*, 6. [CrossRef] [PubMed]
13. Sontheimer-Phelps, A.; Hassell, B.A.; Ingber, D.E. Modelling cancer in microfluidic human organs-on-chips. *Nat. Rev. Cancer* **2019**, *19*, 65–81. [CrossRef]
14. Azadi, S.; Aboulkheyr Es, H.; Kulasinghe, A.; Bordhan, P.; Ebrahimi Warkiani, M. Chapter Five—Application of microfluidic technology in cancer research and therapy. In *Advances in Clinical Chemistry*; Makowski, G.S., Ed.; Elsevier: Amsterdam, The Netherlands, 2020; Volume 99, pp. 193–235.
15. Mejía-Salazar, J.R.; Rodrigues Cruz, K.; Materón Vásques, E.M.; Novais de Oliveira, O., Jr. Microfluidic Point-of-Care Devices: New Trends and Future Prospects for eHealth Diagnostics. *Sensors* **2020**, *20*, 1951. [CrossRef] [PubMed]
16. Azizipour, N.; Avazpour, R.; Rosenzweig, D.H.; Sawan, M.; Aji, A. Evolution of Biochip Technology: A Review from Lab-on-a-Chip to Organ-on-a-Chip. *Micromachines* **2020**, *11*, 599. [CrossRef] [PubMed]

17. Gale, B.K.; Jafek, A.R.; Lambert, C.J.; Goenner, B.L.; Moghimifam, H.; Nze, U.C.; Kamarapu, S.K. A Review of Current Methods in Microfluidic Device Fabrication and Future Commercialization Prospects. *Inventions* **2018**, *3*, 60. [CrossRef]
18. Nguyen, H.-T.; Thach, H.; Roy, E.; Huynh, K.; Perrault, C.M.-T. Low-Cost, Accessible Fabrication Methods for Microfluidics Research in Low-Resource Settings. *Micromachines* **2018**, *9*, 461. [CrossRef]
19. Horejs, C. A tumour chip for drug screening. *Nat. Rev. Mater.* **2020**, *5*, 786. [CrossRef]
20. Park, S.E.; Georgescu, A.; Huh, D. Organoids-on-a-chip. *Science* **2019**, *364*, 960. [CrossRef]
21. Velasco, V.; Shariati, S.A.; Esfandyarpour, R. Microtechnology-based methods for organoid models. *Microsyst. Nanoeng.* **2020**, *6*, 76. [CrossRef]
22. Kim, J.; Koo, B.-K.; Knoblich, J.A. Human organoids: Model systems for human biology and medicine. *Nat. Rev. Mol. Cell Biol.* **2020**, *21*, 571–584. [CrossRef]
23. Driehuis, E.; Kretzschmar, K.; Clevers, H. Establishment of patient-derived cancer organoids for drug-screening applications. *Nat. Protoc.* **2020**, *15*, 3380–3409. [CrossRef]
24. Sato, T.; Stange, D.E.; Ferrante, M.; Vries, R.G.J.; van Es, J.H.; van den Brink, S.; van Houdt, W.J.; Pronk, A.; van Gorp, J.; Siersema, P.D.; et al. Long-term Expansion of Epithelial Organoids From Human Colon, Adenoma, Adenocarcinoma, and Barrett's Epithelium. *Gastroenterology* **2011**, *141*, 1762–1772. [CrossRef]
25. Ooft, S.N.; Weeber, F.; Dijkstra, K.K.; McLean, C.M.; Kaing, S.; van Werkhoven, E.; Schipper, L.; Hoes, L.; Vis, D.J.; van de Haar, J.; et al. Patient-derived organoids can predict response to chemotherapy in metastatic colorectal cancer patients. *Sci. Transl. Med.* **2019**, *11*, eaay2574. [CrossRef]
26. Madureira, M.; Faustino, V.; Schütte, H.; Pinho, D.; Minas, G.; Gassmann, S.; Lima, R. Red Blood Cells Separation in a Curved T-Shaped Microchannel Fabricated by a Micromilling Technique. In Proceedings of the VipIMAGE 2019; Springer: Cham, Switzerland, 2019; pp. 585–593.
27. Badder, L.M.; Hollins, A.J.; Herpers, B.; Yan, K. 3D imaging of colorectal cancer organoids identifies responses to Tankyrase inhibitors. *PLoS ONE* **2020**, *15*, e0235319. [CrossRef]
28. Lai, A.; Altemose, N.; White, J.A.; Streets, A.M. On-ratio PDMS bonding for multilayer microfluidic device fabrication. *J. Micromechanics Microengineering* **2019**, *29*, 107001. [CrossRef]
29. Carvalho, M.R.; Barata, D.; Teixeira, L.M.; Giselsbrecht, S.; Reis, R.L.; Oliveira, J.M.; Truckenmüller, R.; Habibovic, P. Colorectal tumor-on-a-chip system: A 3D tool for precision onco-nanomedicine. *Sci. Adv.* **2019**, *5*, eaaw1317. [CrossRef] [PubMed]
30. Achberger, K.; Probst, C. Merging organoid and organ-on-a-chip technology to generate complex multi-layer tissue models in a human retina-on-a-chip platform. *eLife* **2019**, *8*. [CrossRef]
31. Halldorsson, S.; Lucumi, E.; Gómez-Sjöberg, R.; Fleming, R.M.T. Advantages and challenges of microfluidic cell culture in polydimethylsiloxane devices. *Biosens. Bioelectron.* **2015**, *63*, 218–231. [CrossRef] [PubMed]
32. Grebenyuk, S.; Ranga, A. Engineering Organoid Vascularization. *Front. Bioeng. Biotechnol.* **2019**, *7*. [CrossRef] [PubMed]
33. Yen, D.P.; Ando, Y.; Shen, K. A cost-effective micromilling platform for rapid prototyping of microdevices. *Technology* **2016**, *4*, 234–239. [CrossRef]
34. Guckenberger, D.J.; de Groot, T.E.; Wan, A.M.D.; Beebe, D.J.; Young, E.W.K. Micromilling: A method for ultra-rapid prototyping of plastic microfluidic devices. *Lab Chip* **2015**, *15*, 2364–2378. [CrossRef]
35. Behroodi, E.; Latifi, H.; Bagheri, Z.; Ermis, E.; Roshani, S.; Salehi Moghaddam, M. A combined 3D printing/CNC micro-milling method to fabricate a large-scale microfluidic device with the small size 3D architectures: An application for tumor spheroid production. *Sci. Rep.* **2020**, *10*, 22171. [CrossRef] [PubMed]
36. Chen, Y.W.; Chen, M.C. A Facile Approach for Rapid Prototyping of Microneedle Molds, Microwells and Micro-Through-Holes in Various Substrate Materials Using CO₂ Laser Drilling. *Biomedicines* **2020**, *8*, 427. [CrossRef] [PubMed]
37. Wu, K.-W.; Kuo, C.-T.; Tu, T.-Y. A Highly Reproducible Micro U-Well Array Plate Facilitating High-Throughput Tumor Spheroid Culture and Drug Assessment. *Glob. Chall.* **2021**, *5*, 2000056. [CrossRef] [PubMed]
38. Karzbrun, E.; Kshirsagar, A.; Cohen, S.R.; Hanna, J.H.; Reiner, O. Human brain organoids on a chip reveal the physics of folding. *Nat. Phys.* **2018**, *14*, 515–522. [CrossRef] [PubMed]
39. Wang, Y.; Wang, L.; Guo, Y.; Zhu, Y.; Qin, J. Engineering stem cell-derived 3D brain organoids in a perfusable organ-on-a-chip system. *RSC Adv.* **2018**, *8*, 1677–1685. [CrossRef]
40. Zhang, Y.S.; Aleman, J.; Shin, S.R.; Kilic, T.; Kim, D.; Mousavi Shaegh, S.A.; Massa, S.; Riahi, R.; Chae, S.; Hu, N.; et al. Multisensor-integrated organs-on-chips platform for automated and continual in situ monitoring of organoid behaviors. *Proc. Natl. Acad. Sci. USA* **2017**, *114*, E2293. [CrossRef]
41. Jung, D.J.; Shin, T.H.; Kim, M.; Sung, C.O.; Jang, S.J.; Jeong, G.S. A one-stop microfluidic-based lung cancer organoid culture platform for testing drug sensitivity. *Lab Chip* **2019**, *19*, 2854–2865. [CrossRef]
42. Mazzocchi, A.R.; Rajan, S.A.P.; Votanopoulos, K.I.; Hall, A.R.; Skardal, A. In vitro patient-derived 3D mesothelioma tumor organoids facilitate patient-centric therapeutic screening. *Sci. Rep.* **2018**, *8*, 2886. [CrossRef] [PubMed]
43. Shirure, V.S.; Bi, Y.; Curtis, M.B.; Lezia, A. Tumor-on-a-chip platform to investigate progression and drug sensitivity in cell lines and patient-derived organoids. *Lab Chip* **2018**, *18*, 3687–3702. [CrossRef]
44. Schuster, B.; Junkin, M.; Kashaf, S.S.; Romero-Calvo, I.; Kirby, K.; Matthews, J.; Weber, C.R.; Rzhetsky, A.; White, K.P.; Tay, S. Automated microfluidic platform for dynamic and combinatorial drug screening of tumor organoids. *Nat. Commun.* **2020**, *11*, 5271. [CrossRef]

45. Tehranirokh, M.; Kouzani, A.Z.; Francis, P.S.; Kanwar, J.R. Microfluidic devices for cell cultivation and proliferation. *Biomicrofluidics* **2013**, *7*, 051502. [CrossRef]
46. Duzagac, F.; Saorin, G.; Memeo, L.; Canzonieri, V.; Rizzolio, F. Microfluidic Organoids-on-a-Chip: Quantum Leap in Cancer Research. *Cancers* **2021**, *13*, 737. [CrossRef]
47. Yu, F.; Hunziker, W.; Choudhury, D. Engineering Microfluidic Organoid-on-a-Chip Platforms. *Micromachines* **2019**, *10*, 165. [CrossRef]
48. Simian, M.; Bissell, M.J. Organoids: A historical perspective of thinking in three dimensions. *J. Cell Biol.* **2017**, *216*, 31–40. [CrossRef] [PubMed]
49. Kratochvil, M.J.; Seymour, A.J.; Li, T.L.; Paşca, S.P.; Kuo, C.J.; Heilshorn, S.C. Engineered materials for organoid systems. *Nat. Rev. Mater.* **2019**, *4*, 606–622. [CrossRef] [PubMed]
50. Brassard, J.A.; Lutolf, M.P. Engineering Stem Cell Self-organization to Build Better Organoids. *Cell Stem Cell* **2019**, *24*, 860–876. [CrossRef] [PubMed]



Article

Multilayer Thin-Film Optical Filters for Reflectance-Based Malaria Diagnostics

Mariana S. Costa ¹, Vitória Baptista ^{1,2,3}, Gabriel M. Ferreira ¹, Duarte Lima ¹, Graça Minas ¹ , Maria Isabel Veiga ^{2,3} and Susana O. Catarino ^{1,*}

- ¹ Microelectromechanical Systems Research Unit (CMEMS-UMinho), School of Engineering, Campus de Azurém, University of Minho, 4800-058 Guimarães, Portugal; a77120@alunos.uminho.pt (M.S.C.); id8971@alunos.uminho.pt (V.B.); a81445@alunos.uminho.pt (G.M.F.); a79111@alunos.uminho.pt (D.L.); gminas@dei.uminho.pt (G.M.)
- ² Life and Health Sciences Research Institute (ICVS), School of Medicine, Campus de Gualtar, University of Minho, 4710-057 Braga, Portugal; mariaveiga@med.uminho.pt
- ³ ICVS/3B's-PT Government Associate Laboratory, 4710-057 Braga/Guimarães, Portugal
- * Correspondence: scatarino@dei.uminho.pt

Abstract: Malaria diagnosis relies on optical microscopy and/or rapid diagnostic tests based on detecting specific malaria antigens. The clinical sensitivity of these methods is highly dependent on parasite density, with low levels of detection at low parasite density, challenging the worldwide malaria elimination efforts. Therefore, there is a need for diagnostic methods with higher sensitivity, demanding innovative diagnostics devices able to detect malaria at low parasite density and at early stages of the disease. We propose an innovative optical device for malaria diagnosis, based on optical reflectance spectrophotometry, for the detection of parasites through the quantification of haemozoin. For this purpose, a set of eight thin-film optical filters, based on multilayer stacks of MgO/TiO₂ and SiO₂/TiO₂ thin-films, with high transmittance and low full width at half maximum (FWHM) at specific wavelengths, was designed and fully characterized (both numerically and experimentally). A preliminary assessment of its potential to reconstruct the original spectra of red blood cells was performed, both in uninfected and *Plasmodium falciparum*-infected samples. The obtained results show that, although the experimental filters have a non-ideal performance characteristic, they allow us to distinguish, based on only 8 discrete points in the optical spectrum, between healthy and malaria infected samples, up to a detection limit of 12 parasites/μL of red blood cells. Those results enhance the potential of using such a device for malaria diagnostics, aiming for non-invasiveness.

Keywords: diagnostics; malaria; optical filters; reflectance; spectrophotometry; TFCalc



Citation: Costa, M.S.; Baptista, V.; Ferreira, G.M.; Lima, D.; Minas, G.; Veiga, M.I.; Catarino, S.O. Multilayer Thin-Film Optical Filters for Reflectance-Based Malaria Diagnostics. *Micromachines* **2021**, *12*, 890. <https://doi.org/10.3390/mi12080890>

Academic Editor: Angeliki Tserepi

Received: 9 July 2021

Accepted: 26 July 2021

Published: 28 July 2021

Publisher's Note: MDPI stays neutral with regard to jurisdictional claims in published maps and institutional affiliations.



Copyright: © 2021 by the authors. Licensee MDPI, Basel, Switzerland. This article is an open access article distributed under the terms and conditions of the Creative Commons Attribution (CC BY) license (<https://creativecommons.org/licenses/by/4.0/>).

1. Introduction

Malaria is an infectious disease and a serious public health problem in 87 countries worldwide [1,2]. According to the latest report from the World Health Organization (WHO, Geneva, Switzerland), in 2020, 229 million people were infected with malaria and from those infections resulted 409,000 deaths [2], mainly in the endemic regions with poor economic and sanitary conditions [3]. The main methods for field malaria diagnosis are based on the detection of the etiological agent, *Plasmodium* spp., in the patients' blood through optical microscopy [4] and/or through rapid diagnostic tests (RDT) based on detecting specific malaria antigens [5]. Although these methods are low cost and relatively easy to implement, they face several challenges in many malaria-endemic regions, including the requirement for expert microscopists, inadequate quality control and the possibility of false-negative results due to low parasitaemia (<20 parasites/μL). Consequences of misdiagnosis may delay treatment, increasing the risk of disease severity and increasing the number of persons capable of infecting mosquitoes in the community. Molecular diagnosis by polymerase chain reaction (PCR) [4,6], although it allows the detection of low parasitaemia

infections (down to 1–5 parasites/ μL), implies sophisticated laboratories unavailable in endemic regions and highly skilled personnel and, therefore, it is recommended by the WHO not for diagnosis but only for research purposes [2]. Considering sustainable development goals, there is an urge for malaria control and the eventual elimination of the disease, demanding new technologies allowing higher sensitivity than the current methods, lower cost, non-invasiveness, easy handling, immediate feedback and environmentally more sustainable alternatives.

Malaria is a disease transmitted to human beings by the bite of the female *Anopheles* mosquito, which, when infected, has *Plasmodium* parasites in its salivary glands [7]. Within the complex life cycle of the malaria parasite, the symptomatic stage of the infection happens inside the red blood cells (RBCs), with a 48-h cycle maturation (in case of *Plasmodium falciparum*) that goes from parasite invasion of the RBC, up to RBC burst and release of new parasites ready to invade new RBCs. This stage of infection leads to a set of morphological and biochemical reactions on the RBCs when infected by the parasites. The main phenomena are the uptake and breakdown, by the parasite, of the RBC haemoglobin, as a source of nutrients, which leads to the release of the toxic haem group, that the parasite cannot digest. To detoxicate it, the parasite is capable of polymerising haem into inert crystal particles, called malaria pigment or haemozoin [8]. This process happens inside the parasite throughout its developmental stages, passing from a ring stage, trophozoite and schizont, leading to an increase in haemozoin crystals, while the haemoglobin concentration decreases throughout these stages. Although this process of haemoglobin degradation and haemozoin formation starts at the early ring stage, the major part of this process takes place in further developmental stages (trophozoite and schizont), where most of the metabolic activity happens, this being the reason why the malaria pigment is more visible under light microscopy at later stages. Haemoglobin and haemozoin present distinct optical characteristics, mainly in the visible range, with different absorbance and reflectance spectra, and those spectra diverge depending on the molecules' concentrations in the blood [9]. As healthy human blood does not contain haemozoin in its constitution, this is a unique product that can be used as a biomarker for malaria detection [10]. Based on this principle, optical spectrophotometry has become an alternative solution for the improvement of the current malaria diagnostic methods [11,12]. With this technology, the detection could be performed for all *Plasmodium* species that infect humans, since all of them produce haemozoin during their intraerythrocytic life cycle. Nevertheless, using haemozoin as a biomarker for malaria detection can become challenging if the measurements are based on patients' finger prick blood samples. This relates specifically to the most prevalent and deadly parasite, *P. falciparum*, that presents cytoadherence to venous endothelial cells at mature trophozoites and schizont stages, leaving only the ring stages (containing the least haemozoin) circulating in the blood stream [13]. To overcome this and increase sensitivity, technology would have to consider this limitation.

In this work, a method for optical detection of malaria based on reflectance spectrophotometry is proposed, aiming for the exemption of blood sampling and, therefore, non-invasiveness. This technique will allow the identification of malaria parasites, at all intraerythrocytic developmental stages and from all human *Plasmodium* species, through haemozoin quantification, aiming for a detection limit better than the current microscopy or RDT diagnostic methods (aiming up to 12 parasites/ μL of red blood cells) [14]. For the implementation of such a technique in a full integrated system, it will be expected that the detection system comprises a light source covering the optical visible spectrum (from 400 nm to 800 nm [9]), optical detectors (as photodiodes, that capture the reflected light and convert it into electric currents) and optical bandpass filters, tuned at specific wavelengths, with high transmittance and low full width at half maximum (FWHM). These optical filters, which are the focus of this work, allow the selection of specific wavelengths at the photodetector site, to measure and reconstruct the samples' spectra based on a limited and discrete number of spectral bands (eight, as will be described). The filters will be based on multilayer thin-films, with a Fabry–Perot interferometer structure, compatible with

CMOS (Complementary metal–oxide–semiconductor) processes. Therefore, the main goal of this study is the numerical and experimental characterization of the optical response of eight bandpass thin-film optical filters, as well as the assessment of their potential to reconstruct, based on only eight discrete wavelengths, the original continuous spectra of uninfected and infected RBCs, aiming for their integration on a malaria diagnostic device.

2. Methods

2.1. Optical Reflectance Spectra of Uninfected and Parasite Infected RBCs

In order to select the target wavelengths for the thin-film optical filters, preliminary assays were performed to characterize the optical spectra of *P. falciparum*-infected RBCs. Figure 1 presents the average ($n = 3$) continuous normalized reflectance spectra of uninfected and cultured *P. falciparum*-infected RBCs, at different parasitaemia, from 12 to 500 parasites/ μL of RBCs, both in early (rings) and late (trophozoites) stages [9]. Samples with 40% haematocrit were considered to represent the quantity of RBCs in human whole blood. Healthy human whole blood, needed for the samples' testing and *P. falciparum* in vitro cultures, was provided by Instituto Português do Sangue e Transplantação (IPST; Portuguese Blood and Transplantation Institute), Porto, Portugal. All procedures for blood collection, transport and in vitro experiments were carried out in compliance with the EU directives 2004/23/CE, 2006/17/CE and 2006/86/CE. The spectra were measured with a spectrophotometric top-bench setup, comprising a 200 W Quartz Tungsten Halogen light source (model 66881, Oriel Newport), optical-fibre reflectance probes, a cuvette sample holder and an AvaSpec-ULS2048XL EVO spectrophotometer with an integrated monochromator (Avantes, NS Apeldoorn, The Netherlands). Barium sulphate was used as a reference for reflectance measurements. The samples were measured in 1 mm optical path cuvettes. Reflectance data were collected and post-processed using the AvaSoft 8.11 software.

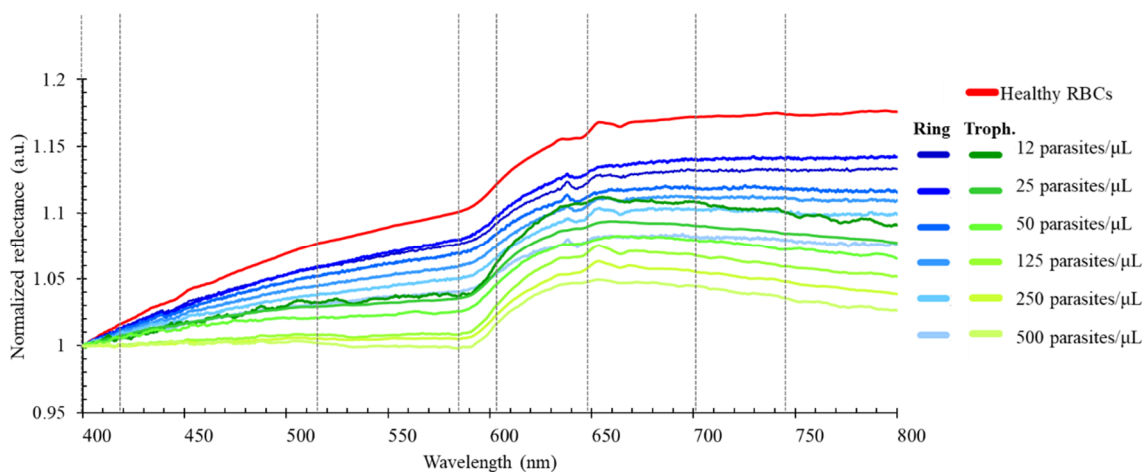


Figure 1. Normalized reflectance spectra (a.u.) of uninfected RBCs (in red) and RBCs with early (rings, in blue) and late (trophozoites, in green) parasites, with different *P. falciparum* parasitaemia, from 12 to 500 parasites/ μL of RBCs, in the 400–800 nm range of the optical spectrum ($n = 3$) [9]. The vertical dashed lines represent the 8 selected spectral bands.

From the presented spectra, we selected a set of 8 specific relevant spectral bands, in the visible range of the optical spectrum—397 nm, 419 nm, 516 nm, 585 nm, 603 nm, 649 nm, 701 nm and 746 nm—for the simulation and experimental characterization of thin-film optical filters. These 8 spectral ranges were selected as they are fairly distributed within the entire spectra and capture the main oscillations of the samples' spectra, as previously presented. Aiming for the future integration of the thin-film optical filters in a malaria diagnostic device, and in order to allow the specific deposition of each of the filters on top of a photodiode array, the selection of 8 spectral bands is justified by a reduction of the size and complexity of the final system (when compared with a previous study of the team considering 16 spectral bands) [14], assuring the essential compromise between

the accuracy of the extraction of the optical spectra and the number of wavelengths (and consequent required optical filters).

2.2. Design and Simulation of the Thin-Film Optical Filters

As referred to in the previous Section 2.1, the set of 8 spectral bands was selected to help to accurately extract the relevant information of the optical spectra and reconstruct the continuous reflectance spectra of the uninfected and malaria infected samples, based on a minimum number of wavelengths. The bandpass thin-film optical filters are based on multilayer structures, forming a Fabry–Perot interferometer structure, with two flat parallel mirrors separated by a resonance cavity layer, with a pre-defined thickness [15,16], as schematically represented in Figure 2.

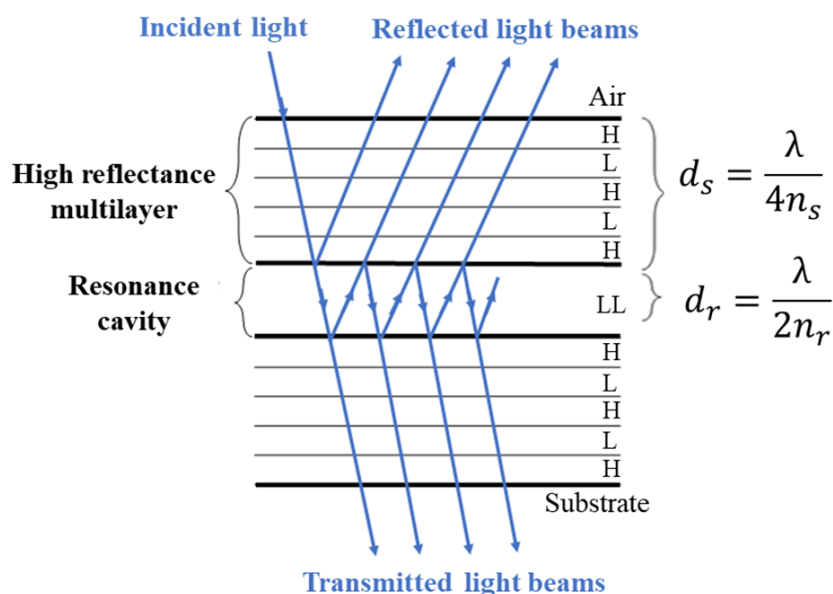


Figure 2. Multilayer thin-film optical filter structure. In the scheme, λ is the transmitted wavelength and n is the refractive index of the resonant cavity material. Considering a first order interference and a light incidence angle of 0° , d_r and d_s expressions describe the calculus of the resonance cavity and mirror thicknesses, respectively [17].

According to the literature, a Fabry–Perot interferometer structure with dielectric mirrors usually contains 9 or more thin-film layers, this number being a compromise between low FWHM, high transmittance and fabrication constraints [18]. After preliminary simulations, aiming for a better filter performance, 11 layers per filter structure [15], comprised of five dielectric layers in each mirror with, alternately, high (H) and low (L) refractive index materials, were chosen. For each filter, the resonance cavity is characterized by a multiple-beam interference, causing a high optical transmission at a narrow band of wavelengths, around a wavelength for which the cavity is a multiple of one-half wavelength thick [17]. Therefore, assuming similar films on both mirrors, the thickness of the resonance cavity determines the tuned wavelength of the filter. Each of these mirrors is composed by dielectric films, characterized by high transmittance at specific wavelengths and low energy absorption rates. Magnesium oxide (MgO) and silicon dioxide (SiO₂), with low refractive indexes, and titanium dioxide (TiO₂), with a high refractive index, were selected as the dielectric materials for the thin-films’ filters, since they are rigid, extremely difficult to remove from the substrate, compatible with CMOS fabrication and their deposition processes are well characterized and documented [17].

The design and computational simulation of the 8 filters (centred at the 397, 419, 516, 585, 603, 649, 701 and 746 nm spectral bands in the visible spectrum) was performed in TFCalc 3.5 (Software Spectra Inc., Portland, OR, USA), a software tool based on finite

element methods. The filters were characterized regarding their transmittance peak and FWHM, aiming for transmittance as high as possible (with at least twice the intensity of any noise peak in the considered spectral range) and FWHM around 10 nm, which can be considered acceptable for the intended application, as it avoids superposition between the spectral bands of neighbouring filters.

The optical filters were divided into three spectral regions: UV/VIS (397–419 nm), VIS (516–603 nm) and VIS/IR (649–746 nm), in order to optimize the design and fabrication processes (allowing simultaneous depositions). Besides the thickness and the properties of the films' materials, in particular their refractive indexes (obtained from the *refractiveindex.info* database), the simulation also took into consideration the properties of the substrate (glass), incident and exit medium (air) and reference wavelength, which have influence on the filters' optical responses. For each of the three spectral regions, a reference wavelength was selected (420 nm, 550 nm and 680 nm, respectively). Table 1 presents the combination of the layers' thickness values for each optical filter, designed using TFCalc, and optimized (through iterative adjustments) for the highest transmittance.

Table 1. Optical filters in the UV/Vis, Vis and Vis/IR spectral regions and respective MgO/TiO₂ and SiO₂/TiO₂ layer thicknesses (RC: Resonance Cavity).

		Maximum Transmittance Peaks Per λ (nm)							
		397	419	516	585	603	649	701	746
		Thickness layer (nm)							
TiO ₂	40	TiO ₂	44		63			80	
MgO	63	SiO ₂	75		97			118	
TiO ₂	40	TiO ₂	44		63			80	
MgO	63	SiO ₂	75		97			118	
TiO ₂	40	TiO ₂	44		63			80	
MgO (RC)	110	SiO ₂ (RC)	141	150	218	236	198	249	294
TiO ₂	40	TiO ₂	44		63			80	
MgO	63	SiO ₂	75		97			118	
TiO ₂	40	TiO ₂	44		63			80	
MgO	63	SiO ₂	75		97			118	
TiO ₂	40	TiO ₂	44		63			80	

As observed in Table 1, the narrow optical filters were divided into four spectral regions: 397 nm, 419 nm, 516–603 nm and 649–746 nm. For each group, the two mirrors are symmetrical and consist of five alternate layers of TiO₂ and MgO thin-films, for the filter centred at 397 nm, and TiO₂ and SiO₂ thin-films, for the other seven filters. During the simulations, MgO led to a better filter performance near the UV region, when compared to SiO₂ and, therefore, it was the selected material for the 397 nm filter. For each filter inside the spectral region, the layers of the same material have the same thickness. This process means that the definition of each spectral band can be performed only by adjusting the thickness of the MgO or SiO₂ resonant cavities.

2.3. Experimental Setup

The proposed and simulated eight thin-film optical filters (397 nm, 419 nm, 516 nm, 585 nm, 603 nm, 649 nm, 701 nm and 746 nm) were fabricated through ion beam deposition in glass substrates and characterized in the CMEMS-UMinho laboratories, regarding their optical transmittance and FWHM. The fabrication process of the optical filters is detailed in [17,19], and it is not the focus of this study. However, it is relevant to note that, after fabrication, the optical filters may not assure the exact same optical properties as the simulated ones, as the deposition techniques and setups may lead to slight variations in the materials' refractive indexes. To perform the experimental characterization of the fabricated optical filters, a set of long pass and short pass commercial optical filters (acquired from Edmund Optics and Thorlabs) was also used, in addition to the thin-film bandpass filters, in order to remove additional transmittance regions and noise signals that could appear outside the

range of interest. Figure 3 presents photographs of the eight thin-film bandpass optical filters, centered at 397, 419, 516, 585, 603, 649, 701 and 746 nm. Figure S1 (Supplementary Material) displays examples of commercial long pass (370 nm, 550 nm and 600 nm) and short pass (500 nm) filters, also used in the experimental assays.

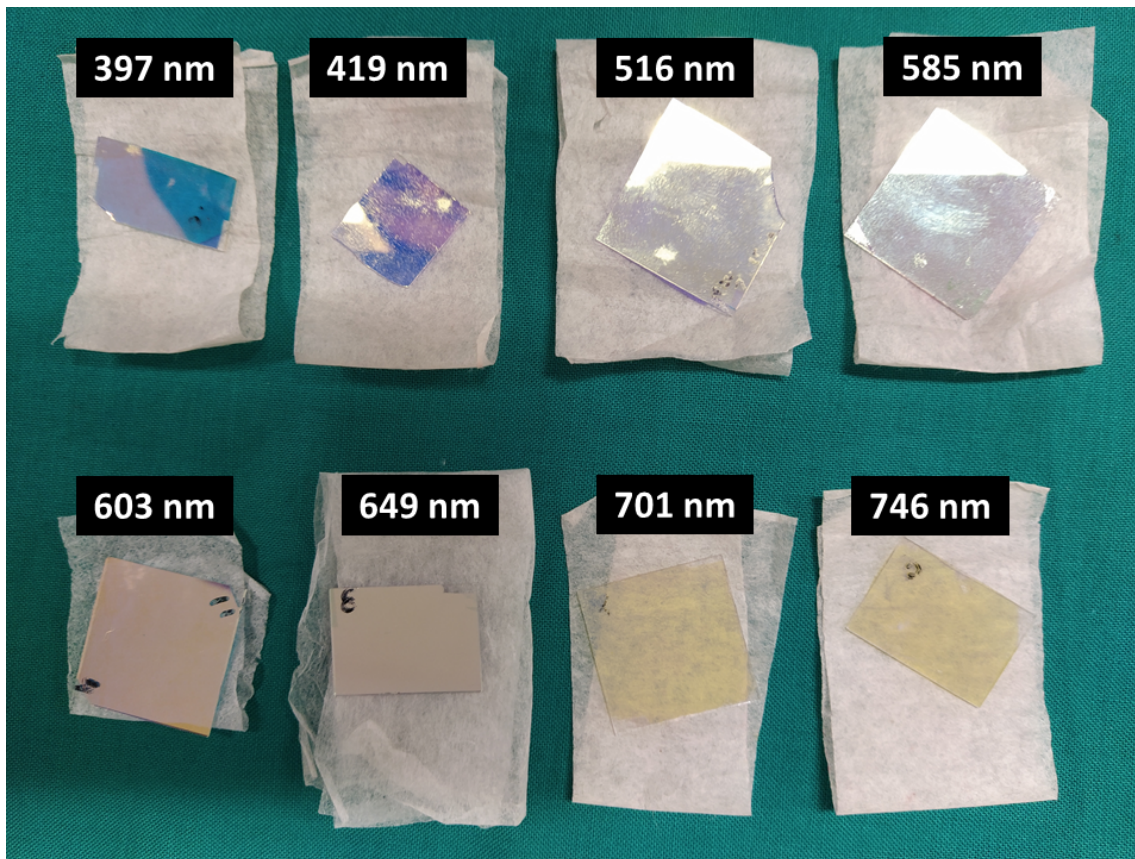


Figure 3. Photographs of the 8 thin-film optical filters experimentally characterized, centred at 397, 419, 516, 585, 603, 649, 701 and 746 nm, used in the experimental assays. In some of the filters, it is clear that some damage of the thin-film surfaces occurred after their prolonged use.

The optical transmittance of the eight bandpass thin-film optical filters was performed in a top bench setup at CMEMS. The setup includes a 200 W Quartz Tungsten Halogen light source (model 66881, Oriel Newport, Irvine, CA, USA), a monochromator (model 74000, Thermo Oriel instruments, Newport, Irvine, CA, USA) that selects the emission wavelength, an optical fiber transmittance probe, a mechanical support for the positioning and alignment of the optical filters, a commercial photodiode (aligned with the filters and the fiber) that converts the light transmitted at each wavelength into an electric current, a picometer (Keithley 487, Cleveland, OH, USA) to measure the current and a computer for data acquisition and post-processing using a LabView custom made tool. Figure 4 presents the incident white light spectral photocurrent as a function of wavelength, which is considered the reference baseline for the optical filters' transmittance measurements. Therefore, for each measurement, the obtained photocurrent at each wavelength (from 350 to 850 nm) is divided by that reference curve and the transmittance spectrum is obtained.

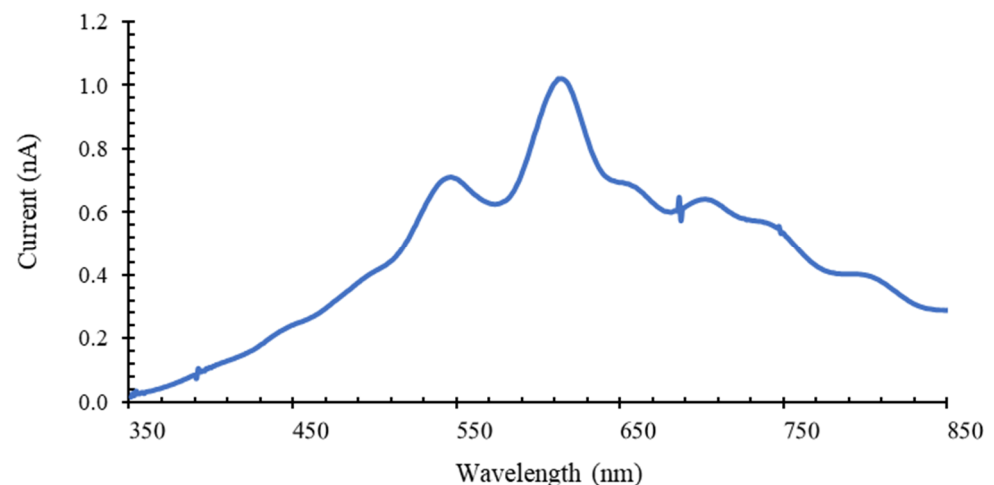


Figure 4. White light spectral current (A), emitted by the 200 W Quartz Tungsten Halogen light source and measured by a commercial photodiode, as function of wavelength (nm).

3. Results

3.1. Optical Filters Characterization

Figure 5 presents the simulation of the central spectrum transmittance for the eight bandpass thin-film optical filters previously designed, according to Table 1. According to the results, in their specific spectral band, the designed filters have high transmittance (above 90% for all).

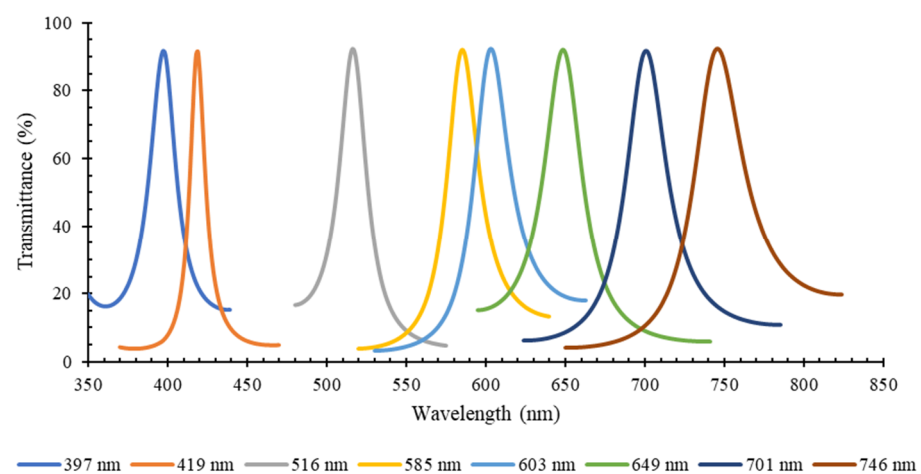
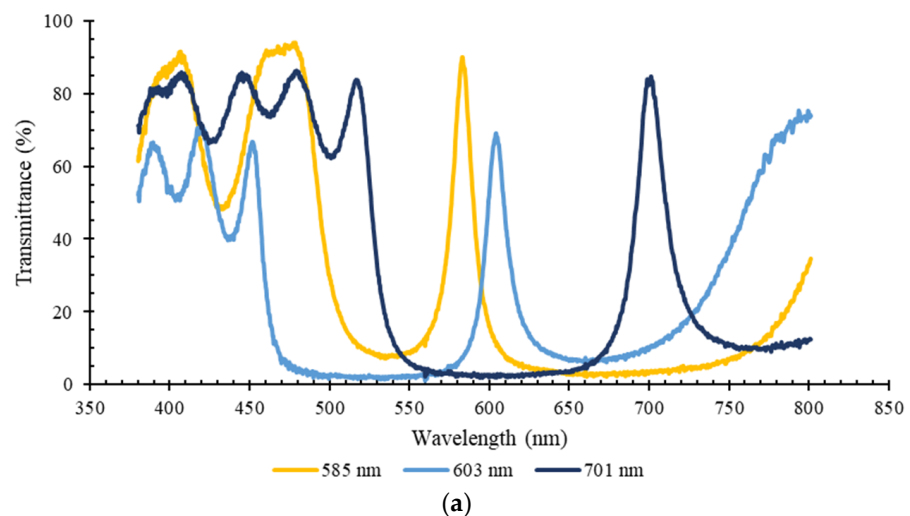


Figure 5. Simulation results of the central spectrum transmittance (%) vs. wavelength (nm), for the 8 designed MgO/TiO₂ and SiO₂/TiO₂ optical filters, according to the structure and dimensions presented in Table 1.

Although the FWHM results show some superposition between the 585 and 603 nm wavelength bandpass filters, these multilayer stacks, comprised of 11 layers of MgO/TiO₂ and SiO₂/TiO₂ thin-films and MgO or SiO₂ resonance cavity layers, assure relatively good optical features. Although the global performance of the optical filters could be theoretically improved by increasing the number of layers to 13, the complexity of the fabrication process would also increase.

After the design, simulation and fabrication of the eight optical filters, they were experimentally characterized using the previously described top bench setup of Section 2.3. Figure 6a presents, for exemplification purposes, the full transmittance spectra of three of the fabricated thin-film optical filters, for the 585, 603 and 701 nm spectral bands, measured in the 350–850 nm range of the optical spectrum. For all the filters, although there is a

high transmittance peak near the expected wavelength (with values always > 70%), it is inferior to the simulated one (as presented in Figure 5). Additionally, in Figure 6a, the high transmittance regions outside the relevant spectral bands are visible. These bands will be experimentally removed by superposing commercial long pass and short pass optical filters on top of the thin-film bandpass filters. This behaviour was observed for all the eight thin-film optical filters. Therefore, Figure 6b presents a list of commercial short and long pass optical filters, which were added to remove the undesired spectral bands in each of the eight targeted bandpass wavelengths. The transmittance spectra of all the commercial short and long pass filters listed in Figure 6b are presented in Figure S2 of the Supplementary Material.



(a)

Wavelength (nm)		
Thin-film bandpass filter	Commercial long pass filters	Commercial short pass filters
397	370 [EO]	450 [EO] + 500 [ThL] + 600 [EO]
419	370 [EO]	450 [EO] + 500 [ThL] + 600 [EO]
516	450 [EO]	650 [EO]
585	500 [ThL]	650 [EO]
603	550 [EO]	650 [EO]
649	600 [EO]	700 [EO]
701	600 [EO]	800 [EO]
746	600 [EO]	800 [EO]

(b)

Figure 6. (a) Experimental results ($n = 3$) of transmittance (%) vs. wavelength (nm), using a spectrophotometric top bench setup for 3 of the $\text{SiO}_2 / \text{TiO}_2$ optical filters centred at 585, 603 and 701 nm, without using commercial filters; (b) list of the commercial long pass and short pass optical filters and respective manufacturers (EO–Edmund Optics; ThL–Thorlabs) used in combination with each of the 8 bandpass thin-film optical filters (see Figure S2 of the Supplementary Material for the optical transmittance spectra of these filters).

In order to assess the effect of the additional commercial long pass and short pass optical filters in the transmittance spectra of the thin-film optical filters, Figure 7 presents the

experimental results of the central spectra from the peak transmittance spectra of the eight bandpass thin-film optical filters, without using any other optical filters to limit the spectral range outside the main peak region (Figure 7a); and using the different combinations of commercial long pass and short pass optical filters, as presented in Figure 6b (Figure 7b). In both cases, the transmittance peaks are clearly visible in their specific spectral bands. However, as expected, when additional filters are included (Figure 7b), the transmittance of the bandpass optical filters significantly decreases according to the combination of the transmittance of the passband commercial filters. All transmittance curves correspond to the average of three measurements.

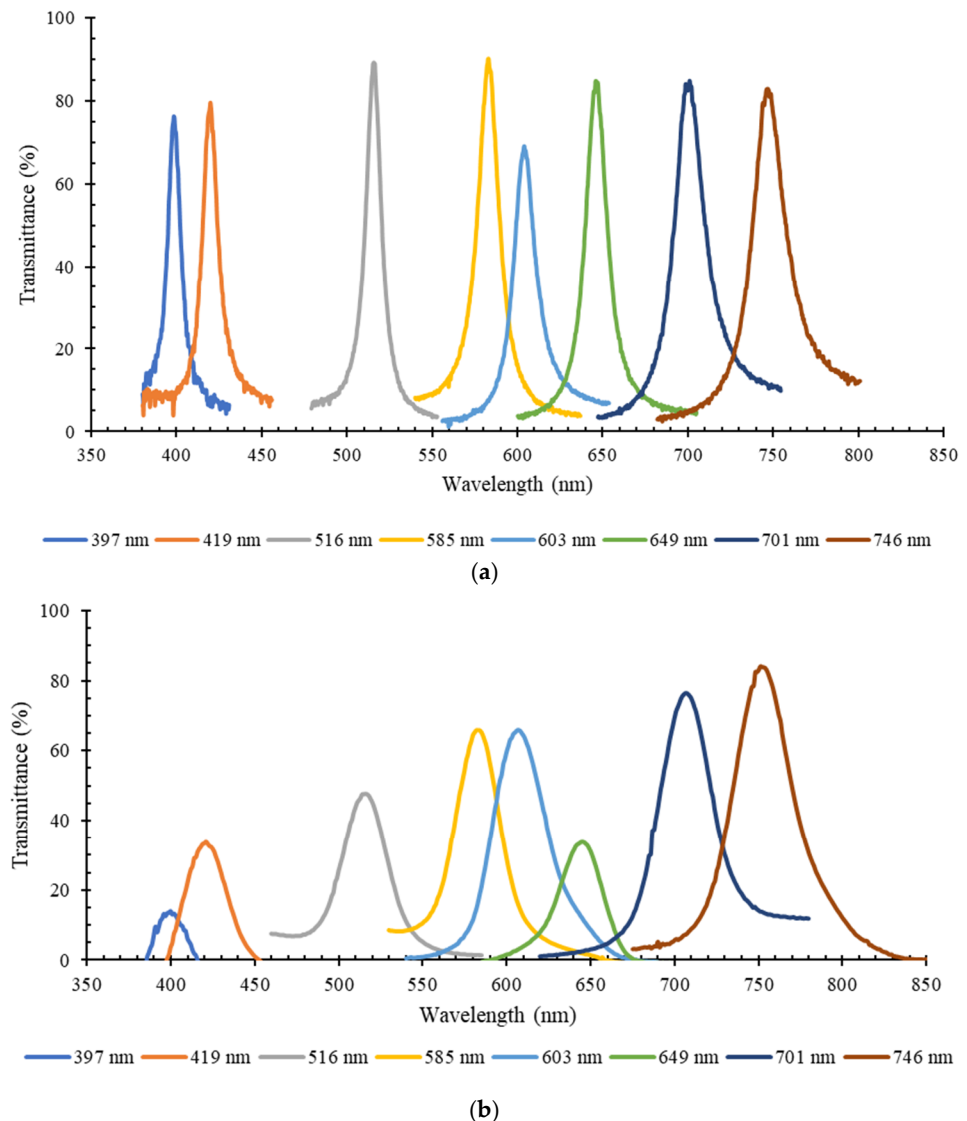


Figure 7. Experimental results ($n = 3$) of transmittance (%) vs. wavelength (nm), for the 8 MgO/TiO₂ and SiO₂/TiO₂ optical filters, measured with a spectrophotometric top bench setup: (a) without using additional commercial filters; (b) using commercial short pass and long pass filters to remove high transmittance components outside the relevant spectral bands.

When compared to the numerical results, the peak transmittance of the eight optical filters, in the absence of additional commercial short and long pass filters, is still high (above 70% for all the fabricated filters). After adding the commercial long and short pass filters, it was observed that almost all optical filters (except the 746 nm filter) present optical transmission values significantly lower than the simulated ones, which result from the combinations of the different required filters. Particularly, two filters closer to the

ultraviolet (UV) region of the spectra (397 and 419 nm) have transmittance below 40%. On the contrary, near the infrared (IR) region, the optical filters (701 and 746 nm) present considerably good transmittance spectra, around or above 80%. For example, for the 649 nm bandpass filter, the significant reduction in the transmittance is explained by the effect of both commercial short pass and long pass filters, as shown in Figure 8. In addition to the 600 nm cutoff long pass filter, needed to remove the high transmittance of the filter in the 350–500 nm region, a 700 nm cutoff short pass filter was also needed to reduce the transmittance effect that is visibly increasing after 750 nm, and still affects the photodiode readout. As seen in Figure 8, this short pass filter has transmittance around 50% in the visible range of the spectrum, which causes the significant decrease in transmittance in the 649 nm relevant wavelength.

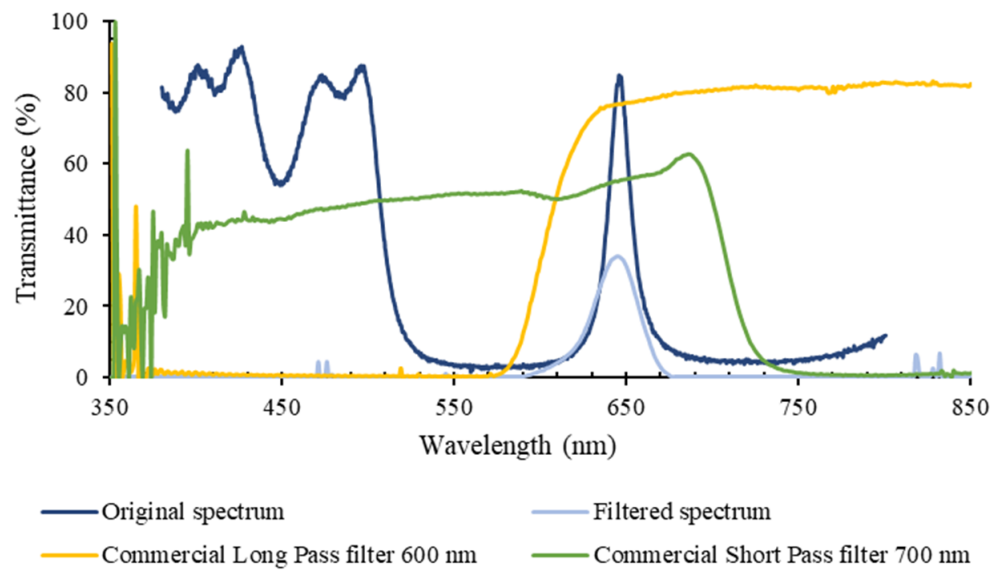


Figure 8. Experimental transmittance (%) vs. wavelength (nm) spectrum ($n = 3$), of the 649 nm bandpass filter, measured with the spectrophotometric top bench setup: without using additional commercial filters (dark blue line); using the commercial short pass and long pass filters (light blue); and spectra of the commercial long pass (yellow) and short pass (green) filters, used to remove high transmittance components outside the relevant spectral bands (as listed in Figure 6b).

Thus, these results show that, although adding short and long pass optical filters helps to reduce the interference of other optical regions in the obtained spectra, they have a significant effect in the transmittance performance of the thin-film optical filters. Regarding FWHM, it is higher than 10 nm (value assumed as ideal for the intended application) for all the optical filters' spectra, and some superposition was observed between the spectra of the 585 nm, 603 nm and 649 nm optical filters. Figure 9 presents a comparison between the numerical and experimental FWHM, obtained for each of the eight optical filters (with and without the additional commercial short and long pass filters). The experimental data in the plot were obtained from Figure 7a,b, and the numerical data were acquired from Figure 5. It is possible to observe that all optical filters have a large FWHM (above 10 nm for all the designed filters), and it is significantly increased by adding the additional optical layers of the commercial filters, which may reduce the wavelength selectivity of the optical reading.

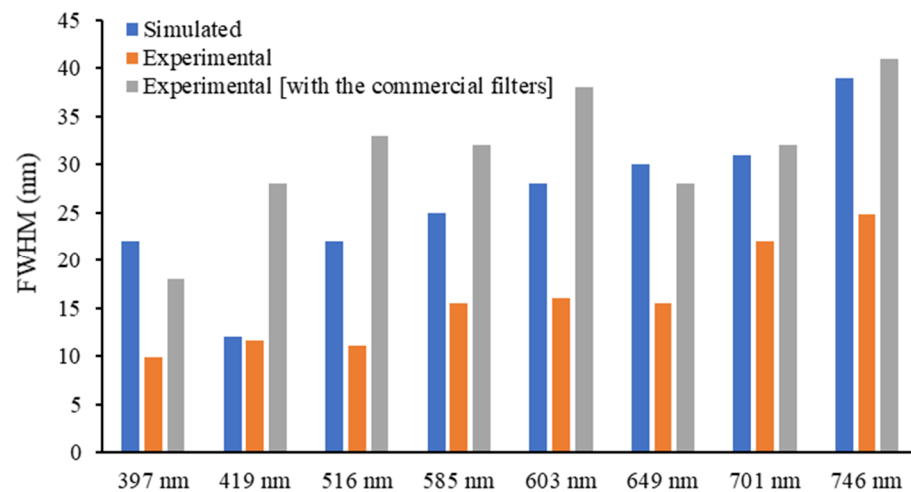


Figure 9. Comparison between the numerical simulated and experimental ($n = 3$) FWHM (nm) for each of the 8 MgO/TiO₂ and SiO₂/TiO₂ optical filters.

3.2. Discrete Reconstruction of the Samples' Original Spectra: Application to Malaria Detection

After the optical characterization of the optical filters, the filters were evaluated to assess if the eight discrete spectral bands allowed them to: (1) accurately extract the optical data and reconstruct optical reflectance spectra representative of the original continuous ones (as in the previous spectra from Figures 1 and 2); (2) detect differences between the optical reflectance spectra of uninfected and *P. falciparum*-infected RBCs, at different parasitaemia, for malaria diagnosis applications. For that purpose, the transmittance data of the designed eight optical filters were combined with uninfected and infected RBCs reflectance spectra, at different parasitaemia and developmental stages (rings and trophozoites), from 12 to 500 parasites/ μ L of RBCs. Figure 10 shows the resultant discrete spectra, based on eight spectral bands, obtained both numerically and experimentally (in the latter, with the addition of the commercial filters according to table of Figure 6b, assuring that only the high transmittance peak of the thin-film bandpass filters was considered).

The results show that, with the numerically simulated optical filters, it is possible to correctly extract the original reflectance spectra (Figure 1), based on only eight spectral bands. The experimental assays showed that the optical filters failed to correctly reconstruct the 649 nm region of the original spectra, with a clear decrease at that spectral band, when compared to the original continuous spectra. That variation is mainly explained by the significantly lower transmittance of the 649 nm optical filter (when the commercial short and long pass optical filters are also considered, as seen in Figures 7b and 8. However, since that trend is the same in all samples, the relative oscillations between different optical filters can be easily removed in a postprocessing phase, through an additional calibration or normalization step. Based on the experimental results of Figure 10b, it is observed that, between 397 nm and 516 nm, there is no visible difference between uninfected and infected RBCs. However, above 516 nm, there is an increase in the resultant spectra up to 600 nm, with slopes becoming higher as the parasitaemia decreases, between the several analysed spectral bands. It is also possible to distinguish between uninfected (red) and infected RBCs when the parasites are at different developmental stages: ring (blue) and trophozoite (green) stage. In order to evaluate the possibility of implementing simple detection and diagnostics algorithms, based on the data from the reflectance spectra, the slopes between the reflectance values at different wavelengths of the spectra were calculated through the $(y_2 - y_1)/(x_2 - x_1)$ expression. Figure 11 presents a selection of calculated slopes, between the reconstructed reflectance values at different wavelengths, obtained from the experimentally reconstructed spectra shown in Figure 10b. Table 2 presents the variation of the slopes (%) obtained for each *P. falciparum*-infected RBCs sample (with different parasitaemia values, between 12 and 500 parasites/ μ L of RBCs), when compared to the

uninfected RBCs, for the different wavelength intervals under analysis. The plot shows that, for a set of wavelength ranges, there is a variation in the slope as the parasitaemia varies in the RBCs samples. Particularly, in the experimental results, as the parasitaemia increases, the slopes clearly decrease, and this variation is higher at the 603–649 nm and 649–701 nm ranges, where different samples can be more easily distinguished. The results allow us to predict that, from a reduced number of optical filters (only eight spectral bands), it is possible to partially reconstruct the optical reflectance spectra of uninfected and infected RBCs samples with different parasitaemia, showing high potential for the intended application.

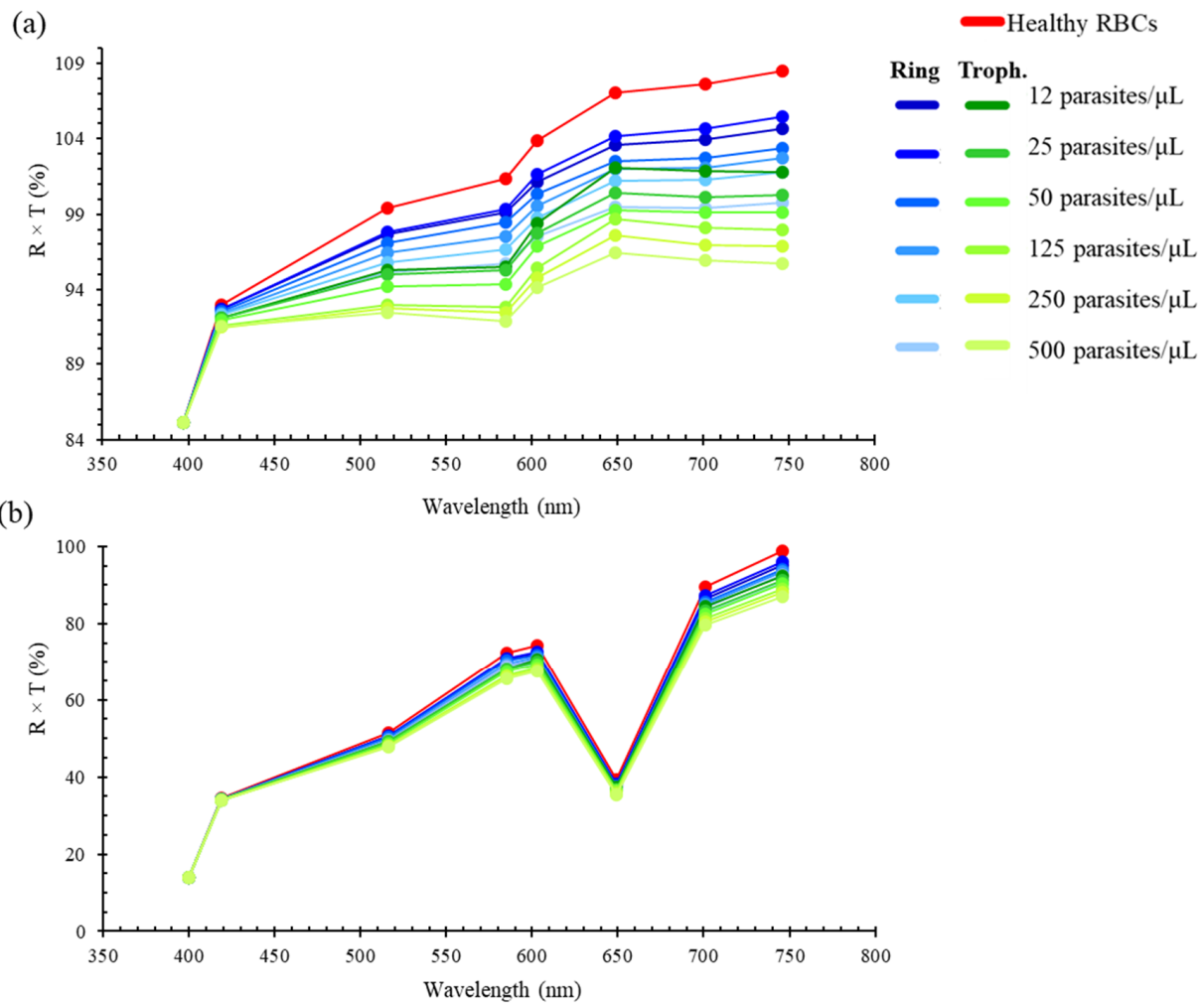


Figure 10. Reconstructed normalized optical reflectance spectra (%), based on 8 discrete wavelengths (represented by points in the plots), obtained from the combination between the transmittance spectra of the thin-film optical filters and the reflectance spectra of uninfected (red) and *P. falciparum*-infected RBCs samples (with different parasitaemia values, ranging from 12 to 500 parasites/ μL of RBCs), in both early (blue, rings) and late (green, trophozoites) stages. (a) Numerical simulation; (b) experimental results.

The analysis of Table 2 shows that, for most wavelength ranges, while for low parasitaemia the variation of the slopes between the uninfected and infected samples may be difficult to detect, it is clearly higher as the parasitaemia increases. The exception is the 585–603 nm range, where no trend is observed. Additionally, from Table 2, it is possible to evaluate the best wavelength intervals to consider for an accurate decision algorithm. For example, while the 397–419 nm interval results in a low variation in the slopes (below 3% for all parasitaemia and parasite stages), the wavelength intervals 516–585 nm and

701–746 nm show that, for 500 trophozoites/uL, the slopes vary up to more than 15% and 20%, respectively, when compared to the uninfected RBCs. At these wavelength ranges, even for the lower parasitaemia values (12 parasites/ μL in the ring stage), the variation is higher than 3% (which was the maximum variation detected at the 397–419 nm range). The lower variation at the 397–419 nm interval is probably due to the lower transmittance of the filters at those wavelengths, which leads to a decrease in the performance of the system in those spectral ranges. These results show that the transmittance of the filters, resultant from the superposition of the thin-film optical filters and the commercial ones, has a significant impact on the distinction between the *P. falciparum*-infected and uninfected samples. Additionally, as the FWHM of the optical filters is high (around 30 nm, as experimentally measured), it means that the filters are not specific for a single or highly narrow wavelength.

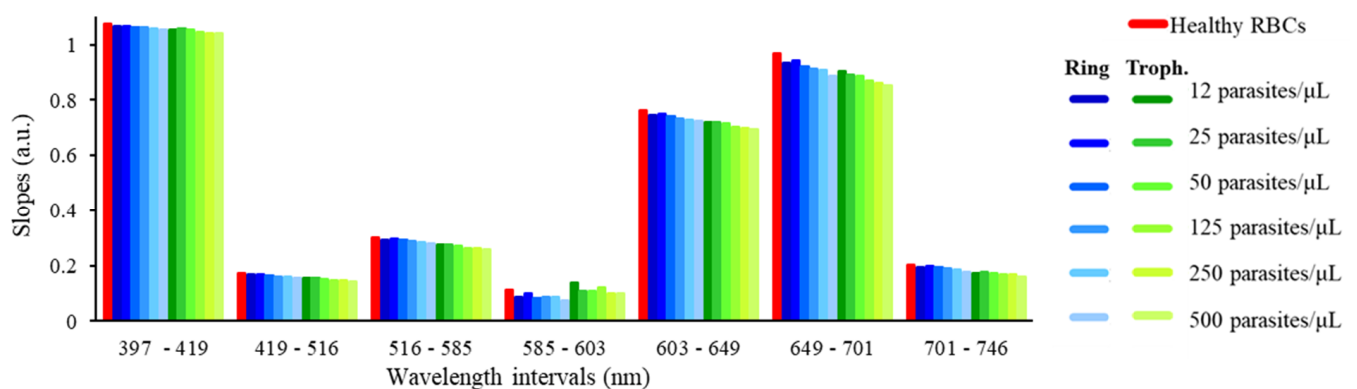


Figure 11. Bar plots representing the slopes of the lines between the experimental reconstructed reflectance spectra (%) at different wavelengths (397–419 nm, 419–516 nm, 516–585 nm, 585–603 nm, 603–649 nm, 649–701 nm, 701–746 nm), for uninfected (red) and *P. falciparum*-infected RBCs samples (with different parasitaemia values, between 12 and 500 parasites/ μL of RBCs), in both early (blue, rings) and late (green, trophozoites) developmental stages.

Table 2. Variation in the slopes (%) obtained for each *P. falciparum*-infected RBCs sample (with different parasitaemia values, between 12 and 500 parasites/ μL of RBCs), when compared to the uninfected RBCs, for the different wavelength intervals: 397–419 nm, 419–516 nm, 516–585 nm, 585–603 nm, 603–649 nm, 649–701 nm, 701–746 nm.

Wavelength Interval (nm)	Slope Variation (%)											
	Rings (Parasites/ μL)						Trophozoites (Parasites/ μL)					
	12	25	50	125	250	500	12	25	50	125	250	500
397–419	0.5	0.5	1.0	1.0	1.3	1.8	2.0	1.6	1.9	2.9	3.0	2.9
419–516	4.5	4.3	5.9	7.8	9.4	10.7	10.2	11.5	13.6	16.0	16.6	17.6
516–585	3.5	2.7	4.0	5.6	6.8	8.4	9.8	9.6	10.6	13.2	13.6	15.1
585–603	22.8	12.0	26.9	22.9	24.1	32.7	−22.7	2.3	5.4	−5.9	11.1	9.6
603–649	2.4	1.8	2.8	3.9	4.7	5.3	5.7	5.7	6.5	8.3	8.7	9.0
649–701	3.7	2.9	5.0	5.6	6.4	8.4	6.7	7.9	8.7	10.1	11.1	12.2
701–746	4.9	3.5	5.4	7.0	8.9	11.9	14.2	12.9	14.3	16.8	17.9	20.8

Despite the limitations of the method, concerning the low transmittance and high FWHM of the filters and the consequent reduced slope variations that were observed for some wavelength ranges, and which may lead to a minor resolution of the detection, it is possible to infer that the system, with the inclusion of a high precision decision algorithm based on line slopes, may be able to distinguish between uninfected and infected RBCs samples, enhancing its potential as a malaria diagnostic tool. It is relevant to notice that a decision algorithm must take into account the maximum possible information, by combining different wavelength ranges, in order to increase, as much as possible, the sensitivity and specificity of the algorithm.

4. Conclusions

This paper presented the design, simulation, experimental characterization and viability of eight narrow bandpass MgO/TiO₂ and SiO₂/TiO₂ thin-film optical filters, for the development of an optical reflectance-based malaria diagnostic device. As the deposition techniques and experimental setups may lead to slight variations in the materials' refractive indexes, the fabricated optical filters may not assure the exact same optical properties as the simulated ones. Thus, to compare the optical features of the filters, they were numerically and experimentally characterized regarding their optical transmittance and FWHM. While in the numerical simulations all the optical filters had transmittance above 90%, in the experimental results the transmittance values (after including the commercial short and long pass filters to remove unwanted transmittance peaks outside the relevant spectral range) were between approximately 18% (minimum, at 397 nm) and 85% (maximum, at 746 nm). The FWHM values, for both experimental and simulated optical filters, were above 10 nm, showing some superposition of the spectra between the 585 and 603 nm spectral bands. Further improvements need to be addressed in the fabrication of the thin-film optical filters, in order to reduce the high transmittance regions outside the targeted wavelength. Such improvements will lead to the reduction of the number of commercial short and long pass filters that are needed to remove the transmittance outside the targeted spectral bands, thus improving the transmittance of the filters and simplifying the final device. Despite some deviations in the transmittance spectra between the simulated and experimental filters, the eight fabricated bandpass optical filters showed success in extracting the optical information and reconstructing the reflectance spectra of uninfected and *P. falciparum*-infected RBCs. The system, based on only eight spectral bands, was able to distinguish them up to a detection limit of 12 parasites/μL of RBCs, even just considering parasites at early ring stage, which revealed superior sensitivity when compared with the currently available diagnostic methods in the field (RDT and microscopy). These results are an improvement towards point-of-care single chip fabrication, in comparison to the previous study with 16 wavelengths [14], showing that even with less spectral bands and a consequent simpler fabrication process, it is still possible to detect parasitaemia variations.

Supplementary Materials: The following are available online at <https://www.mdpi.com/article/10.3390/mi12080890/s1>, Figure S1: Photographs of examples of the commercial long pass (370 nm, 550 nm and 600 nm) and short pass (500 nm) filters, used in the experimental assays; Figure S2: Spectra of the commercial long (a) and short (b) pass optical filters used in the experimental setup and listed in Figure 6b.

Author Contributions: Conceptualization, M.S.C., G.M. and S.O.C.; Methodology, M.S.C., V.B., G.M.F., G.M. and S.O.C.; Validation and analysis, M.S.C., G.M.F. and D.L.; Investigation, M.S.C., V.B., G.M.F. and D.L.; Resources, M.I.V., G.M. and S.O.C.; Writing—original draft preparation, M.S.C.; Writing—review and editing, G.M., M.I.V. and S.O.C.; Supervision, M.I.V. and S.O.C.; Project administration, S.O.C.; Funding acquisition, S.O.C. All authors have read and agreed to the published version of the manuscript.

Funding: This work was supported by Project NORTE-01-0145-FEDER-028178 funded by NORTE 2020 Portugal Regional Operational Program under PORTUGAL 2020 Partnership Agreement through the European Regional Development Fund and the Fundação para a Ciência e Tecnologia (FCT), IP. This work was also supported by national funds, through the Portuguese FCT, under the reference projects UIDB/04436/2020, UIDP/04436/2020, UIDB/50026/2020 and UIDP/50026/2020, and by the ICVS Scientific Microscopy Platform, member of the national infrastructure PPBI-Portuguese Platform of Bioimaging (PPBI-POCI-01-0145-FEDER-022122). V. Baptista thanks FCT for the SFRH/BD/145427/2019 grant. Maria Isabel Veiga thanks FCT for her contract funding provided through 2020.03113.CEECIND. Susana Catarino thanks FCT for her contract funding provided through 2020.00215.CEECIND.

Data Availability Statement: All data are available upon request to the corresponding author.

Acknowledgments: The authors thank Susana Cardoso from INESC-MN, Lisbon, Portugal, for the optical filters' fabrication, and IPST–Instituto Português do Sangue e da Transplantação—Porto for providing the blood samples for the parasites' cultures.

Conflicts of Interest: The authors declare no conflict of interest. The funders had no role in the design of the study; in the collection, analyses, or interpretation of data; in the writing of the manuscript, or in the decision to publish the results.

References

1. Pham, N.M.; Karlen, W.; Beck, H.P.; Delamarche, E. Malaria and the 'last' parasite: How can technology help? *Malar. J.* **2018**, *17*, 260. [CrossRef] [PubMed]
2. World Health Organization. *World Malaria Report 2020*; World Health Organization: Geneva, Switzerland, 2020.
3. Mer, M.; Dünser, M.W.; Giera, R.; Dondorp, A.M. Severe malaria. Current concepts and practical overview: What every intensivist should know. *Intensive Care Med.* **2020**, *46*, 907–918. [CrossRef] [PubMed]
4. World Health Organization. UNICEF/UNDP/World Bank/WHO Special Programme for Research and Training in Tropical Diseases, "Microscopy for the Detection, Identification and Quantification of Malaria Parasites on Stained Thick and Thin Blood Films in Research Settings (Version 1.0)" Procedure, Methods Manual. 2015. Available online: <https://apps.who.int/iris/handle/10665/163782> (accessed on 5 July 2021).
5. Berzosa, P.; de Lucio, A.; Romay-Barja, M.; Herrador, Z.; González, V.; García, L.; Fernández-Martínez, A.; Santana-Morales, M.; Ncogo, P.; Valladares, B.; et al. Comparison of three diagnostic methods (microscopy, RDT, and PCR) for the detection of malaria parasites in representative samples from Equatorial Guinea. *Malar. J.* **2018**, *17*, 333. [CrossRef] [PubMed]
6. Echeverry, D.F.; Deason, N.A.; Davidson, J.; Makuru, V.; Xiao, H.; Niedbalski, J.; Kern, M.; Russell, T.L.; Burkot, T.R.; Collins, F.H.; et al. Human malaria diagnosis using a single-step direct-PCR based on the Plasmodium cytochrome oxidase III gene. *Malar. J.* **2016**, *15*, 128. [CrossRef] [PubMed]
7. Krampa, F.D.; Aniweh, Y.; Kanyong, P.; Awandare, G.A. Recent advances in the development of biosensors for malaria diagnosis. *Sensors* **2020**, *20*, 799. [CrossRef] [PubMed]
8. Francis, S.E.; Sullivan, D.J.; Goldberg, D.E. Hemoglobin metabolism in the malaria parasite Plasmodium falciparum. *Annu. Rev. Microbiol.* **1997**, *51*, 97–123. [CrossRef] [PubMed]
9. Baptista, V.; Calçada, C.; Silva, M.; Teixeira, M.; Ferreira, P.; Minas, G.; Peng, W.K.; Catarino, S.O.; Veiga, M.I. Hemozoin: The future in malaria diagnosis. In Proceedings of the MAM 2020—Molecular Approaches to Malaria Conference, Lorne, Australia, 23–27 February 2020.
10. Silva, I.; Lima, R.; Minas, G.; Catarino, S.O. Spectrophotometric characterization of hemozoin as a malaria biomarker. In Proceedings of the SPIE 10453, Third International Conference on Applications of Optics and Photonics, Faro, Portugal, 8–12 May 2017. [CrossRef]
11. Silva, I.; Lima, R.; Minas, G.; Catarino, S.O. Hemozoin and hemoglobin characterization by optical absorption towards a miniaturized spectrophotometric malaria diagnostic system. In Proceedings of the 2017 IEEE 5th Portuguese Meeting on Bioengineering (ENBENG), Coimbra, Portugal, 16–18 February 2017; pp. 1–4. [CrossRef]
12. Catarino, S.O.; Felix, P.; Sousa, P.J.; Pinto, V.; Veiga, M.I.; Minas, G. Portable Device for Optical Quantification of Hemozoin in Diluted Blood Samples. *IEEE Trans. Biomed. Eng.* **2020**, *67*, 365–371. [CrossRef]
13. Ridley, R.G. Haemozoin formation in malaria parasites: Is there a haem polymerase? *Trends Microbiol.* **1996**, *4*, 253–254. [CrossRef]
14. Costa, M.S.; Baptista, V.; Minas, G.; Veiga, M.I.; Catarino, S.O. Effect of the materials' properties in the design of high transmittance and low FWHM SiO₂/TiO₂ thin film optical filters for integration in a malaria diagnostics device. In Proceedings of the 14th International Joint Conference on Biomedical Engineering Systems and Technologies, Biodevices 2021, Vienna, Austria, 11–13 February 2021; Volume 1, pp. 21–31. [CrossRef]
15. Minas, G.; Wolffenbittel, R.F.; Correia, J.H. An array of highly selective Fabry-Perot optical channels for biological fluid analysis by optical absorption using a white light source for illumination. *J. Opt. A Pure Appl. Opt.* **2006**, *8*, 272–278. [CrossRef]
16. Minas, G.; Ribeiro, J.C.; Martins, J.S.; Wolffenbittel, R.F.; Correia, J.H. An array of Fabry-Perot optical-channels for biological fluids analysis. *Sens. Actuators A Phys.* **2004**, *115*, 362–367. [CrossRef]
17. Pimenta, S.; Cardoso, S.; Miranda, A.; de Beule, P.; Castanheira, E.M.S.; Minas, G. Design and fabrication of SiO₂/TiO₂ and MgO/TiO₂ based high selective optical filters for diffuse reflectance and fluorescence signals extraction. *Biomed. Opt. Express* **2015**, *6*, 3084. [CrossRef] [PubMed]
18. Ferreira, D.S.; Mirkovic, J.; Wolffenbittel, R.F.; Correia, J.H.; Feld, M.S.; Minas, G. Narrow-band pass filter array for integrated opto-electronic spectroscopy detectors to assess esophageal tissue. *Biomed. Opt. Express* **2011**, *2*, 1703. [CrossRef] [PubMed]
19. Pimenta, S.; Cardoso, S.; Castanheira, E.M.S.; Minas, G. Advances towards a miniaturized optical system for gastrointestinal cancer detection using diffuse reflectance and fluorescence spectroscopies. In *Gastrointestinal Cancers: Prevention, Detection and Treatment*; Tyagi, A.K., Prasad, S., Eds.; Nova Science Publishers, Inc.: Hauppauge, NY, USA, 2016; Volume 1, Chapter 13.

MDPI
St. Alban-Anlage 66
4052 Basel
Switzerland
Tel. +41 61 683 77 34
Fax +41 61 302 89 18
www.mdpi.com

Micromachines Editorial Office
E-mail: micromachines@mdpi.com
www.mdpi.com/journal/micromachines



MDPI
St. Alban-Anlage 66
4052 Basel
Switzerland

Tel: +41 61 683 77 34
Fax: +41 61 302 89 18

www.mdpi.com



ISBN 978-3-0365-3228-8